6-12-2012 12:00 AM

High-Pressure Study of Molecular Solids and 1D Nanostructures by Vibrational Spectroscopy and Synchrotron X-ray Diffraction

Zhaohui Dong
The University of Western Ontario

Supervisor
Yang Song
The University of Western Ontario

Graduate Program in Chemistry
A thesis submitted in partial fulfillment of the requirements for the degree in Doctor of Philosophy

Recommended Citation

Dong, Zhaohui, "High-Pressure Study of Molecular Solids and 1D Nanostructures by Vibrational Spectroscopy and Synchrotron X-ray Diffraction" (2012). *Electronic Thesis and Dissertation Repository*. 585.
https://ir.lib.uwo.ca/etd/585

HIGH-PRESSURE STUDY OF MOLECULAR SOLIDS AND 1D NANOSTRUCTURES BY VIBRATIONAL SPECTROSCOPY AND SYNCHROTRON X-RAY DIFFRACTION

(Spine title: High-Pressure Study of Molecules and 1D Nanostructures)

(Thesis format: Integrated-Article)

by

Zhaohui Dong

Graduate Program in Chemistry

A thesis submitted in partial fulfillment
of the requirements for the degree of
Doctor of Philosophy

The School of Graduate and Postdoctoral Studies
The University of Western Ontario
London, Ontario, Canada

THE UNIVERSITY OF WESTERN ONTARIO

School of Graduate and Postdoctoral Studies

CERTIFICATE OF EXAMINATION

Supervisor

Dr. Yang Song

Supervisory Committee

Examiners

Dr. Keith Griffiths

Dr. François Lagugné-Labarthet

Dr. Lyudmila Goncharova

Dr. Serge Desgreniers

The thesis by

Zhaohui Dong

entitled:

High-Pressure Study of Molecular Solids and 1D Nanostructures by Vibrational Spectroscopy and Synchrotron X-ray Diffraction

is accepted in partial fulfillment of the
requirements for the degree of
Doctor of Philosopy

Date

Chair of the Thesis Examination Board

Abstract

Pressure plays a critical role in regulating the structures and properties of materials. Since Percy Bridgeman was recognized by the 1946 Nobel Prize for his contribution to high-pressure physics, high-pressure research as an interdisciplinary area has attracted extensive attentions. Nowadays, high-pressure science involves broad frontier areas, such as chemistry, physics, biology, material and earth science. For instance, brand new classes of inorganic materials of unusual stoichiometries and crystal structures, with wide range of optical, mechanical, electronic and magnetic properties, have been produced at high pressure. Pressure-induced structural transformations between crystalline and amorphous materials, as well as among insulators, conductors and even superconductors, have been extensively documented. This Ph.D. work focused on investigating pressure-induced structural transformations in materials and understanding the involved chemistry, which was assembled into two parts.

In part I, two molecular systems, chlorocyclohexane (CCH) and azobenzene (AB), were investigated to examine the pressure effect on chemical conformations, stability of ring structures and reactivities using Raman spectroscopy. For CCH, pressure-induced conformational change as well as rich phase transformations were observed upon compression. Both AB and hydrazobenzene (HAB) underwent a phase transition at a similar pressure. However, origins of these phase transformations were drastically different. High-pressure structures of both molecules were examined based on spectroscopic data. Their distinctive high-pressure behaviors were analyzed and interpreted with the aid of *ab initio* molecular orbital calculations.

Part II focuses on pressure-induced structural transformations of one dimensional (1D) nanomaterials using vibrational spectroscopy and synchrotron X-ray diffraction. Individual studies were first carried out on BN nanotubes and GaN nanowires aiming at investigating their high-pressure behaviors. Then, systematic studies were conducted on TiO_2 and ZnO nanowires focusing on the size- and morphology- effect on their high-pressure behaviors. These 1D nanomaterials behaved dramatically different from bulk counterparts and nanoparticles, in terms of phase transition pressure, phase transition sequence, and compressibility. In addition, morphology of each material before and after compression was examined by scanning electron microscope. Our studies provide more insight into the understanding of unique high-pressure behaviors of nanomaterials and show profound implications for producing controlled structures with new applications achieved by combined pressure-morphology tuning.

Keywords

High pressure, diamond anvil cell, pressure transmitting medium, synchrotron X-ray diffraction, vibrational spectroscopy, molecular conformation, pressure induced polymerization, phase transition, bulk modulus, nanomaterials, nanowires, nanotubes, size effect, morphology effect

Co-Authorship Statement

The following thesis contains materials from previously published manuscripts written by Zhaohui Dong and co-authored, performed, or edited by others mentioned below. Prof. Yang Song is a co-author on all materials presented in this thesis and is responsible for the supervision of Zhaohui Dong during her Ph.D. studies. Prof. Yang Song played a major role in the editing and revision of the materials presented in all chapters.

The GaN naowire sample in Chapter 5 was supplied by Prof. T. K. Sham's group in the University of Western Ontario. TiO_2 nanowires in Chapter 7 were synthesized by Zhaohui Dong in the Song laboratory. ZnO nanowire samples in Chapters 8 and 9 were obtained from Prof. Song Jin's group in University of Wisconsin, Madison. The rest samples such as chlorocyclohexane (CCH), azobenzene (AB), and hydrazobenzene (HAB) were purchased from Aldrich. Bulk BN and BN nanotubes were purchased from Alfa Aesar and NanoAmor Inc., respectively.

Zhaohui Dong is responsible for most data collection. Raman measurements of CCH in Chapter 3 were performed by undergraduate student Nicholas G. Beilby at Surface Science Western in the University of Western Ontario. Raman data of AB and HAB in Chapter 4 were obtained by undergraduate students Natashia Seeman and Ning Lu under the supervision of Zhaohui Dong using Raman systems in Surface Science Western and the Song Laboratory, respectively. All the X-ray diffraction and infrared spectroscopy data of nanomaterials were collected by Zhaohui Dong except for GaN nanowires in Chapter 5 which were helped by Dr. Dmitry Shakhvorostov and Dr. Chirtra Murli. Scanning electron microscope (SEM) images were taken by Zhaohui Dong at Nanofab at the University of Western Ontario.

All the data analysis was done by Zhaohui Dong except for the *ab intio* calculation in Chapter 4 which was performed by Prof. Yang Song.

To my loving family

Acknowledgments

First of all, I would like to express my gratitude to my supervisor Prof. Yang Song, for his exceptional supervision, encouragement, and unconditional support without which my graduate studies would not have been possible. It is my great honor for having the opportunity to work under the guidance of someone who is not only an expert in the field of high-pressure chemistry, but who is also very liked and respected by many of his colleagues. His passion and enthusiasm are something I will always admire.

I also would like to thank my collaborators, Prof. T. K. Sham and Prof. Song Jin for all their input. In addition, I appreciate all the technical support from beamline staffs that I received at synchrotron facilities: Dr. Zhenxian Liu (NSLS), Dr. Jingzhu Hu (NSLS), Dr. Yue Meng (APS), Dr. Stanislav Sinogeikin (APS), and Dr. Sergey Tkachev (APS). Their expertise and willingness to help made the synchrotron experiments running more smoothly.

I would also like to thank all the members of Dr. Song's group, both present and past, especially Dr. Dmitry Shakhvorostov, Dr. Kirill K. Zhuravlev, Dr. Chirtra Murli and Dr. Vinod Panchal for their helpful discussions and constructive feedbacks. I would like to extend my thanks to my friends, in particular Ru Wang, Jing Chao, Lijia Liu, Yanyu Xiao and Zhongying Mi. Five years' happy time makes them my life time friends. Without them, my life in Canada cannot be so colorful and joyful.

Finally, I would like to give my special thanks to my parents and my husband, without their unconditional support it is impossible for me to finish this Ph.D. thesis. Especially my husband Wei, he selflessly backed me up from every aspect, and gave me encouragement and confidence. With his full support, I can concentrate on my research and enjoy my life here.

Table of Contents

Part I High-Pressure Study of Molecular Solids

Part II Novel Pressure-Induced Structural Transformations of One Dimensional Inorganic Nanomaterials

List of Tables

List of Figures

List of Appendix Figures

List of Abbreviations

AB:	Azobenzene
APS:	Advanced Photon Source
ANL:	Argonne National Laboratory
BS:	Beam splitter
BN:	Bending magnets
BNL:	Brookhaven National Laboratory
BNNT:	Boron nitride nanotube
CCH:	Chlorocyclohexane
CCD:	Charge coupled device
CNT:	Carbon nanotube
c-BN:	Cubic structured BN
DAC:	Diamond anvil cell
DFT:	Density functional theory
EDM:	Electronic discharge machine
FTIR:	Fourier transform medium
GPa:	Giga-Pascal
HAB:	Hydrazobenzene
HOMO:	Highest occupied molecular orbital
IR:	Infrared
IRIS:	Infrared radiation interferometer spectrometer
ID:	Insertion device
KB:	Kirkpatrick-Baez (a kind of mirror)

LOMO:	Lowest unoccupied molecular orbital
LO:	Longitudinal optical
MCT:	Mercury cadmium telluride
MW-BNNT:	Multi-walled BNNT
NF:	Notch filter
NSLS:	National Sychrotron Light Source
PTM:	Pressure transmitting medium
rf:	Radio frequency
SEM:	Scanning electron microscope
SW-BNNT:	Single walled BNNT
TEM:	Transmission electron microscope
TO:	Transverse optical
w-BN:	Wurtzite structured BN
XRD:	X-ray diffraction

Chapter 1 Introduction

1.1 High-pressure effect

Pressure, temperature and chemical composition form the trilogy of thermodynamic variables that determine the stability and reactivity of molecules. So far much effort was focused on the variation of temperature and composition in producing a rich array of structures and compounds. In contrast, the pressure variable in chemistry has remained relatively less explored, especially in the high pressure region. In fact, pressure spans over 60 orders of magnitude in the universe, from 10^{-32} Pascal in intergalactic space to 10^{32} Pascal in the center of neutron star. Materials could exhibit various structures as well as properties under such a broad range of pressure, leaving us huge space for producing new materials by adjusting pressure.

The earliest high-pressure studies can be dated back to the 17th century when Boyle published his gas law. Since then, developments in high-pressure techniques allow the access to high-pressure regions. The anvil technologies were originally developed by Percy Bridgman, who received the Physics Nobel Prize in 1946 for his contribution to high-pressure physics, allow the access to the gigapascal (GPa) region and have led the high-pressure studies to spread in a number of disciplines. The later invention of the diamond anvil cell (DAC), developed at the National Bureau of Standards of USA, laid the foundation of static high pressure studies in modern laboratories.[1] The DAC apparatus has further facilitated high-pressure science by generating pressures of hundreds of GPa (1 GPa = 10^9 Pa = 10^4 atm), comparable to pressure at the core of the Earth.[2]

When applying pressure to materials, the general effect is to reduce the volume of the materials. Pressure can efficiently shorten the inter-molecular and intra-molecular distances, which will increase the free energy of the system.[3] This is simply because pressure (P) and energy (E) are related by eq. 1.1, and thus alternation of the volume will change the E.

$$P = -\frac{\partial E}{\partial V} \qquad (1.1)$$

Consequently, the system becomes thermodynamically unstable. The response of the system to retrieve a new free energy minimum will result in a number of possible processes, such as phase transformation, ionization, polymerization, amorphization, dissociation and, even atomization and metallization. So far, a huge number of striking phenomena have been observed experimentally under high pressure.[4] For instance, as seen in Fig. 1.1, pressure can initiate polymerization without catalyst such as oligomerization of butadiene at 0.7 GPa.[5] Even N_2, which contains the strongest homonuclear bond (bond energy: 945 kJ/mol), forms a polymer at a pressure greater than 120 GPa and a temperature of 2000 K.[6] Under high pressure, metallization could also be achieved even for gases, such as O_2, which has been reported metalized at 95 GPa.[7] Although no metallization has been observed experimentally for H_2, 'broken-symmetry' molecular-ionic solid phase ($H_2^+H_2^-$) was reported formed at a pressure of 150 GPa.[8] In addition to experimental observations, theoretical computations have successfully reproduced experimental observations under extreme pressure, proposed new high-pressure perspectives, and yet posed new challenges.[9-11]

Modern high-pressure research involves broad frontier areas, such as chemistry, physics, biology, materials and earth science. In particular, high-pressure studies in chemistry and material science have shown major breakthroughs in the discovery of numerous exotic structures and properties, for example, in producing super-hard materials, investigating nanocrystalline materials, micro- to nano- porous materials, as well as in synthesis of novel materials.[12-14] Brand new classes of inorganic materials of unusual stoichiometries and crystal structures, which have a wide range of optical, mechanical, electronic, and magnetic properties, have already been extensively reported. For instance, c-BN obtained under high pressure is considered as a candidate replacement of diamond.[14] Hence, exploring pressure-induced phase transitions in materials (e.g., structural change, chemical reaction) as well as understanding the involved chemistry constitutes the core of this thesis.

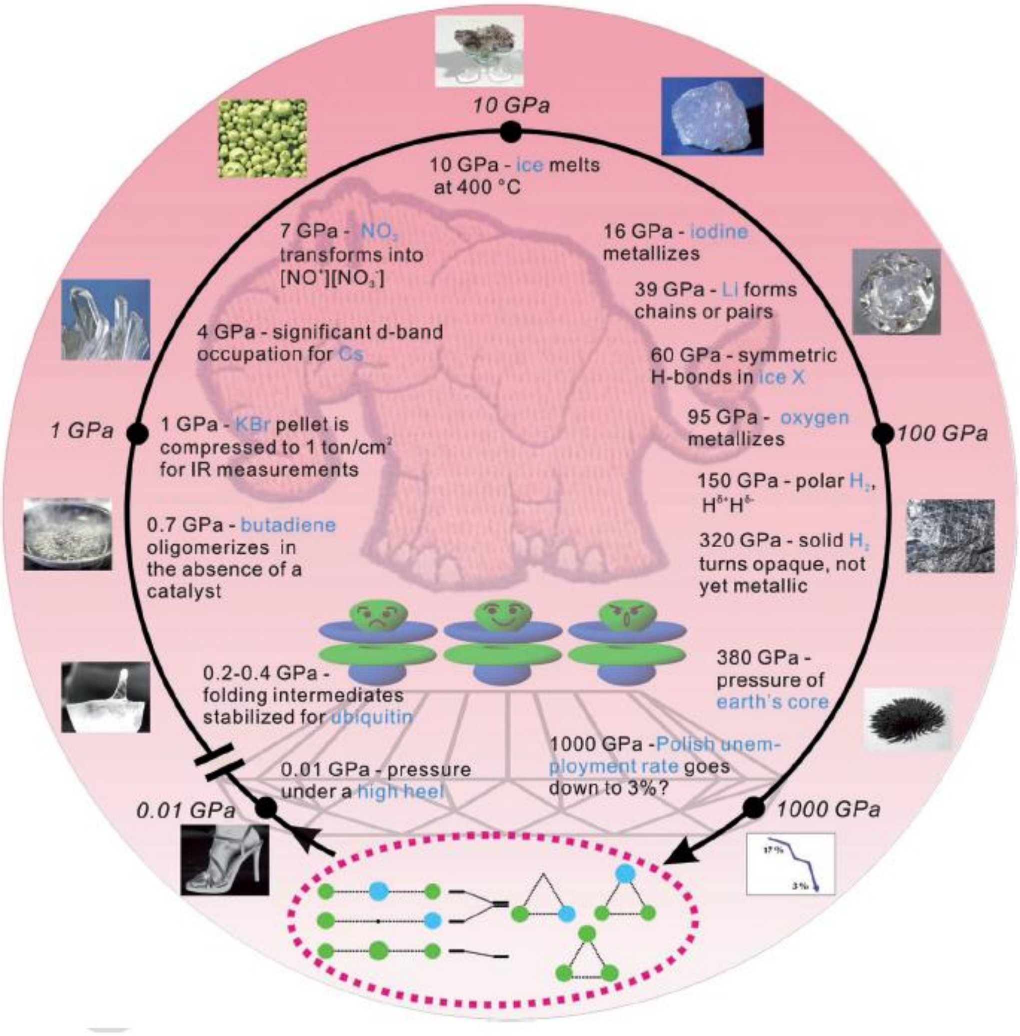

Figure 1.1 Examples of high-pressure phenomena. Copied from Ref. 4.

1.2 Objectives and structures of the thesis

The layout of this thesis is as follows. Chapter 1 provides a general introduction of high-pressure chemistry. Chapter 2 describes the instrumentations used in this thesis. Chapters 3 to 9 constitute the body of the thesis, which has two themes as described in the following. Finally, Chapter 10 summarizes the general conclusions of the thesis and outlines the future work.

Part I High-pressure study of molecular solid systems

Molecular systems can be characterized by strong intra-molecular interactions and bonds as well as weak inter-molecular interactions. In comparison with atomic and ionic crystals, molecular systems are highly compressible, and their volume can be reduced by greater than 1 or 2 order of magnitude with respect to ambient condition.[15] Under these conditions, the consequent increase in free energy can be large enough to exceed the strength of the molecular bonds, which produces wide possibilities in the chemistry of molecular systems, such as conformational changes, phase transformations and chemical transformations.[3,16,17] The inter- and intra- molecular distances are effectively shorten under high pressures, which subsequently causes reversible or irreversible modifications in the molecular structures and associated electronic, optical, or mechanical properties. Therefore, pressure provides an excellent tool to produce new materials even starting from simple molecular solids, especially those with unsaturated bonds or conjugate ring structures.

In this work, two different molecular systems, chlorocyclohexane (CCH) and azobenzene (AB) with its derivative hydrazobenzene (HAB), were investigated at high pressure in order to study the pressure effect on molecular conformations, ring stability and chemical reactivity. The CCH exhibited rich solid to solid transformations upon compression. In the AB and HAB system, it was found that AB behaved dramatically different from HAB under high pressure in terms of chemical transformations and reversibility. However, the ring structures of both systems were surprisingly stable under high pressures. Detailed information of these studies are included in Chapter 3 (CCH) and Chapter 4 (AB and HAB), respectively.

Part II Novel pressure-induced structural transformations of one dimensional inorganic nanomaterials

Nanomaterials refer to materials with dimensions of nanometer scale, typically less than 100 nm. This length scale can be, for instance, particle diameter, grain size, layer thickness, tube diameter or length. In general, it is well known that the physical and chemical properties of materials in nano-scale are substantially different from their bulk counterparts, and are stronger size and morphology dependent. Hence, nanostructured materials are of fundamental importance because of their wide range of tunable electrical, optical and mechanical properties that bulk materials do not possess.

Normally, the properties of nanomaterials are largely determined by the synthetic routes and their compositions. However, high-pressure studies have demonstrated that, in addition to the synthetic approaches, pressure can provide an additional force to modify nanomaterials' structures as well as morphology.[13,18-30] For instance, carbon nanotubes at extremely high pressures were reported to transform into a single crystal diamond or a graphite powder.[31] Pressure induced phase transformation is one of the benefits of high pressure in terms of producing novel structures. In addition, in contrast to the bulk materials, nanomaterials behave drastically differently under high pressure. For instance, ZnS nanobelts have been found to exhibit a much wider stability region up to 6.8 GPa for the wurtzite phase, in strong contrast to bulk ZnS, which is much more stable in the sphalerite phase.[32] In addition, nanomaterials with same composition but with different size also exhibit different pressure responses. For example, although both bulk and nanomaterials CdSe undergo the phase transformation from wurtzite to rocksalt structures under high pressures, the onset phase transition pressures were determined by their particle size.[28] Therefore, high-pressure study of nanomaterials has attracted increasing attentions. So far, there have been many studies carried out on nanoparticles (as summarized in Table 1.1).[33] In addition to nanoparticles, high-pressure studies on 1D nanomaterials is also an indispensable part of understanding pressure effect on nanonmaterials and exploring new structures and properties. Our interests focus on inorganic nanowires and nanotubes, due to their wide applications but lack of understanding in terms of high-pressure behaviors. The related works constituted part II of the thesis. First, high-pressure behaviors of individual cases were investigated by comparing to their corresponding bulk counterparts, which compromised Chapter 5 (GaN nanowires), Chapter 6 (BN nanotubes) and Chapter 7 (TiO_2 nanowires). After these individual case studies, systematic high-pressure study was conducted on ZnO nanowires with a series of different width aiming at understanding the size effect on their behaviors, which was summarized in Chapters 8 and 9.

Table 1.1 Summary of high-pressure studies on one dimensional inorganic nanomaterials.

material	morphology	dimension *	pressure (GPa)**	characterization method	reference
ZnS	Nanobelt	t: ~ 10 nm, w: ~ 1 μm, l: 100 μm	11.4	X-ray diffraction	21
	Nanorod	w: ~ 10 nm	19.4	Raman, Photoluminescence	34
		w: ~ 10 nm	37.2	X-ray diffraction	35
BN	Nanotube	d: 20 – 50 nm	16	Raman	36,37
		d: ~ 50 nm	19.1	X-ray diffraction	38
		d: ~ 100 nm	34.6	FTIR	this work
ZnO	Nanowire	w: 60 – 100 nm, l: tens of μm	21.5	Raman, X-ray diffraction	39
		w: 200 – 300 nm, l: 3 – 4 μm	19.3	X-ray diffraction	this work
		w: 50 – 100 nm, l: 3 – 4 μm	26.4		
		w: 50 – 70 nm, l: 3 – 4 μm	24		
		w: 25 – 35 nm, l: tens of μm	24.8		
	Nanotube	d:10 – 70 nm	21.5	X-ray diffraction	40
SnO_2	Nanowire	w: 50 – 60 nm, l: several μm	37.9	Raman, X-ray diffraction	41
	Nanobelt	t: tens of nm, w: ~ 1 μm, l: several μm	36.2	Raman, X-ray diffraction	
TiO_2	Nanoribbon	t: ~ 20 nm, w: 50 – 200 nm, l: tens of μm	30.9	Raman, X-ray diffraction	42
	Nanowire	w: 50 – 150 nm, l: ~ 12 μm	36.7	Raman, X-ray diffraction	this work
		w: 200 – 300 nm, l: ~ 12 μm	32.3		
GaN	Nanowire	w: tens of μm, l: < 100 nm	65	X-ray diffraction	this work

* d: diameter; w: width; l: length; t: thickness.

**: The highest pressure achieved for each study.

1.3 References

(1) Ferraro, J. R. Vibrational Spectroscopy at High External Pressures. In *Handbook of Vibrational Spectroscopy*; John Wiley & Sons, Ltd, **2006**.

(2) Hemley, R. J.; Mao, H. K. “Overview of static high pressure science”; *Proceedings of the International School of Physics*, "Enrico Fermi" Course CXLVII (High Pressure Phenomena), **2002**.

(3) Hemley, R. J. *Ann. Rev. Phys. Chem.* **2000**, *51*, 763.

(4) Grochala, W.; Hoffmann, R.; Feng, J.; Ashcroft, N. W. *Angew. Chem.-Int. Edit.* **2007**, *46*, 3620.

(5) Citroni, M.; Ceppatelli, M.; Bini, R.; Schettino, V. *Science* **2002**, *295*, 2058.

(6) Eremets, M. I.; Popov, M. Y.; Trojan, I. A.; Denisov, V. N.; Boehler, R.; Hemley, R. J. *J. Chem. Phys.* **2004**, *120*, 10618.

(7) Desgreniers, S.; Vohra, Y. K.; Ruoff, A. L. *J. Phys. Chem.* C **1990**, *94*, 1117

(8) Hanfland, M.; Hemley, R. J.; Mao, H. K. *Phys. Rev. B* **1991**, *43*, 8767.

(9) Lay, T.; Williams, Q.; Garnero, E. J. *Nature* **1998**, *392*, 461.

(10) Mishima, O.; Stanley, H. E. *Nature* **1998**, *396*, 329.

(11) Mujica, A.; Rubio, A.; Munoz, A.; Needs, R. J. *Rev. Mod. Phys.* **2003**, *75*, 863.

(12) San-Miguel, A. *Chem. Soc. Rev.* **2006**, *35*, 876.

(13) Jacobs, K.; Zaziski, D.; Scher, E. C.; Herhold, A. B.; Alivisatos, P. A. *Science* **2001**, *293*, 1803.

(14) McMillan, P. F. *Nat Mater* **2002**, *1*, 19.

(15) McMillan, P. F. *Chem.Soc. Rev.* **2006**, *35*, 855.

(16) Schettino, V.; Bini, R. *Chem. Soc. Rev.* **2007**, *36*, 869.

(17) Schettino, V.; Bini, R. *Phys. Chem. Chem. Phys.* **2003**, *5*, 1951.

(18) Chen, B.; Penwell, D.; Benedetti, L. R.; Jeanloz, R.; Kruger, M. B. *Phys. Rev. B* **2002**, *66*, 144101.

(19) Chen, C.-C.; Herhold, A. B. *Science* **1997**, *276*, 398.

(20) Guo, Q. X.; Zhao, Y. S.; Mao, W. L.; Wang, Z. W.; Xiong, Y. J.; Xia, Y. N. *Nano Lett.* **2008**, *8*, 972.

(21) He, Y.; Liu, J. F.; Chen, W.; Wang, Y.; Wang, H.; Zeng, Y. W.; Zhang, G. Q.; Wang, L. N.; Liu, J.; Hu, T. D.; Hahn, H.; Gleiter, H.; Jiang, J. Z. *Phys. Rev. B* **2005**, *72*, 212102.

(22) Jiang, J. Z.; Gerward, L. *J. Appl. Phys.* **2000**, *87*, 2658.

(23) Jiang, J. Z.; Gerward, L.; Frost, D.; Secco, R.; Peyronneau, J.; Olsen, J. S. *J. Appl. Phys.* **1999**, *86*, 6608.

(24) Jiang, J. Z.; Gerward, L.; Olsen, J. S. *Scripta Mater.* **2001**, *44*, 1983.

(25) Jiang, J. Z.; Olsen, J. S.; Gerward, L.; Morup, S. *Europhys. Lett.* **1998**, *44*, 620.

(26) Park, S.-W.; Jang, J.-t.; Cheon, J.; Lee, H.-H.; Lee, D. R.; Lee, Y. *J. Phys. Chem. C* **2008**, *112*, 9627.

(27) Swamy, V.; Kuznetsov, A.; Dubrovinsky, L. S.; McMillan, P. F.; Prakapenka, V. B.; Shen, G.; Muddle, B. C. *Phys. Rev. Lett.* **2006**, *96*, 135702.

(28) Tolbert, S. H.; Alivisatos, A. P. *Science* **1994**, *265*, 373.

(29) Tolbert, S. H.; Alivisatos, A. P. *Ann. Rev. Phys. Chem.* **1995**, *46*, 595.

(30) Wang, Z.; Saxena, S. K.; Pischedda, V.; Liermann, H. P.; Zha, C. S. *Phys. Rev. B* **2001**, *64*, 012102.

(31) Khabashesku, V. N.; Gu, Z. N.; Brinson, B.; Zimmerman, J. L.; Margrave, J. L.; Davydov, V. A.; Kashevarova, L. S.; Rakhmanina, A. V. *J. Phys.Chem. B* **2002**, *106*, 11155.

(32) Wang, Z.; Daemen, L. L.; Zhao, Y.; Zha, C. S.; Downs, R. T.; Wang, X.; Wang, Z. L.; Hemley, R. J. *Nature Mater.* **2005**, *4*, 922.

(33) Song, Y., and Dong, Z. Novel Pressure-Induced Structural Transformations of Inorganic Nanowires. In *Nanowires - Fundamental Research*; Hashim, A., Ed.; InTech, 2011; pp 552.

(34) Li, Z. P.; Liu, B. B.; Li, X. L.; Yu, S. D.; Wang, L.; Hou, Y. Y.; Zou, Y. G.; Yao, M. G.; Li, Q. J.; Zou, B.; Cui, T.; Zou, G. T. *J. Phys.-Condensed Matter* **2007**, *19*, 425227.

(35) Li, Z.; Liu, B.; Yu, S.; Wang, J.; Li, Q.; Zou, B.; Cui, T.; Liu, Z.; Chen, Z.; Liu, J. *J. Phys. Chem. C* **2011**, *115*, 357.

(36) Saha, S.; Gadagkar, V.; Maiti, P. K.; Muthu, D. V. S.; Golberg, D.; Tang, C.; Zhi, C.; Bando, Y.; Sood, A. K. *J. Nanosci. Nanotechnol.* **2007**, *7*, 1810.

(37) Saha, S.; Muthu, D. V. S.; Golberg, D.; Tang, C.; Zhi, C.; Bando, Y.; Sood, A. K. *Chem. Phys. Lett.* **2006**, *421*, 86.

(38) Muthu, D. V. S.; Midgley, A. E.; Petruska, E. A.; Sood, A. K.; Bando, Y.; Golberg, D.; Kruger, M. B. *Chem. Phys. Lett.* **2008**, *466*, 205.

(39) Yan, X. Q.; Gu, Y. S.; Zhang, X. M.; Huang, Y. H.; Qi, J. J.; Zhang, Y.; Fujita, T.; Chen, M. W. *J. Phys. Chem. C* **2009**, *113*, 1164.

(40) Hou, D.; Ma, Y.; Gao, C.; Chaudhuri, J.; Lee, R. G.; Yang, H. *J. Appl. Phys.* **2009**, *105*, 104317.

(41) Dong, Z.; Song, Y. *Chem. Phys. Lett.* **2009**, *480*, 90.

(42) Li, Q. J.; Liu, B. B.; Wang, L.; Li, D. M.; Liu, R.; Zou, B.; Cui, T.; Zou, G. T.; Meng, Y.; Mao, H. K.; Liu, Z. X.; Liu, J.; Li, J. X. *J. Phys. Chem. Lett.* **2010**, *1*, 309.

Chapter 2 Instrumentation

2.1 High-pressure apparatus

2.1.1 Diamond anvil cell (DAC)

The pressure required for a high-pressure experiment can be produced through the application of a mechanical force perpendicularly to the surface of the sample placed in a vessel. Currently, the widely used high-pressure vessel is the diamond anvil cell (DAC). There are many different types of DACs, for instance, P-type DAC from High Pressure Diamond Optics Inc and membrane cell from Easylab, UK. In addition, customized DACs are also available according to the requirements of different high-pressure experiments, such as symmetric DAC. For the symmetric type (Fig. 2.1 a), the DAC has two parts, piston and cylinder. Four screws are employed to apply force by manual tightening. A pair of diamond anvils are mounted on two tungsten carbide seats, which are aligned to the piston and cylinder. The tips of the diamond anvils are tens to hundreds of microns in diameter, thus, pressure within GPa can be eaily generated (e.g., 1 N can generate 8×10^6 Pa on a 400 μm culet.). Normally with the same anvil base size, the smaller the culet size is, the higher the maximum pressure can be achieved. The smallest culet size used in this thesis was 250 μm, which allowed us to achieve a pressure up to 70 GPa.

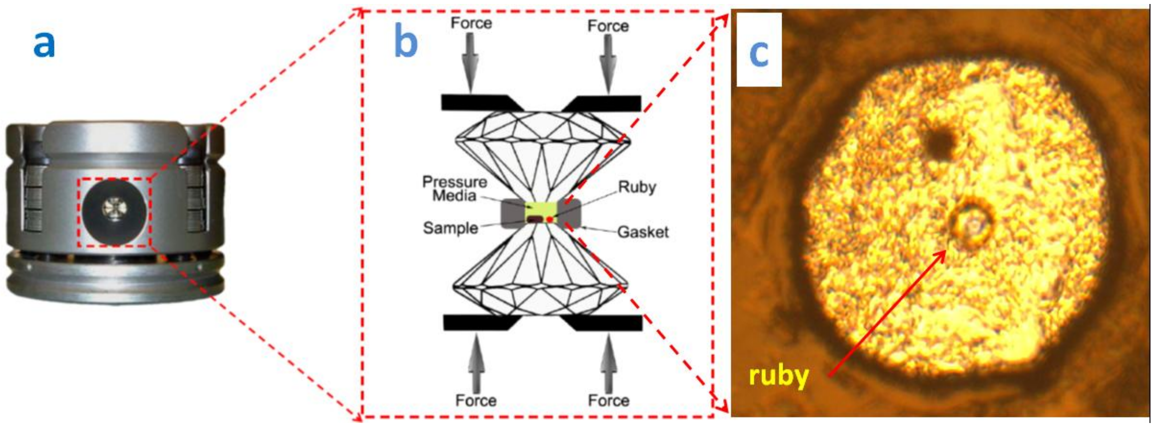

Figure 2.1 **Photo (a) and schematic (b) of a symmetric DAC, and top view (c) of a sample hole in the DAC with a ruby ball loaded.**

Since vibrational spectroscopy is one of the most effective probes for high-pressure studies (as described later), optical transparency is the prime factor in selecting diamond anvils. There are basically two types of diamonds used for different spectroscopic probes, namely types I and II, which can be further classified to types Ia, Ib, IIa and IIb acrroding to the level and type of their chemical impurities. All diamonds have the intense first order Raman line at 1332 cm^{-1} (F_{2g} mode),[1] but with different infrared absorption ranges. Type I stones (with more nitrogen impurities) have two strong absorption regions, which are around 2000 cm^{-1} and 1000 – 1350 cm^{-1}, respectively. In contrast, type II stones (low levels of nitrogen impurities) have a clean window below 2000 cm^{-1} allowing IR measurements in the DAC. Due to their different optical transparencies, type I diamonds are only suitable for Raman spectroscopy, while type II diamonds are mainly used for IR spectroscopy.

Another component of the DAC assembly is the gasket, in which samples are held inside the cell. As shown in Fig. 2.1 b, the gasket is placed between two diamond anvils.

Generally, a gasket is made of metal, such as stainless steel, tungsten, beryllium, etc. To be used in the experiment, the gasket will be first pre-indented to a thickness of tens of microns from initial thickness of 280 μm. Then a hole, the size of which is about one third of the diamond culet, will be drilled at the center of the pre-indented mark using an electric discharge machine (EDM), and used as the sample chamber (Fig. 2.1 c). Under high pressure, gaskets not only provide lateral support to the conical faces of the anvils, but also protect the two diamond anvils by preventing them from touching.

2.1.2 Pressure gauge

Reliable and accurate pressure gauge is an indispensable component in high-pressure experiments. Originally, pressure is obtained indirectly by making reference to the isothermal equations of state of metals (e.g., Au, Cu, Pt, Mo,) derived from shock wave data. In this thesis, all the pressures were determined using the well established ruby fluorescence method.[2-5]

Ruby is Al_2O_3 doped with Cr^{3+}, which is loaded in the sample hole together with samples. When excited by the laser, ruby has two intense luminescent peaks R_1 and R_2 (Fig. 2.2). The positions of R_1 and R_2 peaks are sensitive to pressure and shift to a longer wavelength as pressure increases. Taking primary pressure standards (e.g., Au, Cu, Mo and Pt) as references under quasi-hydrostatic conditions in argon or neon medium, the correlation between pressure and R_1 peak shift can be calibrated up to 80 GPa.[5] With these references, an equation (eq. 2.1) was established to describe the relationship.

$$P = \frac{1904}{B}\left[\left(1+\frac{\Delta\lambda}{694.24}\right)^{B} - 1\right] \qquad (2.1)$$

where P is the *in-situ* pressure in GPa, and $\Delta\lambda$ is the wavelength shift of R_1 in nm. The parameter B equals 7.665 under quasi-hydrostatic condition, and 5 under non-hydrostatic condition. Using this method, the resolution of the pressure can be achieved to ± 0.05 GPa.

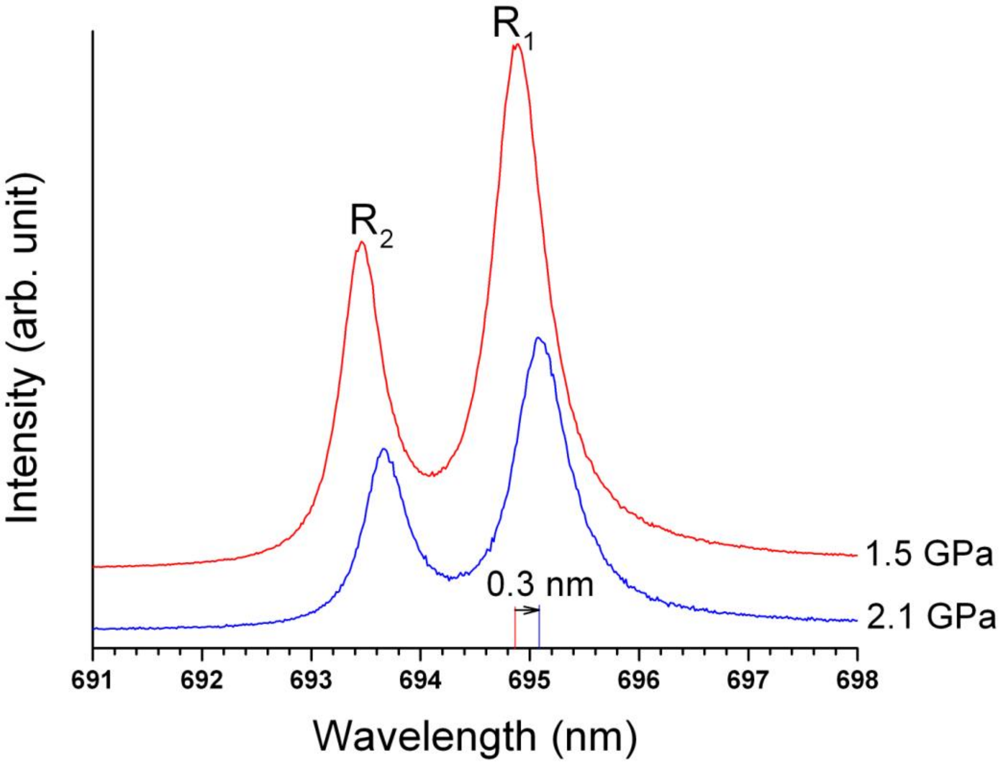

Figure 2.2 Ruby fluorescence measured at different pressures with the two luminescent peaks labeled (R_1 and R_2). The pressure condition for each spectrum is labeled beside.

2.1.3 Pressure transmitting medium

For high-pressure experiments, the ideal compression environment is under hydrostatic conditions, meaning no pressure gradient in the entire sample area. However, the reality is that the pressure inhomogeneity could be a serious problem as the pressure increases. To maintain a hydrostatic condition, the widely used method is to load pressure transmitting medium (PTM) into the sample chamber. The common PTMs are alcohol mixtures made of 4:1 methanol-ethanol or 16:3:1 methanol-ethanol-H_2O, which can maintain a hydrostatic condition up to ~ 10.5 GPa.[6-8] Regarding to experiments requiring pressure greater than 10 GPa, silicone oil is more preferable to these alcohol mixtures. However, the silicone oil is only applicable for pressure below 20 GPa, since it undergoes a glass phase transition at around 20 GPa, beyond which the pressure homogeneity becomes worse.[9] Above 20 GPa, noble gases, such as Ar, He and Ne, etc, are the best quasi-hydrostatic PTM known so far, especially at low temperatures. For instance, Ne can extend the quasi-hydrostatic condition up to 50 GPa or even beyond, which is sufficiently high for most studies of high-pressure chemistry.[9] Moreover, these noble gases can be loaded under moderate pressure (e.g. 150 MPa) and at room temperature by enclosing the DAC in an adequate loading autoclave.[10] The PTM used in this work varies as the studied materials differ and will be mentioned in detail in the experimental section of each chapter.

2.2 Vibrational spectroscopy

2.2.1 Origin of vibrational spectroscopy

Molecules and solids have different types of motion and each of these types can lead to different forms of excitation. Three of the main types are rotational, vibrational, and electronic, which can be considered independent in many circumstances. When a molecule interacts with an electromagnetic field, energy transfers from the field to the molecule. The energy transferred at the vibrational levels can be recorded by vibrational spectroscopy providing information regarding molecular structures, chemical bonding, changes in the circumstance, etc. The most common techniques for vibrational spectroscopy are infrared (IR) and Raman spectroscopy.

Raman and IR spectroscopy provide similar information of molecule vibrations, however, their selection rules are different. Fig. 2.3 describes several examples using symmetric diatomic, asymmetric diatomic and symmetric triatomic molecules as model molecules to distinguish the selection rules between Raman and IR spectroscopy.[11] In the molecules or in the unit cells of a crystal, vibrations could cause a mechanical deformation Q. If Q changes the dipole moment $\vec{P}_D$, the vibration mode is considered as IR-active. If the polarizability α is changed, the vibration is a Raman process. Obviously a vibration can be either Raman-active or IR-active, or active to both probes. In fact, vibrations can also be inactive or silent to both Raman and IR. Thus, for a non-silent molecular vibration, it can be detected by either Raman or IR spectroscopy, which makes Raman and IR techniques complementary to each other by providing a whole picture of molecular vibrations.

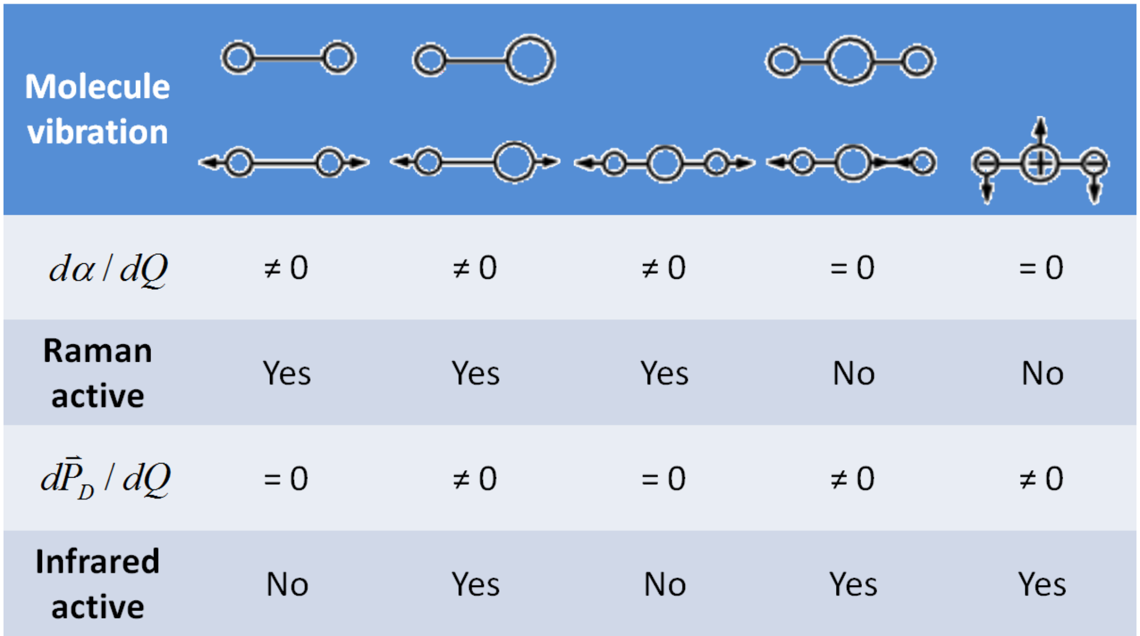

Molecule vibration					
$d\alpha / dQ$	≠ 0	≠ 0	≠ 0	= 0	= 0
Raman active	Yes	Yes	Yes	No	No
$d\vec{P}_D / dQ$	= 0	≠ 0	= 0	≠ 0	≠ 0
Infrared active	No	Yes	No	Yes	Yes

Figure 2.3 Selection rules for Raman and infrared activity of vibrations. Adopted from Ref. 12.

2.2.2 Advantages of vibrational spectroscopy at high pressures

In high-pressure experiments, special consideration must be taken for interfacing the technique with DAC due to the small sample size and the presence of the diamond window. The transparency of diamond windows makes DAC exceptionally useful for optical studies. In addition, the optical instruments in both Raman and IR spectroscopy, i.e., micro-Raman and micro-infrared systems, are designed compatible with DAC, which are widely used in high-pressure studies. Moreover, the developments of both techniques have extended their capability at high pressures as well as variable temperatures.

Raman techniques have been improved substantially in increasing the signal collection efficiency with the help of the developments of extremely sensitive and low background array detector, the holographic transmission optics, and fast imaging spectrometers, and so on. Those developments make Raman spectroscopy much more compact and thus easily coupled with diamond anvil cells for measurements at ultrahigh pressures. Developments in broad band synchrotron IR techniques provide ~ 10^4 times the brightness of a conventional thermal source. With synchrotron source, people are able to conduct IR measurement at low temperature.

Moreover, both Raman and IR spectroscopy can not only be used for probing vibrational states, but also be applied to other studies. For instance, Raman spectroscopy can also be used in studying magnetic and electronic excitations under pressure. In addition, as mentioned above, the pressure tuning of fluorescence spectra of ruby provide a scale for calibrating the pressure. IR spectroscopy provides detailed information on bonding properties of crystals, glasses, and melts, thereby yielding a microscopic basis for thermodynamic parameters, information on bonding and crystal structure, and transformation mechanisms.

2.2.3 Micro-Raman system in the Song Laboratory

In this thesis, a user customized Raman system was used for most of the Raman measurements. The schematic diagram of this Raman system is depicted in Fig. 2.4. The system is constructed on an optical table. An Argon ion laser is used as the excitation source (Coherent Innova 90C Series Ion Laser). Multiple discrete lines with different wavelength are available as excitation converting a spectral range from 488 nm to 514 nm. In this thesis, different excitation wavelengths were used for different projects, which will be specified in each chapter. The maximum output power can reach 6 W for the system. 514 nm and 488 nm are the most used excitation wavelengths with maximum energy outputs of 0.27 W and 0.38 W, respectively. The microscope system (blue area in Fig. 2.4) is used to focus the laser beam onto the specimen containing a 15× eyepiece and 20× objective (Olympus Microscope), two beam splitters built inside and a CCD camera which allows *in-situ* imaging. The 3-D manually adjustable sample stage is designed to align the DAC right bellow the microscope. To record the Raman spectrum, a liquid nitrogen cooled CCD (charge-coupled device) (Spec-10 system, Princeton Instrument) is used to maintain the -120 °C operation condition. A 0.5 m monochromator (SpectroPro-2500i, Acton Research Corporation) is used to analyze Raman signals. A triple gratings system with different resolution (300 lines/mm, 1200 lines/mm, and 1800 lines/mm) is housed inside of the spectrometer. The instrument control and data collection are realized by the WinSpec software, by which the pressure can be obtained directly from the position of R_1 ruby fluorescence. The system is calibrated by using standard neon lines. With its calibration, the Raman system could achieve a resolution of ± 1 cm^{-1}.

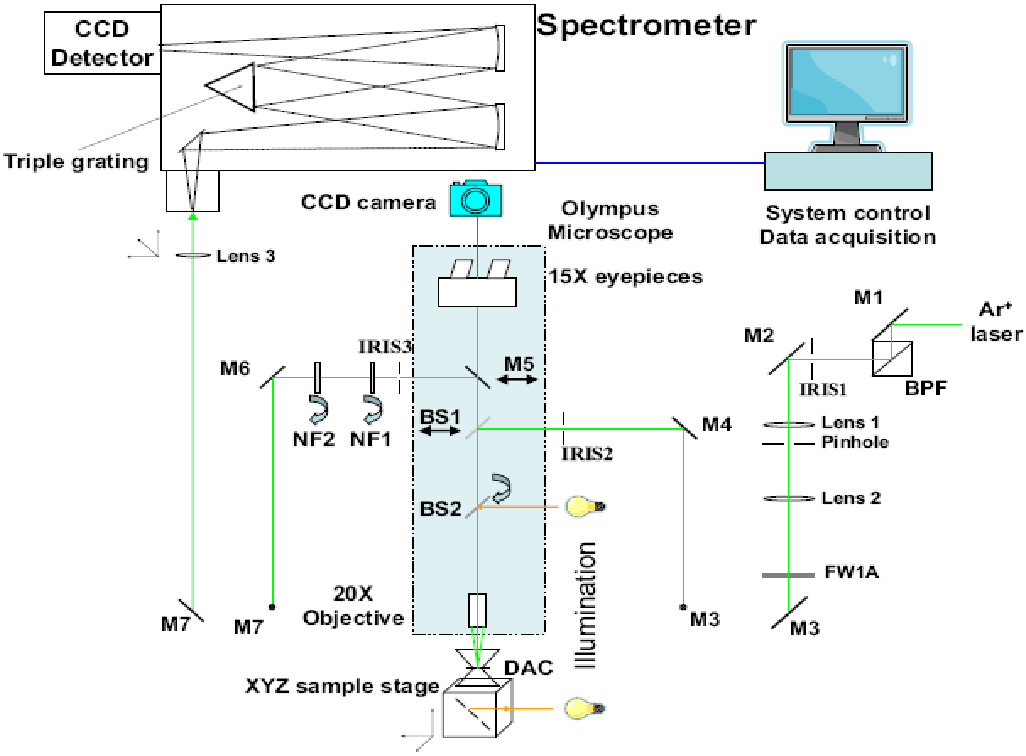

Figure 2.4 Schematic of the Raman system. BPF: band path filter; IRIS: IRIS aperture; M1-7: broadband dielectric reflecting mirrors; FW1A: Six station filter wheel; BS: beam splitter; NF: notch filter; DAC: diamond anvil cell; Triple gratings: 300 lines/mm, 1200 lines/mm, and 1800 lines/mm. Blue area is the microscope system with a CCD camera, which is perpendicular to the other parts.

2.2.4 Micro-IR system in the Song Laboratory

The IR measurements were carried out using a customized IR micro-spectroscopy system constructed in the Song laboratory. Fig. 2.5 shows the schematic diagram of the customized IR system. A commercial Fourier transform infrared (FTIR) spectrometer from Bruker Optics Inc. (model Vertex 80v) equipped with a Globar IR light source constitutes the main component of the micro-IR system, which is operated under a vacuum of less than 5 mbar such that interference from H_2O and CO_2 is efficiently removed. A collimated IR beam of varying diameters set with apertures ranging from 0.25 mm to 8 mm is directed into a relay box through a KBr window on the spectrometer. The beam is then focused onto the sample in the DAC by iris optics and 15× reflective objective lens with a numerical aperture of 0.4. The DAC on the sample XYZ precision stage is aligned with the aid of an optical microscope equipped with an objective lens with variable magnifications (0.75× to 3×) and a 20× eyepiece from Edmund Optics. The size of the IR beam is set to be identical to the entire sample size (e.g., ~ 150 μm) by a series of iris apertures. The transmitted IR beam is collected using another identical reflective objective as the condenser and is directed to a midband mercury cadmium telluride (MCT) detector equipped with a ZnSe window allowing measurements in the spectral range of 600 cm^{-1} to 12000 cm^{-1}. The customized spectroscopy system also allows IR measurements in the reflection mode using reflective optics via the optical path shown in Fig. 2.5. All measurements in our study were undertaken in absorption mode. A resolution of 4 cm^{-1} and 512 - 1000 scans were applied for each spectrum collection with an excellent signal-to-noise ratio. The reference spectrum, that is, the absorption of diamond anvils loaded with KBr but without any sample, was later divided as background from each sample spectrum to obtain the absorbance.

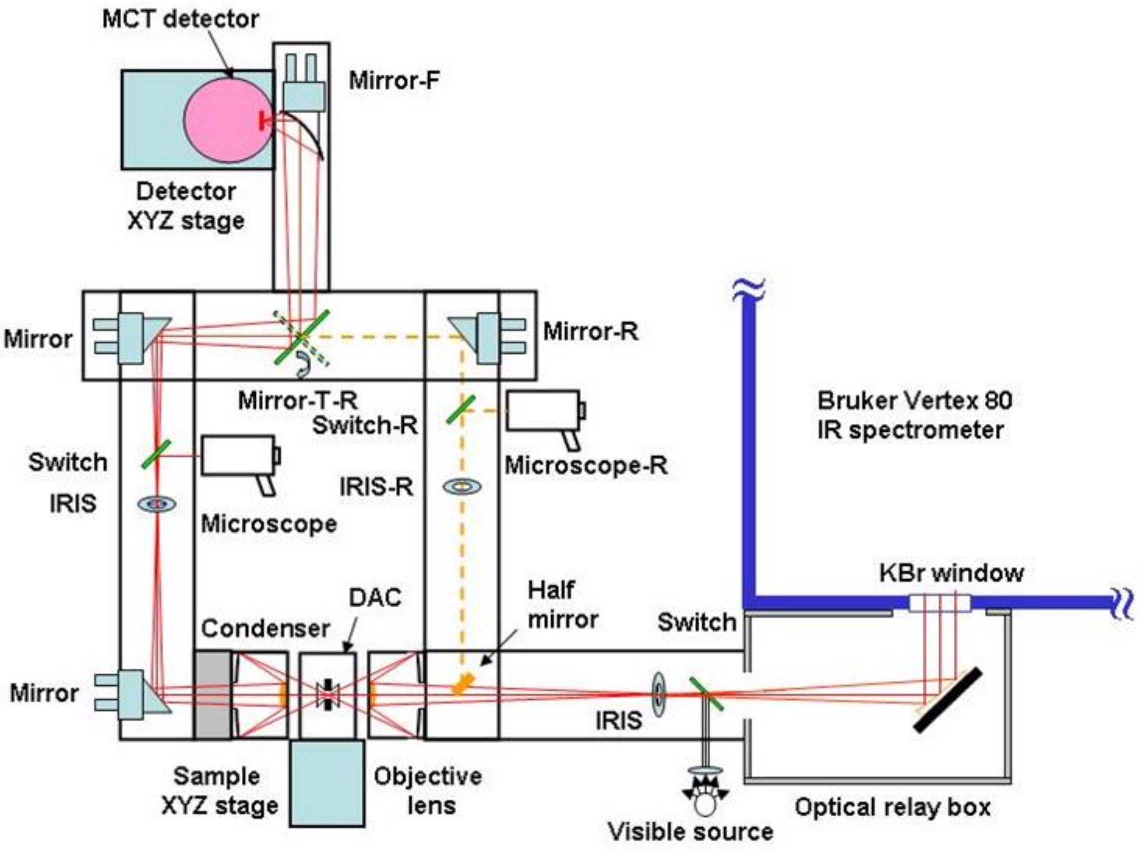

Figure 2.5 **Schematic diagram of the IR microspectroscopy system. The IR spectrometer (model Vertex 80) from Bruker is operated under vacuum. The collimated IR beam comes out through a KBr window. The rest of the optics is purged using CO_2-free dry air in closed boxes or frames. All major optical components are labeled. Those with "-R" and half mirror are for reflection measurements, whereas the rest are for transmission/absorption measurements. "Switch" refers to switchable mirrors for illumination purposes. "Mirror-T-R" is a mirror used to switch between transmission and reflection modes. "Mirror-F" is used to focus the IR signal to the detector.**

2.3 Synchrotron X-ray diffraction (XRD)

2.3.1 Principles of synchrotron radiation

Synchrotron radiation is emitted when charged particles travelling at relativistic speeds change velocity, such as when they are made to follow a curved trajectory by a magnetic field. As illustrated in Fig. 2.6, the high energy electrons are first accelerated to speeds close to that of light, and then are injected to the storage ring guided by arrays of magnets. The storage rings are made of several segments, comprising a straight section followed by a curved section where electrons are steered via a bending magnet into the curved sections.

In the straight sections arrays of magnets, which are generally referred to the insertion devices, can be positioned to produce alternating magnetic fields that cause the path of the electrons to oscillate (as seen in Fig. 2.7: undulator and wiggler). Each oscillation leads to the emission of synchrotron radiation which can be tailored for various applications by choosing the number, amplitude, frequency and direction of the oscillations.

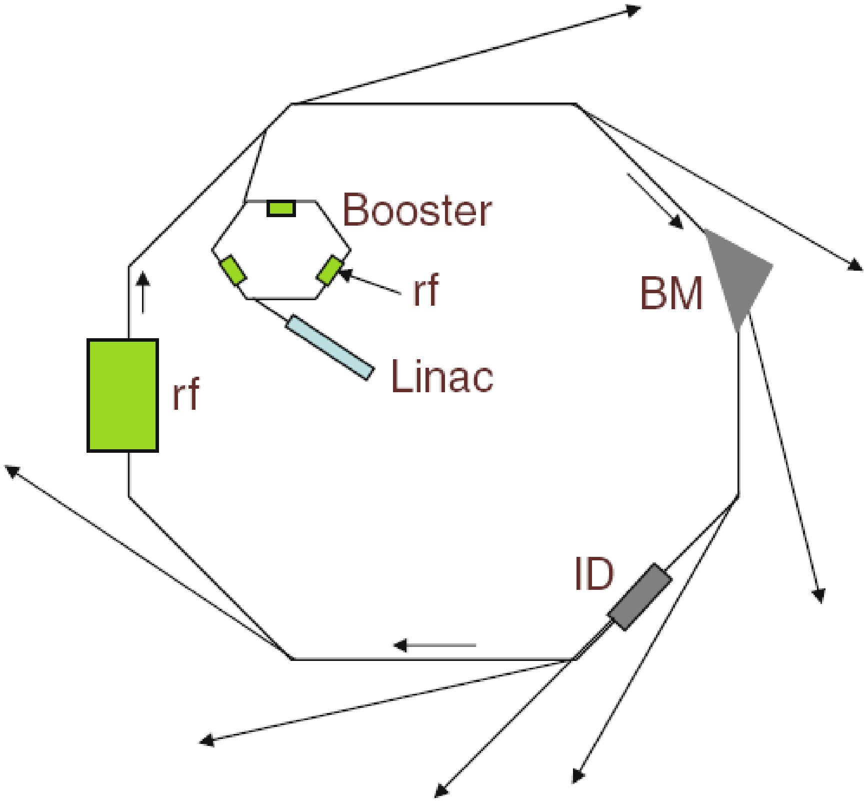

Figure 2.6 Schematic view of a synchrotron radiation source. The injection-accelerating system (Linac+Booster) is inside the storage ring which is actually like a polygon with the bending magnets at their vertices. Bending magnets (BM), provoke the deflection of the electron trajectory, and as a consequence, it produces the synchrotron radiation which escapes forwardly. Insertion devices (ID), can be allocated in the straight sectors to produce specific synchrotron light. The radio frequency cavity of the storage ring and those of the booster synchrotron are also indicated.

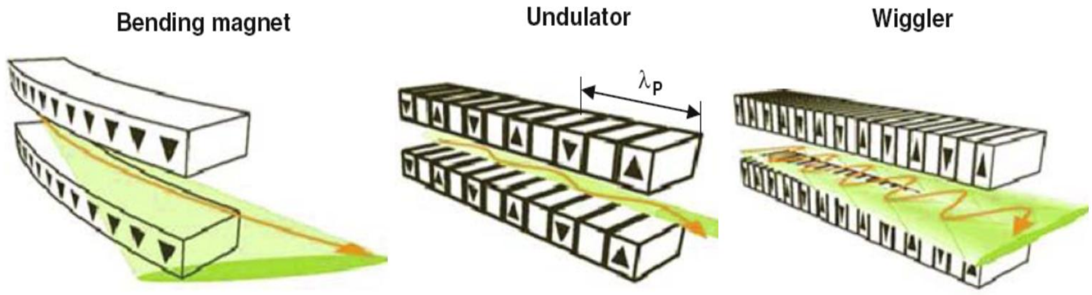

Figure 2.7 Comparative illustration of the generation process of synchrotron light by a bending magnet (left) and by two different insertion devices (middle and right): periodic, weak deflection of the electron beam in a flat undulator of period length and larger transverse oscillations of the beam produced in a wiggler. Differences in photon beam collimation achieved for the three magnetic elements are shown.

Bending magnets and the insertion devices have their magnetic field in the vertical direction causing deflection of the electrons in the horizontal plane. The radiation is therefore linearly polarized with the electric component lying in the plane of the synchrotron orbit. The radiation emitted by a single electron forms a narrow cone of angular width, leading to the very high vertical collimation of the X-ray beam. The spectrum of synchrotron radiation depends on the energy of electrons in the storage ring, the curvature of their path, and, for an undulator, the interference effects. As a general rule, the greater the electron energy in the storage rings, the higher the energy of the emitted X-rays.

Synchrotron radiation has many extraordinary properties in contrast to the corresponding local sources. First, its energy range extends continuously from the far IR (10^{-3} eV) to hard X-ray (10^{5} eV), thereby providing probes over an exceptionally wide portion of the electromagnetic spectrum. Second, synchrotron light source is extremely bright. For example, the brightness of a synchrotron infrared radiation has up to about 10^4 times of that for a conventional thermal (lamp) source. Third, the highly collimated radiation originates from a very small source (0.01 mm – 0.1 mm), allowing a very small focal spot (submicron in X-ray region) with exceptional brightness or spatial resolution to be achieved. Because of these unique properties, synchrotron radiation source has been used widely in studies of materials under extreme pressures in a DAC via their diamond window.[12]

2.3.2 Synchrotron X-ray diffraction at high pressures

The basic principle for X-ray diffraction (XRD) is given by Bragg equation (eq. 2.2).

$$\lambda = 2d_{hkl}\sin\theta \tag{2.2}$$

where λ is the wavelength of (elastically) scattered radiation, d_{hkl} is the spacing of the lattice planes with the Miller indices h, k, l. θ is the angle of Bragg reflection with respect to these planes. The diffraction angle, defined as the angle between the incident primary beam and the diffracted beam, is therefore equal to 2θ. For a monochromatic radiation, maxima in the scattered intensity are observed at some discrete values of $2\theta_{hkl}$ corresponding to the lattice spacing d_{hkl}. For ideal polycrystalline samples, where all possible orientations of the individual microcrystalline grains are equally probable, the radiation is scattered symmetrically around the primary beam into discrete diffraction cones, which can be registered photographically as concentric circles on a flat film, or more commonly, as Debye-Scherrer rings on a cylindrical film wrapped around the sample with the primary beam passing through the film on one side, and through the collimator hole on the other side.

In high-pressure studies, due to the bulk anvils and small sample sizes, X-ray diffraction measurements can only be performed with intense high energy X-ray beam and very small beam size (e.g., tens of microns), which can hardly be achieved in local X-ray diffraction facilities using Co, Cu, and Mo as the excitation sources. Therefore, synchrotron radiation source becomes the best choice for high-pressure research due to its extraordinary properties mentioned above.

2.3.3 Synchrotron X-ray diffraction facilities

The XRD patterns in this thesis were collected in angle dispersive X-ray diffraction mode as described in Fig. 2.8. The monochromatic synchrotron X-ray beam is focused at the center of the sample. Diffraction patterns of the samples are collected as Debye-Scherrer rings by a 2D detector. The XRD experiments were carried out using the synchrotron facilities at beam-line X17C at the National Synchrotron Light Source (NSLS) in Brookhaven National Laboratory (BNL), and beam-line 16ID-B at Advanced Photon Source (APS) in Argonne National Laboratory (ANL).

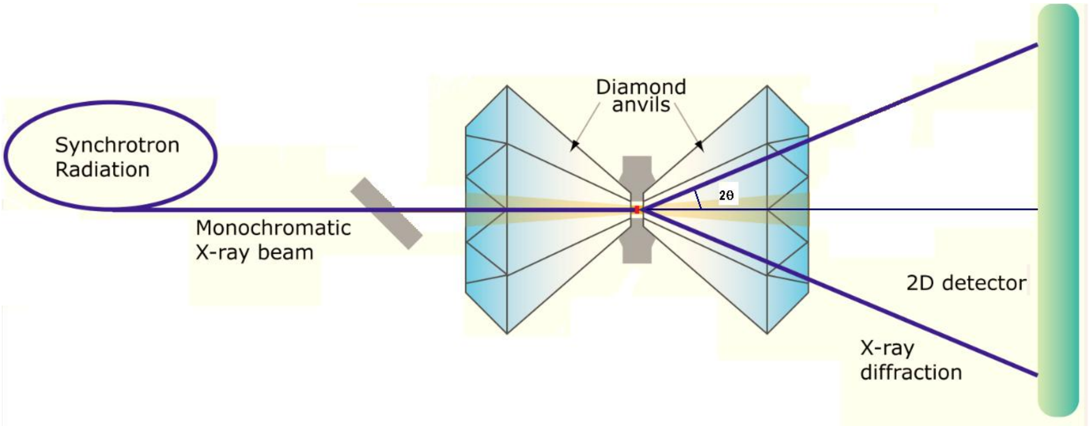

Figure 2.8 **Schematic diagram of angle dispersive XRD.**

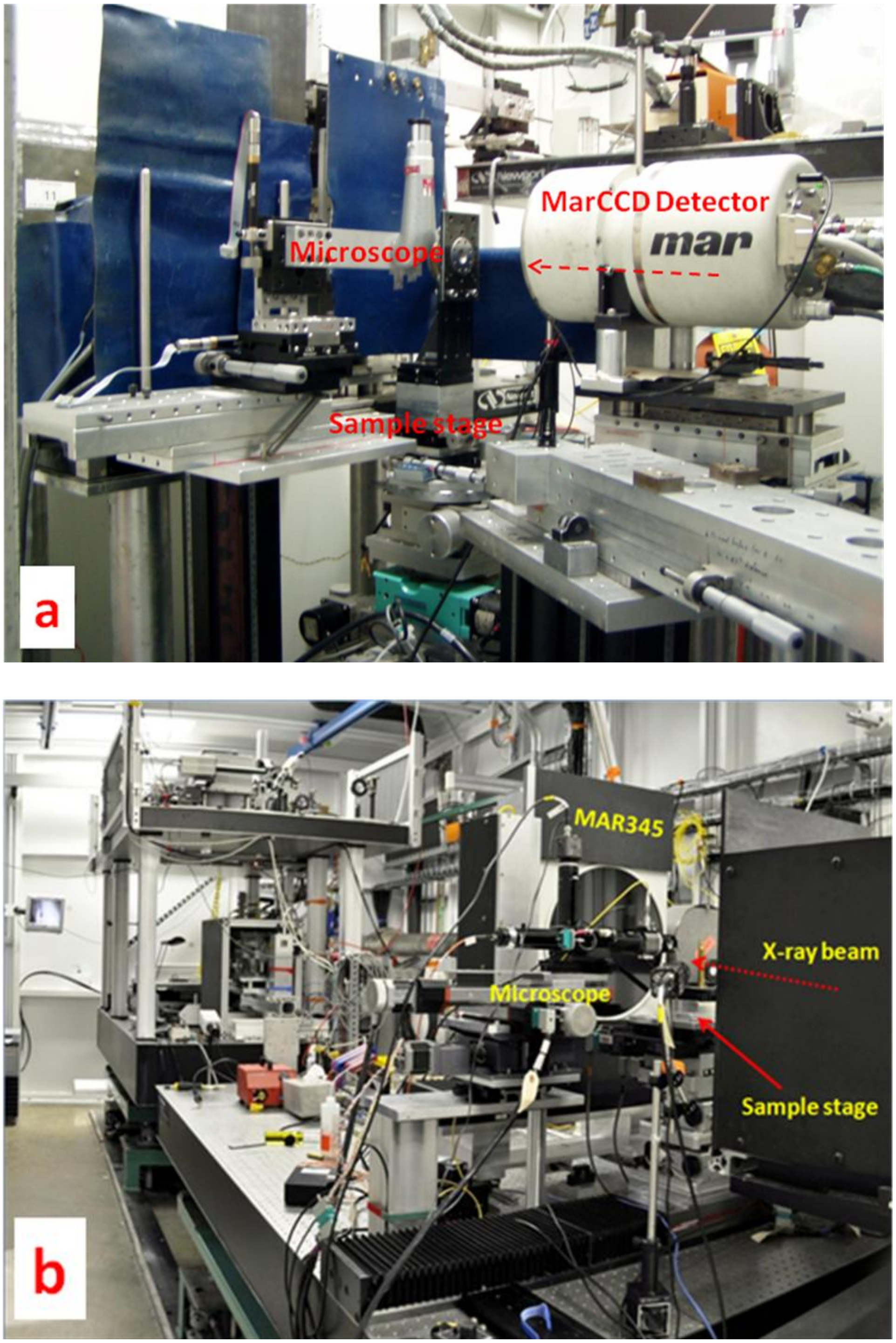

Figure 2.9 ADXRD set up at X17C of NSLS (a) and 16IDB of APS (b). Components such as microscopes, detectors, sample stage and etc. were labeled for each facility. The dashed arrows for both figures indicate the incident direction of X-ray beam.

X17C is a side branch of the high energy, high intensity superconducting wiggler X-ray beam line built in 1984. The experimental setup at X17C hutch is shown in Fig. 2.9 a. A high-energy fixed-exit monochromator with Sagitally-bent double Si crystal Laue mode (transmission) is employed to improve the energy resolution, which is optimized for high energy synchrotron X-ray from 20 KeV to 40 KeV and provides an energy resolution of $\Delta E/E=10^{-3}$. A pair of 100 mm length Kirkpatrick–Baez (KB) mirrors consisting of Si crystals coated with Pt are used for focusing the white x-ray beam at a glancing angle of approximately 1 mrad. With a 180 μm × 180 μm incident beam size, a 25 μm (horizontal) × 27 μm (vertical) focused beam size can be obtained. The sample in the DAC is located at the rotation centre of a goniometer (sample stage in Fig. 2.9 a). The system has motorized ω and χ rotation stages and linear translation stages in the X, Y, and Z directions. Via this system, the X-ray beam is fine focused at the center of the sample. Then a MARCCD X-ray detector is used to collect the X-ray images. A 2θ range from 5 degree to 30 degree can be collected with a spatial resolution of 0.150 mm.

The 16ID-B beamline in APS is also a dedicated high-pressure beamline for X-ray diffraction measurements. The work station for 16IDB is shown in Fig. 2.9 b. The principle for experimental setting up is similar as that at X17C in NSLS. The source for 16ID-B is the dual undulator Type A, which provides X-ray in the energy region from 6 keV – 40 keV (normal) up to 60 keV – 70 keV. A Si double crystal was employed as monochromator. 200 mm KBr mirrors are also used to focus the beam, from which the beam size can reach as small as 4×5 μm^2. After the X-ray beam was focused, a flux of 5×10^{10} ph/s is obtained at the sample position. Such a small beam size and high energy at the sample position allow the XRD measurement taken on different sample spots within a short accumulation time. A MAR345 imaging plate detector is also used to record the diffraction patterns. In addition to the XRD technique, 16IDB also provides many excellent technical supports such as the membrane and mechanical pressure control, online ruby and Raman system, and offline alignments and Ruby system, which make 16IDB more efficient to conduct the high-pressure experiments.

2.4 Other characterization techniques

2.4.1 Powder X-ray diffraction

The powder X-ray diffraction facility in the Department of Earth Science was used to examine the crystallinity of the as synthesized products. The X-ray diffraction facility has a Rigaku X-ray diffractometer and uses the Co K-α radiation as the X-ray source.

2.4.2 Scanning electron microscope (SEM)

SEM images were collected in the Nanofab at the University of Western Ontario using the Leo-Zesis 1540XB FIB/SEM Crossbeam. The crossbeam combines a high resolution SEM for imaging with a focused ion beam (FIB) for micromachining by sputter milling with a sub-100 nm lateral resolution. The spatial resolution of the images can focus down to 1 nm depending on the materials. The SEM system has two chambers, delivery chamber and specimen chamber. Delivery chamber with a small volume is used to pre-vacuum before the sample is delivered to the specimen chamber, which can protect the emission tip from repeated vacuuming. Upon evacuation, the sample is delivered to the specimen chamber, and SEM images are collected. Our sample recovered from decompression with the gasket was fixed to the sample stage and taken into the delivery chamber with a 10^{-6} mbar – 10^{-7} mbar vacuum. SEM images were collected under different scales from µm to nm.

2.5 References

(1) Solin, S. A.; Ramdas, A. K. *Phys. Rev. B* **1970**, *1*, 1687.

(2) Mao, H. K.; Bell, P. M. *Science* **1976**, *191*, 851.

(3) Mao, H. K.; Bell, P. M. *Science* **1978**, *200*, 1145.

(4) Xu, J. A.; Mao, H. K.; Bell, P. M. *Science* **1986**, *232*, 1404.

(5) Mao, H. K.; Xu, J.; Bell, P. M. *J. Geophys. Res.-Solid* **1986**, *91*, 4673.

(6) Marshall, W. G.; Francis, D. J. *J. Appl. Crystallogr.* **2002**, *35*, 122.

(7) Angel, R. J.; Bujak, M.; Zhao, J.; Gatta, G. D.; Jacobsen, S. D. *J. Appl. Crystallogr.* **2007**, *40*, 26.

(8) Klotz, S.; Strassle, T.; Rousse, G.; Hamel, G.; Pomjakushin, V. *Appl. Phys. Lett.* **2005**, *86*, 031917.

(9) Klotz, S.; Chervin, J. C.; Munsch, P.; Le Marchand, G. *J. Phys. D-Appl. Phys.* **2009**, *42*, 075413.

(10) Mills, R. L.; Liebenberg, D. H.; Bronson, J. C.; Schmidt, L. C. *Rev. Sci. Instrum.* **1980**, *51*, 891.

(11) Kuzmany, H. *Solid-State Spectroscopy; Springer Berlin Heidelberg,* **2009**.

(12) Hemley, R. J.; Mao, H. K.; Struzhkin, V. V. *J. Synchrot. Radiat.* **2005**, *12*, 135.

Chapter 3 Conformational and Phase Transformations of Chlorocyclohexane at High Pressure by Raman Spectroscopy[*]

3.1 Introduction

Conformational and phase transformations as well as unusual chemical reactivities of simple molecular species observed under high pressures have opened new avenues to produce novel structures that are generally inaccessible at ambient condition.[1] Pressure can significantly alter the interatomic distances and thus the nature of intermolecular interactions, chemical bonding, molecular configurations, crystal structures, and stabilities of solids. With rapid advances in high-pressure techniques,[2] it is feasible to achieve a large compression of lattice, under which condition materials can be easily forced into new physical and chemical configurations. High pressure thus offers enhanced opportunities to discover new phases, either stable or metastable, and to tune exotic properties in a wide range of atomic length scale, substantially greater than those achieved by other thermal and chemical means.[3] Recent studies show that high pressures can essentially lead to physical and chemical changes of molecular solids and modification of their chemical bonds to more delocalized states such as polymeric and metallic phases.[4] Even at moderate pressure region, e.g., < 20 GPa, rich conformational and phase transformations have been observed in several simple molecular systems.[5,6] For instance, we have recently reported a comprehensive analysis of structures of 1,2-

---

[*] The content of this chapter has been published as: Dong Z., Beiby N. G., Huang Y., and Song Y., *J. Chem. Phys. C.*, **2008**, *128*, 125108

dicholorethane, a simple organic molecule with interesting conformational properties at high pressures using *in-situ* Raman spectroscopy.[6]

Similarly, halogen substituted cyclohexane represents another class of simple organic molecules with stereoring structures that exhibit unique conformational behavior. At ambient conditions, it has been well established that the "chair" isomer is thermodynamically more stable than the "boat" isomer by 28 kJ/mol, resulting in the chair isomer being the dominant conformation of cyclohexane.[7] Depending on the spatial orientation of the halogen atom with respect to the ring, for example, chlorocyclohexane (CCH) exhibits two conformations, i.e., axial (a) and equatorial (e), as shown in Fig. 3.1. The structures of CCH have been extensively studied in all gas, liquid, and solid phases by vibrational spectroscopy.[8-12] In gas, liquid, solution as well as amorphous solid phases, CCH exists as equilibrium mixtures of a- and e-conformers with higher abundance of the latter, while the crystalline phase consists only e-conformer. In addition, the conformational equilibrium was found to change with solvents.[13,14] As either reagent or solvent, CCH has been widely used in many organic reactions, in which the conformational equilibrium plays an important role in determining the product yield as well as reaction kinetics. In addition, the halogenated carbon represents a reaction center to produce stereoisomers as the result of a-/e-conformation. Therefore, conformational study of this classical ring compound is of fundamental interest.

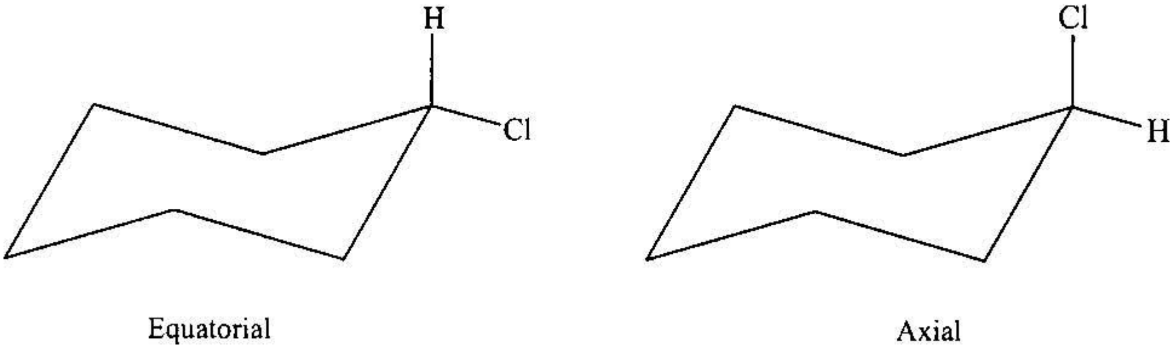

Figure 3.1 Equatorial and axial conformers of CCH

More intriguingly, CCH exhibits rich temperature and pressure-induced polymorphs especially in the solid phase. CCH was found to crystallize into a cubic phase at low temperature and ambient pressure.[15,16] Later on, Diky *et al.*[17] reported a comprehensive study of thermodynamic properties of crystalline CCH. They discovered that crystal I phase, which consists of a mixture of a- and e-conformers, can be formed by cooling down to 229 – 220 K. When CCH were further cooled to 217 and 206 K, two additional solid-to-solid transitions were identified, resulting in the formation of crystals II and III phases, respectively, both with e-conformation exclusively. It has been previously reported that CCH can also form an amorphous phase at 90 K.[10] Independent of temperature tuning, pressure also played a significant role in forming new CCH phase. Using a diamond anvil cell, Woldbaek reported infrared measurements of CCH at room temperature up to 4 GPa.[10] Detailed analysis indicates that a polycrystalline phase was formed at high pressures and room temperature, which has only e-conformer.

Despite the numerous observations of new phases of CCH, no detailed crystallographic structures have been determined due to the lack of high-quality single crystal X-ray data. Furthermore, high pressure can often induce the same phases existing at low temperature as dictated by the phase diagram. However, for CCH low temperature so far has induced many more new phases than observed at high pressures. Up to date, CCH has only been investigated up to 4 GPa and no further high-pressure Raman measurements have been conducted beyond this pressure. Moreover, the stability of molecules with ring architecture upon extreme compression is of particular interest. An intriguing question is whether the CCH ring will break down as many conjugated ring systems such as benzene[18,19] and furan[20] at certain level of compression. Therefore, it is necessary to extend the previous study to higher pressures to fully understand the structures and properties of CCH. In this study, we report the *in-situ* Raman measurements of CCH at high pressures up to 20 GPa, far beyond those previously achieved. Our objective is to explore the unknown pressure domain which may provide important insight in the interpretation of general behaviors of simple organic molecular solids under extreme conditions. We observed rich pressure behavior of CCH and examined the reversibility of phase transformations by both compression and decompression. These new observations contribute to the understanding of high-pressure structures, stability, as well as thermodynamic properties of CCH.

3.2 Experimental section

Pure CCH (99%) was purchased from Aldrich and used without further purification. In the low pressure region, a lever-arm type DAC (purchased from High Pressure Diamond Optics Inc.) equipped with type I diamonds with culet size of 650 μm was used, which allows the accurate control and fine increments of the pressure up to 4 GPa. Stainless steel gaskets were predrilled with a hole of 250 μm as the sample chamber. In the high-pressure region, another symmetric piston-cylinder type DAC equipped with 400 μm culet diamond anvils was used to achieve pressures up to 20 GPa. The samples were loaded at room temperature as liquid with nominal pressure slightly above ambient. Then the cell was carefully pressurized with small steps and allowed to stabilize for a few minutes after each pressure change before Raman spectra were taken. A few ruby chips as the pressure calibrant were carefully placed inside the gasket sample chamber before the sample was loaded for pressure determination.[21] For the entire pressure region, ruby fluorescence spectra obtained on different ruby chips across the sample chamber indicate no significant pressure gradient. Especially at the lower pressure region (e.g., < 10 GPa), the ruby spectral profiles suggest no obvious nonhydrostatic effects. Therefore, no pressure transmission media was used.

A commercial Renishaw Ramam spectrometer (model 2000) was used for pressure determination and Raman measurements. This model is a compact laser Raman microprobe capable of both spectroscopy and imaging. A HeNe laser with wavelength of 632.8 nm was used as the excitation source with an average power of several miliwatts on the sample. A Leica microscope with objective lenses of multiple magnifications together with other Raman optics enables measurements with backscattering geometry. An edge filter is installed to remove the Rayleigh and anti-Stokes lines enabling a measurable spectral range above 120 cm^{-1}. The spectrometer is equipped with an imaging spectrograph and a sensitive thermoelectronically cooled CCD detector allowing a spectral resolution of 1 cm^{-1}. Frequency calibration of the Raman spectrum was realized using silicon and diamond standards achieving an accuracy of ± 0.5 cm^{-1}. Due to the strong T_{2g} mode of type I diamond Raman signal at 1334 cm^{-1}, the spectra were collected in the ranges of 120 – 1300 and 2400 – 3300 cm^{-1}. These frequency ranges covered almost all the Raman-active modes of CCH that are playing important roles in characterizing the conformational and phase transformations. Pressure effects on CCH were examined both in the compression and decompression directions. Experiments were conducted up to 20 GPa and reproduced several times. All measurements were conducted at room temperature.

3.3 Results

3.3.1 Raman spectra of CCH at ambient condition

Raman spectrum of liquid CCH was collected at ambient pressure and room temperature as a starting point, which is depicted in Fig. 3.2 (a). The assignments are labeled above each mode and also listed in Table 3.1 in comparison with previous measurements under different conditions. Both axial and equatorial conformers have *Cs* symmetry which thus results in 48 fundamental (of 27 A' and 21 A'' symmetries), all of which are both Raman and IR active. We note that some vibrations, such as ν_{24}, ν_{23}, ν_{22}, and ν_{21} are observed in both *a*- and *e*-conformations but with drastically different frequencies. The difference is indicated in parentheses in Table 3.1 and implied in the context. As can be seen, almost all 48 Raman modes are observed, and their frequencies are consistent with those previously reported under similar conditions. In the liquid phase, CCH exists as a mixture of *a*- and *e*-conformers with the latter being the dominant conformation.

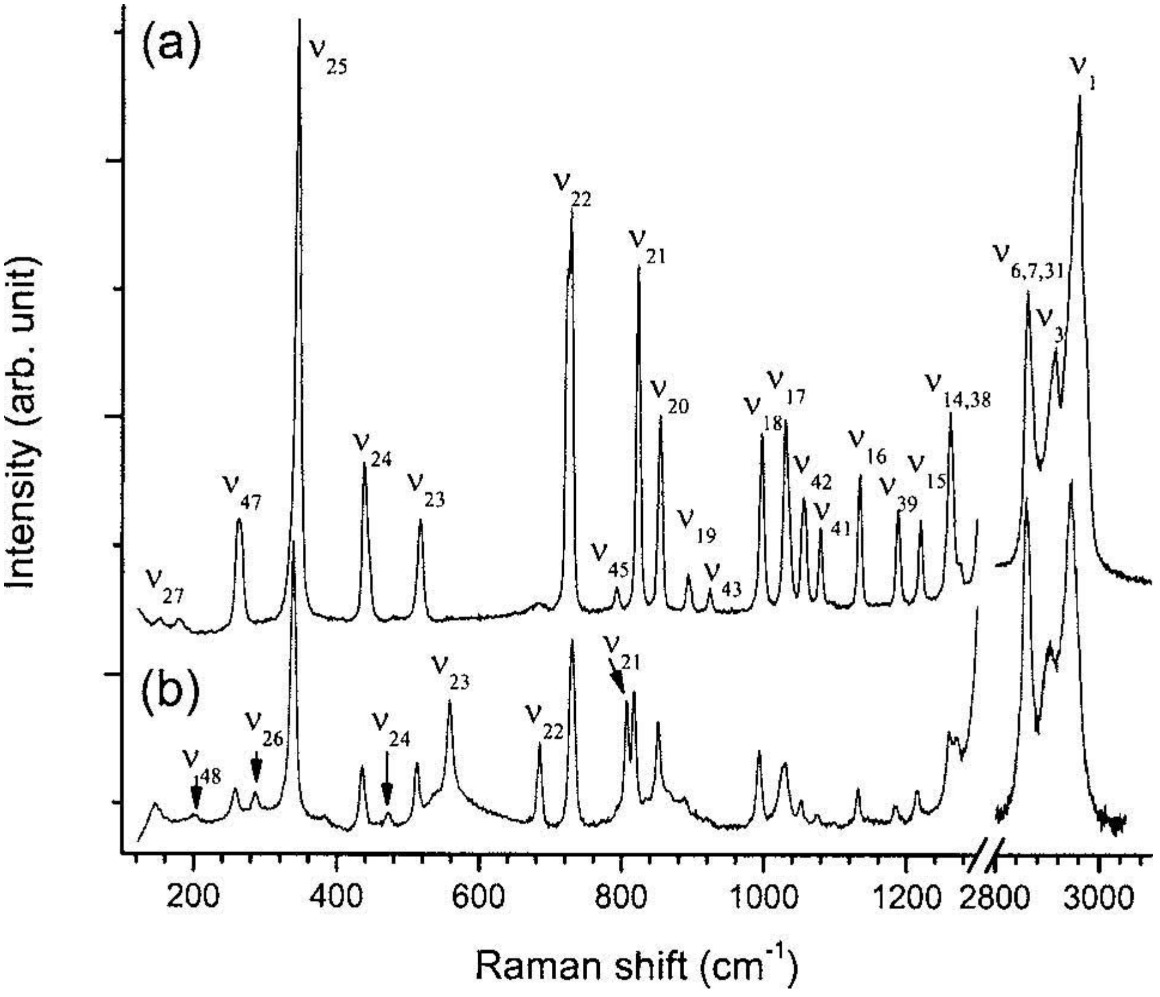

Figure 3.2 Raman spectra of CCH collected at (a) ambient pressure in comparison with that (b) collected upon slight compression (0.03 GPa). CCH exists as a mixture of axial and equatorial conformers with the latter dominant at condition (a) and thus the assignment labeled above each Raman modes refers to equatorial conformation. Axial and equatorial conformers share majority of common Raman modes and thus only those exclusively associated with axial conformer are labeled in spectrum (b). The spectral region of 1300 – 2800 cm^{-1} is omitted due to the strong T_{2g} Raman mode of diamond anvil and that only a few insignificant Raman modes occur in that region.

Table 3.1 Assignment of vibrational frequencies of observed Raman modes of chlorocyclohexane at near ambient pressure and room temperature. Because of strong Raman signal from the diamond anvils, the nearby modes (around 1330 cm^{-1}) were not observed or tabulated.

this work		reference (cm^{-1})[a]				
0 GPa	0.03 GPa	liquid	crystal (90 K)	calculated	assignment[b]	description
151/181	145	145	150/167	154	$\nu_{27}A'$	C-Cl bend
	201	200		182	$(\nu_{48}A'')$	Ring bend
262	258	260	260	263	$\nu_{47}A''$	
	286	287		290	$(\nu_{26}A')$	
347	339	341	342	342	$\nu_{25}A'$	
438	438	437	436	428	$\nu_{24}A'$	
	473	473		482	$(\nu_{24}A')$	
517	513	513	513	508	$\nu_{23}A'$	
	560	560		552	$(\nu_{23}A')$	
	682	687		680	$\nu_{22}A'$	C-Cl stretch
729	729	732	726	733	$(\nu_{22}A')$	
794		790	791	787	$\nu_{45}A''$	CH$_2$ rock
	809	809		806	$(\nu_{21}A')$	
823	818	819	819	819	$\nu_{21}A'$	Ring stretch
855	852	853	851	839	$\nu_{20}A'$	
895	890	890	890	892	$\nu_{19}A'$	
921	919	922	922	928	$\nu_{43}A'$	CH$_2$ rock
997	992	995	996	992	$\nu_{18}A'$	Ring stretch
1030	1030	1030	1028	1028	$\nu_{17}A'$	
1058	1050	1052	1053	1051	$\nu_{42}A''$	CH$_2$ twist and wag, CH def
1080	1075	1075	1076	1083	$\nu_{41}A''$	
1134	1133	1132	1133	1121	$\nu_{16}A'$	
1188	1185	1186	1186	1182	$\nu_{39}A''$	
1220	1215	1216	1218	1221	$\nu_{15}A'$	
1263	1262	1261	1261	1251	$\nu_{14}A'$	
				1245	$\nu_{38}A''$	
2864	2859	2861	2855	2853	$\nu_{6}A'$	CH$_2$ and CH stretch
				2852	$\nu_{7}A'$	
				2851	$\nu_{31}A''$	
2915	2903	2908	2907	2914	$\nu_{3}A'$	
	2944	2946	2943	2922	$\nu_{2}A'$	
2958			2957	2956	$\nu_{1}A'$	

[a] Ref. 10

[b] The Raman modes exclusively associated with axial conformation are denoted in parentheses. Other assignments apply to both equatorial and axial conformers.

3.3.2 Raman spectra of CCH on compression

When CCH is slightly compressed from ambient pressure to 0.03 GPa, dramatic changes of the Raman spectrum are observed as shown in Fig. 3.2 (b). New bands at 201, 286, 560, 682, and 809 cm^{-1} with significant intensities are attributed to the respective ν_{48}, ν_{26}, ν_{24}, ν_{23}, ν_{22}, and ν_{21} modes exclusively associated with *a*-conformation. Simultaneously, peaks at 262, 438, 517, and 729 cm^{-1} due to the respective ν_{47}, ν_{24}, ν_{23}, and ν_{22} modes are depleted significantly, indicating these modes are mainly associated with *e*-conformation. All other modes shift to low frequencies systematically by a few wave numbers compared to the ambient pressure measurement. The two conformers of CCH have the same symmetry with the only difference in the orientation of chlorine atom. Thus, the shifts can be attributed to the con-formational difference between the same modes involved rather than pressure effect, since the pressure difference of 0.03 GPa is negligible. All these observations indicate that the conformational equilibrium has shifted from equatorial to axial significantly. Among these modes, ν_{26}, ν_{24}, ν_{23}, and ν_{21} modes (286, 473, 560, and 729 cm^{-1}), and particularly ν_{22} mode (680 cm^{-1}), which are associated with carbon-chlorine stretching, can be used to monitor the abundance of axial conformation quantitatively. When pressure is increased to 0.5 GPa, for instance, the intensity of all these characteristic Raman modes increased significantly, indicating that the equilibrium is further shifted to axial by pressure.

Instead of continuous enhancement, however, the above mentioned characteristic modes of axial conformation suddenly disappeared completely when pressure is increased to around 0.7 GPa (Fig. 3.3). In addition, the intensities of the Raman modes of the lowest two frequencies (ν_{27} and ν_{48}) are significantly depleted. In contrast, the modes associated with equatorial conformer, such as ν_{45}, ν_{19}, and ν_{43} at respective 789, 891, and 923 cm^{-1} are markedly enhanced. The observation of such a discontinuity indicates a complete transformation from a mixture of two conformers with axial being dominant to pure equatorial conformation, concurrent to the phase transition from liquid to solid, which is further confirmed by visual inspection under the optical microscope. This is consistent with previous report that solid CCH is composed of equatorial conformers only.[8-12]

The next transformation is observed when CCH is compressed to 2.4 GPa. The most prominent evidence is the observation of the splitting of the ν_{21} mode at 729 cm^{-1}, which appears with a shoulder and then evolves into a well resolved doublet at 4.8 GPa. Furthermore, the Raman modes associated with C–H stretching in the high frequencies (e.g., 2800 – 3000 cm^{-1}) are significantly weakened by compression to 2.4 GPa, which confirmed the phase transition around this pressure.

When pressure is elevated to 4.8 GPa, modifications of the Raman profile with new features are observed in addition to the pressure induced frequency shift of all Raman modes. Specifically, a new peak appeared in low frequency region at 142 cm^{-1}, which is likely associated with lattice vibrations. Another interesting observation is that in addition to the continuing enhancement of ν_{45}, ν_{19}, and ν_{43} modes, the relative intensities of the ν_{21} and ν_{20} modes exhibit a switchover at 4.8 GPa, below which ν_{20} dominates but above which ν_{21} is much stronger. In addition to the splittings of the ν_{22} mode, many other modes also experienced significant splittings, such as ν_{20}, ν_{17}, and ν_{42} modes. The high frequency C-H stretching modes remain weak. All these observations suggest another transition around 4.8 GPa.

As the CCH is compressed to 10.1 GPa, all Raman bands become significantly broader with low frequency modes greatly depleted. Simultaneously, many of the doublets start to merge, such as the ν_{22}, ν_{20}, ν_{17}, and ν_{42} modes. This trend is continuing with increasing pressure up to about 20 GPa, the highest pressure of the present study, where the spectrum displays a profile with broad bands with two strongest modes (ν_{25} and ν_{22}), which are also the strongest observed at low pressures.

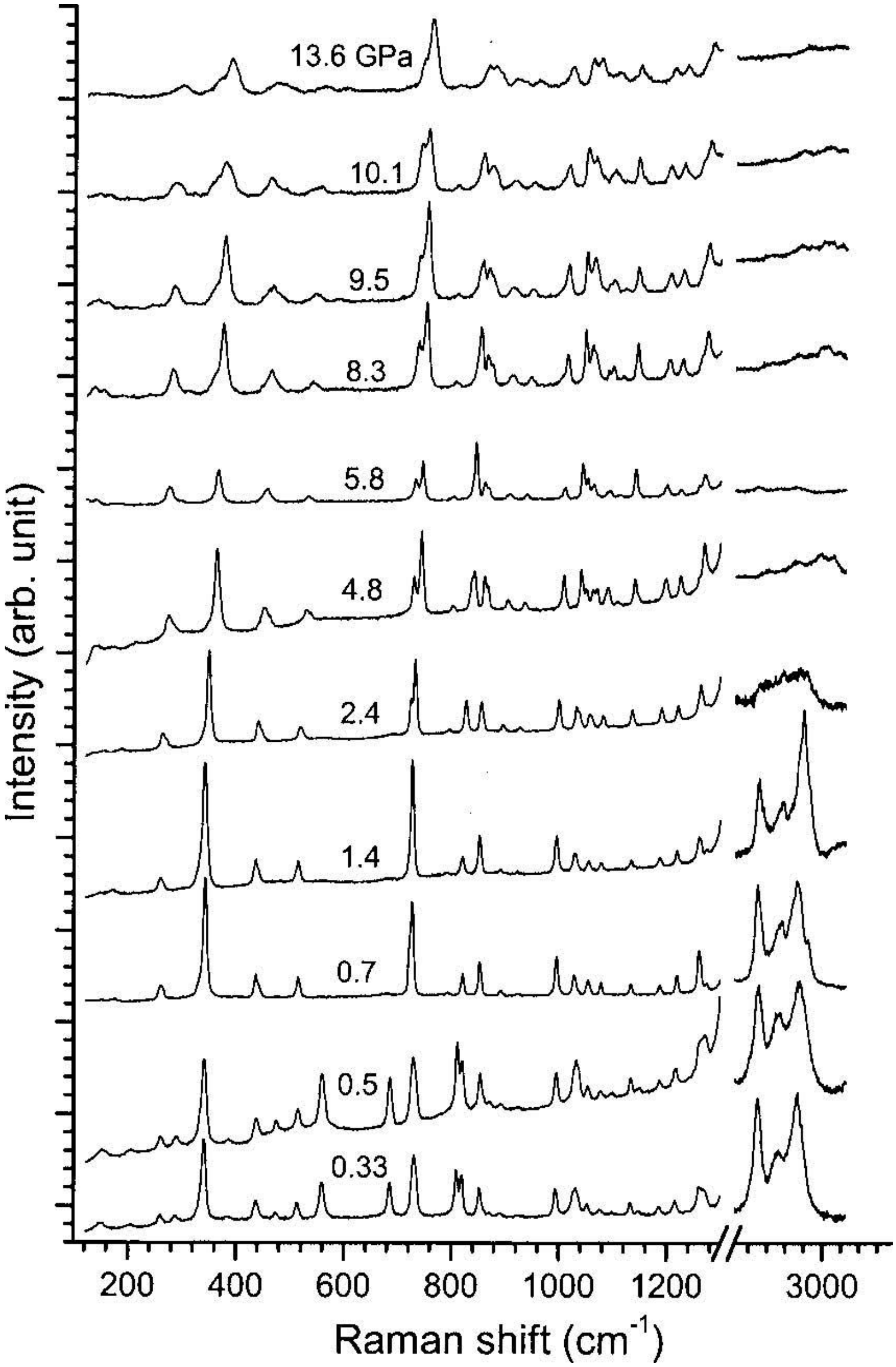

Figure 3.3 Selective Raman spectra of CCH on compression in the pressure region of 0 – 14 GPa in the spectral ranges of 120 – 1300 and 3800 – 3200 cm^{-1}. The relative intensities are normalized and thus are directly comparable. The pressures in gigapasicals are labeled for each spectrum. The spectra are offset vertically for clarity.

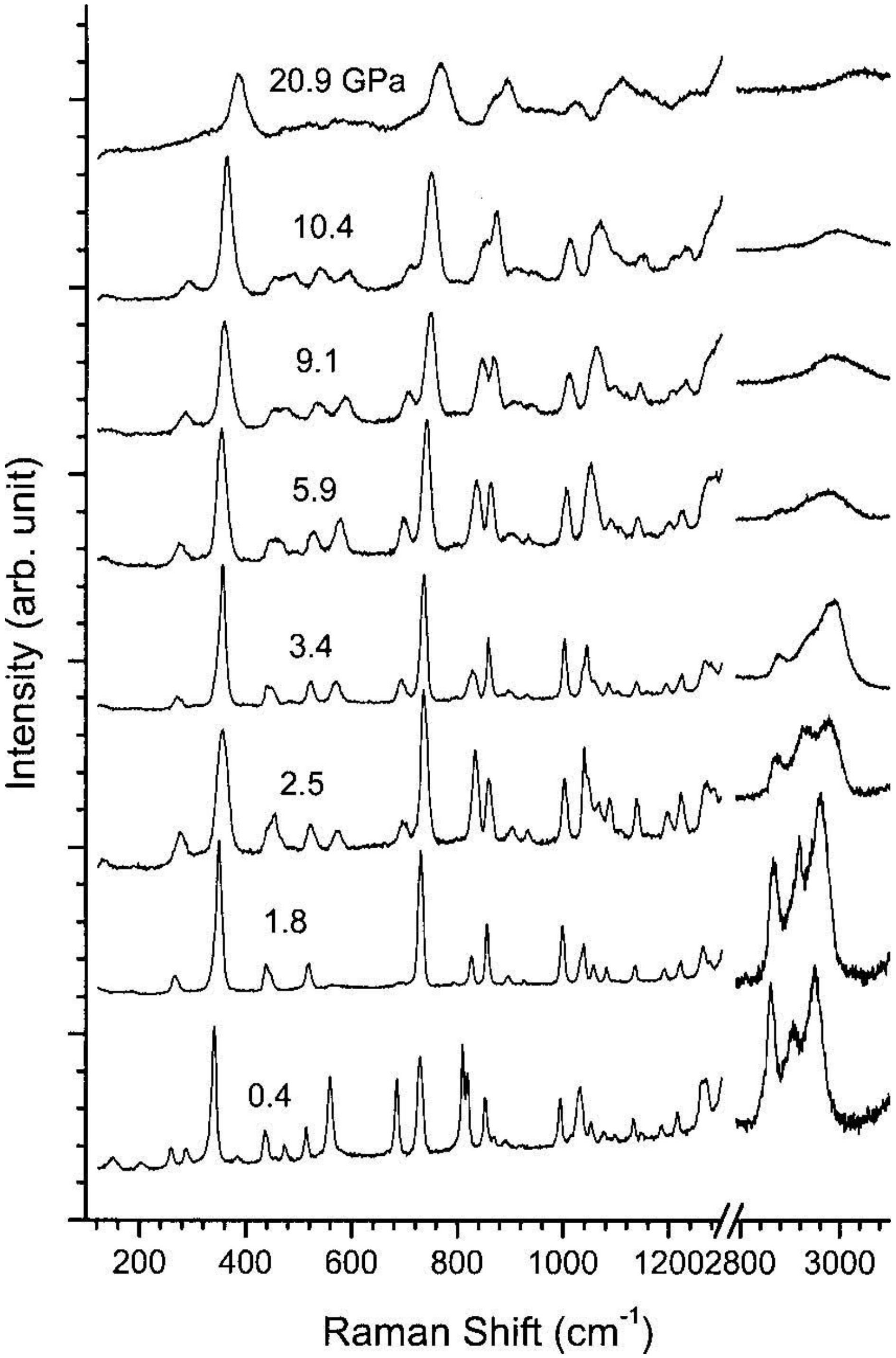

Figure 3.4 Selective Raman of CCH on decompression from around 20 GPa all the way down to ambient pressure. The relative intensities are normalized and thus are directly comparable. The pressures in gigapascals are labeled for each spectrum. The spectra are offset vertically for clarity.

3.3.3 Raman spectra of CCH on decompression

The reversibility of pressure effect on molecular structures provides important information on transformation mechanisms. Therefore, upon compression of CCH to the highest pressure of 20 GPa, we conducted Raman measurements on decompression all the way down to the ambient pressure. The spectra are depicted in Fig. 3.4. In general, the change of Raman profile is very gradual with decompression. Not until 10.4 GPa, did all the characteristic modes start to be observed. Compared to the compression data at 10.1 GPa (Fig. 3.3), a striking difference is the appearance of a new peak at 595 cm^{-1}. In addition, the ν_{22} mode (at 743 cm^{-1}) which appears as a doublet during compression between 2.4 and 10.1 GPa seems to remain a singlet at all pressures during decompression. Instead of being a branch of the doublet, the shoulder peak preceding the ν_{22} mode at 10.4 GPa apparently evolves as an independent mode as pressure is further released and is observed all the way down to 2.5 GPa. Furthermore, the relative intensities of ν_{21} and ν_{20} modes are drastically different between compression and decompression. During compression, the ν_{21} mode remains dominant while the ν_{20} mode is always stronger or equally strong as ν_{21} on decompressions until 2.5 GPa. In addition, many doublet modes observed upon compression, such as ν_{20}, ν_{17}, and ν_{42} modes, appear as a broad singlet during decompression. For example, the most evident comparison can be made between the decompression spectrum at 5.9 GPa (Fig. 3.4) with the compression spectrum at 5.8 GPa (Fig. 3.3). In general, the decompression spectra are broader than the compression spectra at corresponding similar pressures. Decompression spectra do not exhibit clear low frequency lattice modes until 2.5 GPa. All these observations indicate that the structural transformations have certain hysteresis upon decompression and are thus not completely reversible at the high-pressure region (> 2.5 GPa).

When pressure is released to 2.5 GPa, the Raman spectrum is more or less similar to the one at 2.4 GPa upon compression, except for slightly different intensities as well as the above mentioned new modes, which remains the most distinctive difference. Another major difference is observed in the high frequency C-H stretching region where the decompression spectrum showed three clearly resolved bands, in contrast to a broad profile in the compression spectrum. When pressure is further released to 1.8 GPa, the Raman pattern exhibits exactly the same features as the one at 1.4 GPa during compression, indicating that the transformation at this pressure is completely reversible. Further releasing the pressure to 0.4 GPa results in the Raman pattern exactly the same as the one at 0.5 GPa during compression, which is attributed to the mixtures of axial and equatorial conformations of CCH. Again, the transformation here is reversible.

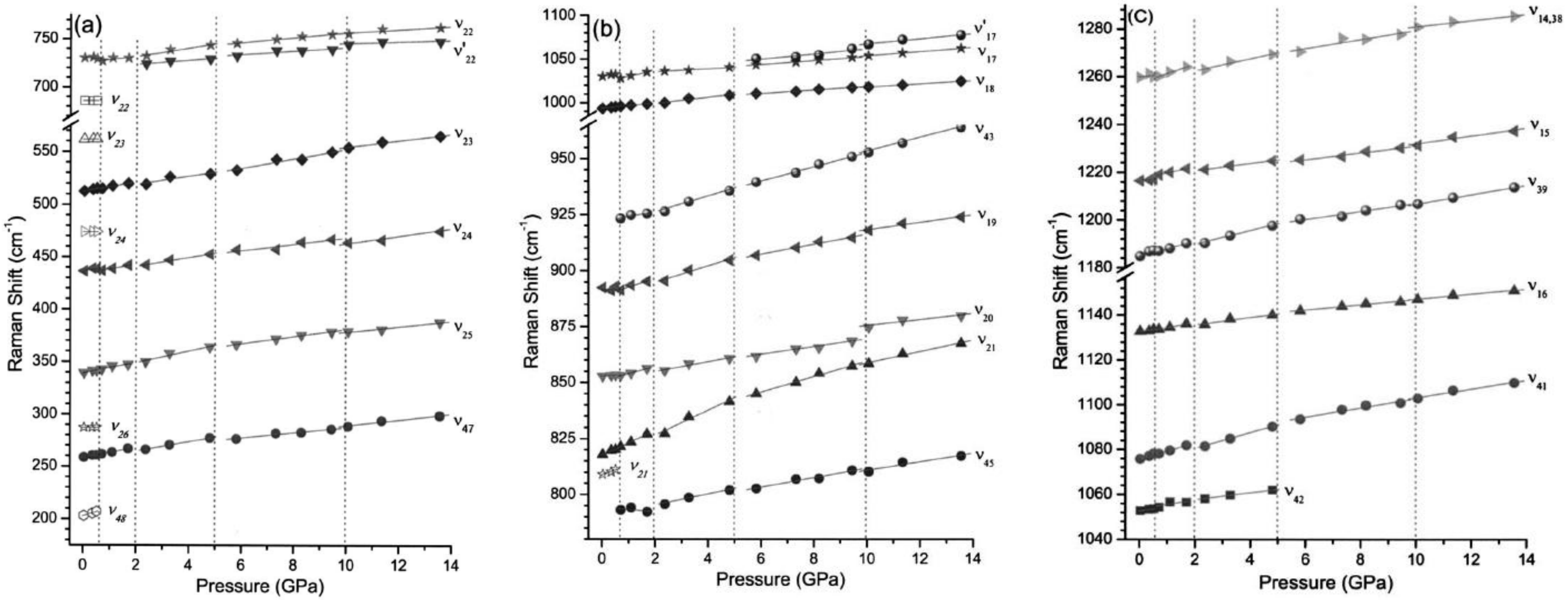

Figure 3.5 **Pressure dependence of Raman shift of CCH on compression in (a) the ring bending and C–Cl stretching region (180 – 750 cm^{-1}); (b) the ring stretching and CH$_2$ rocking region (790 – 1100 cm^{-1}); and (c) the CH$_2$ twisting and wagging as well as the CH deformation region (1050 – 1280 cm^{-1}). Different symbols denote Raman modes with different origins. Open and closed symbols denote axial and equatorial conformers of CCH, respectively. The solid lines crossing the symbols are based on linear fit. The vertical dashed lines denote the proposed phase boundaries.**

3.3.4 Pressure effect on Raman modes of CCH

Pressure dependence of selected Raman modes of CCH on compression is depicted in Fig. 3.5 in the frequency region below 1300 cm^{-1}. Since the C-H stretching modes at 2800 – 3000 cm^{-1} are observed clearly only below 2.4 GPa, they were not included in the analysis here. The pressure dependences ($d\nu/dP$) of selected Raman modes are listed in Table 3.2 as well. In general, all Raman modes exhibit pressure induced blue shifts (with only a few exceptions in the low pressure region as discussed below), consistent with that the bonds become stiffened by pressure. However, at different pressure regions, the shift rates are different, providing evidence for phase transformations.

The first phase transition corresponding to a fluid to solid transition occurs at about 0.7 GPa as indicated by the first vertical dashed line in Fig. 3.5. Below this pressure, the CCH is composed of a mixture of *a*- and *e*-conformers. Most Raman modes associated with *a*-conformer, such as the ν_{26}, ν_{24}, and ν_{23} (ring bending) modes at respective frequencies of 286, 473, and 560 cm^{-1} as well as the ν_{22} (CH rocking) mode at 729 cm^{-1}, are fairly insensitive to pressure (i.e., $d\nu/dP\approx 0$). Other modes, such as ν_{48} and ν_{21} at 201 and 809 cm^{-1}, shift with pressure more significantly. On the other hand, all modes associated with *e*-conformer generally exhibit large, linear, and positive pressure dependences except for the ν_{22} and ν_{19} modes, which have negative $d\nu/dP$ values (−1.4 and −0.4 cm^{-1} /GPa, respectively). At 0.7 GPa, all the characteristic *a*-conformer modes (ν_{48}, ν_{26}, ν_{24}, ν_{23}, and ν_{22}) disappeared abruptly, indicating that the solid phase is exclusively *e*-conformer.

Table 3.2 Pressure dependence of vibrational frequencies of major Raman modes for CCH at room temperature. All the Raman modes monitored are associated with the equatorial conformation. The modes for CH_2 and CH stretching region (2800 – 3000 cm^{-1}) are not tabulated since they are observed only in low pressure region (< 2.4 GPa).

Raman mode[a]	**peak origin (cm^{-1})**	**$(d\nu/dp)_T$(cm^{-1}/GPa)**				
		0 – 0.7 GPa	**0.7 – 2 GPa**	**2 – 5 GPa**	**5 – 10 GPa**	**> 10 GPa**
ν_{47}	262	4.4	5.2	4.5	2.5	2.8
ν_{25}	347	4.8	4.3	5.6	3.4	2.6
ν_{24}	438	5.0	4.9	4.2	3.1	3.7
ν_{23}	517	5.5	4.7	3.8	4.5	3.1
ν'_{22}	…	…	…	2.1	1.8	0.8
ν_{22}	729	-1.4	2.8	4.5	2.6	1.7
ν_{45}	794	…	-1.0	2.4	2.2	1.9
ν_{21}	823	4.5	5.8	5.6	3.5	2.6
ν_{20}	855	1.0	3.2	2.2	1.7	1.3
ν_{19}	895	-0.4	3.9	3.7	2.2	1.6
ν_{43}	921	…	2.1	3.6	3.2	3.0
ν_{18}	997	4.0	2.6	3.5	2.0	1.9
ν_{17}	1030	5.1	8.0	1.7	2.3	2.4
ν'_{17}	…	…	…	…	3.0	2.9
ν_{42}	1058	1.7	2.0	1.5	…	…
ν_{41}	1080	4.6	3.7	3.5	2.1	2.0
ν_{16}	1134	1.5	2.4	1.7	1.1	1.1
ν_{39}	1188	5.0	3.3	2.9	1.7	2.0
ν_{15}	1220	1.2	2.5	1.5	1.4	1.6
$\nu_{14,38}$	1263	1.1	4.0	2.5	1.8	1.3

[a] The assignments of the Raman modes are consistent with Table 3.1 except for ν'_{22} and ν'_{17}, which are new modes observed as a result of splitting of the ν'_{22} and ν'_{17} modes, respectively.

The major evidence for the second phase transition around 2.4 GPa is the observation of the splittings of ν_{22} C-Cl stretching mode at 729 cm^{-1} into a doublet. Above 2.4 GPa, the two branches of the doublet (labeled as ν_{22} and ν'_{22}) exhibit different pressure dependences with 4.5 versus 2.1 cm^{-1}/GPa. All other modes have similar pressure dependences across the transition boundary around 2 GPa with two exceptions: (1) the ν_{45} mode has a negative $d\nu/dP$ below 2.4 GPa, which becomes positive above 2.4 GPa;

and (2) the ν_{17} mode has a much larger pressure dependence (8.0 cm^{-1}/GPa) below 2.4 GPa than above (1.7 cm^{-1}/GPa). These observations, together with the weakening and disappearance of C-H stretch modes at 2859, 2903, and 2944 cm^{-1} (not shown in Fig. 3.5), clearly confirm the phase transition.

For the phase between 5 and 10 GPa, all Raman modes exhibit smooth pressure shifts and similar shift rates as those for the phase between 2 and 5 GPa. As described previously, however, several modes exhibit significant splittlings in this pressure region, such as ν_{22}, ν_{20}, ν_{17}, and ν_{42} modes, although not all of them are plotted in Fig. 3.5 for clarity purpose. The most distinctive discontinuity is the abrupt disappearance of ν_{42} modes above 5 GPa. These features label the second solid-to-solid transition at this pressure. The last transition at around 10 GPa is characterized with much less prominent changes of pressure dependences than the previous several transition pressures.

3.4 Discussion

Quantitative analysis of conformational equilibrium of CCH at low pressure region has been addressed by both IR spectroscopy in a solution[13] and Raman spectroscopy as a pure substance.[11] By monitoring the relative intensities of the respective ν_{22} modes at 682 and 729 cm^{-1} associated with axial and equatorial conformations, the equilibrium constant K and volume difference ΔV between the two conformers at certain pressures can be related by eq. 3.1.

$$\Delta V = -RT\left(\frac{\partial \ln K}{\partial P}\right)_T \tag{3.1}$$

where T is the temperature, R the gas constant, and K can be evaluated by the ratio of the integrated intensities of the two modes.[6,11] The volume difference ΔV between the two conforms was determined to be −2.33 cm^3 mol^{-1} by Gardiner, in contrast to that by Christian who reported −1.87 cm^3 mol^{-1}, but the latter was obtained in carbon disulphide solution.[13] Based on our measurement, we determine the ΔV to be −2.2 cm^3 mol^{-1} for pure CCH, closer to that by Gardiner as expected.

Studies of volume difference between conformers have been carried out in several other systems under various pressures, temperatures, as well as solvent conditions. For instance, Gardiner conducted a similar study on bromocyclohexane and reported a similar ΔV value (−2.2 cm^3 mol^{-1}) between the axial and equatorial conformers.[22] For different molecular systems, the relative magnitude of ΔV values derived under different conditions (e.g., as a pure substance versus in solutions) is strongly contrasting. In our previous high-pressure Raman study of 1,2-dichloroethane, we found the ΔV that value between *trans* and *gauche* conformers of pure substance (0.58 cm^3 mol^{-1}) is much smaller than in solutions (1.8 – 4.5 cm^3 mol^{-1}),[6] in contrast to those for CCH where ΔV value in solution is smaller. It has been known that several factors, such as orientation of the substituent, inter-molecular interactions, as well as relative packing efficiency, strongly affect the volume difference between the two conformations.[22] Therefore, the combination of different conditions (pressure, temperature and use of solvent with different polarities) will contribute differently to the ΔV values between two conformers with very different structures. Apparently, the larger volume difference between two conformers observed in pure CCH indicates that one or more of the three factors are manifested more than in solutions.

Based on the high-pressure Raman measurements, the first solid phase exists between 0.7 and 2.4 GPa. This solid phase consists of equatorial conformer exclusively, consistent with previous studies conducted at room temperature and high pressure where CCH forms a polycrystalline phase when compressed up to 4 GPa from liquid.[10] It is well known that high pressure and low temperature generally result in the formation of phases with the same crystalline structure. In an IR study of CCH at ambient pressure and low temperatures,[17] however, the first crystalline phase (crystal I) which was formed by cooling the liquid to 224 K consists of a mixture of axial and equatorial conformers instead of pure *e*-conformer observed as the first solid phase here. Crystal I phase remains stable between 220 and 229 K. Therefore, our observation of systematic absence of characteristic Raman modes associated with axial conformer indicates that the first solid phase of CCH induced by pressure is different from that induced by temperature and is possibly a polycrystalline phase as reported by Klaeboe and Woldbaek.[8,10] The sharp Raman profile characterized by very narrow bandwidth (e.g., ν_{25} and ν_{22} modes) together with the complete phase trans-formation is consistent with the formation of a crystalline structure under a near perfect hydrostatic condition. However, the detailed structure of this polycrystalline phase has not been characterized by X-ray diffraction to date.

The next solid-to-solid phase transition is observed at 2.4 GPa, which is evidenced by the splitting of ν_{22} mode at 729 cm^{-1} and the disappearance of C-H stretching modes at high frequencies. The splitting and disappearance of certain modes can be interpreted as enhanced intermolecular interactions within the same crystal structure. First of all, the splitting indicates that there are at least two molecules per unit cell in this phase. Pressure induced splitting of Raman modes have been observed in many other molecular solids.[5,6] In addition, dramatic change of the Raman intensity of C-H stretching mode suggests that solid CCH is highly compressible in this pressure region as characterized by much shorter intermolecular distance and smaller molecular volume. As a result, the polarizability of symmetrical stretching and other vibrations associated with a significant change of volume is reduced by the application of pressure and thus their intensities are markedly lowered.[11]

The phase change above 4.8 GPa can be consider as a continuation of enhanced intermolecular interaction as a result of compression. The lack of sharp changes of Raman profiles indicates the transition may involve mixed phases. In addition to the complete deconvolution of the ν_{22} mode, new splittings are observed for many other modes. Furthermore, a new lattice mode was observed. Due to use of an edge filter of our Raman spectrometer, low frequency modes below 120 cm^{-1} cannot be recorded from the spectrum. Thus the observation of this mode could be due to either the pressure induced blue shift of a mode below 120 cm^{-1} or a new lattice mode as a result of the formation of a new phase. Most significantly, all the Raman modes exhibit a distinct break in their pressure dependences at this pressure. Therefore, all these observations warrant a phase transition with significantly different molecular orientations within the unit cell. The observation of the lattice mode indicates that the ordered crystal phase is stable up to 9.5 GPa. In Diky's low-temperature IR study, two additional solid phases are observed when temperature is lowered below 220 K.[17] The phase observed at 217 K has a dramatically different IR pattern than that above 220 K in that the two strong bands at 480 and 556 cm^{-1} observed at 220 K completely disappeared at 217 K. Since we did not observe any significant change of Raman patterns at either 2.4 or 4.8 GPa, the new phases formed at low temperatures (< 220 K) likely are different from those observed around 2.4 and 4.8 GPa and room temperature.

The phase above 10.1 GPa is characterized with broad or convoluted profiles for all Raman modes. Together with the disappearance of the lattice modes, the phase can be interpreted as undergoing a gradual transition to a disordered structure or amorphous phase. Similar features have been observed in 1,2-dichloroethane when pressure is elevated above 9 GPa.[6] Although pressure gradient as a result of non-hydrostatic condition may contribute to the profile broadening, the sudden increase in the bandwidth of several modes (e.g., ν_{47} and ν_{25}) from 9.5 to 10.1 GPa signifies the phase transition. Beyond 10.1 GPa, the profile broadening may be associated with the combination of structural disordering and increasing pressure gradient. At the highest pressure of the present study, the Raman band maintained a similar profile with dominant characteristic Raman modes of ν_{25} and ν_{22}, indicating the six-member ring although highly distorted, still maintains its molecular identity.

The distinctive pressure dependence of all Raman active modes in different pressure regions provides further evidence of phase transitions discussed above. Although the crystal structures of CCH and thus the equation of states characterized by bulk moduli are still unknown, the pressure dependence of most of the Raman modes provides insight on the compressibilities of CCH in different phases. From Fig. 3.5 and Table 3.2, the majority of the Raman modes exhibits the largest $d\nu/dP$ values below 2 GPa (and especially for the phase between 0.7 and 2 GPa), while those above 5 GPa become significantly smaller, especially beyond 10 GPa. These observations indicate that CCH is more compressible at low pressures less than 2 GPa but relatively less compressible above 10 GPa. The greater compressibility at lower pressure regions is consistent with the general understanding that intermolecular distances are more sensitive to compression and thus make a major contribution to the reduction of the volume.[23]

The most interesting observation is the partial reversibility upon decompression. The decompression measurements reveal a large pressure hysteresis in the high-pressure region above 10 GPa as characterized by the much broader spectral profile upon decompression than compression. Between 10.4 and 2.5 GPa, two new peaks (595 and 711 cm^{-1} at 10.4 GPa or 573 and 697 cm^{-1} at 2.5 GPa) are observed in all the decompression spectra, indicating that the phases formed in this pressure region by decompression are different than those produced by compression. Careful examination of these two new peaks indicates that the frequencies are close to the characteristic ν_{23} and ν_{22} modes of axial conformer. Although other modes associated with axial conformer were not observed, it is plausible to conclude that the phases in this pressure region formed by decompression have the CCH molecules adopting both equatorial and axial conformation. The relative intensity of these two new modes in this pressure region is much smaller than in the liquid phase, indicating that the relative abundance of axial conformation is small. When pressure is further released, the transformation to the first solid phase as well as to the liquid phase is completely reversible as evidenced by almost identical Raman patterns regardless via compression or decompression. The decompression experiment further established that the ring of the CCH sustained compression up to 20 GPa.

It is intriguing that the high-pressure region exhibits hysteresis and partial reversibility. Similar phenomenon was also observed in the low pressure region by Klaeboe.[8] CCH was found to form a polycrystalline phase at about 4 GPa. By carefully releasing pressure followed by gradual compression, a single crystal can be easily grown. On the other hand, considerable "super-pressing" results in the spontaneous formation of polycrystalline phase which can be released to 2 – 2.5 GPa without forming single crystals. All these observations indicate the formation of different phases of CCH is highly *P*-*T* path dependent. It has also been reported that several organic solids can form the so called plastic crystals which are characterized with high plasticity in contrast to "normal" organic crystals, which have hard lattice structures and sharp phase transition boundaries.[24] For example, the unsubstituted cyclohexane is a well known plastic crystal at −87 °C and melts at 6 °C.[25] Therefore, the observed pressure hysteresis and partial reversibility between compression and decompression may be associated with the intrinsic nature of the plasticity of CCH. As plastic crystals have many applications, further detailed structural characterization of CCH at high pressures and different temperatures using more direct probes, such as x-ray diffraction, would be of fundamental interest.

3.5 Conclusions

We conducted *in-situ* Raman measurements on CCH at room temperature and high pressures up to 20 GPa on both compression and decompression. Below 0.7 GPa, CCH exists as a fluid phase with a mixture of axial and equatorial conformations in equilibrium, which is shifted to axial upon compression. The shift was attributed to the smaller volume of axial conformer with a volume difference of -2.2 cm^3 mol^{-1} compared to equatorial conformation, consistent with previous studies. When pressure is increased to 2.4 GPa, splittings of the ν_{22} mode as well as the depletion of C–H stretching mode at high frequency indicate a phase transition. The splittings are further enhanced at 4.8 GPa together with the observation of a new lattice mode, suggesting another phase transition. These phases are compared with previously observed phases at low temperatures, which indicates that high-pressure phases are likely different from the low-temperature phases. Compression beyond 9.5 GPa results in significant broadening of Raman profiles, indicating that CCH is undergoing gradual disordering at high pressures. The six-member ring is found to sustain high pressures up to 20 GPa and CCH is fully recoverable upon releasing of pressure. However, the observation of two new modes upon decompression indicates that phase transformation of CCH is partially irreversible at high pressures above 2.5 GPa. The phase formed by decompression is found to have a contribution from axial conformation of CCH. The partial irreversibility or pressure induced hysteresis is attributed to the plastic nature of the CCH crystals.

3.6 References

(1) Hemley, R. J. Annu. *Rev. Phys. Chem.* **2000**, *51*, 763.

(2) Mao, R. J. H. a. H. K. *Proceedings of the International School of Physics Enrico Fermi;* R. J. Hemley, G. L. C., M. Bernasconi, and L, Ulivi, Ed.; *IOS: Amsterdam,* **2002**; Vol. *147*.

(3) Manaa, M. R. Chemistry at Extreme Conditions; Elsevier: Amsterdam, **2005**.

(4) Chen, X. J.; Struzhkin, V. V.; Song, Y.; Goncharov, A. F.; Ahart, M.; Liu, Z. X.; Mao, H.; Hemley, R. J. *Proc. Natl. Acad. Sci. U. S. A.* **2008**, *105*, 20.

(5) Song, Y.; Liu, Z. X.; Mao, H. K.; Hemley, R. J.; Herschbach, D. R. *J. Chem. Phys.* **2005**, *122*, 174511.

(6) Sabharwal, R. J.; Huang, Y. N.; Song, Y. *J. Phys. Chem. B* **2007**, *111*, 7267.

(7) Gill, G.; Pawar, D. M.; Noe, E. A. *J. Org. Chem.* **2005**, *70*, 10726.

(8) Klaeboe, P. *Acta Chem. Scand.* **1969**, *23*, 2641.

(9) Klaeboe, P.; Lothe, J. J.; Lunde, K. *Acta Chem. Scand.* **1956,** *10*, 1465.

(10) Woldbaek, T. *Acta Chemica Scandinavica Series a-Physical and Inorganic Chemistry* **1982**, *36*, 641.

(11) Gardiner, D. J.; Littleton, C. J.; Walker, N. A. *J. Raman Spectrosc.* **1987**, *18*, 9.

(12) Klaeboe, P. *J. Mol. Struct.* **1997**, *408*, 81.

(13) Christian, S. D.; Grundnes, J.; Klaboe, P. *J. Am. Chem. Soc.* **1975**, *97*, 3864.

(14) Waliszewska, G.; Abramczyk, H. *J. Mol. Liq.* **1995**, *64*, 73.

(15) Sommerfeldt, O. H. a. A. M. Z. *Phys. Chem. Abt. B* **1938**, *40*, 391.

(16) Leibler, K.; Przedmojski, J. *J. Chim. Phys.-Chim. Biol.* **1962**, *59*, 1084.

(17) Diky, V. V.; Kabo, G. J.; Kozyro, A. A.; Krasulin, A. P.; Sevruk, V. M. *J. Chem. Thermodyn.* **1994**, *26*, 1001.

(18) Ciabini, L.; Santoro, M.; Bini, R.; Schettino, V. *Phys. Rev. Lett.* **2002**, *88*, 085505.

(19) Ciabini, L.; Santoro, M.; Gorelli, F. A.; Bini, R.; Schettino, V.; Raugei, S. *Nat. Mater.* **2007***, 6*, 39.

(20) Ceppatelli, M.; Santoro, M.; Bini, R.; Schettino, V. *J. Chem. Phys.* **2003**, *118*, 1499.

(21) Mao, H. K.; Xu, J.; Bell, P. M. *J. Geophys. Res.-Solid* **1986**, *91*, 4673.

(22) Gardiner, D. J.; Walker, N. A. *J. Mol. Struct.* **1987**, *161*, 55.

(23) Ferraro, J. R. *Vibrational Spectroscopy at High External Pressures: The Dimaond Anvil Cell; Academic Press: Orlando*, **1984**.

(24) Timmermans, J. *J. Phys. Chem. Solids* **1961**, *18*, 1.

(25) MacFarlane, D. R.; Forsyth, M. *Adv. Mater.* **2001**, *13*, 957.

Chapter 4 Effects of High Pressure on Azobenzene and Hydrazobenzene Probed by Raman Spectroscopy[*]

4.1 Introduction

Molecular solids are soft materials that are subject to conformational change, phase transitions, or chemical transformations upon the application of external pressures.[1-3] Compression can effectively shorten the intermolecular and intramolecular distances, thus subsequently causing reversible or irreversible modifications in the molecular structures and associated electronic, optical or mechanical properties.[4] Therefore, pressure provides an excellent tool to produce new materials even starting from simple molecular solids, especially those with unsaturated bonds or conjugate ring structures.[5] For example, pressure-induced transformations have been reported for butadiene, benzene, furan, thiophene, pyridine and other aromatic derivatives.[6-12] As the most basic aromatic system, in particular, benzene was found to undergo a series of pressure-induced phase transitions up to 30 GPa, beyond which pressure-induced structural amorphization was observed.[9-12] More recently, pyridine was reported to undergo a similar pressure-induced transformation sequence as benzene in a similar pressure region.[6] These pressure-induced products are interesting from a technological point of view because of their unique properties desirable for possible applications in optics, electronics, mechanics and even as coating materials for biomedical applications.[11] So far, unsaturated hydrocarbons represent a major class of materials of interest for which

---

[*] The content of this chapter has been published as: Dong Z., Seemann M. N., Lu N., and Song Y., *J. Phys. Chem. B*, **2011**, *115*, 14912.

different reactivities of the π bonds under compressions critically influence the reaction pathways and, thus, the products.[13-15]

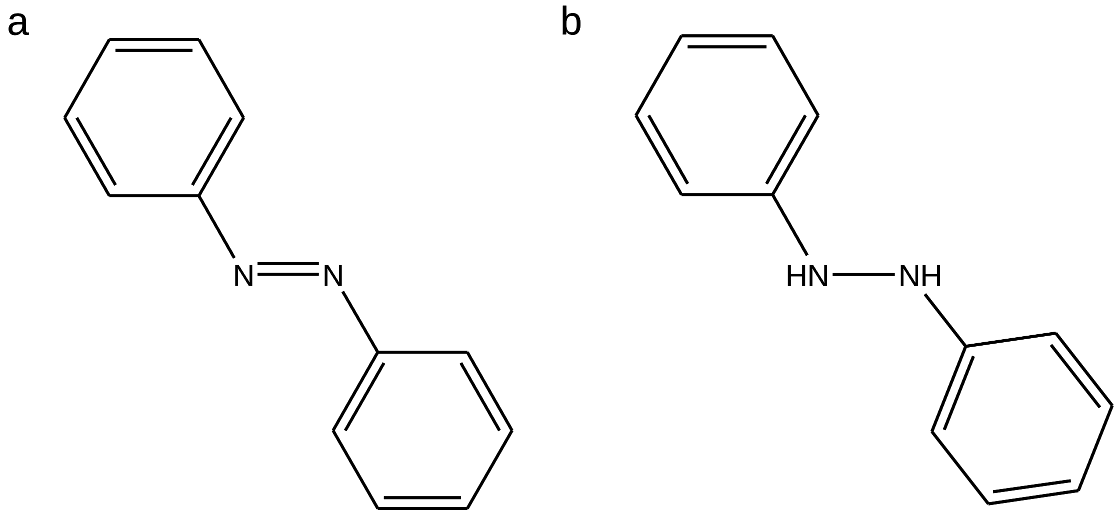

Figure 4.1 **The molecular structures of trans-azobenzene (a) and hydrazobenzene (b).**

Azobenzene (AB) is a conjugate aromatic molecule with two phenyl rings attached to an azo group (Fig. 4.1a). Due to its unique photochromic properties, azobenzene has been used as a moiety embedded in organic or biological macromolecules such as proteins and nucleic acids to provide special photo-functionality.[16] Moreover, based on its reversible trans-cis coupled photochemical and electrochemical isomerization,[17-19] azobenzene has been extensively studied as a photoswitch in numerous molecular systems and functional materials for applications such as high-density information storage.[20] Because the energy difference between the trans- and the cis- conformers is relatively small (i.e., 15 kcal·mol^{-1} or 0.6 eV), a visible photon can easily induce an electronic excitation via either the $n \rightarrow \pi^*$ or the $\pi \rightarrow \pi^*$ pathways, a topic under intense experimental and theoretical investigations.[17,18,21,22] The strong activities associated with π electrons make azobenzene an interesting system for the examination of the combined pressure-photon effects based on the fact that both pressure and photon can effectively induce electronic excitations and thus subsequent structural transitions.[5] In parallel, high-pressure effects on phenyl rings have been studied in a wide variety of aromatic systems in a broad pressure range. Since the N=N bond constitutes the conjugation center of azobenzene, it is expected to play a vital role responsible for the entire property of azobenzene regardless of the bulky phenyl substituents. To examine the importance of total conjugation to the properties of azobenzene, a high-pressure study of another similar molecule, hydrazobenzene (HAB) (Fig. 4.1b) with a broken conjugation along the N-N bond, may help to understand the isolated pressure effect on the phenyl rings and the nitrogen-nitrogen bond.

Here we report a comparative study of azobenzene and hydrazobenzene under high pressures of up to ~ 28 GPa by *in-situ* Raman spectroscopy. Our results suggest strongly contrasting high-pressure behaviors between these two compounds. Moreover, a study of the high-pressure effect on N=N and N-N bonds may provide valuable insight into the development of high energy density materials that contain singly bonded nitrogens.[23]

4.2 Experimental section

Both azobenzene (96%) and hydrazobenzene (99%) were purchased from Aldrich and were used without further purification. Azobenene appears as orange crystals whereas hydrazobenzene is mostly colorless and transparent. A symmetric diamond anvil cell with a pair of type Ia diamonds with a 400 μm culet was used. A hole with a diameter of 150 μm was drilled in a stainless steel gasket as the sample chamber. A few ruby chips were inserted in the sample chamber for pressure calibrant using the ruby fluorescence method.[24] [25] No pressure transmitting medium was used for either sample.

In-situ high-pressure Raman measurements were carried out using a customized Raman micro-spectroscopy system. A He-Ne laser with a wavelength of 632.8 nm was used as the excitation source. The Raman system was equipped with an Olympus microscope, which can focus the laser to less than 5 μm dameter on the sample. The laser power measured on the sample was less than 5 mW. The Raman system adopeted a backscattering geometery, and the scattered light was dispersed using an imaging spectrograph equipped with a 1200 lines/mm grating, achieving a resolution of 0.2 cm^{-1}. The system was calibrated using neon lines with an uncertainty of ±1 cm^{-1}. An edge filer was installed to remove the Rayleigh and anti-Stokes lines enabling a measurable range above 100 cm^{-1}. The Raman signal was then recorded using an ultrasensitive liquid-nitrogen-cooled, back-illuminated CCD detector from Acton. The Raman spectra were collected in several spectral windows to cover the entire region of interest (i.e., 100 – 3500 cm^{-1}) and to avid the interference from the dominant diamond Raman band at ~ 1340 cm^{-1}. During data acquisition, all parameters (e.g., laser power, accumulation time, etc.) were kept the same, such that the Raman intensities from different spectra were qualitatively comparable and, thus, were normalizable. All Raman measurements were conducted at room temperature and were reproduced several times.

4.3 Results and discussion

4.3.1 Raman spectra of AB and HAB at ambient pressure

The Raman spectra of both azobenzene and hydrazobenzene at ambient condition are shown in Fig. 4.2. Azobenzene adopts the trans-configuration as the more thermally stable form with the two phenyl rings on opposite sides of the N=N bond thus exhibiting a C_{2h} symmetry (Fig. 4.1a). Therefore, a total of 66 normal vibrational modes, out of which 33 are Raman active (10 B_g, out-of-plane and 23 A_g, in-plane modes), are expected for a single azobenzene molecule.[26,27] Solid azobenzene is known to have a monoclinic crystal structure with a space group $P2_1$/a and Z=2,[21] and thus 66 Raman-active modes are predicted. In our Raman measurements, however, only 18 modes were observed indicating that the magnitude of the correlation field splitting was small and cannot be observed with the current experimental set up. The assignment of each Raman mode is listed in Table 4.1 in comparison with previous studies of azobenzene in the trans-configuration. As can be seen, our Raman measurements agree with those obtained in both the theoretical and experimental studies.[18,26,28,29] Hydrazobenzene does not exhibit a significant molecular symmetry due to the free rotation along the N-N bond and thus all vibrational modes are Raman-active. However, due to the very similar molecular skeleton to azobenzene, hydrazobenzene has a very similar Raman spectrum correspondingly, except that most Raman modes of hydrazobenzene shift to lower frequencies due to the replacement of the N=N bond by the N-N single bond. The Raman peaks for hydrazobenzene in this study are therefore assigned by adopting the assignment for azobenzene without rigor (with the corresponding Raman modes labeled by a prime), due to the lack of assignment from previous studies. In the Raman spectrum for hydrazobenzene, the bands at 3329 cm^{-1} and 1027 cm^{-1} are assigned as the N-H and N-N stretching vibrational modes, respectively, while the band observed at 845 cm^{-1} is assigned as the H-N-N-H bending mode.

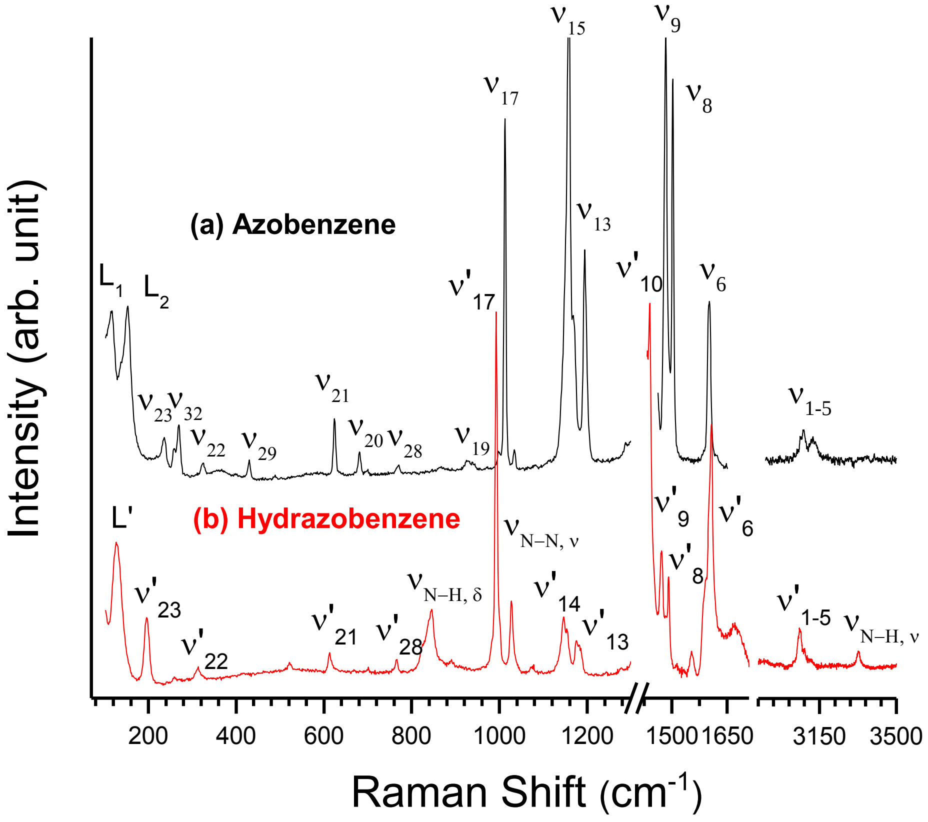

Figure 4.2 Raman spectra of azobenzene (a) and hydrazobenzene (b) collected at ambient conditions. The two spectra are offset vertically for clarity. The spectral region of 1250 – 1400 cm^{-1} is omitted due to the strong T_{2g} Raman mode of the diamond anvils.

Table 4.1 Assignment and frequencies (cm^{-1}) of observed Raman internal modes of azobenzene (AB) and hydrazobenzene (HAB) in comparison with references.

		reference		this work	
Raman	**assignment**[b]	**calculation**[c]	**experimental**[d]	**AB**	**HAB**
$\nu_{N\text{-}H}$	N-H stretching				3329
ν_1 (A_g)	phenyl C-H stretching	3221	*3085*		
ν_2 (A_g)	phenyl C-H stretching	3210	*3073*		
ν_3 (A_g)	phenyl C-H stretching	3197	*3066*		
ν_4 (A_g)	phenyl C-H stretching	3187	*3060*	3074	3058
ν_5 (A_g)	phenyl C-H stretching	3178	*3044*		
ν_6 (A_g)	phenyl C-C stretching	1622	1591/*1595*	1601	1607
ν_7 (A_g)	phenyl C-C stretching	1614			
ν_8 (A_g)	Azo stretching	1519	1491/*1443*	1502	1491
ν_9 (A_g)	Azo stretching	1504	1470/*1493*	1480	1471
ν_{10} (A_g)	Azo stretching	1450	1440/*1473*		1440
ν_{11} (A_g)	phenyl C-H bending	1395	1312/*1379*		
ν_{12} (A_g)	phenyl C-H bending	1368	*1315*		
ν_{13} (A_g)	phenyl C-H bending	1235	1185/*1184*	1194	1176
ν_{14} (A_g)	phenyl C-H bending	1226	1155/*1158*	1168	1147
ν_{15} (A_g)	C-N bending	1195	1143/*1146*	1157	
ν_{16} (A_g)	phenyl C-C stretching	1110	1068/*1071*	1033	
$\nu_{N\text{-}N}$	N-N stretching				1027
ν_{17} (A_g)	phenyl C-H bending	1047	1021/*1023*	1013	992
ν_{18} (A_g)	phenyl C-H bending	1024	1000/*1003*	998	
ν_{19} (A_g)	C-N bending	933	914/*913*	931	
$\nu_{N\text{-}H}$	H-N-N-H bending				845
ν_{20} (A_g)	C-N bending	691	667/*670*	682	
ν_{21} (A_g)	phenyl C-H bending	634	611/*614*	623	613
ν_{22} (A_g)	C-N bending	307		324	313
ν_{23} (A_g)	C-N bending	226	*219*	235	196
ν_{24} (B_g)	phenyl C-H wagging	857	*968*		
ν_{25} (B_g)	phenyl C-H wagging	851	967/*938*		
ν_{26} (B_g)	phenyl C-H wagging	825	935		
ν_{27} (B_g)	phenyl C-H wagging	778	834/*836*		
ν_{28} (B_g)	phenyl C-H wagging	702	773/*755*	770	765
ν_{29} (B_g)	phenyl C-H wagging	444		430	
ν_{30} (B_g)	phenyl C-H wagging	400			
ν_{31} (B_g)	phenyl C-H wagging	381	406/*403*		
ν_{32} (B_g)	phenyl flags	213	218/*251*	269	
ν_{33} (B_g)	phenyl flags	-85			

[a] The symmetry in the parentheses refers to azobenzene only while the mode numbering applies to both compounds (i.e., with the prime omitted for hydrazobenzene). [b] Refs. 26 and 27. [c] Ref. 26. [d] Frequencies in regular font are from Ref. 28 while those in italics are from Ref. 29.

4.3.2 Raman spectra of AB upon compression and decompression

Selected Raman spectra of azobenzene collected upon compression at pressures of up to 17.8 GPa and followed by decompression are shown in Fig. 4.3. As the pressure increased, all the Raman bands shifted progressively toward higher frequencies accompanied by peak broadening. Other than the blue shift, all the internal modes (> 200 cm^{-1}) maintained the ambient-pressure Raman profile until 10.4 GPa, indicating that the azobenzene molecular structure was stable below 10.4 GPa. Compression beyond 10.4 GPa resulted in the dramatically reduced intensity of all the internal modes with the Raman modes below 1000 cm^{-1} being significantly depleted. Concurrently, two new bands at 565 cm^{-1} and 733 cm^{-1} became prominent at pressures above 10.4 GPa (Fig. 4.3). These two bands appeared to be even more intense with increasing the pressure up to 16.0 GPa. In addition, the triple peaks initially located at 1160 cm^{-1} eventually merged to a single broad peak at this pressure. Finally, all Raman peaks vanished at the highest pressure achieved in this study for azobenzene (i.e., 17.8 GPa). The featureless Raman profile at high pressures suggested that azobenzene had undergone a major structural modification.

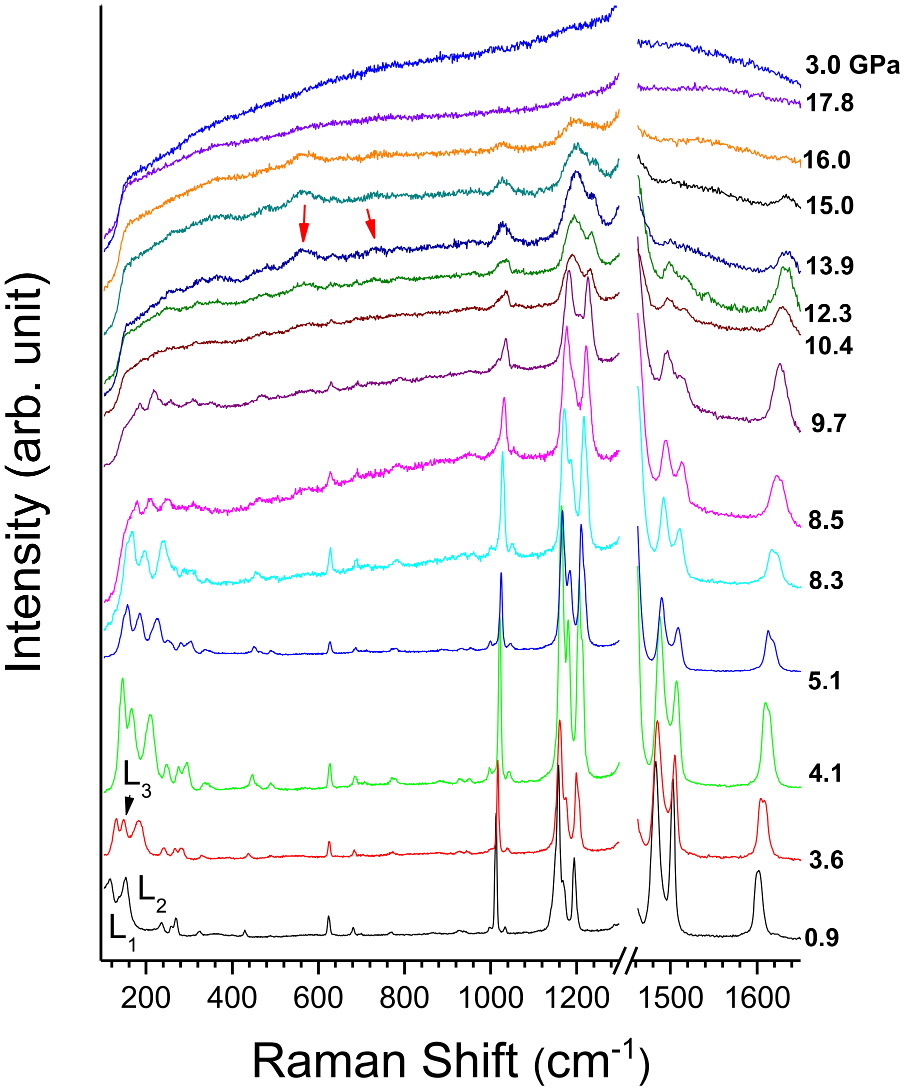

Figure 4.3 **Selected Raman spectra of azobenzene collected along a compression-decompression cycle at room temperature in the region of 100 – 1700 cm^{-1}. The relative intensities are normalized and thus are directly comparable. The pressures in gigapascals are labeled for each spectrum. The vertical long arrow on the right shows the sequence of the compression. Two red arrows indicate new peaks appearing at high pressures. The spectra are offset vertically for clarity.**

Consistent with the high-pressure behavior of internal vibrational modes, the external modes (< 200 cm^{-1}) also shifted to a higher frequency upon compression, but were more prominently accompanied with major changes of the lattice profile. For instance, a new lattice mode at 148 cm^{-1} was observed at 3.6 GPa. All the lattice modes sustained up to 10.4 GPa and completely vanished beyond this pressure (Fig. 4.3). The disappearance of external Raman modes strongly suggests a structural amorphization at pressure of 10.4 GPa, whereas the complete destruction of all Raman modes at 17.8 GPa can be attributed to a chemical transformation. Upon releasing the pressure, no Raman mode was recovered indicating that the pressure-induced transformation at 17.8 GPa was completely irreversible.

4.3.3 Raman spectra of HAB on compression and decompression

Selected Raman spectra of hydrazobenzene on compression and decompression are shown in Fig. 4.4. Upon compression, the internal modes shifted to a higher frequency accompanied with peak broadening, similar to those observed in azobenzene. However, the Raman spectrum did not change significantly with pressures of up to 9.3 GPa. The most noticeable change was that two lattice modes at 168 cm^{-1} and 229 cm^{-1}, which were first observed at 3.5 GPa and then vanished at 9.3 GPa, suggesting the possible distortion of the molecular crystal lattice. Above 9.3 GPa, some internal modes below 1000 cm^{-1} disappeared. This observation further indicates the pressure-induced structural disorder and the eventual amorphization upon compression above this pressure. Concurrently, two new bands at 551 cm^{-1} and 712 cm^{-1} were observed above this pressure, which were also found in azobenzene upon compression, indicating the enhanced intermolecular interactions due to the smaller intermolecular distances.

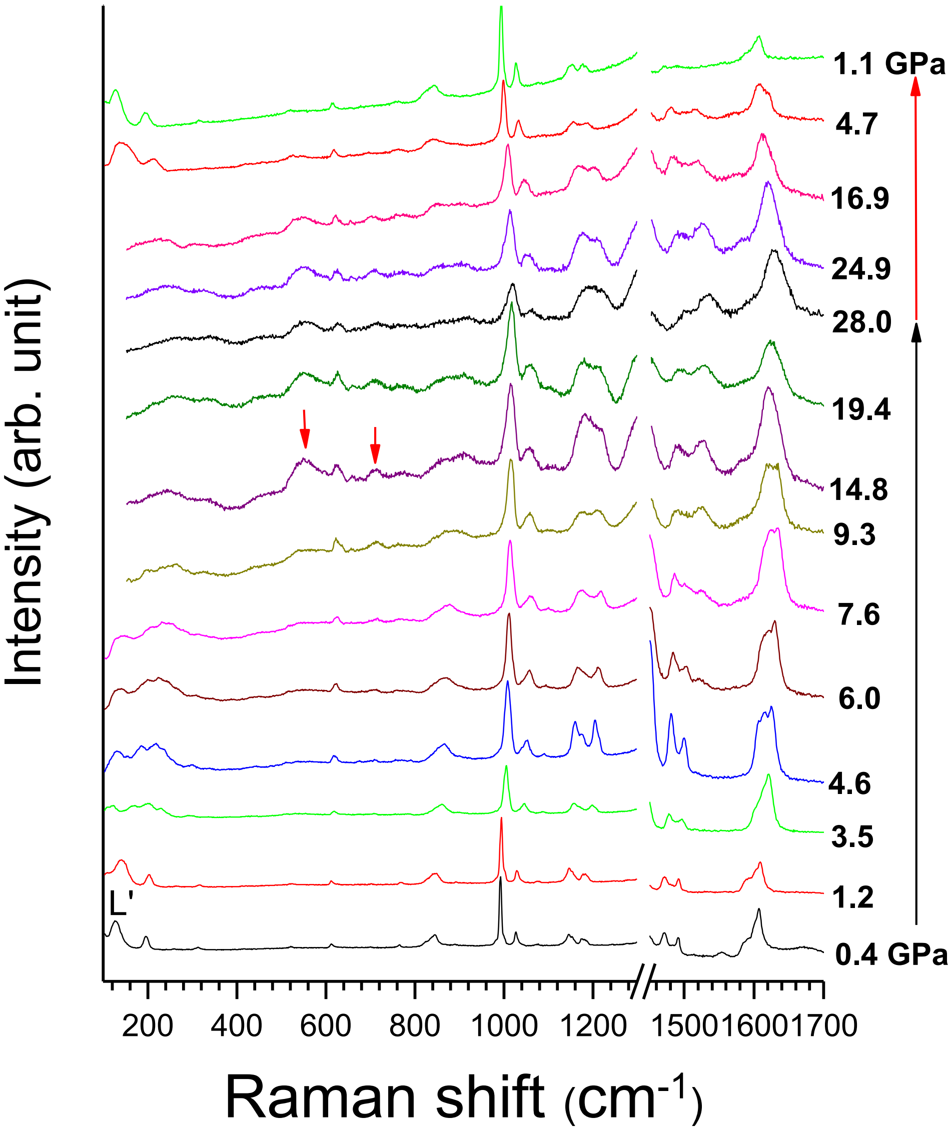

Figure 4.4 Selected Raman spectra of hydrazobenzene collected along a compression-decompression cycle at room temperature in the region of 100 – 1700 cm^{-1}. The relative intensities are normalized and thus are directly comparable. The pressures in gigapascals are labeled for each spectrum. The long arrows represent compression and decompression sequence in black and red, respectively. Two short arrows (red) show new peaks appeared at high pressures. The spectra are offset vertically for clarity.

However, the most dominant Raman modes of hydrazobenzene could still be observed easily (e.g., at 1020 cm^{-1}) at the highest pressure achieved in this study (i.e., 27.8 GPa), in strong contrast to azobenzene.

Upon decompression, most Raman modes of the hydrazobenzene followed a similar backward pressure sequence as upon compression. In particular, the two new bands observed above 9.3 GPa on compression as transient bands disappeared at 4.7 GPa during decompression. When pressure was released to ambient, we were able to recover the Raman spectrum of hydrazobenzene that was almost identical to that observed before compression in the entire spectral region, indicating that the phase transformation observed in hydrazobenzene was totally reversible.

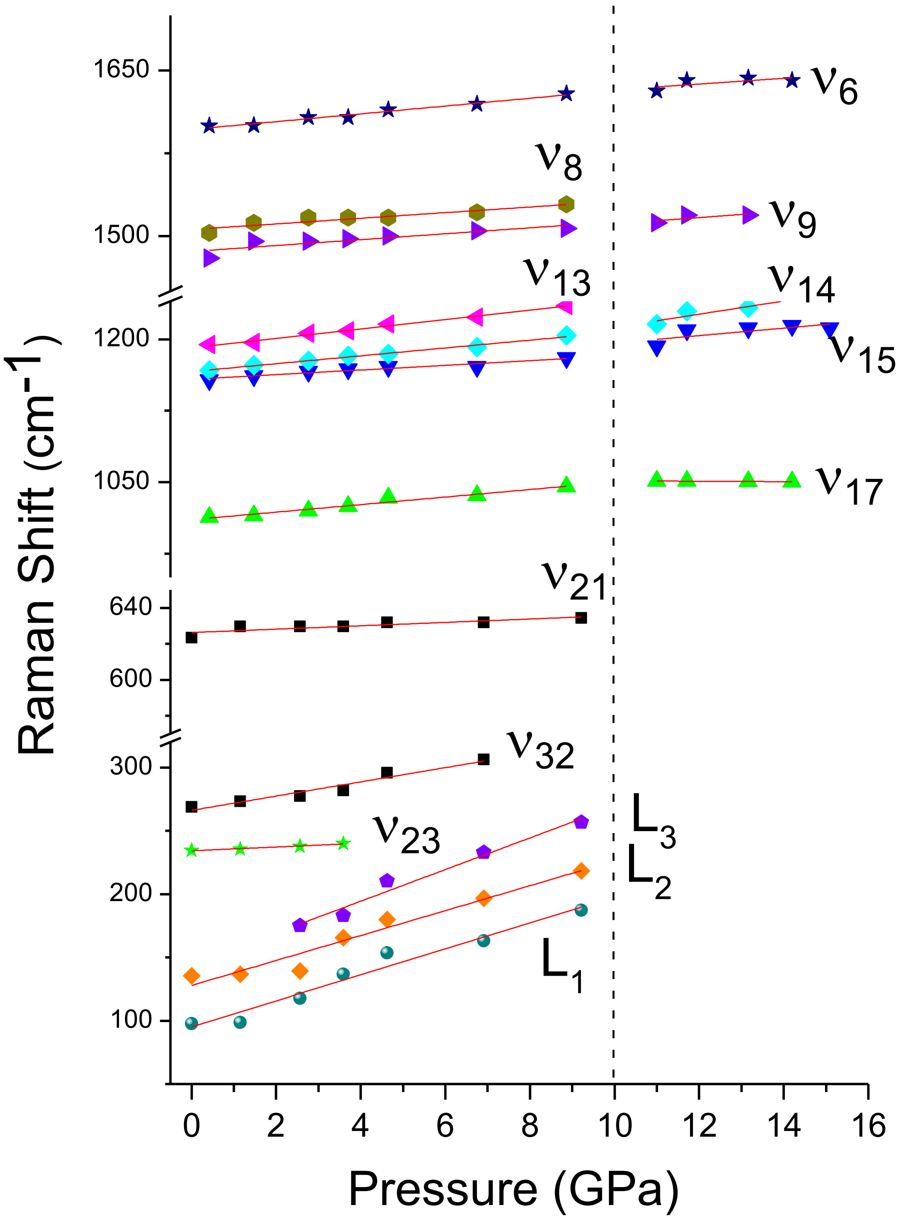

Figure 4.5 **Pressure dependence of the Raman modes of azobenzene on compression. Solid straight lines are linear fits to the data. The vertical dashed line denotes the suggested transition boundary. Different symbols denote different Raman modes with assignment labeled.**

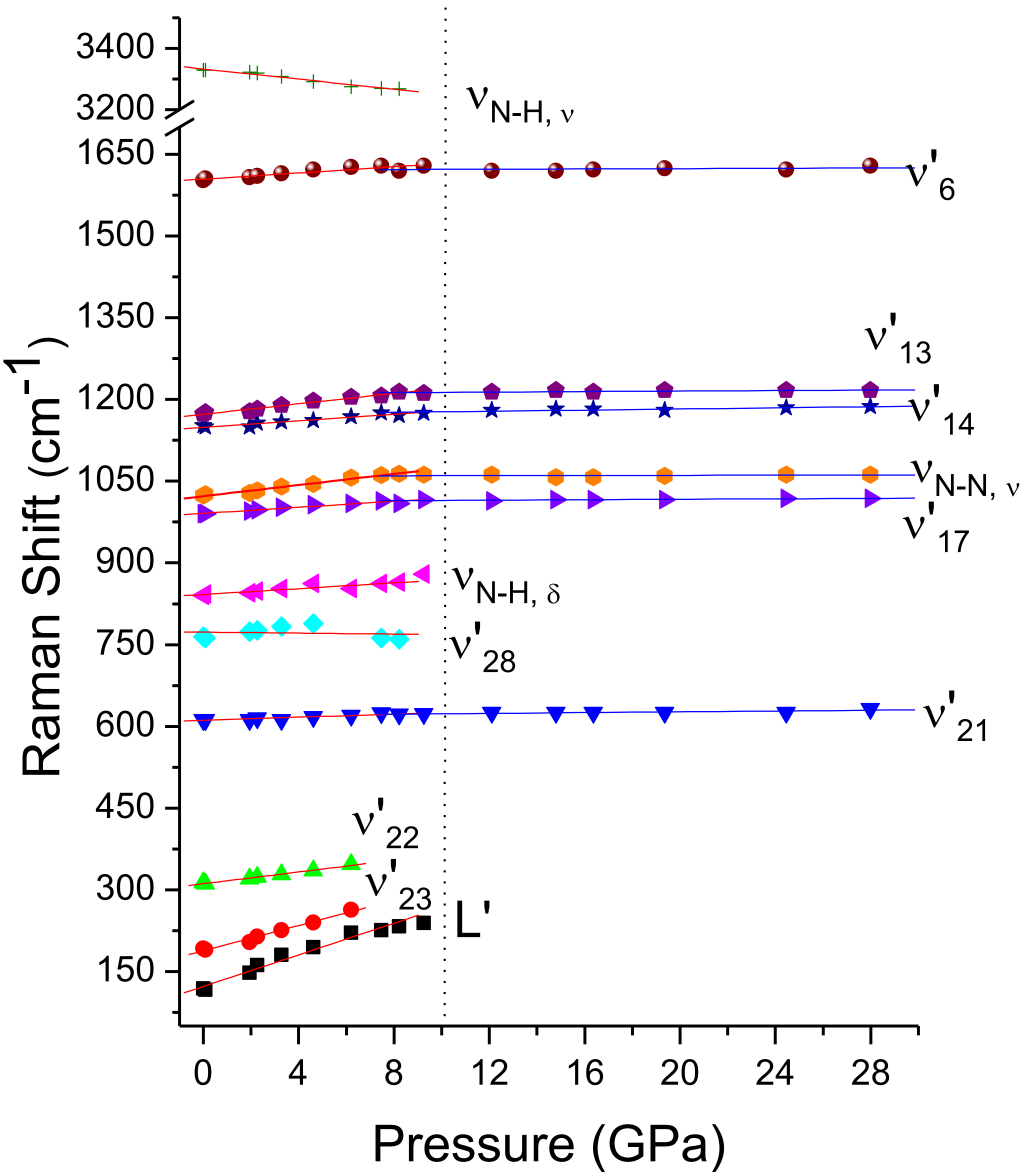

Figure 4.6 Pressure dependence of the Raman modes of hydrazobenzene on compression. Solid straight lines are linear fits to the data. The vertical dashed line marks the suggested phase transition boundary. Different symbols denote different Raman modes with assignment labeled besides.

4.3.4 Pressure effects on Raman modes of AB and HAB

Pressure dependences of selected Raman modes of azobenzene and hydrazobenzene on compression are depicted in Figs. 4.5 and 4.6, respectively. Since the C-H stretching modes of azobenzene at 2800 – 3200 cm^{-1} were clearly observed only below 3.5 GPa, they are not included in the analysis here. The pressure dependences (dν/dp) of the selected Raman modes are listed in Table 4.2 as well. In general, all Raman modes exhibit pressure-induced blue shifts except the N-H stretching bond of hydrazobenzene as discussed below, consistent with that the bonds become stiffened by pressure. However, in different pressure regions, the shift rates are different, providing evidence for phase transformations.

A possible solid to solid phase transition occurs at about 10.0 GPa in azobenzene as indicated by the vertical dashed line in Fig. 4.5. Below this pressure, Raman modes in the low frequency region, such as the phenyl flag mode (ν_{32}) and the lattice modes (L_1, L_2, and L_3), are more sensitive to pressure suggested by the relatively larger pressure coefficients (dν/dP), in contrast to the internal Raman modes in the higher frequency region (> 600 cm^{-1}) as summarized in Table 4.2. Similarly, the vertical dashed line in Fig. 4.6 denotes the phase transition boundary in hydrazobenzene at about 10.0 GPa. The lattice mode (L' at 121 cm^{-1}) and the C-N bending mode (ν'_{23} at 196 cm^{-1}) are highly sensitive to compression with the largest pressure coefficients of 14.5 cm^{-1}/GPa and 11.6 cm^{-1}/GPa, respectively. Moreover, most Raman modes show a positive slope below 10 GPa except the N-H stretching mode at 3329 cm^{-1}, which has a strongly negative slope (i.e., - 8.3 cm^{-1}/GPa). The mode softening in this case can be interpreted as the N-H bond weakening as a result of the formations of hydrogen bonding with neighboring N-H bonds during the compression. In addition, most Raman modes had generally larger slopes (i.e., > 2 cm^{-1}/GPa) before the phase transformation than those after (i.e., < 0.5 cm^{-1}/GPa), indicating a smaller compressibility for HAB in the higher pressure region as a result of denser molecular packing upon compression.

Table 4.2 Pressure dependence *dν/dP* (cm^{-1}/GPa) of Raman modes of azobenzene and hydrazobenzene.

azobenzene				hydrazobenzene			
Raman mode	**frequency (cm^{-1})**	**0 - 10 GPa**	**10 - 16 GPa**	**Raman mode[b]**	**frequency (cm^{-1})**	**0 - 10 GPa**	**10 - 28 GPa**
ν_6	1590	3.1	2.4	$\nu_{N\text{-}H,\ \nu}$	3329	- 8.3	
ν_8	1483	2.2		ν'_6	1607	2.8	0.1
ν_9	1460	2.3	2.6	ν'_{13}	1176	4.8	0.2
ν_{13}	1182	4.5		ν'_{14}	1147	3.0	0.5
ν_{14}	1156	4.9	6.3	$\nu_{N\text{-}N,\ \nu}$	1027	5.1	0.1
ν_{15}	1142	3.7	3.6	ν'_{17}	992	2.8	0.2
ν_{17}	998	2.8	- 0.2	$\nu_{N\text{-}H,\ \delta}$	845	2.7	
ν_{21}	605	0.8		ν'_{28}	765	- 0.4	
ν_{32}	243	5.6		ν'_{21}	613	1.4	0.4
ν_{23}	235	4.8		ν'_{22}	313	5.4	
L_3	183[a]	12.5		ν'_{23}	196	11.6	
L_2	135	9.8		L'	121	14.5	
L_1	98	10.3					

[a] Observed at 3.6 GPa. [b] Subscript ν: stretching; δ: bending.

4.3.5 Discussion

Although both azobenzene and hydrazobenzene underwent a pressure-induced structural transformation at the same pressure of around 10.0 GPa, the nature of the transformation was drastically different. In particular, the transition of azobenzene was initiated by structural disorder at 10.0 GPa followed by complete amorphization above 17.8 GPa as evidenced by the disappearance of all the characteristic Raman modes. The irreversible amorphization suggests that the transformation was chemical in nature, possibly via a polymerization process, resulting in highly disordered cross-linked structures. Such a chemical transformation was accompanied by the striking change in the physical appearance of the sample: the original transparent orange crystals turned completely gray and sooty upon compression, and the gray sample showed no change after the pressure was completely released. Pressure-induced amorphization has also been reported in other organic molecular crystals such as benzophenone[30] at 11 GPa and hexanmethylenetetramine[31] at 15 GPa. In addition, interesting transformations that are believed to involve the formation of a polymerized phase were also observed in acetophenone azine, which has a similar structure as azobenzene.[32] From the high-pressure Raman spectra, we suggest that the polymerization occurs involving the entire molecule instead of the preferential transformation of the N=N double bond to the N-N single bond. This was evidenced by the absence of the N-N characteristic vibrational frequency at 1023 cm^{-1}, which would have been observed if the N=N double bond were to be converted to a N-N single bond, and the fact that the azo stretching modes (e.g., ν_8 and ν_9) responded to compression concertedly with those of the phenyl ring vibrations (e.g., ν_6 and ν_{16}) in the polymerization process.

More detailed polymerization mechanisms can be understood in parallel with benzene, the basic building unit of azobenzene. Similarly, benzene was reported to polymerize or amorphize by compression but at a much higher pressure (i.e., > 30 GPa) by Ciabini *et al.*[11,12] Their studies suggest that when a threshold distance (2.6 Å) between two carbon atoms on adjacent benzene rings is reached by compression, the polymerization process can be triggered by fluctuations in the atom positions that are caused by thermal vibrations. Theoretical calculations of the process indicate large fluctuations on a femtosecond timescale occurring in the electron density distribution between newly-bonded atom pairs.[11] These extremely fast charge fluctuations propagated throughout the compressed benzene lattice and resulted in the formation of an amorphous network of linked carbon rings. Considering azobenzene as an extended aromatic system of benzene rings, the polymerization may occur in a similar manner, except that the threshold pressure is much lower for bulkier monomers.

In contrast, hydrazobenzene is much more stable under high pressure. The irreversible phase transition is physical rather than chemical, i.e., it is characterized by the distortion rather than the destruction of the skeleton of molecules under high pressure. Instead of having a planar configuration reinforced by the N=N double bond in azobenzene, hydrazobenzene contains only a N-N single bond, which allows the free rotation of the two phenyl rings along the N-N axis. Thus, the net pressure effect on hydrazobenzene can be understood as being the modification of the molecular conformation that takes place before a polymeric reaction involving the phenyl ring occurs. This pressure-induced conformational change accompanied with structural disordering has been observed in other smaller molecular crystals.[1]

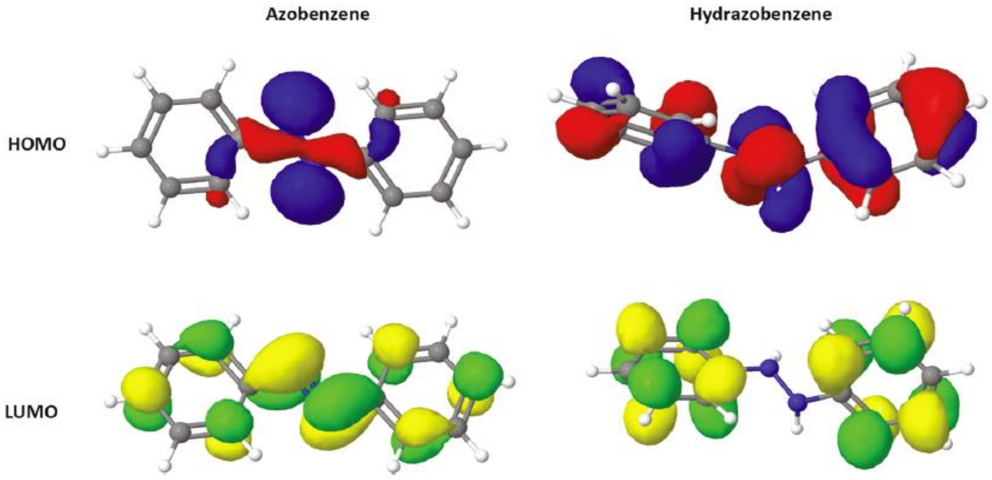

Figure 4.7 The frontier orbitals, i.e., HOMO (top row) and LUMO (bottom row) orbitals of azobenzene (left column) and hydrazobenzene (right column) calculated at the B3LYP/6-311+G(d,p) level of theory. An arbitrary isosurface value was used for all the plots.

From the above comparisons, it is therefore easy to understand why the two hydrazine derivatives behave so differently under high pressure. It is the complete conjugate electronic configuration of azobenzene that makes the entire molecule subject to cross-linking, whereas hydrazobenzene behaves almost equivalently like independent benzene rings. We therefore speculate that upon compression to a higher pressure (e.g., > 30 GPa), similar irreversible transformations may be observed as those for benzene. To confirm the different reactivities of azobenzene and hydrazobenzene, we performed *ab initio* molecular orbital calculations based on the DFT method using the GASSIAN 98 program package.[33] Previous extensive DFT calculations using the gradient corrected hybrid B3LYP function have reproduced geometries and vibrational properties of azobenzene reasonably well.[18,22,34] It was also demonstrated that the incorporation of diffuse functions and polarization functions could improve the estimation of various properties of azobenzene. Therefore, in our calculations we chose the prevailing B3LYP function with Pople's basis set 6-311+G (d, p), which is comparable or slightly better than that of previous studies.[18,22] Fig. 4.7 shows the frontier orbitals that would contribute to the polymerization process if the irreversible chemical transformation occurs. We note that Crecca and Roitberg[22] reported very similar frontier molecular orbitals for azobenzene using density functional theories at a similar level of theory, i.e., B3LYP/6-31G* (Fig. 3 of Ref. 22), but no corresponding studies had been performed on hydrazobenzene before. As can be seen, the LUMO orbital of azobenzene shows a reinforced conjugation with the contribution of the π ($2p_z$ of carbon and nitrogen) orbitals especially by nitrogen atoms, whereas the electron density for hydrazobenzene is mainly situated on the phenyl carbons rather than the two nitrogens, consistent with the above interpretation. In addition, our calculation shows a HOMO-LUMO gap of 3.91 eV for azobenzene, also in good agreement with that calculated by Crecca and Roitberg.[22] Compared to the gap of 5.19 eV for hydrazobenzene, the 25% smaller energy gap for azobenzene may correlate with its higher reactivity upon compression. Such a level of calculations, therefore, provides a reasonably good, qualitative understanding of the different pressure behaviors of the two hydrazine derivatives.

4.4 Conclusions

Using *in-situ* Raman spectroscopy, we investigated the structures and transformations of azobenzene and hydrazobenzene at high pressures of up to 28 GPa, comparatively. Upon compression, both compounds exhibited a pressure-induced structural transition at around 10 GPa. Further compression of azobenzene to 18 GPa resulted in an irreversible destruction of the molecular structure. In contrast, hydrazobenzene was found to sustain pressures up to 28 GPa without chemical transformations, and the structural evolutions with pressure were totally reversible in the entire pressure region. The high-pressure behaviors and possible structures of these two molecules were analyzed in comparison with the results of previous studies on other aromatic structures. While hydrazobenzene retains a disordered but chemically stable phase at high pressures, azobenzene undergoes an amorphization process accompanied by polymerization via cross-linking involving the entire molecule. The drastically different high-pressure stabilities of the two compounds are attributed to their intrinsically different electronic configurations in terms of conjugation. The molecular orbital calculations using density functional theories further supported the experimental observations and the spectroscopic interpretations.

4.5 References

(1) Sabharwal, R. J.; Huang, Y. N.; Song, Y. *J. Phys. Chem. B* **2007**, *111*, 7267.

(2) Dong, Z.; Beilby, N. G.; Huang, Y.; Song, Y. *J. Chem. Phys.* **2008**, *128*, 074501.

(3) Murli, C.; Song, Y. *J. Phys. Chem. B* **2010**, *114*, 9744.

(4) Hemley, R. J. *Annu. Rev. Phys. Chem.* **2000**, *51*, 763.

(5) Bini, R. *Accounts Chem. Res.* **2004**, *37*, 95.

(6) Zhuravlev, K. K.; Traikov, K.; Dong, Z. H.; Xie, S. T.; Song, Y.; Liu, Z. X. *Phys. Rev. B* **2010**, *82*, 064116.

(7) Citroni, M.; Ceppatelli, M.; Bini, R.; Schettino, V. *J. Chem. Phys.* **2003**, *118*, 1815.

(8) Citroni, M.; Ceppatelli, M.; Bini, R.; Schettino, V. *Chem. Phys. Lett.* **2003**, *367*, 186.

(9) Pruzan, P.; Chervin, J. C.; Thiery, M. M.; Itie, J. P.; Besson, J. M.; Forgerit, J. P.; Revault, M. *J. Chem. Phys.* **1990**, *92*, 6910.

(10) Ciabini, L.; Santoro, M.; Bini, R.; Schettino, V. *Phys. Rev. Lett.* **2002**, *88*, 085505.

(11) Ciabini, L.; Santoro, M.; Gorelli, F. A.; Bini, R.; Schettino, V.; Raugei, S. *Nat. Mater.* **2007**, *6*, 39.

(12) Ciabini, L.; Santoro, M.; Bini, R.; Schettino, V. *J. Chem. Phys.* **2002**, *116*, 2928.

(13) Chelazzi, D.; Ceppatelli, M.; Santoro, M.; Bini, R.; Schettino, V. *J. Phys. Chem. B* **2005**, *109*, 21658.

(14) Schettino, V.; Bini, R. *Chem. Soc. Rev.* **2007**, *36*, 869.

(15) Ceppatelli, M.; Fontana, L. *Phase Transit.* **2007**, *80*, 1085.

(16) Asanuma, H.; Ito, T.; Yoshida, T.; Liang, X. G.; Komiyama, M. *Angew. Chem.-Int. Edit.* **1999**, *38*, 2393.

(17) Tanaka, S.; Itoh, S.; Kurita, N. *Chem. Phys. Lett.* **2002**, *362*, 467.

(18) Stepanic, V.; Baranovic, G.; Smrecki, V. *J. Mol. Struct.* **2001**, *569*, 89.

(19) Tong, X.; Pelletier, M.; Lasia, A.; Zhao, Y. *Angew. Chem.-Int. Edit.* **2008**, *47*, 3596.

(20) Liu, Z. F.; Hashimoto, K.; Fujishima, A. *Nature* **1990**, *347*, 658.

(21) Harada, J.; Ogawa, K. *J. Am. Chem. Soc.* **2004**, *126*, 3539.

(22) Crecca, C. R.; Roitberg, A. E. *J. Phys. Chem. A* **2006**, *110*, 8188.

(23) Eremets, M. I.; Gavriliuk, A. G.; Trojan, I. A.; Dzivenko, D. A.; Boehler, R. *Nat. Mater.* **2004**, *3*, 558.

(24) Mao, H. K.; Bell, P. M.; Shaner, J. W.; Steinberg, D. J. *J. Appl. Phys.* **1978**, *49*, 3276.

(25) Mao, H. K.; Xu, J.; Bell, P. M. *Journal of Geophysical Research-Solid Earth and Planets* **1986**, *91*, 4673.

(26) Armstrong, D. R.; Clarkson, J.; Smith, W. E. *J. Phys. Chem.* **1995**, *99*, 17825.

(27) Tecklenburg, M. M. J.; Kosnak, D. J.; Bhatnagar, A.; Mohanty, D. K. *J. Raman Spectrosc.* **1997**, *28*, 755.

(28) Gruger, A.; Lecalve, N. *J. Chim. Phys.-Chim. Biol.* **1972**, *69*, 743.

(29) Kellerer, B.; Brandmul.J; Hacker, H. H. *Indian J. Pure Appl. Phys.* **1971**, *9*, 903.

(30) Zhang, D. L.; Lan, G. X.; Hu, S. F.; Wang, H. F.; Zheng, J. M. *J. Phys. Chem. Solids* **1995**, *56*, 27.

(31) Rao, R.; Sakuntala, T.; Deb, S. K.; Roy, A. P.; Vijayakumar, V.; Godwal, B. K.; Sikka, S. K. *Chem. Phys. Lett.* **1999**, *313*, 749.

(32) Tang, X. D.; Ding, Z. J.; Zhang, Z. M. *Solid State Commun.* **2009**, *149*, 301.

(33) Frisch, M. J. T., G. W.; Schlegel, H. B.; Scuseria, G. E.; Robb, M. A.; Cheeseman, J. R.; Zakrzewski, V. G.; Montgomery Jr., J. A.; Stratmann, R. E.; Burant, J. C.; Dapprich, S.; Millam, J. M.; Daniels, A. D.; Kudin, K. N.; Strain, M. C.; Farkas, O.; Tomasi, J.; Barone, V.; Cossi, M.; Cammi, R.; Mennucci, B.; Pomelli, C.; Adamo, C.; Clifford, S.; Ochterski, J.; Petersson, G. A.; Ayala, P. Y.; Cui, Q.; Morokuma, K.; Salvador, P.; Dannenberg, J. J.; Malick, D. K.; Rabuck, A. D.; Raghavachari, K.; Foresman, J. B.; Cioslowski, J.; Ortiz, J. V.; Baboul, A. G.; Stefanov, B. B.; Liu, G.; Liashenko, A.; Piskorz, P.; Komaromi, I.; Gomperts, R.; Martin, R. L.; Fox, D. J.; Keith, T.; Al-Laham, M. A.; Peng, C. Y.;

Nanayakkara, A.; Challacombe, M.; Gill, P. M. W.; ohnson, B. ;Chen, J. W.; Wong, M. W.; Andres, J. L.; Gonzalez, C.; Head-Gordon, M.; Replogle, E. S. and Pople, J. A. ; Inc.: Pittsburgh, PA, **2001**.

(34) Biswas, N.; Umapathy, S. *J. Phys. Chem. A* **1997**, *101*, 5555.

Chapter 5 Transformations of Cold-compressed Multi-walled Boron Nitride Nanotubes Probed by Infrared Spectroscopy*

5.1 Introduction

Structurally similar to graphite, layered hexagonal boron nitride (h-BN) has important technological applications in the materials industry, especially as a lubricant under extreme conditions.[1] In more recent years, its nanostructured counterpart, boron nitride nanotubes (BNNTs), which are formed by rolling a single sheet of h-BN into a cylinder, have attracted significant interest.[2] First theoretically predicted[3] and subsequently synthesized,[4] BNNTs were found to exhibit unique properties that are significantly different from their isoelectronic analogue, carbon nanotubes (CNTs). For instance, BNNTs have an insulating nature with a large and structure-independent band gap of > 5.5 eV,[5] which is in strong contrast to metallic or semiconducting CNTs whose electronic properties critically depend on tube diameter and chirality. In addition, BNNTs have enhanced thermal stability,[6] high resistance to oxidation at high temperatures,[7] high thermal conductivity,[8] and remarkable yield strength (Young's modulus ~1.2 TPa).[9] These attractive chemical, physical, and mechanical properties make BNNTs an extremely promising advanced material that could be used for a wide range of applications, such as spacecraft coatings,[10] photoluminescence devices,[11] piezoelectric materials,[12] and optoelectronic devices.[13]

---

[*] The content of this chapter has been published as: Dong Z., and Song Y., *J. Phys. Chem.*, **2010**, *114*, 1782.

Despite the great promises of BNNTs for practical applications, our knowledge on their structure-property relationship is still limited. An important approach for structure modification is to subject materials to extreme conditions, such as high pressure, followed by *in-situ* structural characterization and subsequent property evaluations. Investigations of the structural and phase transformations of nanomaterials under high pressures are receiving greater attention[14-20] simply because, in addition to composition and synthetic routes, pressure provides an additional effective driving force to tune the structures and thus properties of the nanostructured materials.[21] The most interesting aspect is the observation nanomaterials behave quite differently than their corresponding bulk counterparts under pressure. For example, CdSe[14,15] and TiO_2[19] have specific size-dependent phase transformations that greatly enhance the opportunities for producing new structures. In addition, morphology can play an important tuning role in pressure-induced transformations in these nanostructured materials. For instance, different morphologies of ZnS were found to have strikingly different phase stabilities when compressed.[18] These examples demonstrate that pressure can drastically alter the structures and stabilities of nanomaterials and that these pressure responses can be substantially different than those for bulk materials.

Transformations involving compressed bulk h-BN have been recently investigated both experimentally[22] and theoretically.[23] It has been well established that, under high pressure and temperature, bulk h-BN can be converted to a more closely packed wurtzite structure (w-BN)[24] or to a dense cubic structure (c-BN),[25] depending on the *P-T* conditions. Structurally similar to c-BN with almost identical compressibility, w-BN is believed to be a metastable phase.[26] Particularly intriguing is the surprising superhardness (i.e., harder than natural diamond) recently predicted for w-BN, which is similar to that for lonsdaleite (hexagonal diamond).[23] However, very few high-pressure studies on BNNTs have been reported,[27-29] in contrast to the numberous investigations of CNTs under high pressure, for which Raman spectroscopy was used as the most effective characterization probe.[30] More importantly, because of the close proximity of the extremely intense T_{2g} mode (1334 cm^{-1}) of diamond to the major Raman mode (E_{2g}) of BNNTs (~ 1367 cm^{-1}),[27,28,31,32] monitoring pressure-induced transformations in DACs by Raman spectroscopy is, therefore, subject to some ambiguity. As a result, the Raman measurements on the transformation of BNNTs lead to conclusions that are inconsistent with the later X-ray diffraction measurements by the same research group.[27] In addition, depending on their synthetic route and final composition, BNNTs often produce a strong fluorescent background, which makes Raman measurements on a single mode very difficult and less reliable. Moreover, Raman intensity critically depends on excitation power and polarization, sample orientation, exposure time, detector sensitivity and stability as well as many other factors, which makes Raman a less desirable quantitative probe. *In-situ* infrared (IR) measurements, in contrast provide not only supplementary but also more quantitative and sometimes critical information than Raman spectroscopy. Nanostructured BN at ambient pressures has been characterized by several groups.[32-35] However, *in-situ* high-pressure IR measurements have been sparse. Here, we report the first *in-situ* IR measurements on BNNTs in comparison with bulk h-BN, which provide new and quantitative evidence for pressure-induced transformation of BNNTs.

5.2 Experimental section

Multi-walled (MW) BNNTs (purity 99.5%) purchased from NanoAmor Inc. and h-BN (purity 99.5%) purchased from Alfa Aesar were used without further processing. Morphology analysis by transmission electron microscopy (TEM) showed that the BNNTs had an inner diameter of 10 – 40 nm and an outer diameter of 30 – 100 nm (Fig. 5.1 inset). The number of walls was estimated to be 10 or more. The sample was loaded into a DAC equipped with type II diamonds with a culet size of 300 μm. KBr was used as pressure transmitting medium and sample diluter to avoid IR absorption saturation. The sample was ~ 150 μm in diameter and ~ 35 μm thick. A few Rudy chips were inserted as pressure calibrant. The *in-situ* IR measurement was carried out using a customized IR microscopy system in the Song laboratory using the customized micro-IR system (referring to Chapter 2).

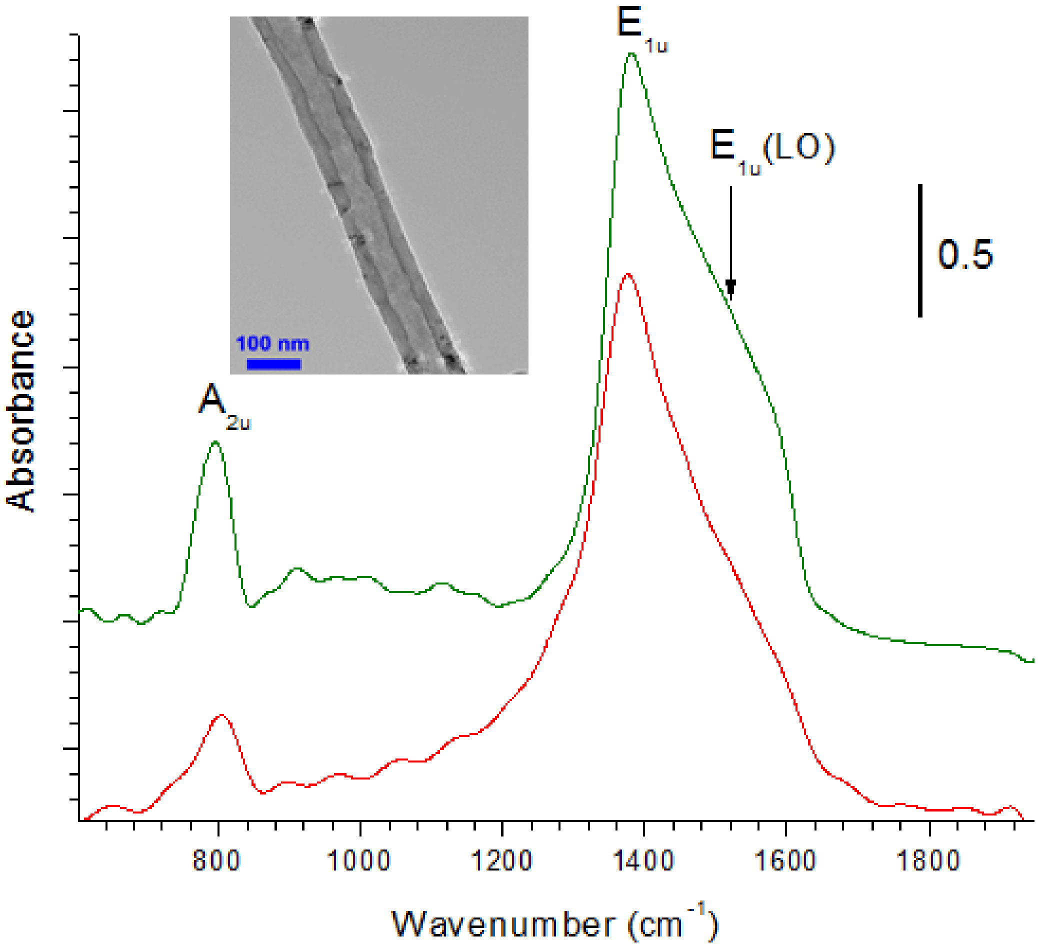

Figure 5.1 Infrared spectra of BNNT (a) in comparison with bulk h-BN (b) both at ambient pressure before compression. The inset shows the TEM image of a selected BNNT.

5.3 Results and discussion

Fig. 5.1 shows the infrared absorption spectra for BNNTs and bulk h-BN under ambient pressure. In both spectra, two major IR bands are observed at slightly different wavenumbers, that is, 794 and 1380 cm^{-1} for BNNTs and 804 and 1377 cm^{-1} for bulk h-BN. These bands are characteristic of hexagonal BN with symmetries of A_{2u} and E_{1u}, respectively.[36] In addition to the similar IR frequencies between the BNNTs and h-BN, a slightly more asymmetric E_{1u} mode was seen for the BNNTs, which can be deconvoluted with a shoulder peak at 1554 cm^{-1} because of the splitting between the longitudinal optical (LO) and transverse optical (TO) modes. This asymmetric profile manifested by the E_{1u} (LO) mode is believed to be endemic to BNNTs and is distinct from bulk h-BN, which is consistent with that observed by Borowiak-Palen[33] and Han.[34] However, the symmetric peak profile for the A_{2u} mode of BNNTs observed in the present study seems different from that observed in the above studies in that the band showed prominent asymmetry in Borowiak-Palen's research, whereas it was significantly broadened in Han's. Although MW-BNNTs are the subject materials in all these studies, detailed morphologies may differ due to the different synthetic routes and processing methods. Because of this and the different characterization conditions, therefore, detailed spectroscopic features may not be the same. For example, in the IR measurements of BNNTs by Zhi *et al.*[32], frequencies of 820 and 1366 cm^{-1} were reported for the A_{2u} and E_{1u} (TO) modes, whereas Chen *et al.*[35] observed only a single symmetric band at 1367 cm^{-1} for hollow BN nanoribbons, both of which were significantly different from all other IR measurements on BNNTs. Even for bulk h-BN, for which the IR measurements have been extensively conducted, different IR frequencies are still reported for different studies. Table 5.1 listed the results of typical IR measurements for both BNNTs and bulk h-BN for comparison. In general, our measurements are consistent with the majority of others, which provides a reliable starting point for the investigation of pressure-induced transformations. In particular, the A_{2u} and E_{1u} modes correspond to the B-N stretch perpendicular and parallel to the tube axis for BNNTs or out-of-plane and in-plane vibrations for bulk h-BN, respectively. Their responses to compression will provide critical information about their structural and bonding changes.

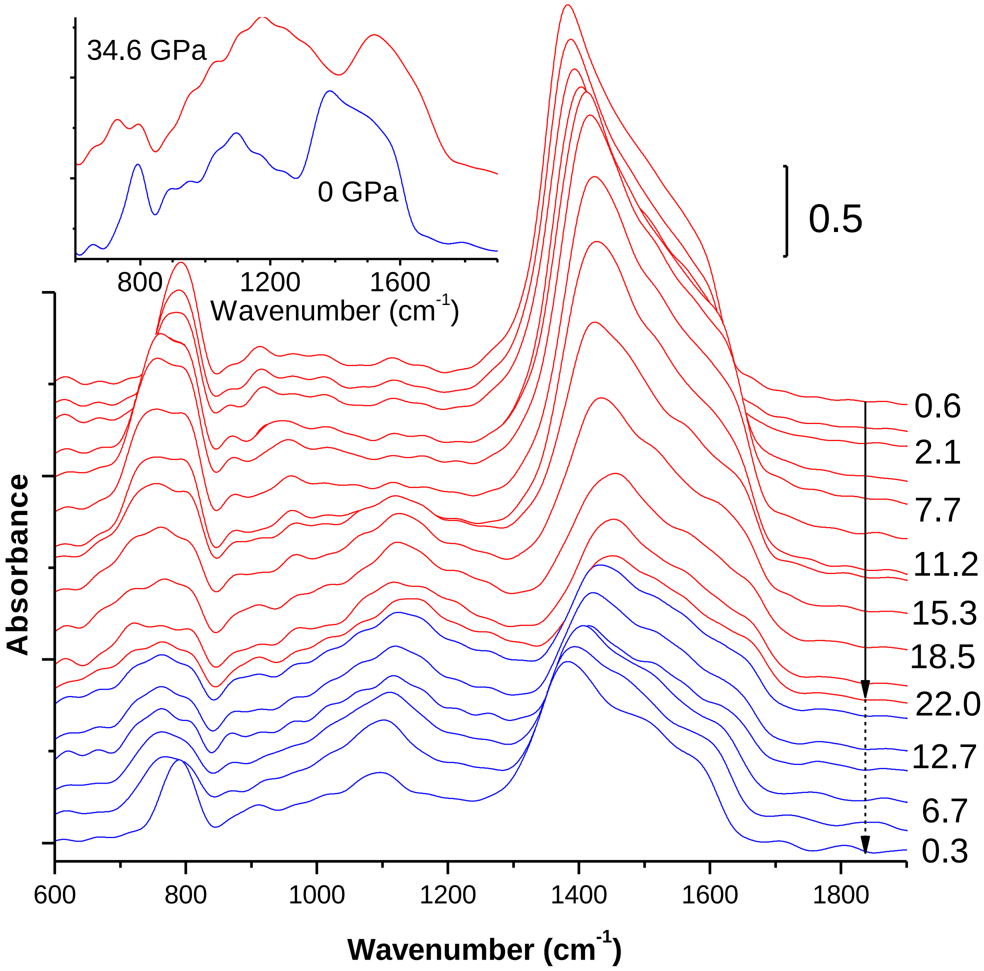

Figure 5.2 Infrared spectra of BNNTs at selected pressures upon compression (red lines) and decompression (blue lines) in the spectra region of 600 – 1900 cm^{-1}. The solid and dashed arrows indicate the compression and decompression sequence. The spectra are vertically offset for clarity. The pressures in GPa are labeled along selected spectra. The inset shows spectra from another run at highest pressure of 34.6 GPa on compression (red solid line) and complete pressure release (blue solid line).

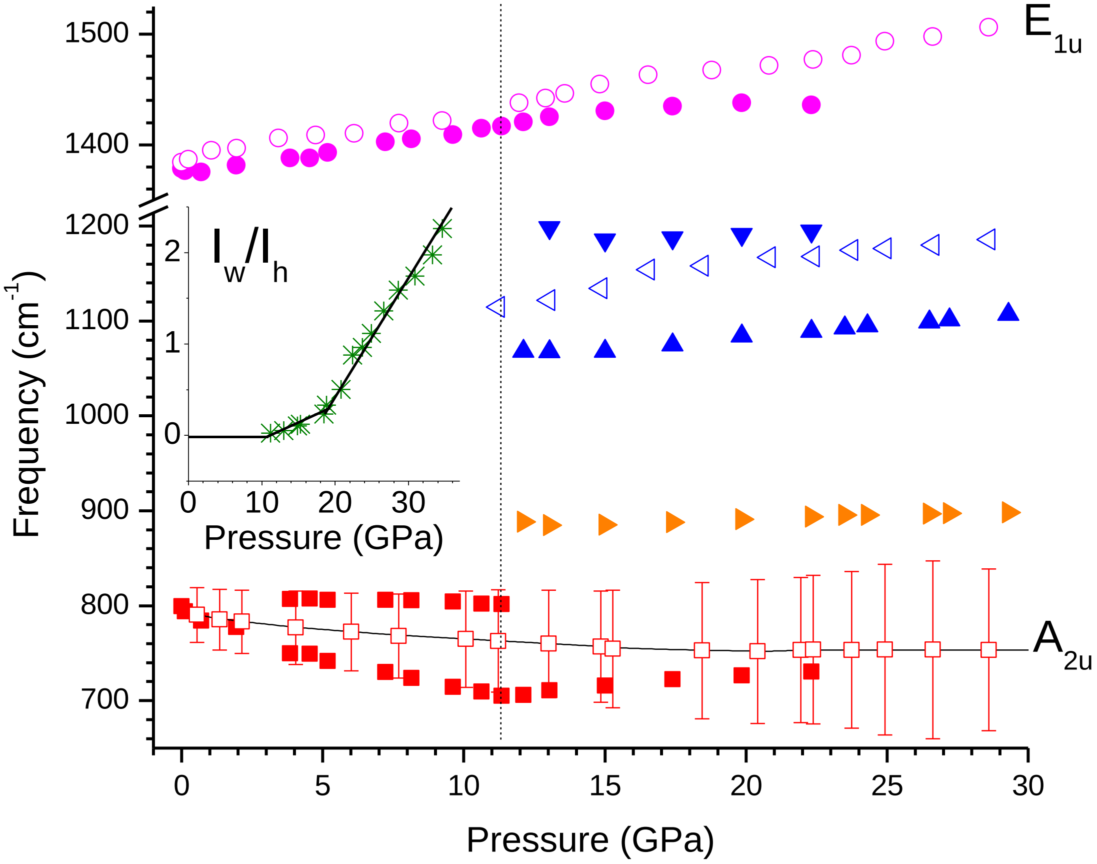

Figure 5.3 **Pressure dependence of characteristic IR bands of BNNTs on compression (open symbols) and in comparison with those for bulk h-BN (solid symbols). The squares and circles denote A_{2u} mode and E_{1u} of h-BN structure respectively. Other symbols represent IR modes for w-BN structure. The dashed line at around 11 GPa indicates the transition onset for both BNNTs and bulk h-BN. The vertical bars for A_{2u} mode represent the full width at half maximum for BNNTs. The inset shows the ratio of the IR band intensity of the mode at 1125 cm^{-1} for w-BN over the E_{1u} mode for h-BN observed in BNNTs labeled as I_w/I_h. The solid lines are for eye guidance showing three distinctive conversion regions.**

Table 5.1 Frequencies of IR active modes observed in nano-BN and bulk h-BN at ambient pressure and temperature[a].

reference	A_{2u} (cm^{-1})	E_{1u} (cm^{-1})	note
nano			
this work	794	1380 (1554)	MW-NT; diameter, 30-100 nm
Borowiak-Palen[b]	800	1372 (1540)	MW-NT; 2 – 10 walls; diameter, 3 ± 1 nm
Han[c]	800	1376	MW-NT; ~10 walls; diameter, 20 – 120 nm
Zhi[d]	772 (820)	1366 (1464)	NT in polymer composite
Chen[e]	818	1367	hollow nanoribbon
bulk			
this work	804	1377	Powder
Borowiak-Palen[b]	811	1377 (1514)	polycrytalline
	767 (783)	1367 (1510)	Pyrolytic h-BN
Rokuta[f]	790	1395	On Ni (1 1 1)
Geick[g]	783 (828)	1367 (1610)	Pyrolytic polycrystalline

[a] In both nano and bulk BN, the symmetries of IR-active modes are A_{2u} and E_{1u}. The frequencies in the parenthesis denote the LO branch if observed or resolved (see text). [b] Ref. 33. [c] Ref. 34. [d] Ref. 32. [e] Ref. 35. [f] Ref. 44. [g] Ref. 36.

Fig. 5.2 depicts the selected IR absorption spectra for BNNTs compressed to 22 GPa, followed by decompression. Clearly, the E_{1u} band shifts to higher frequencies whereas the A_{2u} band shifts to red on compression. The pressure dependences of IR frequencies are plotted in Fig. 5.3. As seen in Fig. 5.2, both A_{2u} and E_{1u} bands exhibit significant broadening upon compression. The broadenings with asymmetric band profiles which change significantly under pressure are apparently associated with multiple highly convoluted components. Therefore, we monitored the pressure behavior of the entire band instead of deconvolution to reduce arbitrariness. For example, we characterized the broadening of the entire A_{2u} band by its bandwidth, which was found to increase significantly from 58 cm^{-1} at ambient pressure to over 150 cm^{-1} above 21 GPa, as indicated by the vertical bars in Fig. 5.3. Starting at 11.2 GPa, the broadening of the E_{1u} mode resulted in a further enhanced asymmetric band profile in which the third component can be seen in addition to the TO/LO bands. At this pressure, the most significant change of the IR absorption profile is the observation that a new band formed at 1125 cm^{-1}, which is a characteristic IR mode of w-BN (as will be discussed along with bulk h-BN). Upon further compression, the intensity of this band grew very gradually, indicating the sequential transformation of the hexagonal structure of BNNT to a wurtzite structure. However, even compressed to 22 GPa, the A_{2u} and E_{1u} bands associated with the hexagonal structure remained as the dominant bands, suggesting the transformation to w-BN was far from complete. When the pressure was released, the band associated with the wurtzite structure maintained its intensity, whereas the bands associated with the hexagonal structure showed no obvious change in intensity, except that the bandwidth of the A_{2u} mode almost reverted to its original level. These observations indicate that, once formed, the transformation of wurtzite structured BNNTs back to the hexagonal is irreversible. The incomplete transformation to w-BN motivated us to conduct several additional compressions to higher pressures. We found even at around 35 GPa, the transformation of BNNTs to wurtzite structure is still very incomplete, as shown in the inset of Fig. 5.2. Although the band associated with w-BN becomes the dominant band, quantitative analysis indicates there are about 30% of the BNNTs remained in h-BN structure (Fig. 5.4). Upon decompression from 35 GPa, the IR spectrum of the recovered BNNTs resembles that on decompression from 22 GPa in terms of the relative band intensities between the two structures. These observations indicate that, although higher compression pressure resulted in more complete conversion to wurtzite structure, this phase can be recovered at ambient pressure only with a relatively constant abundance, regardless of the compression pressure.

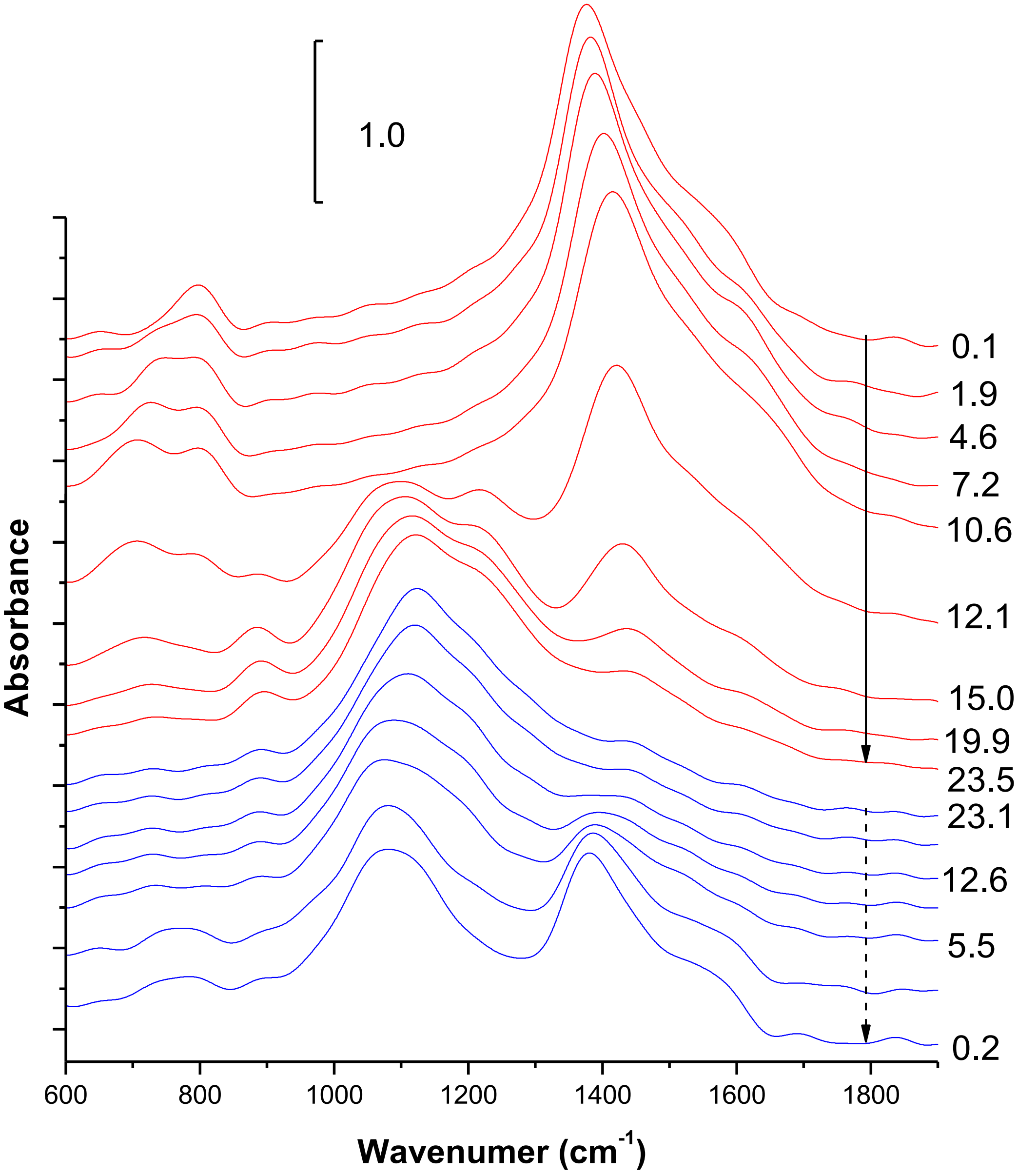

Figure 5.4 **Infrared spectra of bulk h-BN at selected pressures upon compression (red lines) and decompression (blue lines) in the spectra region of 600 – 1900 cm^{-1}. The solid and dashed arrows indicate the compression and decompression sequences. The spectra are vertically offset for clarity. The pressures in GPa are labeled along selected spectra.**

To understand the pressure-induced transformations observed in BNNTs, we also conducted comparative studies on bulk h-BN as well. To our knowledge, IR measurements on bulk h-BN at high pressures have not been reported previously. Fig. 5.5 shows selected IR absorption spectra for bulk h-BN on compression to around 23 GPa, followed by decompression. In addition to the similar broadening, as observed for BNNTs, the A_{2u} mode exhibited more prominent splitting, which allowed deconvolution analysis. As seen in Fig. 5.3, the magnitude of the splitting increased with increasing pressure, with the low-frequency branch significantly shifted to red. We note that the split magnitude is roughly consistent with the bandwidth of this mode for BNNTs below 11.4 GPa. In contrast, the E_{1u} mode for h-BN shifted to blue, similar to that for BNNTs. Dramatic changes were observed at 11.4 GPa: three new bands emerge at 890, 1095 and 1221 cm^{-1}. The middle band at 1095 cm^{-1} with strongest intensity can be assigned as the characteristic mode of w-BN, comparable to the band at 1125 cm^{-1} at similar pressures for BNNTs. However, the other two bands have not been reported before. Further compression from 11.4 GPa resulted in the diminishing of the band at 1221 cm^{-1}, along with the A_{2u} and E_{1u} modes of the h-BN structure, while the band at 890 cm^{-1} remained strong. At 23.5 GPa, only the bands originally at 1095 cm^{-1} and 890 cm^{-1} were observed, while the A_{2u} and E_{1u} modes of the h-BN structure had negligible intensities only, indicating that bulk h-BN almost completely converted to w-BN at this pressure, which strongly contrasts what occurred for BNNTs. Upon decompression, the E_{1u} band gained its intensity back gradually along with the broad A_{2u} band. At near ambient pressure, the recovered bulk h-BN was composed of almost equal amounts of the two h-BN and w-BN structures, as indicated by the comparable intensities of the two characteristic bands.

Again, the structural composition of recovered bulk h-BN is in contrast to that of the BNNTs, for which h-BN was the dominant phase. In addition, this finding indicates that the transformation of bulk h-BN to w-BN is partially reversible, which contradicts previous room-temperature Raman studies in which complete reversibility was claimed [27,28].

Evidently, BNNTs and bulk h-BN are distinct from each other and exhibit significantly contrasting pressure responses that convey important structural and bonding information. To understand their different pressure behaviors, we attempted to address the pressure-induced structural changes of the bulk h-BN first. Both h-BN ($\rho = 2.48$ g/cm^3) and w-BN ($\rho = 3.46$ g/cm^3) - its denser form - belong to a hexagonal crystal system, and their detailed crystal structures have been well established.[24] The bonding patterns of the two forms are shown in Fig. 5.5. As seen, h-BN is composed of discrete layers of hexagons with alternating BN units connected by sp^2 hybrid bond but no interlayer covalent interactions, similar to its isoelectronic analogue, graphite. However, a critical difference between BN and graphite is that BN takes the “eclipsed” conformation in which each boron atom is aligned with a nitrogen atom in adjacent layers. Graphite, however, crystallizes in “staggered” conformation with half of the hexagon vertices aligned with vertices and the other half aligned with the centers of the hexagons in the adjacent layers. As a result, Mao *et al.* demonstrated that, upon compression of graphite, a superhard graphite phase was formed in which half of the sp^2 bonds converted to sp^3 bonds.[37] In contrast, h-BN can be converted to a much denser w-BN structure via the planar-to-chair conformational transition such that each B-N pair between two adjacent layers is 100% connected by sp^3 bonds, which is similar to the bonding patterns observed for cubic BN (c-BN). The w-BN belongs to space group 186 ($P6_3mc$, Z = 2) and thus the factor group analysis predicted that only A_1 and E_1 modes would be IR-active. Until now, the only data for the IR frequencies of these two bands were theoretical predictopms, that is, 1001/1249 and 1041/1267 for A_1 (TO/LO) and E_1 (TO/LO), respectively.[38] Because of the extremely close frequencies between the two bands, it is not clear which symmetry the bands observed at 1095 and 1221 cm^{-1} at 11.4 GPa possess, although they are likely a TO/LO pair. The h-BN band seen at 890 cm^{-1} is a new observation and remains to be explained. One possibility is that, because compression results in a strong lattice distortion, the symmetry of the wurtzite structure is no longer strictly hexagonal. As a result, the E_2 mode, which is originally Raman-active only, becomes IR-active. This mode was calculated to occur at 938 cm^{-1} in the IR reflectance spectrum.[38] Interestingly, a weak band at similar frequency, i.e., 920 cm^{-1}, was also observed for BNNT Raman measurements by Zhi *et al*.[32] This was believed to originate from lattice distortion as well, which is analogous to the disorder-induced D band for CNTs.[28]

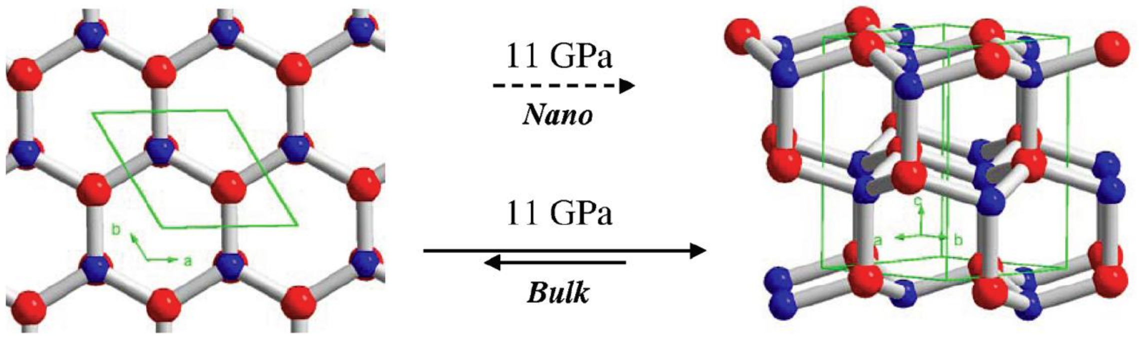

(a) h-BN

(b) w-BN

Figure 5.5 Crystal structures and bonding patterns of (a) h-BN and (b) w-BN. The transformation conditions for BNNT and bulk h-BN are labeled. The dashed arrow for BNNT indicates incomplete irreversible transformation, while the solid arrows with different length for bulk h-BN indicate partial reversibility (see text).

Using inelastic X-ray scattering (IXS), Meng *et al.*[22] has characterized the bonding changes in compressed h-BN. The structural transformations and bonding changes we observed for bulk h-BN using IR spectroscopy are consistent with those measured by IXS. In addition, our IR data also agree with Raman studies undertaken by Saha *et al.*[27,28] These results are listed in Table 5.2. As seen, the transformation pressures determined by different studies are in the range of 11 – 14 GPa, with reasonable agreement. However, the reversibility remains an open issue. Although this issue was not addressed in the IXS study,[22] Raman studies suggest that the transformation of bulk h-BN is completely reversible. We noticed that the Raman measurements relied primarily on a single weak mode (E_{2g}) in close vicinity to the overwhelming T_{2g} mode of diamonds. However, the IR measurements in the present study have the advantage of the quantitative nature of IR absorption of the multiple characteristic modes that are active in both h-BN and w-BN.

This permitted the unambiguous characterization of the partial reversibility of the structural transformations and bonding changes. Furthermore, a recent X-ray diffraction study of MWBNNTs[29] yielded high-pressure behaviors that contradicted previous Raman measurements as well.

The major difference in the pressure responses between BNNTs and bulk h-BN is the completeness of the transformation. Even at over 35 GPa, the h-BN structure remains prominent in BNNTs, whereas bulk h-BN converts completely to w-BN at 23 GPa. This difference, together with other spectroscopic features, can be understood from the topological and mechanical aspects of BNNT nanostructures. MW-BNNTs are formed by wrapping hexagonal BN sheets into concentric cylinders, similar to the formation of MW-CNTs. The similar spectroscopic features of bulk h-BN and BNNTs, including Raman scattering and IR absorption, indicated that the walls of BNNTs are aligned in a similar way to the layers of bulk h-BN. If the diagonal length (or parallel edge distance) of each hexagon in h-BN is considered to be 2.891 Å (or 2.504 Å), the narrowest tube in this study, with an inner diameter of 10 nm, can be estimated to be formed by wrapping 109 to 125 hexagons. The difference in IR absorption profile and band frequencies could be due to the actual wall curvatures and/or the slightly displaced alignment between the walls compared to the near perfectly aligned layers in bulk h-BN. Upon compression, it is highly likely that the tubes first form bundles characterized by very short inter-tubular distances, as observed for CNTs.[21,30] When the pressure is high enough (e.g., 11 GPa), sp^3 bonds are formed first between the tubes within the bundles. Above 20 GPa, the formation of sp^3 between the tubes is saturated and further compression results in cross-linking between the walls by sp^3 bonds within the tube. However, such a linkage that requires the deformation and/or displacement of the walls is much more limited than the very complete inter-tubular linking because of the intrinsic mechanical strength of BNNTs. As a result, the two phases can coexist at much higher pressure in BNNTs than in h-BN. Such a transformation sequence is analogues of the preferential orders of inter- and intra-molecular responses to compression. Upon decompression, the intra-tubular sp^3 bonds revert, first, as the result of stress release, whereas some of the inter-tubular sp^3 bonds survive, resulting in the recovery of h-BN as the major phase in the mixture.

Golberg *et al.* recently measured the elastic deformations of individual MW-BNNTs using integrated TEM-atomic force microscopy (AFM).[39] It was found that BNNTs survive at very large bending angles corresponding to the elastic moduli of 0.6 TPa and the elastic deformation is entirely reversible with no traces of residue. The pressure-induced transformation sequence proposed here is, therefore, also consistent with the investigated mechanical strength of BNNTs. Furthermore, such a proposed transformation mechanism can be substantiated by the detailed spectroscopic features observed in the IR measurements. Below 12 GPa, the A_{2u} mode associated with the B-N stretch normal to the tube axis (or along the direction of the sp^3 bond formation between the walls) exhibited a soft behavior as a precursor to the structural transition for both h-BN and BNNTs. The significantly different band profile between the two morphologies suggests that there is a different microscopic environment under stress. For instance, the BNNT mode had a much less sensitive pressure dependence (with a pressure coefficient of -2.5 cm^{-1}/GPa) than that for bulk h-BN (-8.7 cm^{-1}/GPa) below the transition pressure (Fig. 5.3). Above 12 GPa, this mode entered an extended plateau region to 35 GPa, indicating a strong “resistance” to compression. Prominent band broadening at high pressures could be interpreted as sequential cross-linking between the walls of nanotubes in which the uniformity and spatial distribution of the sp^3 connections between the walls contribute to the bandwidths. Furthermore, the multiple frequencies from the convoluted BNNT E_{1u} mode are markedly different from those for bulk h-BN, which had a significantly different band profile. This is consistent with the finding that the BNNT wurtzite structure may be contributed by both the inter- and the intra-tubular linking, whereas the bulk h-BN structure arose only from interlayer linking. The abundance ratio of w-BN to h-BN (Fig. 5.3) along the BNNT transitions provided a possible estimate of the threshold pressure above which intra-tubular linking becomes significant. That is, the second region of 11 – 20 GPa likely corresponds to inter-tubular linking, whereas in the third region above 20 GPa, intra-tubular linking might play a major role in the conversion to a wurtzite structure. These observations strongly support the different mechanisms of sp^3 bonding formation between the two BN materials. Additional theoretical investigations on high-pressure structures and MWBNNT bonding patterns would be helpful for understanding the detailed transformation process. Further *in-situ* structural investigations, such as synchrotron X-ray diffraction and inelastic X-ray scattering,[22] would provide new experimental insight into the proposed transformation mechanism.

Table 5.2 Comparison of pressure-induced transformations of BNNTs and CNTs[a] with their bulk counterparts.

initial form	transformed form	transformation pressure (GPa)	characterization method	note
BNNT[b]	w-BN	11	IR	incomplete, irreversible
BNNT[c]	w-BN	12	Raman	irreversible
h-BN[b]	w-BN	11	IR	complete, partially reversible
h-BN[c]	w-BN	13	Raman	reversible
h-BN[d]	w-BN	14	IXS	
CNT (SW)[e]	deformed tube	2	Raman	reversible
CNT (MW)[f]	diamond	7	Raman	at high temperature
Graphite[g]	distorted graphite	17	IXS	superhard phase, reversible

[a]For pressure-induced transformations of CNTs, only selected studies were listed since it is impossible to exhaust numerous high-pressure studies (see text and Ref. 30). [b]This work. [c]Refs. 27 and 28. [d]Ref. 22. [e]Ref. 30. [f]Ref. 40. [g]Ref. 37.

Finally, because BN and graphite are isoelectronic, it would be interesting to compare the pressure behavior of BNNTs with that for CNTs, which have been studied extensively under high pressures, both experimentally and theoretically.[30] Table 5.2 lists representative experimental high-pressure studies of CNTs[30,40] and BNNTs together with the corresponding bulk materials.[22,37] Using Raman spectroscopy, CNTs were found to have a reversible pressure-induced anomaly at 2 GPa, which is characterized by the discontinuous reduction of the Raman intensity.[30] Theoretical studies interpret this anomaly as deformations of the circular nanotubes.[41,42] In addition, the transformations were found to depend on tube diameter, chirality, and choice of transmitting media, as well as many other factors, especially those associated with the synthesis process.[21] High-pressure studies of MW-CNTs suggest that their behaviors also depend on the intrinsic parameters, such as the diameter and wall thickness of the tube. However, structural evolutions characterized by the tangential mode show substantially less pressure dependence, indicating that MW-CNTs have a more elastic nature than SW-CNTs. Interestingly, BNNTs similarly seem to exhibit more enhanced elasticity than does bulk h-BN, as evidenced by the fairly pressure-independent A_{2u} mode and its significant resistance to compression above 20 GPa. Although SW-BNNTs are difficult to obtain experimentally, theoretical calculations have predicted that the mechanical stiffness of BNNTs is comparable with that of CNTs. For example, it has been shown that, although SW-BNNTs have a lower elastic modulus, the ability of BNNTs to resist yield and thermal degradation exceeds that of CNTs.[43] Thus, the combined mechanical and chemical properties of BNNTs make them a highly promising advanced material that may replace CNTs for many unique applications.

5.4 Conclusions

Complementary to previous high-pressure studies using Raman spectroscopy, *in-situ* FTIR spectroscopic measurements on MW-BNNTs were carried out up to 35 GPa in comparison with bulk h-BN material for the first time. A hexagonal-to-wurtzite structural transformation characterized by the formation of sp^3 bonding was observed at around 11 GPa in both materials. However, such transformation is near complete at 23 GPa for bulk h-BN but far from complete for BNNTs even at ~35 GPa. Furthermore, the back transformation from a wurtzite to a hexagonal structure is partially reversible for bulk BN but irreversible for BNNTs. These observations strongly contrast previous Raman studies. We attempted to address the differences in compression behaviors between bulk BN and BNNTs by proposing a two-step, sequential pressure-induced transformation mechanisms inter-tubular sp^3 bonds form, first, in the lower pressure region, while intra-tubular connections (i.e., linkages between walls) become significant upon further compression. Additional theoretical and experimental investigations are required to justify the proposed mechanism.

5.5 References

(1) Greim, J.; Schwetz, K. A. *Ullmann's Encyclopedia of Industrial Chemistry* **2006**, DOI:10.1002/14356007.a04_295.pub2.

(2) Golberg, D.; Bando, Y.; Tang, C. C.; Zhi, C. Y. *Adv. Mater.* **2007**, *19*, 2413.

(3) Rubio, A.; Corkill, J. L.; Cohen, M. L. *Phys. Rev. B* **1994**, *49*, 5081

(4) Chopra N.G.; Luyken R.J.; Cherrey K.; Crespi V.H.; Cohen M.L.; Louie S.G.; Zettl, A. *Science* **1995**, *269*, 966.

(5) Blase, X.; Rubio, A.; Louie, S. G.; Cohen, M. L. *Europhys. Lett.* **1994**, *28*, 335.

(6) Golberg, D.; Bando, Y.; Kurashima, K.; Sato, T. *Scripta Mater.* **2001**, *44*, 1561.

(7) Chen, Y.; Zou, J.; Campbell, S. J.; Le Caer, G. *Appl. Phys. Lett.* **2004**, *84*, 2430.

(8) Han, W. Q.; Mickelson, W.; Cumings, J.; Zettl, A. *Appl. Phys. Lett.* **2002**, *81*, 1110.

(9) Chopra, N. G.; Zettl, A. *Solid State Commun.* **1998**, *105*, 297.

(10) Yu, J.; Chen, Y.; Elliman, R. G.; Petravic, M. *Adv. Mater.* **2006**, *18*, 2157.

(11) Wu, J.; Han, W. Q.; Walukiewicz, W.; Ager, J. W.; Shan, W.; Haller, E. E.; Zettl, A. *Nano Lett.* **2004**, *4*, 647.

(12) Mele, E. J.; Kral, P. *Phys. Rev. Lett.* **2002**, *88*, 056803.

(13) Lauret, J. S.; Arenal, R.; Ducastelle, F.; Loiseau, A.; Cau, M.; Attal-Tretout, B.; Rosencher, E.; Goux-Capes, L. *Phys. Rev. Lett.* **2005**, *94*, 037405.

(14) Tolbert, S. H.; Alivisatos, A. P. *Science* **1994**, *265*, 373.

(15) Tolbert, S. H.; Alivisatos, A. P. *Annu. Rev. Phys. Chem.* **1995**, *46*, 595.

(16) Chen, C.-C.; Herhold, A. B. *Science* **1997**, *276*, 398.

(17) Jacobs, K.; Zaziski, D.; Scher, E. C.; Herhold, A. B.; Alivisatos, P. A. *Science* **2001**, *293*, 1803.

(18) Wang, Z.; Daemen, L. L.; Zhao, Y.; Zha, C. S.; Downs, R. T.; Wang, X.; Wang, Z. L.; Hemley, R. J. *Nat. Mater.* **2005**, *4*, 922.

(19) Swamy, V.; Kuznetsov, A.; Dubrovinsky, L. S.; McMillan, P. F.; Prakapenka, V. B.; Shen, G.; Muddle, B. C. *Phys. Rev. Lett.* **2006**, *96*, 135702.

(20) Guo, Q. X.; Zhao, Y. S.; Mao, W. L.; Wang, Z. W.; Xiong, Y. J.; Xia, Y. N. *Nano Lett.* **2008**, *8*, 972.

(21) San-Miguel, A. *Chem. Soc. Rev.* **2006**, *35*, 876.

(22) Meng, Y.; Mao, H. K.; Eng, P. J.; Trainor, T. P.; Newville, M.; Hu, M. Y.; Kao, C. C.; Shu, J. F.; Hausermann, D.; Hemley, R. J. *Nat. Mater.* **2004**, *3*, 111.

(23) Pan, Z. C.; Sun, H.; Zhang, Y.; Chen, C. F. *Phys. Rev. Lett.* **2009**, *102*, 055503.

(24) Bundy, F. P.; Wentorf, R. H. *J. Chem. Phys.* **1963**, *38*, 1144.

(25) Eremets, M. I.; Takemura, K.; Yusa, H.; Golberg, D.; Bando, Y.; Blank, V. D.; Sato, Y.; Watanabe, K. *Phys. Rev. B* **1998**, *57*, 5655.

(26) Solozhenko, V. L.; Hausermann, D.; Mezouar, M.; Kunz, M. *Appl. Phys. Lett.* **1998**, *72*, 1691.

(27) Saha, S.; Muthu, D. V. S.; Golberg, D.; Tang, C.; Zhi, C.; Bando, Y.; Sood, A. K. *Chem. Phys. Lett.* **2006**, *421*, 86.

(28) Saha, S.; Gadagkar, V.; Maiti, P. K.; Muthu, D. V. S.; Golberg, D.; Tang, C.; Zhi, C.; Bando, Y.; Sood, A. K. *J. Nanosci. Nanotechnol.* **2007**, *7*, 1810.

(29) Muthu, D. V. S.; Midgley, A. E.; Petruska, E. A.; Sood, A. K.; Bando, Y.; Golberg, D.; Kruger, M. B. *Chem. Phys. Lett.* **2008**, *466*, 205.

(30) Loa, I. *J. Raman Spectrosc.* **2003**, *34*, 611.

(31) Zhi, C. Y.; Bando, Y.; Tang, C. C.; Honda, S.; Sato, K.; Kuwahara, H.; Golberg, D. *Angew. Chem.-Int. Edit.* **2005**, *44*, 7929.

(32) Zhi, C. Y.; Bando, Y.; Tang, C. C.; Golberg, D.; Xie, R. G.; Sekigushi, T. *Appl. Phys. Lett.* **2005**, *86*, 213110.

(33) Borowiak-Palen, E.; Pichler, T.; Fuentes, G. G.; Bendjemil, B.; Liu, X.; Graff, A.; Behr, G.; Kalenczuk, R. J.; Knupfer, M.; Fink, *J. Chem. Commun.* **2003**, *1*, 82.

(34) Han, W. Q.; Yu, H. G.; Zhi, C.; Wang, J.; Liu, Z.; Sekiguchi, T.; Bando, Y. *Nano Lett.* **2008**, *8*, 491.

(35) Chen, Z. G.; Zou, J.; Liu, G.; Li, F.; Wang, Y.; Wang, L. Z.; Yuan, X. L.; Sekiguchi, T.; Cheng, H. M.; Lu, G. Q. *ACS Nano* **2008**, *2*, 2183.

(36) Geick, R.; Perry, C. H.; Rupprech.G. *Phys. Rev.* **1966**, *146*, 543.

(37) Mao, W. L.; Mao, H. K.; Eng, P. J.; Trainor, T. P.; Newville, M.; Kao, C. C.; Heinz, D. L.; Shu, J. F.; Meng, Y.; Hemley, R. J. *Science* **2003**, *302*, 425.

(38) Cai, Y. Q.; Zhang, L. T.; Zeng, Q. F.; Cheng, L. F.; Xu, Y. D. *Solid State Commun.* **2007**, *141*, 262.

(39) Golberg, D.; Costa, P.; Lourie, O.; Mitome, M.; Bai, X. D.; Kurashima, K.; Zhi, C. Y.; Tang, C. C.; Bando, Y. *Nano Lett.* **2007**, *7*, 2146.

(40) Tang, D. S.; Chen, L. C.; Wang, L. J.; Sun, L. F.; Liu, Z. Q.; Wang, G.; Zhou, W. Y.; Xie, S. S. *J. Mater. Res.* **2000**, *15*, 560.

(41) Venkateswaran, U. D.; Rao, A. M.; Richter, E.; Menon, M.; Rinzler, A.; Smalley, R. E.; Eklund, P. C. *Phys. Rev. B* **1999**, *59*, 10928.

(42) Peters, M. J.; McNeil, L. E.; Lu, J. P.; Kahn, D. *Phys. Rev. B* **2000**, *61*, 5939.

(43) Dumitrica, T.; Bettinger, H. F.; Scuseria, G. E.; Yakobson, B. I. *Phys. Rev. B* **2003**, *68*, 8.

(44) Rokuta, E.; Hasegawa, Y.; Suzuki, K.; Gamou, Y.; Oshima, C.; Nagashima, A. *Phys. Rev. Lett.* **1997**, *79*, 4609.

Chapter 6 Abnormal Pressure-Induced Structural Transformations of Gallium Nitride Nanowires*

6.1 Introduction

Gallium nitride (GaN) is a wide band gap semiconductor of great technological importance.[1] Due to the high degree of hardness, low compressibility, high ionicity, and high thermal conductivity, GaN has been considered as a promising candidate for optoelectronic devices operating under extreme conditions such as high pressure.[2] It is well established that GaN transforms from a wurtzite (B4) structure ($P6_3mc$) to a rocksalt (B1) structure ($Fm\bar{3}m$) at high pressures.[3-11] However, there were large discrepancies in the reported transition pressures (e.g., 42 – 54 GPa for experimental results [4,7,12] and 37 – 55 GPa for other theoretical studies[3,13-17]). GaN can also be synthesized in the nanocrystalline form, either as nanowires or as quantum dots.[9,18,19] Compared to bulk GaN, nanostructured GaN exhibits attractive properties and thus enhanced performance for applications such as optoelectronic devices because of its excellent tunability of its direct band gap.[20] Therefore, studies on structural tuning of nano-GaN, such as by the application of pressure in comparison with the bulk materials, are of fundamental interest.[21] To date, only Jorgensen *et al.* have investigated the phase transformations and compressibility of GaN nanocrystals in comparison with the bulk GaN. In this paper, we reported the *in-situ* high-pressure X-ray diffraction investigation of one-dimensional

---

* The content of this chapter has been published as: Dong Z., and Song Y., *Appl. Phys. Lett.*, **2010**, *96*, 151903.

nanostructured GaN in the form of zigzagged nanowires where unusual pressure behaviors were observed.

6.2 Experimental section

The GaN nanowires were synthesized by passing ammonia through a mixture of Ga and Ga_2O_3 at a high temperature using Au nanoparticles as the catalyst.[19] The SEM images (Fig. 6.1a) revealed that the GaN nanowires had a wire-like structure comprised of zigzag periodic units with a length of tens to hundreds of microns and a thickness of several tens of nanometers. The culet size of the diamond anvil was 250 μm. A hole with diameter of 80 μm was drilled in a tungsten gasket and used as the sample chample. Silicone oil was used as the pressure-transmitting medium and pressure was determined by the ruby fluorescence method.

The synchrotron angle-dispersive X-ray diffraction measurements were performed using an incident wavelength of 0.3680 Å and a beam size of 15 μm × 10 μm. GaN nanowires were compressed up to 65 GPa. The detailed description of experimental set up can be found in Chapter 2.

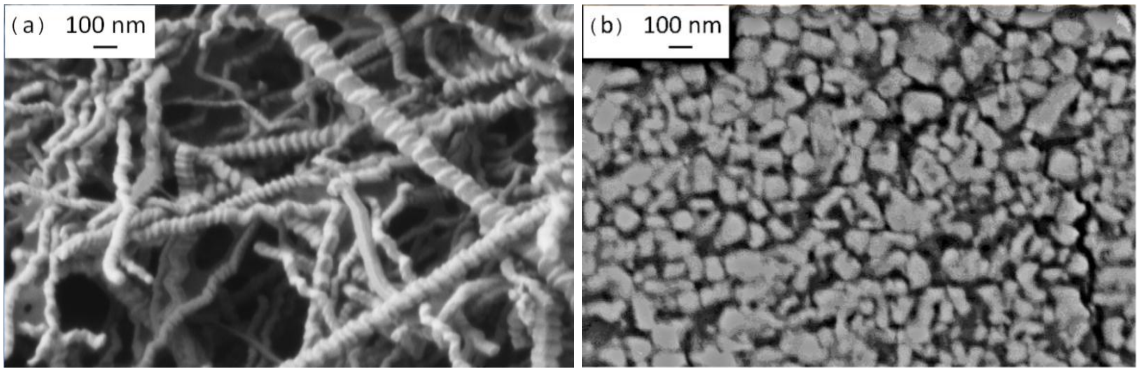

Figure 6.1 **SEM images of GaN nanowires before compression (a) and after decompression (b) with scales labeled in each panel.**

6.3 Results and discussion

Selected X-ray diffraction patterns of GaN nanowires are shown in Fig. 6.2. The diffraction pattern at near ambient pressure (i.e., 0.5 GPa) can be indexed with a hexagonal wurtzite structure ($P6_3mc$) with cell parameters consistent with the previous diffraction measurement of GaN nanowires.[19] In contrast to the diffraction pattern of nanocrystalline GaN, which is characterized by significantly broadened reflection profiles,[9] however, the narrow and sharp reflections for GaN nanowires observed here suggest an excellent crystalline phase that resembles bulk GaN. Upon compression, the wurtzite phase was found to persist to 65 GPa as indicated by the consistent indexing of the first six reflections associated with this phase. At 55 GPa, a new reflection appeared at 10.4519°, which can be indexed as (2 0 0) for the rocksalt phase, suggesting the onset of a phase transformation. We note that the phase transition pressure of 55 GPa was higher than that in most of the previous studies for bulk GaN[5,7] but lower than that for nanocrystalline GaN (i.e.,~ 60 GPa).[9] Size and morphology-dependent enhancements of transition pressures have been observed in other nanostructured materials.[21] Currently it is the general understanding that surface energy plays an important role in nanostructures and contributes to the enhanced transition pressures. The GaN nanowires in the current study had an initial wire-like morphology and converted to smaller nanoparticles upon compression with an average size of 50 – 200 nm (Fig. 6.1b), which resulted in an increased surface area. Comparing with the particle size of the nanocrystalline GaN (i.e., 2 – 8 nm) studied previously,[9] it can be inferred that the surface energy of GaN increased from bulk to nanowires and to nanoparticles with decreasing sizes, giving rise to the corresponding different transition pressures.

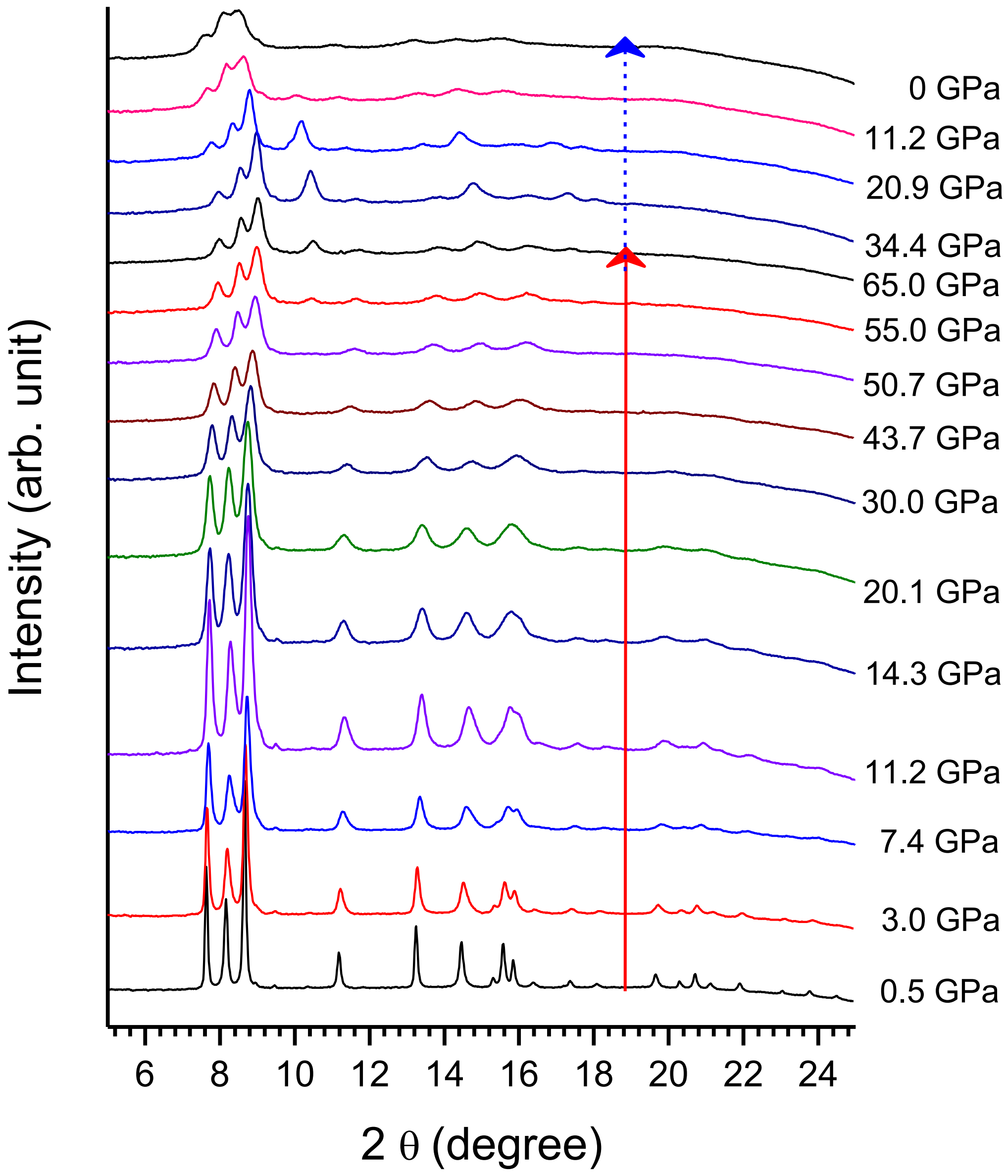

Figure 6.2 X-ray diffraction patterns (λ=0.3680Å) at selected pressures. The solid and dashed arrows indicate the compression and decompression sequence.

Another significant difference from previous studies is that the wurtzite-to-rocksalt transformation for GaN nanowires was far from complete even at 65 GPa. Rietveld analysis of the GaN nanowire diffraction pattern at 65 GPa shown in Fig. 6.3 indicates that the wurtzite and rocksalt phases coexist at this pressure with a respective abundance of 88% and 12%. In contrast, an abundance of almost 100% was reported for the rocksalt phase of bulk GaN at a pressure of less than 60 GPa in most of the previous studies.[4,7,8,12] Our observation was consistent with that for nanocrystalline GaN where the wurtzite to rocksalt phase transition was found to be incomplete even at 63.5 GPa.[9] Similar results were also obtained in other one-dimensional nanomaterials, such as boron nitride nanotubes.[22] In addition to the intrinsic properties of nanostructures, nonhydrostaticity due to use of silicone oil as the pressure-transmitting medium may also contribute to the "sluggish" phase transformations, as manifested by the significant broadening of all the reflections especially at high pressures. Furthermore, severe distortions in the Debye-Scherrer 2D diffraction patterns were observed in the high-pressure region (Fig. A4 in Appendix II), indicating a pressure-induced enhancement of the lattice strain. All of these factors may interactively affect the phase stabilities and thus the extent of transformations.

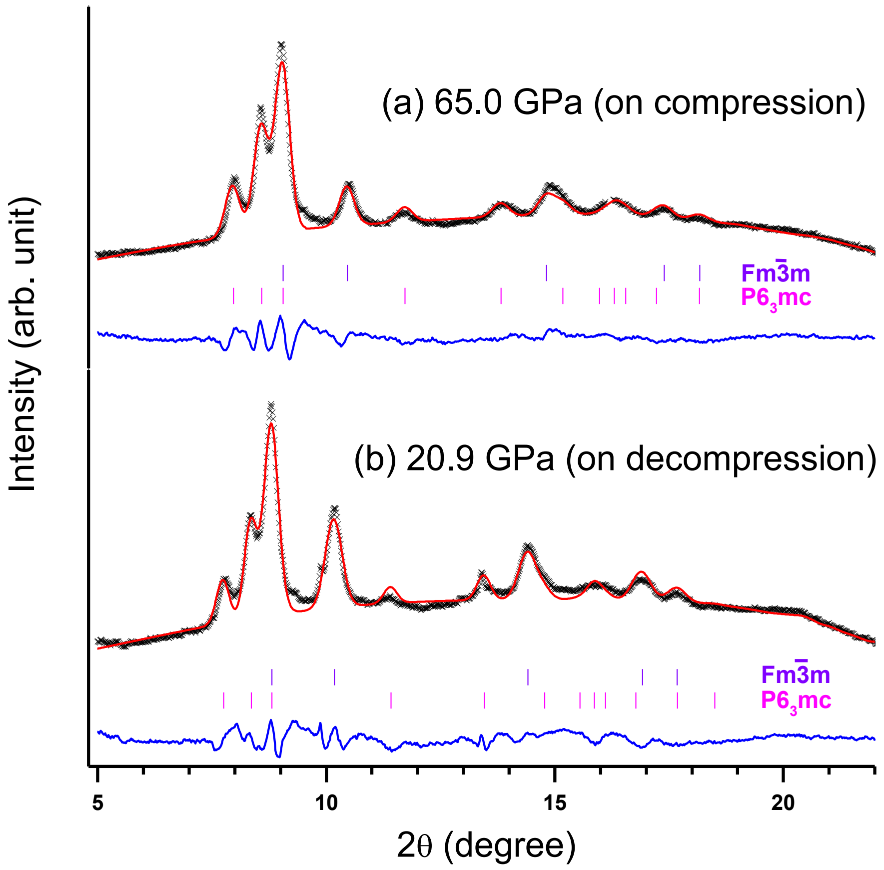

Figure 6.3 Rietveld refinement of the X-ray diffraction patterns for GaN nanowires at (a) 65 GPa on compression and (b) 20.9 GPa on decompression. The red cross is experimental X-ray intensity and the green line is the calculated diffraction patterns based on refinement with the blue curve at the bottom showing the difference between the calculated and observed intensities. The vertical bars denote the indexed reflections for each phase with the space groups labeled beside. The characteristic reflection for the cubic rocksalt phase is labeled as c-(2 0 0). Rietvled refinement of X-ray patterns at near ambient pressure (e.g., 0.5 GPa) and pressure (e.g., 50.7 GPa) right before the phase transition can also be found in Fig. A5 and A6 in Appendix II.

An interesting and unusual phase transformation was observed during decompression. Upon releasing the pressure from 65 GPa, the abundance of the rocksalt phase was found to increase significantly. For instance, Rietveld refinement (Fig. 6.3b) suggested that the fraction of the rocksalt phase had increased from 12 % at 65.0 GPa to 29 % at 20.9 GPa upon releasing the pressure. Below 20.9 GPa, the rocksalt phase gradually retransformed to the wurtzite phase, and was retained even at very low pressures (e.g., < 16.4 GPa). The recovered phase at ambient pressure can be identified as a single wurtzite phase, but the significantly broadened diffraction pattern suggests a pressure-induced reduction of the grain size, consistent with the SEM result (Fig. 6.1b). All of the previous studies found that the B4 - B1 phase transformation was reversible for both bulk GaN and nanocrystalline GaN[4,8,12] indicating that the wurtzite phase was thermodynamically stable in the low pressure region. However, the strongly contrasting, unprecedented decompression behavior of the GaN nanowires characterized by a large hysteresis, suggests that the rocksalt phase is a metastable phase. Prominent hysteresis was likely associated with different kinetic barriers that impeded the sharp transitions often involving a metastable phase.[21]

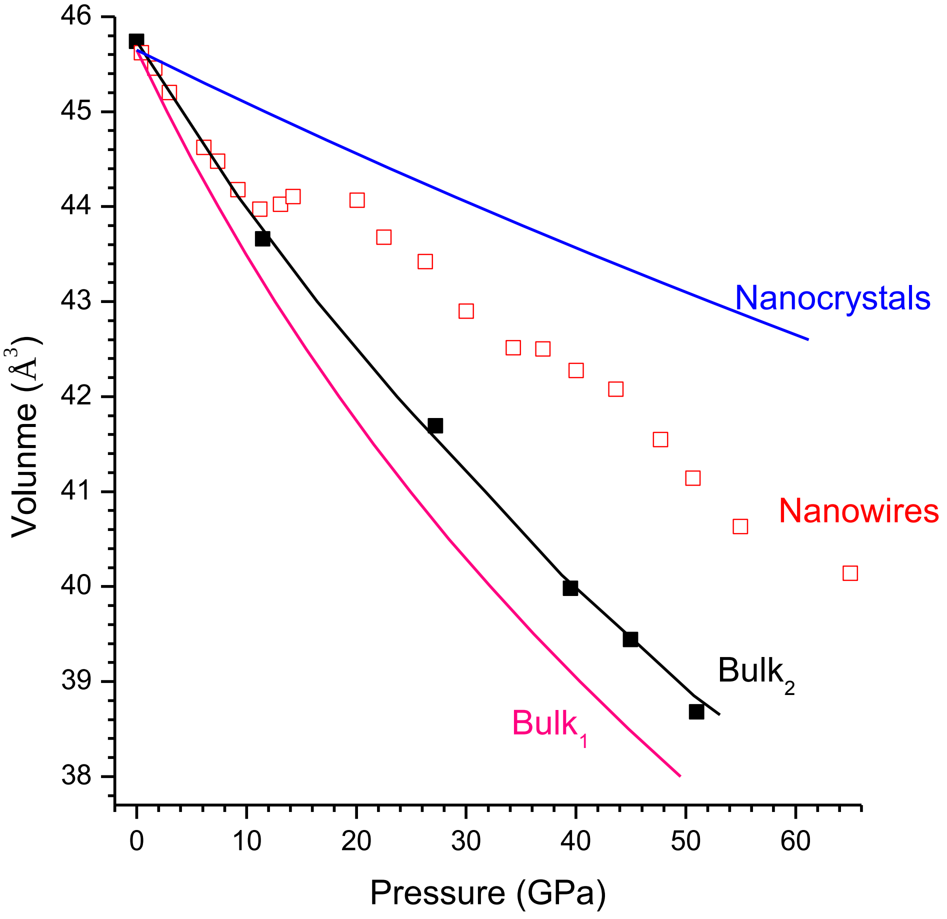

Figure 6.4 **Unit cell volume as a function of pressure for GaN nanowire (open squares) in comparison with that for bulk and nanocrystal GaN. Solid lines are fitted EOS curves for bulk GaN using bulk moduli of 187 GPa (bulk1) and 237 GPa (bulk2) from Ref. 9 and 7 respectively. The dashed line is fitted EOS curve for nanocrystalline GaN using bulk modulus of 319 GPa from Ref. 9.**

Finally, the unit cell volume of GaN nanowires for the wurtzite phase was plotted against the pressures shown in Fig. 6.4 in comparison with previous studies. The P-V curve of GaN nanowires exhibited a noticeable discontinuity in the pressure region of 11

– 20 GPa. The previously established equation of states (EOS) for bulk GaN (B_0 = 187 – 237 GPa)[7,9] and for nanocrystalline GaN (B_0 = 319 GPa)[9] suggest that the bulk modulus for GaN nanowires in the pressure region above 20 GPa can be estimated to be somewhere in between, consistent with that an increase in the surface area may enhance the bulk modulus. This observation can be further understood from the fact the GaN nanowires break into nanoparticles when the external stress surpasses the yield strength at around 20 GPa, resulting in the size-induced enhancement of the bulk modulus. The correlation between the reduction of the particle size and the increasing bulk modulus has been found in other nanomaterials, such as AlN nanocrystals.[23] A similar discontinuity was also found in the P-V curve for nanocrystalline CeO_2.[24] However, a decrease in the bulk modulus of nanocystalline CeO_2 was found above ~ 20 GPa, a pressure that was believed to signify the onset of a size-induced weakening of the elastic stiffness of nanocrystalline CeO_2. Therefore, the discontinuity in the EOS for both nanocystalline CeO_2 and GaN nanowires can be understood from the nano-size effect while the different shapes of the EOS curves may be associated with opposite pressure-induced changes in particle size. It is probable, too, that the P-V behavior observed in the region of 11 – 20 GPa is associated with the combined effect of the original nanowires and the yield-generated nanoparticles. The high yield strength observed in the GaN nanowires thus furthers the understanding of the morphology-tuned improvement in yield strength and hardness in hard materials applications. Moreover, the choice of silicone oil as the pressure-transmitting medium may also contribute to the discontinuity observed in the P-V curve. An anomalous behavior inherent in silicone oil at ~ 12 GPa, which is believed to be the result of phase transition,[25,26] seems to have further complicated the abnormal behavior of GaN nanowires in the pressure region of 11 – 20 GPa. It would therefore be interesting to use better pressure transmitting media, such as helium, to study the compressibility of GaN nanowires under hydrostatic conditions.

6.4 Conclusions

In summary, we have investigated the high-pressure structures and properties of the one-dimensional nanostructured GaN using X-ray diffraction. A wurtzite to rocksalt phase transformation was observed to start at 55 GPa but was still far from complete even at pressures of up to 65 GPa. Upon decompression, the abundance of the rocksalt phase was found to first increase and then to decrease until the ambient pressure was reached, at which time only the wurtzite phase was recovered, indicating a reversible transformation but with a large hysteresis. A discontinuity in the EOS for GaN nanowires was found in the pressure region of 11 – 20 GPa. These abnormal pressure behaviors of GaN nanowires were compared with those obtained in previous high pressure studies of bulk and nanocrytalline GaN and can be attributed to the nano-size and morphology-dependent thermodynamic and kinetic properties of the GaN nanowires with the additional complication of the nonhydrostatic conditions.

6.5 References

(1) Nakamura, S.; Senoh, M.; Nagahama, S.; Iwasa, N.; Yamada, T.; Matsushita, T.; Sugimoto, Y.; Kiyoku, H. *Appl. Phys. Lett.* **1997**, *70*, 1417.

(2) Liu, Z. X.; Goni, A. R.; Syassen, K.; Siegle, H.; Thomsen, C.; Schottker, B.; As, D. J.; Schikora, D. *J. Appl. Phys.* **1999**, *86*, 929.

(3) Munoz, A.; Kunc, K. *Phys. Rev. B* **1991**, *44*, 10372.

(4) Perlin, P.; Jauberthiecarillon, C.; Itie, J. P.; Miguel, A. S.; Grzegory, I.; Polian, A. *Phys. Rev. B* **1992**, *45*, 83.

(5) Xia, H.; Xia, Q.; Ruoff, A. L. *Phys. Rev. B* **1993**, *47*, 12925.

(6) Pandey, R.; Jaffe, J. E.; Harrison, N. M. *J. Phys. Chem. Solids* **1994**, *55*, 1357.

(7) Ueno, M.; Yoshida, M.; Onodera, A.; Shimomura, O.; Takemura, K. *Phys. Rev. B* **1994**, *49*, 14.

(8) Cui, Q.; Pan, Y.; Zhang, W.; Wang, X.; Zhang, J.; Cui, T.; Xie, Y.; Liu, J.; Zou, G. *J. Phys.-Condes. Matter* **2002**, *14*, 11041.

(9) Jorgensen, J. E.; Jakobsen, J. M.; Jiang, J. Z.; Gerward, L.; Olsen, J. S. *J. Appl. Crystallogr.* **2003**, *36*, 920.

(10) Saib, S.; Bouarissa, N. *Physica B: Condensed Matter* **2007**, *387*, 377.

(11) Xiao, H. Y.; Gao, F.; Wang, L. M.; Zu, X. T.; Zhang, Y.; Weber, W. J. *Appl. Phys. Lett.* **2008**, *92*, 241909.

(12) Halsall, M. P.; Harmer, P.; Parbrook, P. J.; Henley, S. J. *Phys. Rev. B* **2004**, *69*.

(13) Cai, J.; Chen, N. X. *Phys. Rev. B* **2007**, *75*, 134109.

(14) Abu-Jafar, M.; Al-Sharif, A. I.; Qteish, A. *Solid State Commun.* **2000**, *116*, 389.

(15) Pandey, R.; Causa, M.; Harrison, N. M.; Seel, M. *J. Phys.-Condes. Matter* **1996**, *8*, 3993.

(16) Serrano, J.; Rubio, A.; Hernandez, E.; Munoz, A.; Mujica, A. *Phys. Rev. B* **2000**, *62*, 16612.

(17) Mujica, A.; Rubio, A.; Munoz, A.; Needs, R. J. *Rev. Mod. Phys.* **2003**, *75*, 863.

(18) Liu, J.; Meng, X. M.; Jiang, Y.; Lee, C. S.; Bello, I.; Lee, S. T. *Appl. Phys. Lett.* **2003**, *83*, 4241.

(19) Zhou, X. T.; Sham, T. K.; Shan, Y. Y.; Duan, X. F.; Lee, S. T.; Rosenberg, R. A. *J. Appl. Phys.* **2005**, *97*, 104315.

(20) Qian, F.; Gradecak, S.; Li, Y.; Wen, C. Y.; Lieber, C. M. *Nano Lett.* **2005**, *5*, 2287.

(21) Dong, Z.; Song, Y. *Chem. Phys. Lett.* **2009**, *480*, 90.

(22) Dong, Z.; Song, Y. *J. Phys. Chem. C*, **2010**, *114*, 1782.

(23) Wang, Z. W.; Tait, K.; Zhao, Y. S.; Schiferl, D.; Zha, C. S.; Uchida, H.; Downs, R. T. *J. Phys. Chem. B* **2004**, *108*, 11506.

(24) Wang, Z. W.; Zhao, Y. S.; Schiferl, D.; Zha, C. S.; Downs, R. T. *Appl. Phys. Lett.* **2004**, *85*, 124.

(25) Klotz, S.; Chervin, J. C.; Munsch, P.; Le Marchand, G. *J. Phys. D: Appl. Phys.* **2009**, *42*, 075413.

(26) Chervin, J. C.; Canny, B.; Besson, J. M.; Pruzan, P. *Rev. Sci. Instrum.* **1995**, *66*, 2595.

Chapter 7 Pressure-Induced Structural Transformations of Anatase TiO_2 Nanowires by Raman Spectroscopy and Synchrotron X-ray Diffraction

7.1 Introduction

Titanium dioxide (TiO_2), or titania, is a well known semiconductor with a wide band gap. At ambient condition, it has rich structures (as seen in Fig. 7.1), such as rutile (space group $P4_2$/mnm), anatase (space group $I4_1$/amd), brookite (space group *P*bca), and α-PbO_2 (space group *P*bcn). Accordingly, TiO_2 has versatile physical and chemical properties, and is extensively used in high efficiency solar cells,[1,2] photocatalysis,[3] and super-hard materials,[4] etc. However, specific to a particular application, the preferred structure is different. For instance, anatase TiO_2 is found to be more active than rutile in photocatalysis applications,[5] but rutile TiO_2 possesses better photo-absorption property in the visible light range.[6] Nanostructured TiO_2 has demonstrated improved performance in photocatalysis, electrochemistry, and photovoltaic.[7,8] Especially for photocatalysis applications, superior properties have been obtained in one dimensional (1D) nanostructured TiO_2 such as nanowires, nanofibers and nanoribbons.[9-12]

With the development of synthetic techniques of nanomaterials, such as chemical vapor deposition (CVD), electrochemistry, and hydrothermal methods, etc., TiO_2 nanomaterials of various morphologies (e.g., nanoparticles, nanoribbon, nanowires and nanotubes) have been synthesized successfully.[11,13-19] In addition to tuning structures and morphology of nanomaterials via these well established synthetic routes, high pressure provides an external driving force to produce new structures. Thus, exploring new structures with the means of high pressure has received increasing attentions. To date, pressure-induced structural transformations have been observed in many nanomaterials (i.e., ZnS,[20] CdSe[21,22] and CeO_2[23], etc.). Additionally, our previous studies of 1D nanostructured SnO_2,[24] BN[25] and GaN[26] suggest that pressure can be also used to tune the morphology. Therefore, bulk TiO_2 as well as its corresponding nanomaterials has been extensively investigated under high pressure both experimentally and theoretically.[27-37]

Among the various structures of TiO_2, anatase and rutile are the most promising phases in advanced technical applications. Therefore, most high-pressure studies are carried out on TiO_2 in either anatase or rutile phase. The early high-pressure study of anatase TiO_2 showed that a new phase was formed at ~ 4.3 GPa using Raman spectroscopy, but without identifying its crystal structure.[30] Later, X-ray diffraction investigations demonstrated that this new high-pressure phase had an α-PbO_2 type structure.[28] So far, it has been well known that bulk TiO_2 undergoes a phase transition sequence from either anatase or rutile phase to α-PbO_2 phase, and then to baddeleyite phase (space group $P2_1/c$) under high pressure.[27-34] However, this phase transition sequence was not applicable to nanostructured TiO_2. For instance, the α-PbO_2 type phase was observed missing from the compression in TiO_2 nanoparticles, which was obtained later upon decompression.[27,36,37]

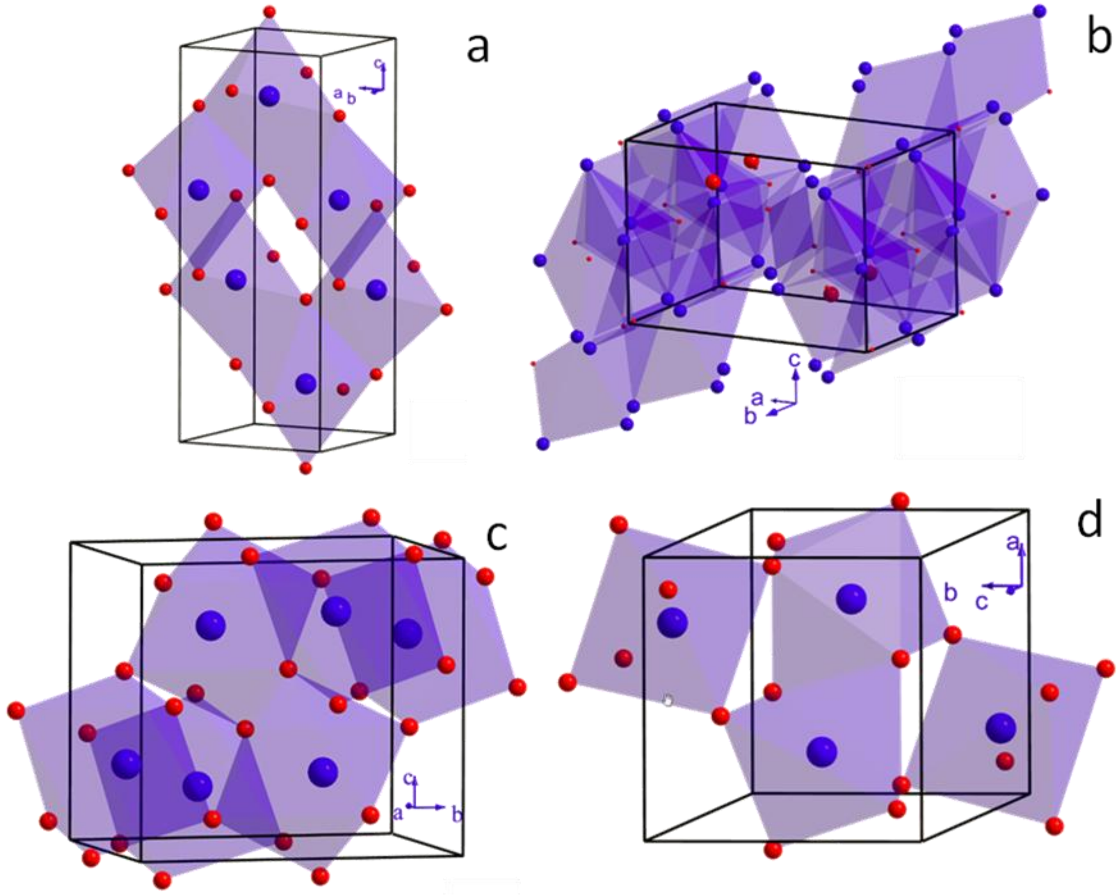

Figure 7.1 Crystal structures of TiO_2. a: anatase phase (space group $I4_1$/amd); b: TiO_2-B phase (space group $P2_1$/m); c: α-PbO_2 phase (space group *P*bcn).; d: baddeleyite phase (space group $P2_1$/c). The red and blue balls stand for the O atoms and Ti atoms, respectively.

Although TiO_2 nanoparticles have been studied extensively under high pressure, their high-pressure behaviors, in terms of phase transition pressure, compressibility and phase stability are variable. For instance, both crystalline phase to crystalline phase transition and pressure-induced amorphization were observed in TiO_2 nanoparticles under high pressure.[27,34,36-38] Such a large discrepancy was believed due to the variation in the grain size of the nanoparticles. Thus, several systematic studies were carried out focusing on the size effect on high-pressure behaviors of TiO_2 nanoparticles. Swamy *et al.* reported a critical size of 10 nm existing in TiO_2 nanoparticles.[38] When the particle size is larger than the critical size, the nanoparticles will undergo the anatase to baddeleyite phase transition directly; otherwise pressure-induced amorphization will occur. Besides the particle size, morphology also plays an important role in affecting the high-pressure behaviors of nanomaterials, especially in 1D nanomaterials.[24-26] However, in contrast to the extensive investigations of TiO_2 nanoparticles, TiO_2 nanowires were sparsely investigated under high pressure.

In this work, a comparative high-pressure study was carried out on anatase TiO_2 nanowires with various widths using *in-situ* Raman spectroscopy and synchrotron X-ray diffraction. Through this study, we attempt to understand the size- and morphology-effect on high-pressure behaviors of TiO_2 nanowires. In addition to our previous studies of other 1D inorganic materials, the pressure-morphology tuning effect was further investigated, which could shed a new light in searching for new structures and properties.

7.2 Experimental section

TiO_2 nanowires were prepared using the hydrothermal method.[15,18] Commercial anatase TiO_2 nanoparticles with a size of ~ 25 nm were used as the starting material. In a typical preparation procedure, 1 g of TiO_2 white powders was placed into a Teflon-lined bottle with a capacity of 60 ml. Then, the Teflon bottle was filled with 40 ml NaOH aqueous solution with the molarities varied from 10 M to 11 M, and then sealed into a stainless steel autoclave and maintained at a temperature of 200 °C for 24 h without shaking or stirring. After the autoclave was naturally cooled to room temperature, the obtained samples were sequentially washed with diluted HCl aqueous solution, deionized water, and anhydrous ethanol alternatively until pH = ~ 7. The after-washed samples were dried at 70 °C for 6 h in air atmosphere, at which step the obtained products were white soft fibrous powder. Finally, the obtained samples were post-heated in air atmosphere at 650 °C for 2 h.

Microstructures of the as-synthesized samples were examined by SEM/EDX (Leo-Zeiss 1540XB FIB/SEM). The crystal structures of the as synthesized products were examined by X-ray diffraction on a Rigaku diffractometer equipped with a graphite monochromator using Co Kα radiation ($\lambda = 1.7902$ Å).

The diamond anvil cell used in this study has a pair of type I diamonds with a 250 μm culet. A hole with a diameter of 80 μm was drilled on a stainless steel gasket and used as the sample chamber. Silicone oil was used as the pressure transmitting medium (PTM) for Raman measurements, whereas neon gas was loaded as the PTM for X-ray diffraction measurements.

Raman experiments were carried out using a customized micro-Raman spectroscopy system in the Song laboratory. The wavelength of the laser was 488 nm. *In-situ* angle-dispersive X-ray diffraction measurements were carried out at room temperature at the 16ID-B beamline at the Advanced Photon Source. The incident wavelength of the monochromatic beam was 0.3980 Å. Detailed information regarding to the instruments can be found in Chapter 2.

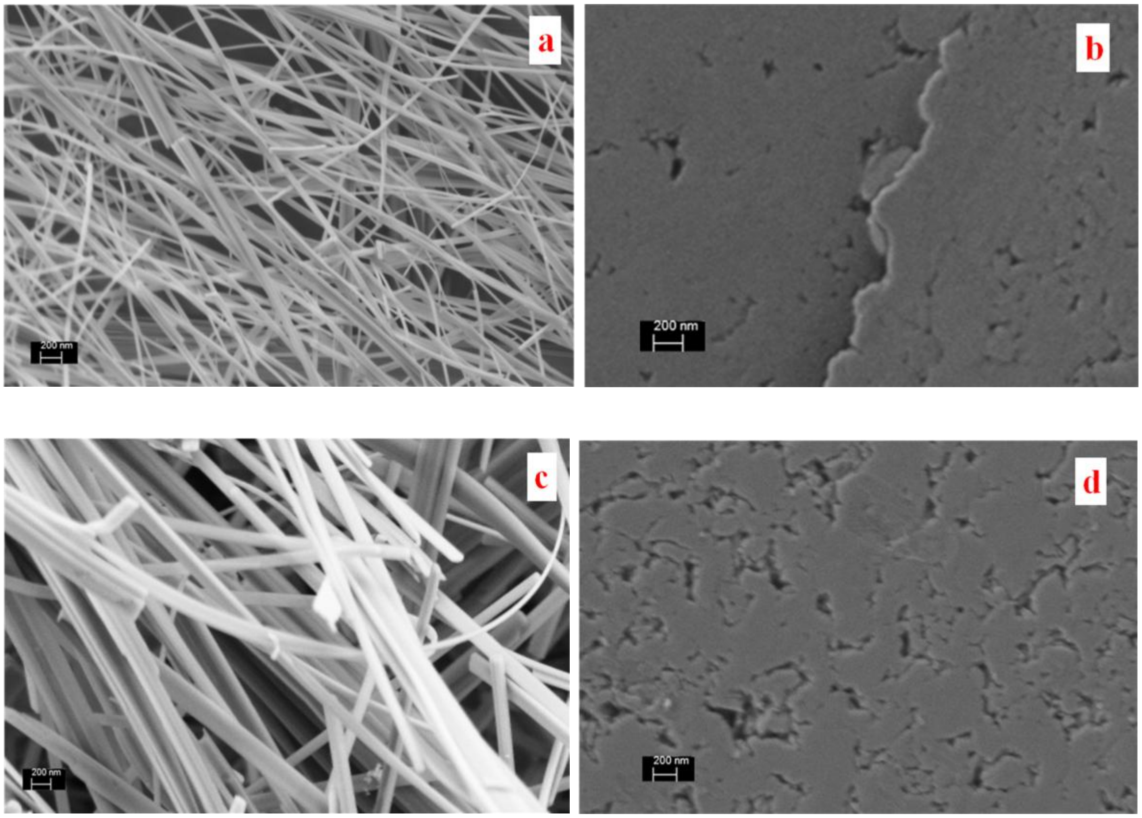

Figure 7.2 SEM images of TiO_2 nanowires taken before (a and b) and after (c and d) compression. a and b are SEM images for NW1, while c and d are the SEM images for NW2.

7.3 Results and discussion

7.3.1 Characterization of TiO_2 nanowires

SEM images of two as synthesized TiO_2 nanowires, NW1 and NW2, were shown in Fig. 7.2 a and c, which suggested NW1 and NW2 had distinctive widths of 50 – 100 nm and 150 – 250 nm, respectively. Lengths for both samples were estimated to be 10 – 12 μm. The anatase phase of TiO_2 has a space group of D_{4h}^{19} ($I4_1$/amd, $Z=2$). According to the factor group analysis, 15 optical modes with the following irreducible representation of normal vibrations were predicted: $1A_{1g} + 1A_{1u} + 2B_{1g} + 1B_{2u} + 3E_g + 2E_u$, among which six modes (A_{1g}+$2B_{1g}$+$3E_g$) were Raman-active and three modes (A_{1u}+$2E_u$) were infrared-active.[30]

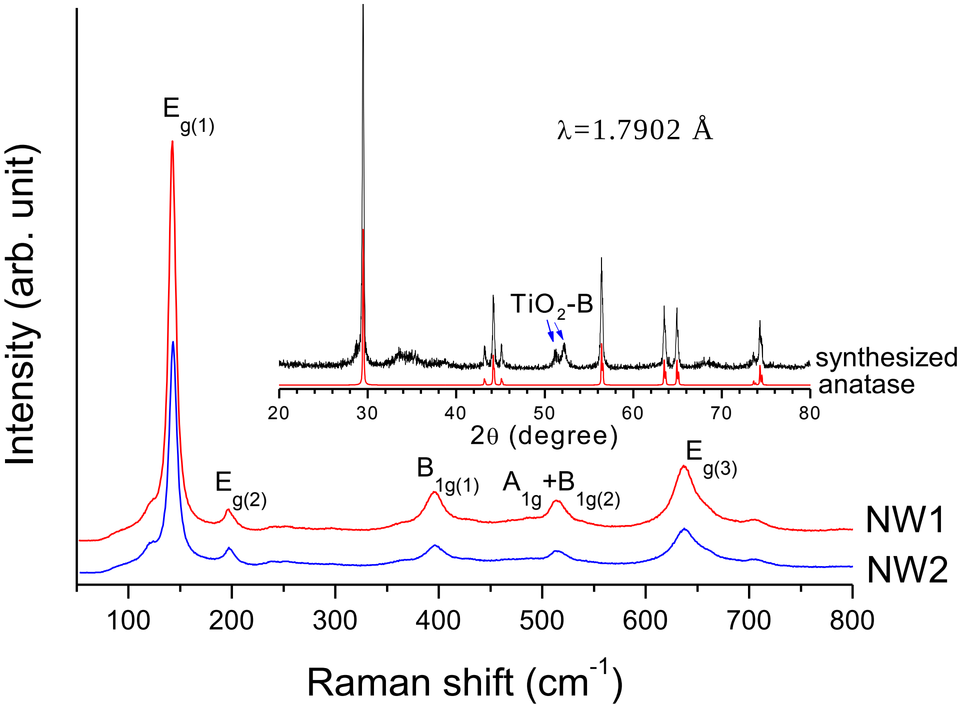

Figure 7.3 Raman spectra for as-made TiO$_2$ nanowires collected at ambient condition. Spectra a and b represent NW1 and NW2, respectively. All the Raman peaks are assigned to the anatase phase and labeled according to Ref. 33. The inset is the representative XRD pattern (black color) of synthesized TiO$_2$ nanowires in comparsion with standard XRD pattern of anatase TiO$_2$ (red color).

Raman spectra for both products, as seen in Fig. 7.3, contained 5 Raman peaks, which were assigned to $E_{g(1)}$ (143 cm^{-1}), $E_{g(2)}$ (197 cm^{-1}), $B_{1g(1)}$ (396 cm^{-1}), A_{1g} + $B_{1g(2)}$ (515 cm^{-1}) and $E_{g(3)}$ (639 cm^{-1}), respectively, consistent with the anatase phase. The numbers labeled in the brackets of the subscripts were used for distinguishing peaks with the same Raman mode. Compared to bulk TiO_2, the Raman peaks shifted to higher frequency (as listed in Table 7.1), which might be due to the deviations from the stoichiometry known to affect both Raman peak positions and bandwidths.[39] Furthermore, the typical powder X-ray diffraction pattern (inset of Fig. 7.3) also confirmed the synthesized products were in the anatase phase with minor TiO_2-B (space group $P2_1/m$).

7.3.2 Raman results of NW1 upon compression and decompression

Selected Raman spectra of NW1 collected upon compression at a pressure of up to 36.7 GPa were shown in Fig. 7.4. Upon compression, all the Raman modes shifted to higher frequencies except for the $E_{g(2)}$ mode, which exhibited a red shift before its disappearance at 6 GPa. The anatase phase persisted to 12.3 GPa indicated by the consistent assignment of all the characteristic Raman modes of the anatase phase. Beyond 12.3 GPa, new Raman peaks at 214, 244, 313, 459 and 491 cm^{-1} were observed, denoting the onset of a phase transition. Compression beyond 12.3 GPa resulted in the reduced intensity of all the Raman peaks associated with the anatase phase. These Raman peaks were depleted above 19.9 GPa, indicating the completion of the phase transition. As listed in Table 7.1, the Raman peaks of the observed high-pressure phase were consistent with those of the baddeleyite phase,[31,32] suggesting the structure of the new phase. In contrast to bulk TiO_2, the α-PbO_2 phase was missing from compression. At 36.7 GPa, the Raman profile was significantly broadened but characteristic Raman peaks of baddeleyite phase, such as peaks originally appeared at 244 and 491 cm^{-1}, can still be identified, which suggested pressure-induced disorder occurred instead of pressure-induced amorphization.

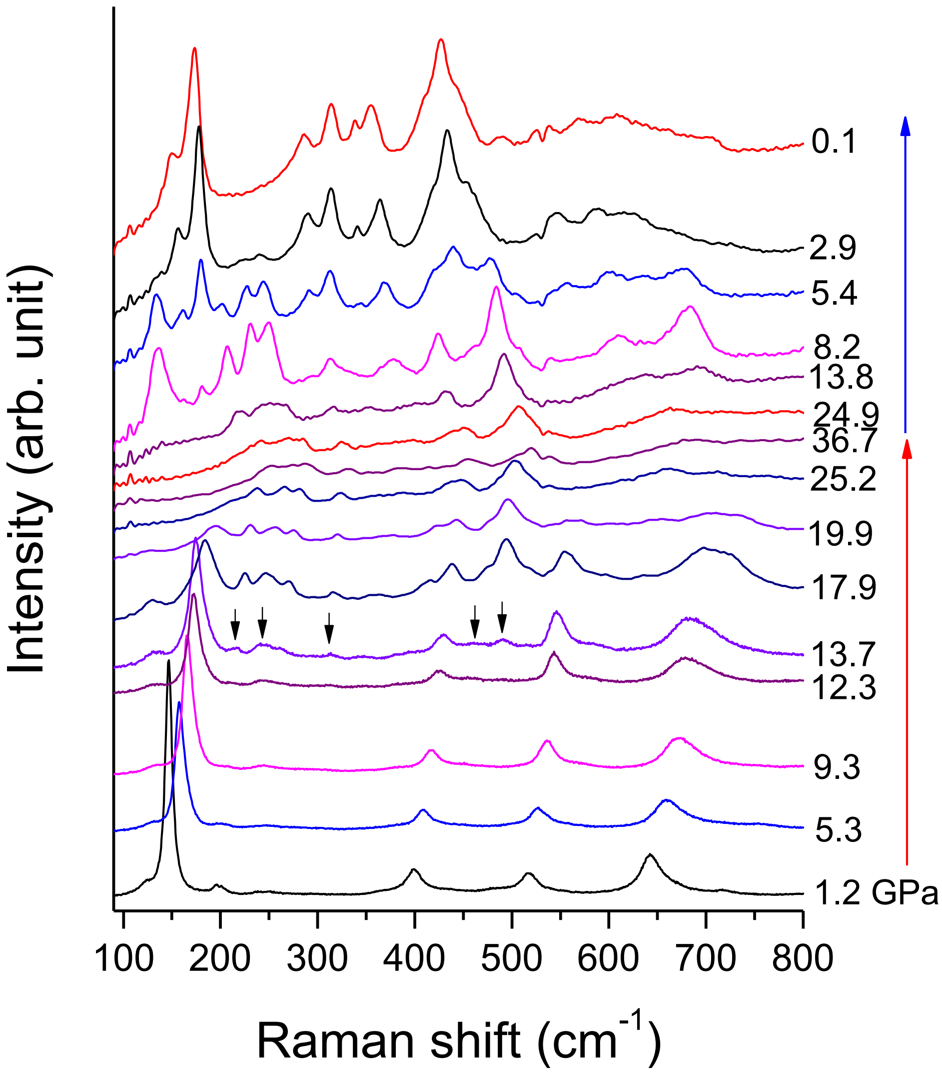

Figure 7.4 Selected Raman spectra for NW1 upon compression and decompression. Pressures in GPa are labeled for each spectrum. The red and blue arrows indicate the compression and decompression sequence, respectively. The black arrows represent new Raman peaks of the new phase. All the spectra are offset vertically for clarity.

Table 7.1 Raman shift (cm^{-1}) for TiO_2 nanowires for phases involved upon compression and decompression (anatase, baddeleyite and α-PbO_2 phase) in comparison with references.

anatase phase				baddeleyite phase				α-PbO_2 phase			
Raman modes	bulk1[a]	this work[c]		reference		this work[d]		reference		this work[e]	
		NW1	NW2	bulk1[a]	bulk2[b]	NW1	NW2	bulk1[a]	bulk2[b]	NW1	NW2
$E_{g(1)}$	137.8	142.4	143.1	209.6	206	204.4	203.7		128		108.7
$E_{g(2)}$	193.2	196.6	196.9	218.7		213.6	218.7	145.3	152	150.4	150.6
$B_{1g(1)}$	392.6	395.9	396.9	238.1	237	234.5	237.4		170*		
$A_{1g}+B_{1g(2)}$	513.7	514.5	514.9	266.0	266	261.1	262.2	169.4	171	173.0	174.0
$E_{g(3)}$	635.6	638.5	639.4	283.4	281	279.4	282.0		214		
				325.5	323	321.5	325.0		269*	265.3*	
					375			283.4	285	285.9	286.8
				393.4	385	381.2		310.9	314	313.9	314.1
				439.3	435	432.8	430.5	335.2	339	338.6	338.2
				455.0	448	444.9	440.2	351.9	358	354.0	354.9
				492.0		482.8*	485.7*	406.7		408.3*	405.3*
				501.2	502	497.9	503.0	424.0	426	426.8	427.4
				527.6	562	539.0	540.0	440.9	443*	445.6*	451.5*
				670.5	658	651.1	658.8				486.6
				726.6	714	710.6	710.2	528.0	531	538.4	537.8
				767.2	737			567.4	570	568.4	570.3
								609.1	602	608.1	609.9
									811		664.2

[a] Ref. 32. [b] Ref. 31.

[c] Spectra taken at ambient condition.

[d] Spectra taken at 19.9 GPa and 23.8 GPa upon compression for NW1 and NW2, respectively.

[e] Spectra taken after pressure was completely released.

* Shoulder peaks.

The reversibility of pressure effect on crystal structures provides important information on transformation mechanism. Therefore, after compressed to 36.7 GPa, Raman measurements of NW1 were also conducted upon decompression (Fig. 7.4). In general, intensity of all the Raman peaks increased gradually as the pressure was releasing. At 8.2 GPa, the appearance of new peaks at 180 and 376 cm^{-1} indicated a phase transition occurred. Compared to the compression data in the entire pressure region, these new peaks were different from either the anatase phase or the baddeleyite phase, implying a new structure formed upon decompression. Below 2.9 GPa, Raman peaks associated with baddeleyite phase were completely suppressed, indicating the baddeleyite phase was a meta-stable phase and was only stable under high pressure (e.g., > 2.9 GPa). The new phase was quenched to ambient condition. This new phase was the α-PbO_2 phase which was bypassed during compression, because all the Raman peaks observed at the near ambient pressure were consistent with those of α-PbO_2 phase as listed in Table 7.1.[27-34] Upon decompression, no Raman peak of anatase phase was retrieved suggesting that the anatase to baddeleyite phase transition was irreversible. Morphology of the recovered sample was also examined. As can be seen in Fig. 7.2 b, the nanowires were significantly altered with no wire shape preserved. Such an alternation of the morphology further supported that the phase transformation observed upon compression was irreversible.

7.3.3 Raman results of NW2 upon compression and decompression

In order to investigate the size effect on high-pressure behaviors of TiO_2 nanowire, NW2, which had a larger width of 150 – 250 nm, was also studied under high pressure. The selected Raman spectra upon compression and decompression were depicted in Fig. 7.5. Upon compression, pressure-induced blue shifts for all the Raman modes were observed including the $E_{g\ (2)}$ mode which exhibited a red shift in NW1. At 10.9 GPa, several weak peaks appeared at 242, 313, 445 and 491 cm^{-1}, characteristic of the baddeleyite phase denoting the occurrence of the anatase to baddeleyite phase transition. Upon further compression, these weak peaks, especially the peak at 491 cm^{-1}, were clearly discerned at pressure of 14.0 GPa and beyond. The phase transformation completed at 23.8 GPa, illustrated by the depletion of all the characteristic Raman peaks associated with anatase phase. A significantly broadened Raman profile, similar to that of NW1 at 36.7 GPa, was observed at 29.9 GPa, further supported that the high-pressure baddeleyite phase was disordered.

During decompression, intensity of all Raman peaks became intense. The baddeleyite to α-PbO_2 phase transformation was observed to start at 10.7 GPa and to complete at 3.5 GPa, indicated by the apparent change of Raman profiles. The recovered sample was in the pure α-PbO_2 phase, since all the remained Raman peaks were consistent with those for α-PbO_2 phase (Table 7.1). The SEM image (Fig. 7.2d) of the recovered NW2 illustrated a similar morphology as the recovered sample of NW1, which indicated that the phase transition was irreversible regardless of the size.

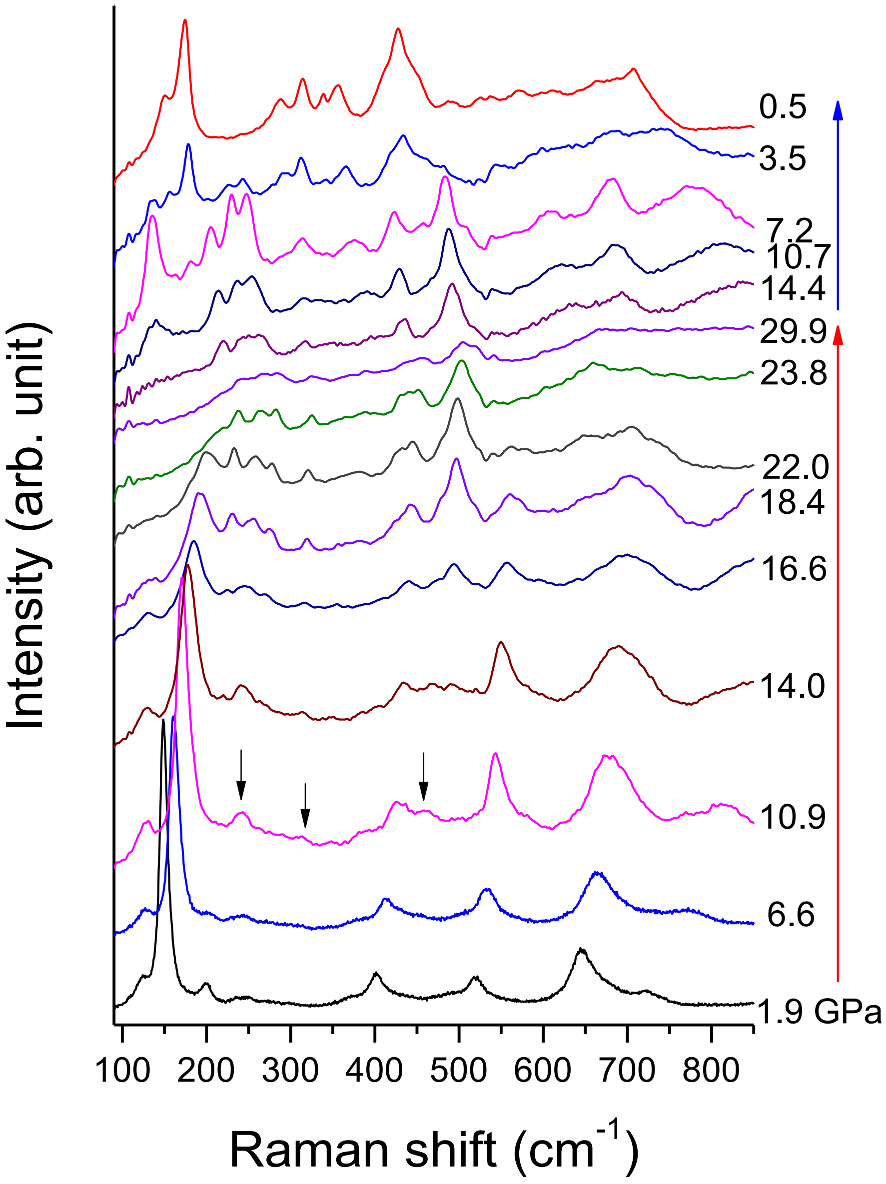

Figure 7.5 **Selected Raman spectra for NW2 upon compression and decompression. Pressures in GPa are labeled for each spectrum. The red and blue arrows indicate the compression and decompression sequence, respectively. The black arrows represent new Raman peaks of the new phase. All the spectra are offset vertically for clarity.**

7.3.4 X-ray diffraction results of NW1 and NW2

In-situ high-pressure X-ray diffraction measurements were performed on NW1 and NW2 upon compression up to 33 GPa. Representative diffraction patterns were depicted in Fig. 7.6. As mentioned before, both NW1 and NW2 were in the anatase structure with minor TiO_2-B phase. As seen in Fig. 7.6, when the pressure was increased to 13.3 GPa, NW1 was still in the same phases as its starting phase, since all the prominent reflections can be indexed to the anatase and TiO_2-B. In contrast, at 12.6 GPa, two reflections, (1 1 -1) and (1 1 1), associated with the baddeleyite phase were already observed in NW2, suggesting the baddeleyite phase formed at a relative lower pressure in NW2 than in NW1, consistent with our Raman results. At the highest pressures of 33.3 and 32.3 GPa, the baddeleyite phase became the main phase for both samples as almost all the reflections were indexed with the baddeleyite structure. However, reflections for both samples were significantly broadened, indicating the poor crystallinity of the high-pressure phase. However, reflections of the baddeleyite phase could still be discernible, suggesting the samples were still in a crystalline phase instead of an amorphous phase. It was noticed that the starting materials contained the TiO_2-B impurity, which was no longer observed in the high-pressure phase. Liu *et al.* reported that TiO_2-B nanoribbon underwent a pressure-induced amorphization at 13.6 GPa.[40] Therefore, it is possible that the TiO_2-B phase transformed to an amorphous phase at the highest pressures achieved in this study.

Table 7.2 Summary of the results of high-pressure studies of anatase TiO_2

starting TiO_2		phase transitions pressure (GPa)				bulk modulus (GPa)		
morphology	**size (nm)**	**anatase to α-PbO_2 type**	**α-PbO_2 type to baddeleyite**	**anatase to baddeleyite**	**anatase to amorphous**	**anatase phase**	**baddeleyite phase**	**technique**
Bulk	> 100 μm	4.3 – 4.6[a]						Raman
		~ 5[b]	12 – 15					
		5.4[c]	~ 10			59 (5)	522 (28)	XRD
		4.5 – 7[d]	13 – 17					Raman
		4.5[e]	~ 13			179	290	XRD
Nano -particles	4[f]				> 24			Raman
	8[f]				> 21			Raman
	7 – 11[g]				> 24			Raman
	12[b]			~ 18				Raman
	20[f]			15 – 16				Raman
	32[f]			11 – 15				Raman
	30 – 34[e]			18 – 20		243 (3)		XRD
Nanowire [h]	50 – 100			~ 14		266.5	127.8	Raman & XRD
	150 – 250			~ 9		188.3	114.8	

[a] Ref. 32. [b] Ref. 27. [c] Ref. 28. [d] Ref. 32. [e] Ref. 34. [f] Ref. 38. [g] Ref. 44. [e] Ref. 38. [h] this work.

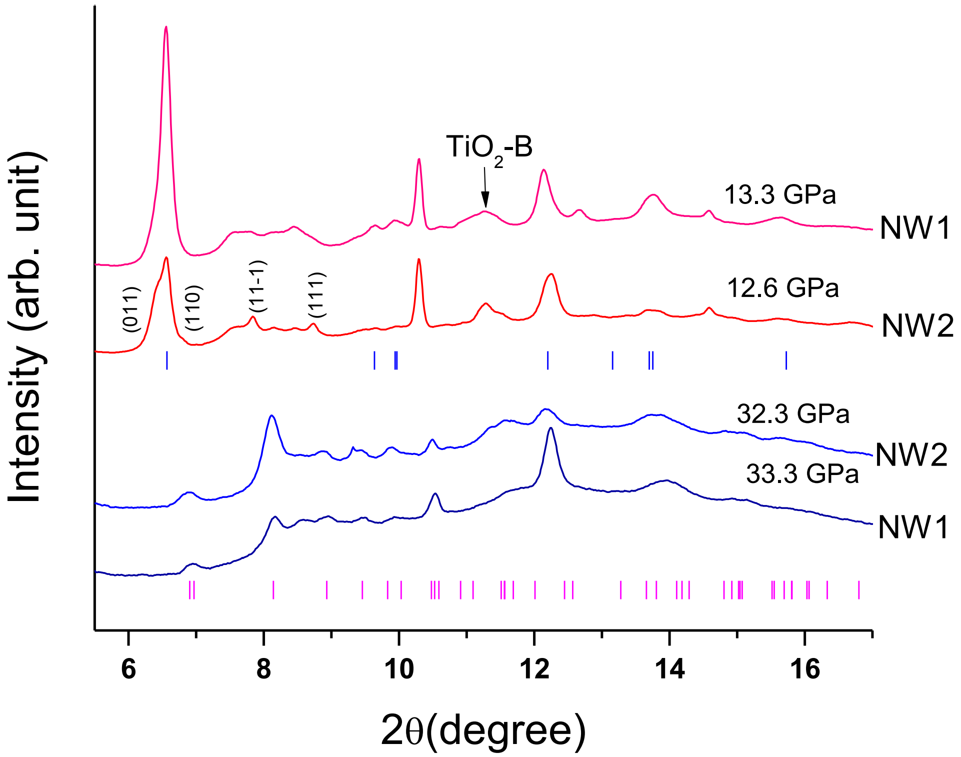

Figure 7.6 Representative X-ray diffraction patterns for NW1 in comparison with NW2 at similar pressures. The vertical bars in magenta color represent for the indexing of baddeleyite phase, while the blue vertical bars represent the indexing for anatase phase. Miller indices for reflections of baddeleyite phase are also labeled for the X-ray pattern at 12.6 GPa.

7.3.5 Discussion

Upon compression, a phase transformation sequence of anatase to α-PbO_2 phase, and then to baddeleyite phase has been well documented in the bulk TiO_2.[27-34] In this study, however, the α-PbO_2 phase was bypassed in both nanowires. The same scenario was also observed in TiO_2 nanocrystals.[27,36,37] There were several attempts to explain why α-PbO_2

was hindered in TiO_2 nanoparticles.[27,36,37] According to the interpretations in the references,[27,36,37] the missing α-PbO_2 phase in nanocrystals might be due to the increased surface energy of nanocrystals comparing to their bulk counterparts. Thus, the missing of the α-PbO_2 phase during the compression in NW1 and NW2 suggested both samples had higher surface energy than their corresponding bulk materials.

The pressure dependences of characteristic Raman modes of NW1 and NW2 were plotted in Fig. 7.7. It clearly showed that the anatase to baddeleyite phase transition occurred in NW1 at 13 GPa, which was significantly enhanced in contrast to the phase transition pressure of 9 GPa in NW2. Similar size-induced enhancement of the phase transition pressure was also observed in other nanomaterials, such as nanocrystals (e.g., CdSe,[22] ZnS[20] and PbS[41]), as well as 1D nanomaterials (e.g., GaN nanowires,[26] SnO_2 nanowires and nanobelts,[24] ZnO nanotubes[42] and BN nanotubes[25]). However, some oxide nanocrystals, such as CeO_2[23] and γ-Fe_2O_3[43], exhibited reduced transition pressures. In general, such variations of transition pressure were due to the competition between the volume collapse and surface energy difference which contributed most to the change of Gibbs free energy. [24,43,44] In NW1and NW2, the unit cell volume were found to be reduced by 14.2% and 13.5%, respectively, at the transition pressures. Thus the volume collapse ratio between these two nanowires can be negligible within the experimental tolerance. Therefore, the surface energy difference became the main factor that contributed to the different transition pressures of NW1 and NW2. In addition, increasing surface energy leaded to an enhanced transition pressure.[24,43,44] In this study, the transition pressure observed in NW1 was higher than NW2. Therefore, we speculated the surface energy of NW1 was higher than that of NW2.

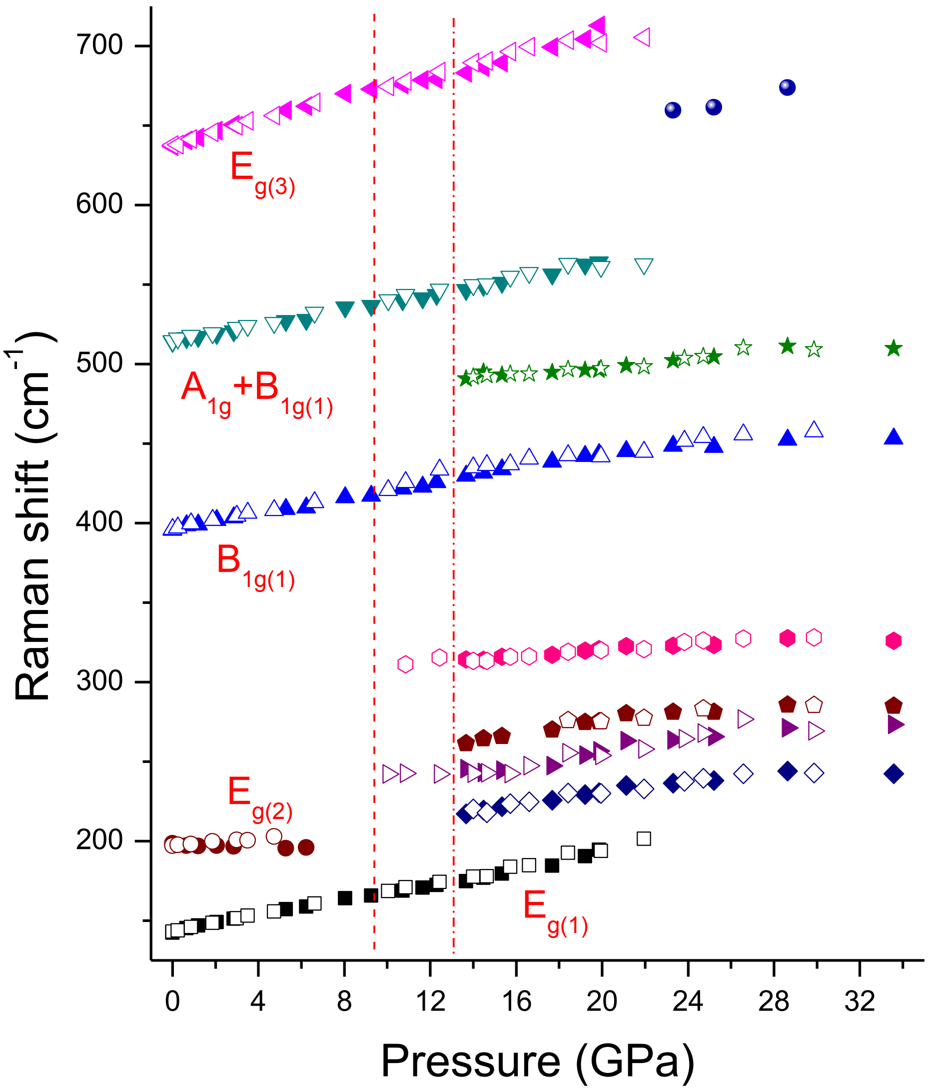

Figure 7.7 Pressure dependence of the Raman modes for NW1 and NW2 upon compression. The solid symbols stand for data points obtained in NW1, while the open symbols represent those for NW2. The dash-dotted and dashed lines suggest the phase transition boundaries for NW1 and NW2, respectively. Raman modes with assignment labeled besides.

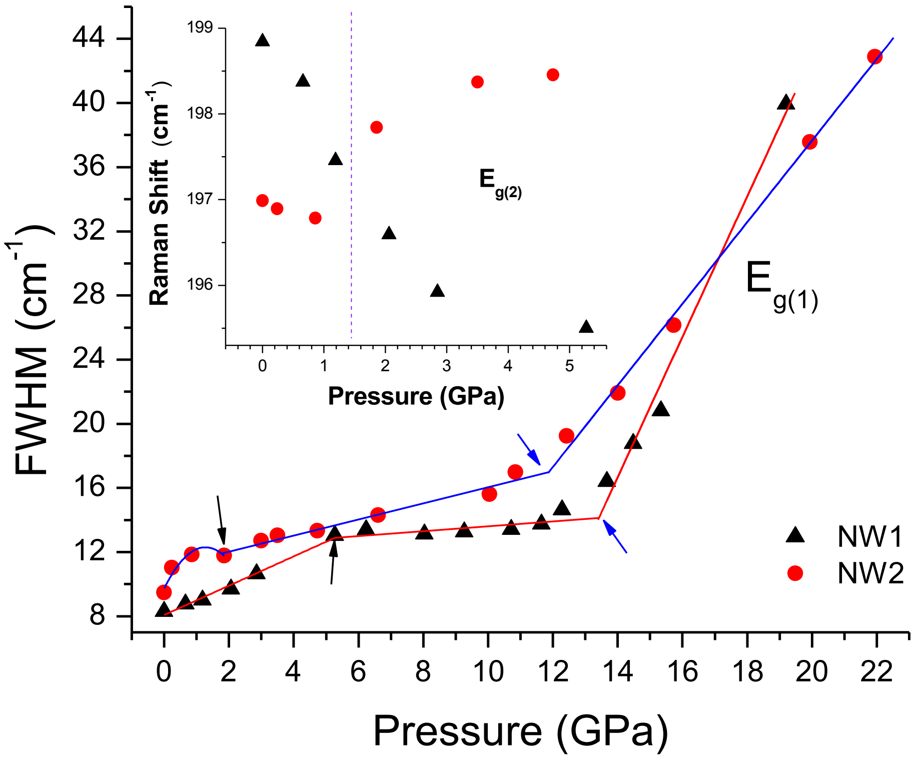

Figure 7.8 FWHM of Raman mode *E*$_{g(1)}$ as a function of pressure for NW1 and NW2. Solid triangle and circle symbols represent data for NW1 and NW2, respectively. The solid lines are only for eye guidance. Arrows indicate the first (*P*$_1$: black) and second (*P*$_2$: blue) turning points for each TiO$_2$ nanowires. The inset is the pressure dependence of *E*$_{g(2)}$ Raman mode for NW1 and NW2. Size of the symbols indicates the error bar for each data point.

For both samples, as shown in Fig. 7.7, all the Raman modes shifted to higher frequencies upon compression, except for the *E*$_{g(2)}$ mode of NW1 which exhibited a red shift with a negative slope of -0.38 cm^{-1}/GPa. Differing from NW1, this *E*$_{g(2)}$ mode for NW2 firstly exhibited a red shift below 2 GPa and then blue shift before its disappearance at ~ 5 GPa (inset of Fig. 7.8). The red shift of the $E_{g(2)}$ mode was believed to be associated with the anatase to α-PbO_2 phase transformation, however, the mechanism was still unclear.[30,33,35] The bandwidth of the most intense $E_{g(1)}$ mode for both samples were plotted in Fig. 7.8 as well. Both samples had two turning points P_1 and P_2. The P_1 and P_2 of NW1, at 6 GPa and 13 GPa, were in coincidence with the disappearance pressure of $E_{g(2)}$ mode and the onset anatase to baddeleyite phase transition pressure, respectively. In NW2, the pressure at P_2 was the same as its phase transition pressure, however, pressure at P_1 corresponded to the pressure where the red shift of the $E_{g(2)}$ mode ended (inset of Fig. 7.8). Both samples had a pressure region in which the $E_{g(2)}$ mode showed a red shift, and missed the α-PbO_2 phase upon compression. As mentioned above, the red shift of the $E_{g(2)}$ mode was highly likely associated with the formation of the α-PbO_2 phase.[30,33,35] Therefore, it was likely that the phase transformation in TiO_2 nanowires followed a three stage process, which involved the competition between formations of the α-PbO_2 phase and baddeleyite phase. At the first stage ($0 – P_1$), where red shift of the $E_{g(2)}$ mode was observed, TiO_2 nanowires followed the anatase to α-PbO_2 phase transition route. However, due to the increased surface energy of nanowires, a higher energy barrier may existed in forming the α-PbO_2 structure, leading to inhibition of the α-PbO_2 phase.[44] Therefore, before the α-PbO_2 phase eventually formed, the baddeleyite phase became the more energetically favored structure and competed with α-PbO_2 phase at the second stage ($P_1 – P_2$). At the third stage ($> P_2$), the phase transformation followed anatase to baddeleyite phase route, where the bandwidth of the $E_{g(1)}$ mode increased much faster than the first two stages.

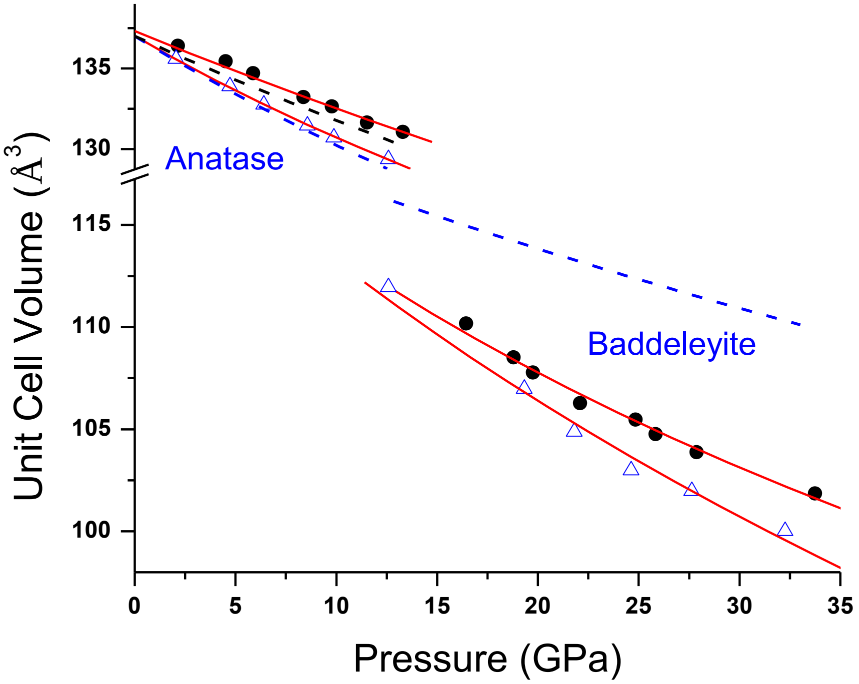

Figure 7.9 Equation of state for anatase and baddeleyite phases in NW1 and NW2 upon compression. The blue dashed line is the equation of state for anatase and baddeleyite phases in bulk TiO_2 accepted from Ref. 28, while the black dashed line is the equation of state for TiO_2 nanocrystals adapted from Ref. 34.

In addition, compressibility for both samples was also examined. The unit cell volumes for anatase and baddeleyite phases of NW1and NW2 were plotted as function of pressure in Fig. 7.9, and their P-V curves were fitted using the third order Birch-Murnaghan equation by fixing the $B_0^{'}$ at 4. The obtained bulk moduli (B_0) were summarized in Table 7.2 in comparison with reference values. The B_0 values of both anatase and baddeleyite phase (266.5 GPa and 127.8 GPa, respectively) for NW1 were higher than those for NW2 (188.3 GPa and 114.8 GPa, respectively). Comparing to TiO_2 nanocrystals and the corresponding counterparts, NW1 had a similar bulk modulus to that for the nanocrystals, while NW2 was close to that for bulk materials. The width of NW2 (150 – 250 nm) approached to the size for bulk materials. Hence, the nano-effect became less prominent and exhibited a similar behavior to its bulk counterpart. Moreover, the impurity in the samples may also contribute to such low bulk moduli. B. Chen's study reported a critical grain size of 15 nm existed in TiO_2 nanoparticles, beyond which bulk modulus increases as the grain size decreases, and versa vice.[45] In this study, the nanowires exhibited an enhanced B_0 as the width of nanowires decreased. Thus, if there was a critical size in TiO_2 nanowires, we speculated that this critical size would be much lower than the widths of our samples.

7.4 Conclusions

Two synthesized TiO_2 samples, NW1 and NW2, were investigated under high pressure using *in-situ* Raman spectroscopy and synchrotron X-ray diffraction. Upon compression, both samples underwent a phase transformation from anatase to baddeleyite phase without via the α-PbO_2 phase. However, the phase transition occurred at a higher pressure of 13 GPa in NW1 than that in NW2 of 9 GPa. Such size induced enhancements of phase transition pressures was understood in parallel with other nanomaterials interpreted by examining the thermodynamical function. Upon decompression, the α-PbO_2 phase missing from the compression was obtained and quenched to ambient condition. Explanation for the inhibition of the α-PbO_2 phase upon compression was also discussed in terms of surface energy. A three stage process was proposed for the possible anatase to baddeleyite phase transformation route. Moreover, compressibility for both anatase and baddeleyite phases was also studied. For the anatase phase, NW2 exhibited a similar behavior as the bulk counterpart, where NW1 behaved more similarly as nanocrystals.

7.5 References

(1) Boercker, J. E.; Enache-Pommer, E.; Aydil, E. S. *Nanotech.* **2008**, *19*, 095604.

(2) Mattesini, M.; de Almeida, J. S.; Dubrovinsky, L.; Dubrovinskaia, N.; Johansson, B.; Ahuja, R. *Phys. Rev. B* **2004**, *70*, 115101.

(3) Lee, J. S.; You, K. H.; Park, C. B. *Adv. Mater.* **2012**, *24*, 1084.

(4) Koci, L.; Kim, D. Y.; de Almeida, J. S.; Mattesini, M.; Isaev, E.; Ahuja, R. *J. Phys.-Condes. Matter* **2008**, *20*, 345218.

(5) Augustynski, J. *Electrochim. Acta* **1993**, *38*, 43.

(6) Yin, S.; Hasegawa, H.; Maeda, D.; Ishitsuka, M.; Sato, T. *J. Photochem. Photobiol. A-Chem.* **2004**, *163*, 1.

(7) Tiwari, J. N.; Tiwari, R. N.; Kim, K. S. *Prog. Mater. Sci.* **2012**, *57*, 724.

(8) Jitputti, J.; Suzuki, Y.; Yoshikawa, S. *Catal. Commun.* **2008**, *9*, 1265.

(9) Liu, B. S.; Nakata, K.; Liu, S. H.; Sakai, M.; Ochiai, T.; Murakami, T.; Takagi, K.; Fujishima, A. *J. Phys. Chem. C* **2012**, *116*, 7471.

(10) Tokudome, H.; Miyauchi, M. *Chem. Commun.* **2004**, *8*, 958.

(11) Zhu, H. Y.; Gao, X. P.; Lan, Y.; Song, D. Y.; Xi, Y. X.; Zhao, J. C. *J. Am. Chem. Soc.* **2004**, *126*, 8380.

(12) Yamabi, S.; Imai, H. *Chem. Mat.* **2002**, *14*, 609.

(13) Wei, M.-D.; Konishi, Y. *Method to produce titanium oxide nanowire structure.* In *Jpn. Kokai Tokkyo Koho* **2006**, pp 8.

(14) Peng, L. M.; Chen, Q.; Du, G. H.; Zhang, S.; Zhou, W. Z. *Nanowires Nanobelts* **2003**, *2*, 157.

(15) Kasuga, T.; Hiramatsu, M.; Hoson, A.; Sekino, T.; Niihara, K. *Langmuir* **1998**, *14*, 3160.

(16) Yuan, Z. Y.; Su, B. L. *Colloid Surf. A-Physicochem. Eng. Asp.* **2004**, *241*, 173.

(17) Pavasupree, S.; Suzuki, Y.; Yoshikawa, S.; Kawahata, R. *J. Solid State Chem.* **2005**, *178*, 3110.

(18) Yoshida, R.; Suzuki, Y.; Yoshikawa, S. *J. Solid State Chem.* **2005**, *178*, 2179.

(19) Uchida, S.; Sanehira, Y.; Chiba, R.; Tomiha, M.; Masaki, N.; Shirai, M. *Proceedings of the International Symposium on Hydrothermal Reactions* **2003**, *57*, 513.

(20) Jiang, J. Z.; Gerward, L.; Frost, D.; Secco, R.; Peyronneau, J.; Olsen, J. S. *J. Appl. Phys.* **1999**, *86*, 6608.

(21) Tolbert, S. H.; Alivisatos, A. P. *Annu. Rev. Phys. Chem.* **1995**, *46*, 595.

(22) Tolbert, S. H.; Alivisatos, A. P. *Science* **1994**, *265*, 373.

(23) Rekhi, S.; Saxena, S. K.; Lazor, P. *J. Appl. Phys.* **2001**, *89*, 2968.

(24) Dong, Z.; Song, Y. *Chem. Phys. Lett.* **2009**, *480*, 90.

(25) Dong, Z.; Song, Y. *J. Phys. Chem. C* **2010**, *114*, 1782.

(26) Dong, Z.; Song, Y. *Appl. Phys. Lett.* **2010**, *96*, 151903.

(27) Hearne, G. R.; Zhao, J.; Dawe, A. M.; Pischedda, V.; Maaza, M.; Nieuwoudt, M. K.; Kibasomba, P.; Nemraoui, O.; Comins, J. D.; Witcomb, M. J. *Phys. Rev. B* **2004**, *70*, 134102.

(28) Haines, J.; Leger, J. M. *Phys. B* **1993**, *192*, 233.

(29) Kurita, S.; Ohta, S.; Sekiya, T. *High Pressure Res.* **2002**, *22*, 319.

(30) Ohsaka, T.; Yamaoka, S.; Shimomura, O. *Solid State Commun.* **1979**, *30*, 345.

(31) Liu, L. G.; Mernagh, T. P. *Eur. J. Mineral.* **1992**, *4*, 45.

(32) Lagarec, K.; Desgreniers, S. *Solid State Commun.* **1995**, *94*, 519.

(33) Sekiya, T.; Ohta, S.; Kamei, S.; Hanakawa, M.; Kurita, S. *J. Phys. Chem. Solids* **2001**, *62*, 717.

(34) Arlt, T.; Bermejo, M.; Blanco, M. A.; Gerward, L.; Jiang, J. Z.; Olsen, J. S.; Recio, J. M. *Phys. Rev. B* **2000**, *61*, 14414.

(35) Sekiya, T.; Okumura, M.; Kurita, S.; Hamaya, N. *High Pressure Res.* **2003**, *23*, 333.

(36) Swamy, V.; Dubrovinsky, L. S.; Dubrovinskaia, N. A.; Langenhorst, F.; Simionovici, A. S.; Drakopoulos, M.; Dmitriev, V.; Weber, H. P. *Solid State Commun.* **2005**, *134*, 541.

(37) Wang, Y. J.; Zhao, Y. S.; Zhang, J. Z.; Xu, H. W.; Wang, L. P.; Luo, S. N.; Daemen, L. L. *J. Phys.-Condes. Matter* **2008**, *20*, 125224.

(38) Swamy, V.; Kuznetsov, A.; Dubrovinsky, L. S.; McMillan, P. F.; Prakapenka, V. B.; Shen, G.; Muddle, B. C. *Phys. Rev. Lett.* **2006**, *96*, 135702.

(39) Parker, J. C.; Siegel, R. W. *Appl. Phys. Lett.* **1990**, *57*, 943.

(40) Li, Q. J.; Liu, B. B.; Wang, L.; Li, D. M.; Liu, R.; Zou, B.; Cui, T.; Zou, G. T.; Meng, Y.; Mao, H. K.; Liu, Z. X.; Liu, J.; Li, J. X. *J. Phys. Chem. Lett.* **2010**, *1*, 309.

(41) Jiang, J. Z.; Gerward, L.; Secco, R.; Frost, D.; Olsen, J. S.; Truckenbrodt, J. *J. Appl. Phys.* **2000**, *87*, 2658.

(42) Dong, Z.; Zhuravlev, K. K.; Morin, S. A.; Li, L.; Jin, S.; Song, Y. *J. Phys. Chem. C* **2012**, *116*, 2102.

(43) Jiang, J. Z.; Olsen, J. S.; Gerward, L.; Morup, S. *Europhys. Lett.* **1998**, *44*, 620.

(44) Wang, Z. W.; Saxena, S. K. *Solid State Commun.* **2001**, *118*, 75.

(45) Chen, B.; Zhang, H.; Dunphy-Guzman, K. A.; Spagnoli, D.; Kruger, M. B.; Muthu, D. V. S.; Kunz, M.; Fakra, S.; Hu, J. Z.; Guo, Q. Z.; Banfield, J. F. *Phys. Rev. B* **2009**, *79*, 125406.

Chapter 8 Pressure-Induced Structural Transformations of ZnO Nanowires Probed by X-ray Diffraction*

8.1 Introduction

As an important wide band gap semiconductor (E_g = 3.37 eV), ZnO has a wide range of applications, such as in piezoelectric transducers, chemical sensors, optical coatings, photovoltaics, and ceramics.[1-3] In contrast to the corresponding bulk counterparts, nanostructured ZnO has enhanced electronic, and photoconducting properties.[4,5] Because of the unique crystal quality and photonic properties, in particular, one dimensional (1D) ZnO nanomaterials have been used as functional units in the fabrication of electronic, piezoelectronic, electrochemical, and highly sensitive gas sensors with nanoscale dimensions.[6-8] Therefore, an increasing research effort has been focused on nanostructured ZnO, especially in exploring new structures, properties, as well as synthetic methods. In addition to the traditional synthetic and fabrication routes, external pressure can provide an alternative effective driving force to tune the structures and thus the properties of the nanostructured materials.[9] Therefore, investigations of the structural and phase transformations of nanomaterials under high pressure represent a prevailing materials research frontier.[10-13] One of the most interesting observations in those studies is that the compressed nanomaterials behave significantly differently than their corresponding bulk counterparts under pressure. For example, our previous studies on 1D nanomaterials (e.g., SnO_2 nanowires and nanobelts,[11] GaN nanowires,[10] and BN

---

[*] The content of this chapter has been published as: Dong Z., Zhuravlev K. K., Morin S., Li L., Jin S., and Song Y., *J. Phys. Chem. C,* **2012**, *116,* 2102.

nanotubes[12]) have demonstrated profound implications for producing controlled structures by combined pressure-morphology tuning.

Under ambient conditions, ZnO has a wurtzite-type (B4) structure (space group $P6_3mc$) regardless of the morphologies.[14-17] The wurtzite phase transforms to a rocksalt-type (B1) phase (space group $Fm\overline{3}m$) upon compression to some certain threshold pressure (e.g., >8.8 GPa).[18] This B4-to-B1 phase transition in ZnO has been extensively investigated using different experimental and theoretical approaches,[13,14,17,19-25] but the transition pressure varies in a broad range depending on the morphology of ZnO as well as other experimental conditions. For instance, it was well-established that the B4-to-B1 phase transition for bulk ZnO takes place at ~ 9 ± 0.2 GPa.[19,23-25] However, the transition pressure for ZnO nanocrystals falls in the broad range from 10.5 to 15.1 GPa as the grain size of the nanocrystals varies from 50 to 12 nm.[13,14,17,20-22]

In contrast to bulk ZnO and nanocrystals, which have been extensively studied, only a few high-pressure studies have been carried out on 1D ZnO so far. Hou *et al.* reported a high-pressure study on ZnO nanotubes showing that the B4-to-B1 phase transition took place at 10.5 GPa, the same as ZnO nanocrystals with a grain size of 50 nm. However, the pressure at which the transformation is completed (i.e., 18.4 GPa)[16] was significantly higher than that for bulk ZnO[18] and ZnO nanocrystals[21] (i.e., 13 and 15 GPa, respectively). In addition, Yan *et al.*[26] examined the doped ZnO nanowires with Raman spectroscopy under high pressures. A phase transformation was claimed between 10.3 and 12.2 GPa, but no detailed structural information was provided. The results of all of these high-pressure studies on nanostructured ZnO are summarized in Table 8.1 together with some representative studies on bulk ZnO.

In this Article, we report the first high-pressure study of ZnO nanowires using the synchrotron X-ray diffraction technique. Starting with laboratory synthesized ZnO nanowires, we compressed the nanomaterials to high pressures of up to 26 GPa, followed by decompression. The quantitative analysis of the diffraction patterns revealed new and interesting structural information that allows for the understanding of the high-pressure behavior of ZnO nanowires as well as the associated transition mechanisms.

8.2 Experimental section

ZnO nanowires were synthesized in a continuous flow reactor by mixing equimolar precursor solutions of $Zn\ (NO_3)_3{\cdot}(H_2O)_6$ and hexamethylenetetramine (HMT) both at a concentration of 100 μM and a temperature of 95 ℃. This catalyst-free growth of nanowires was driven by screw-dislocations,[27] and the detailed apparatus, synthetic procedures, as well as the experimental parameters that control the morphologies of ZnO nanowires have been reported elsewhere.[28] The scanning electron microscope (SEM) images (Fig. 8.1 a) revealed that the ZnO had a very good wire morphology and uniformity with an average length of 3 to 4 μm and width of 50 – 100 nm.

The DAC used in this work had a pair of type-I diamonds with a culet size of 400 μm. A preindented stainless-steel gasket drilled with a 130 μm hole at the center was used as the sample chamber. Neon gas was compressed into the DAC with the sample by a special gas-loading system and was used as the pressure-transmitting medium to maintain the hydrostatic conditions. A motorized gear box was also employed to regulate the pressure with fine increments.

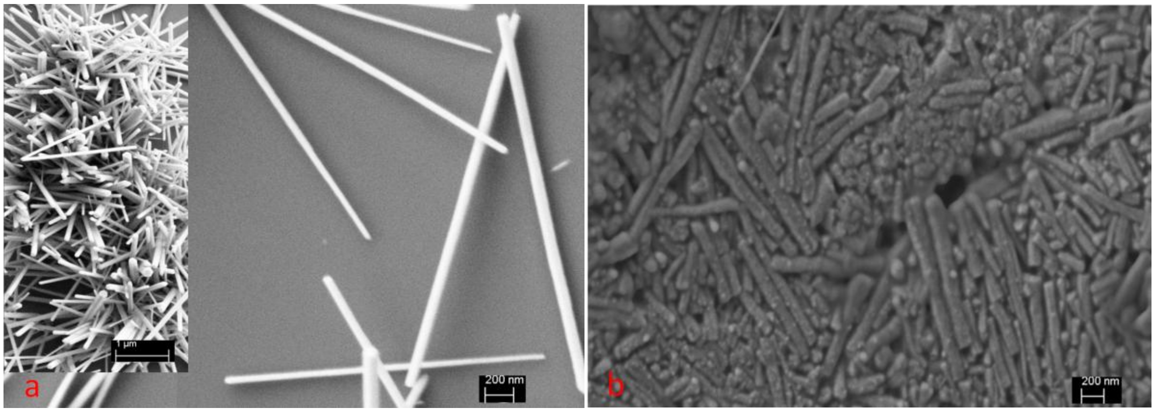

Figure 8.1 SEM images of ZnO nanowires before (a) and after compression (b). The inset of (a) shows a larger scale image of the nanowires.

In-situ angle-dispersive X-ray diffraction measurements were carried out at room temperature using the 16ID-B beamline of the HPCAT at the Advanced Photon Source. The incident wavelength of the monochromatic beam was 0.4072 Å. The exposure time for each XRD pattern was 60 s; then, the 2D Debye-Scherrer diffraction patterns were integrated by using the Fit2D program. A detailed Rietveld analysis was performed using the GSAS package. The XRD experimental setup can be found in Chapter 2, and detailed information regarding the data analysis was included in Appendix I and III.

8.3 Results and discussion

X-ray diffraction measurements were performed on ZnO nanowires on compression of up to 26.4 GPa followed by decompression. The selected X-ray patterns are depicted in Fig. 8.2. All diffraction reflections at the near ambient pressure can be indexed to the known B4 structure with lattice constants of a = b = 3.2517 Å and c = 5.2006 Å, consistent with the previous diffraction measurement of ZnO.[26] Upon compression, the B4 phase was found to persist to 12.9 GPa, as indicated by the consistent indexing of all reflections associated with this phase. At 13.7 GPa, a new reflection appeared at 10.8431° with discernible intensity, which can be indexed as (2 0 0) for the B1 phase, indicating the onset of the wurtzite-to-rocksalt phase transformation. This onset phase transition pressure is significantly higher than that observed in the ZnO nanocrystals, nanotubes, or the corresponding bulk material in general, as shown in Table 8.1. Then, the B4 and B1 phases coexisted when compressed, even to 22.4 GPa. The Rietveld analysis (Figure 8.3 a) indicates that at this pressure the initial B4 phase still has a significant abundance of ~35%. Upon further compression, the wurtzite-to-rocksalt phase transition was completed at 24.1 GPa, as suggested by the disappearance of all diffraction reflections associated with the B4 phase. We note that both the onset and especially the completion pressure for the wurtzite-to-rocksalt transition are higher for ZnO nanowires in the current study than those for bulk or nanocrystal ZnO previously studied (Table 8.1). The ZnO nanowires were found to maintain the pure B1 phase up to 26 GPa, the highest pressure achieved in this study. The rocksalt phase was reported to persist up to 200 GPa before undergoing another phase transition.[29,30] Therefore, no further compression was carried out.

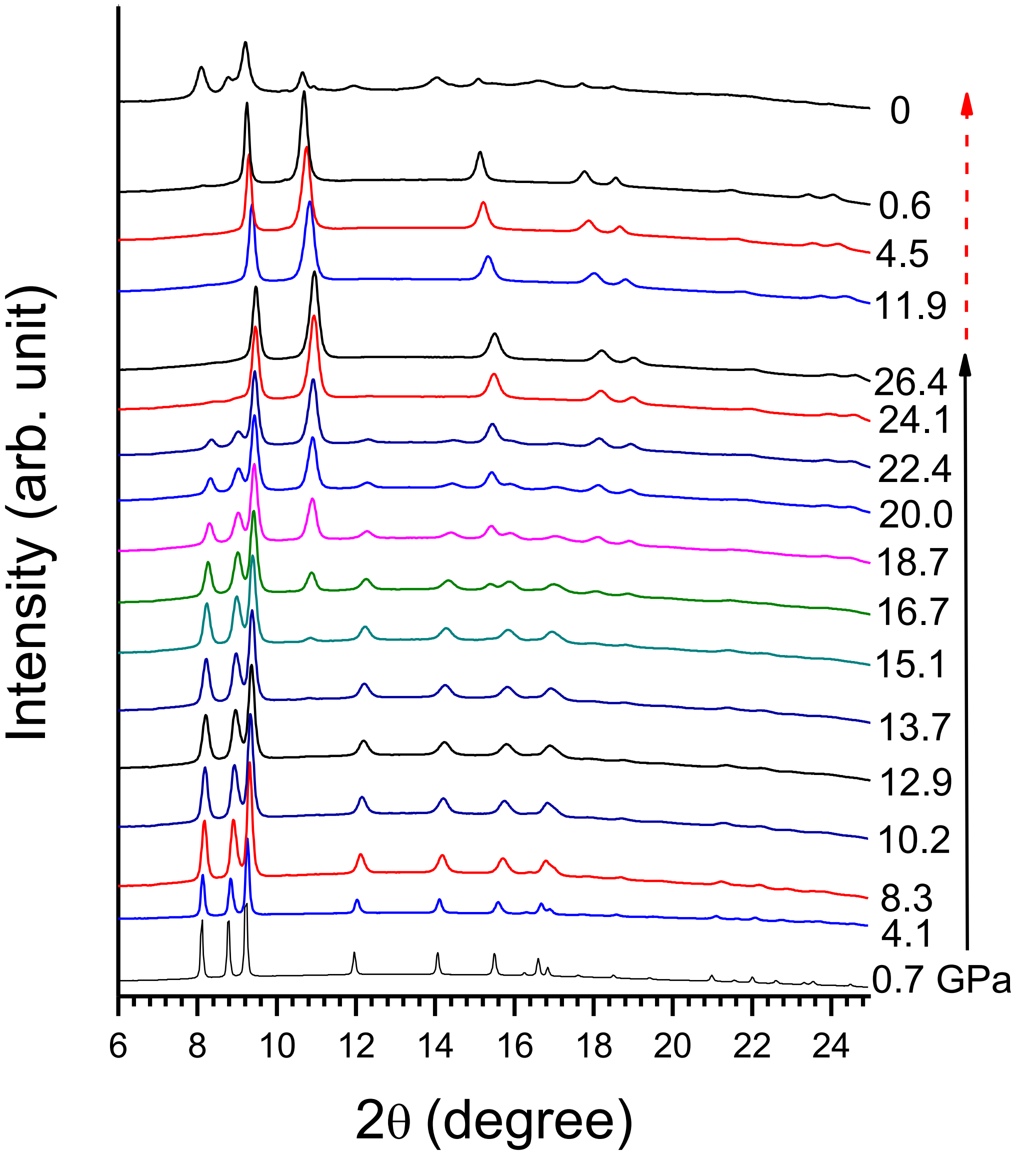

Figure 8.2 Selected X-ray diffraction patterns of ZnO nanowires upon compression to 26.4 GPa and decompression to ambient pressure. The pressures in GPa are labeled. The solid and dash arrows indicate the compression and decompression sequence, respectively.

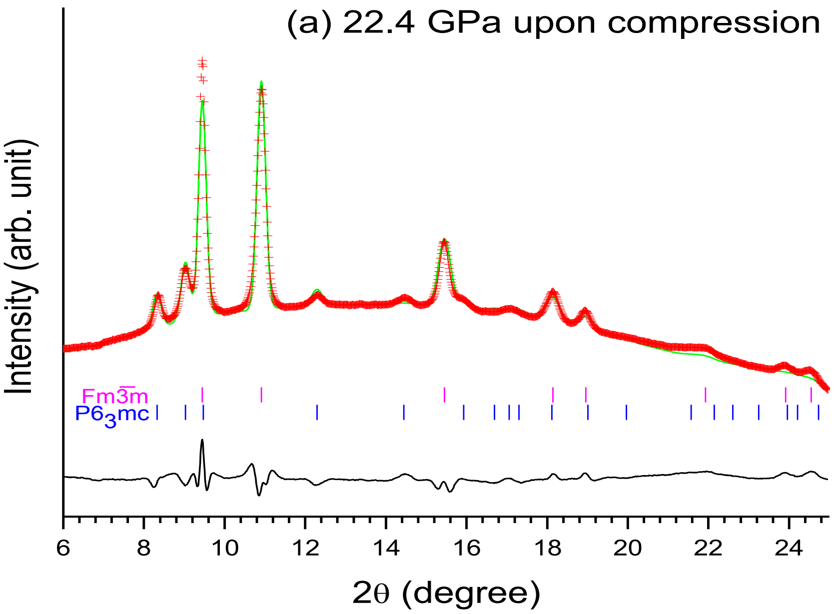
(a) 22.4 GPa upon compression

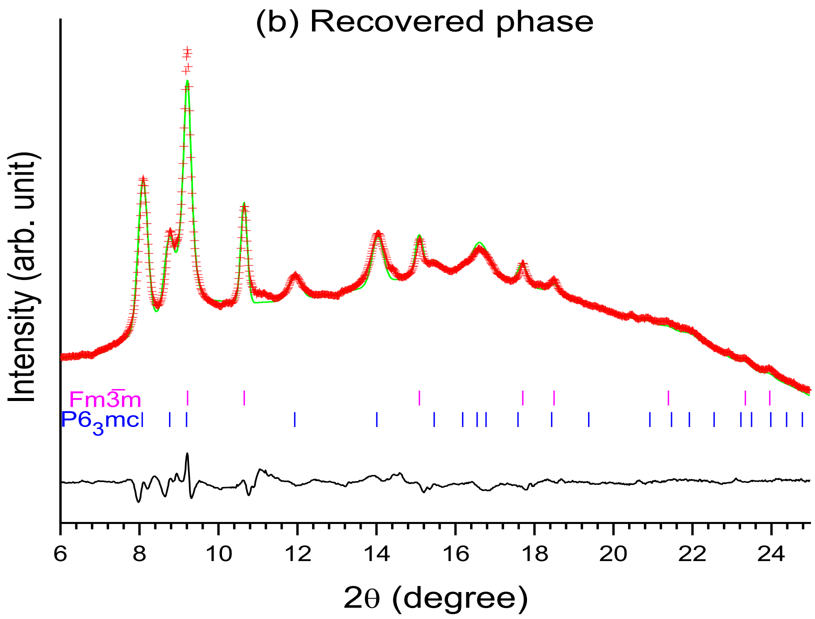
(b) Recovered phase

Figure 8.3 Rietveld refinements of XRD patterns at 22.4 GPa upon compression (a) and the recovered phase (b). The red cross is experimental X-ray intensity whereas the green solid line is the calculated diffraction pattern based on refinement with the black curve at the bottom showing the difference between the calculated and observed intensities. The vertical bars with different color indicate the characteristic reflections of different phases labeled in the front. Rietveld refinements of XRD patterns at othe representative pressures are included in Appedix III.

The differences in the pressure-induced phase transitions between nanostructured and bulk materials have also been observed in other materials with either enhanced or reduced transition pressures. Transition pressure enhancement has been observed in many nanomaterials, such as nanocrystal (e.g., CdSe,[31] ZnS,[32] and PbS[33]) and 1D nanomaterials (e.g., GaN nanowire,[10] SnO_2 nanowire and nanobelt,[11] ZnO nanotube,[16] and BN nanotube[12]). However, some oxide nanocrystals, such as CeO_2[34] and γ-Fe_2O_3,[35] exhibited reduced transition pressures. According to Jiang *et al.,*[21] such variations of transition pressure can be generally understood by examining the contributing thermodynamic functions. The driving force of the structural transformation characterized by the change in Gibbs free energy, ΔG, between the involved phases, can be interpreted as the change of three components: the ratio of volume collapse ($P\Delta V$), the surface energy difference ($A\Delta\gamma$), and the internal energy difference (ΔU).[11] In most cases mentioned above, the internal energy difference can be negligible for transitions involving solid phases. A larger ratio of volume collapse is typically associated with the reduction in the transition pressure,[35] whereas increasing surface energy can contribute to the enhancement of transition pressure.[21] As a result, the directions in which the transition pressures shift would be mainly determined by the competition between the volume collapse and surface energy difference. In all high-pressure studies of ZnO, a volume collapse was estimated to be around 16.5% at the transition pressure regardless of the morphologies.[21] Thus, the component of the ratio of volume collapse can be considered to contribute to the overall ΔG negligibly. Therefore, it can be inferred that the surface energy difference would be the dominant factor leading to variations in the transition pressures of ZnO in different forms. From Table 8.1, the enhanced transition pressures were observed for both nanocrystals and nanowires, and the values varied with the morphology and grain size among these nanomaterials. The above analysis suggests that the surface energy increase in nanocrystals and nanowires is associated with both the grain size and nanomorphologies. After all, it can be inferred from the relative transition pressures that the surface energy increases from nanocrystals of a large size (e.g., 50 nm) to nanowires (< 100 nm) and then to nanocrystals with a small size (e.g., 12 nm).

In addition, the much higher completion pressure Pc for B4-to-B1 phase transition (i.e., 24.1 GPa) can be attributed to the pressure-induced morphology tuning effect.10 Even with a pressure-transmitting medium (i.e., the neon), the morphology of the nanomaterial can be modified by the pressure, resulting in a broader distribution in morphology and dimensions than the starting nanomaterials upon compression. The SEM images taken before and after the compression (Fig. 8.1a, b) revealed that some ZnO nanowires were converted to smaller nanoparticles under the compression. The modification of the morphology with a broadened size (and thus surface energy) distribution in ZnO nanowires could contribute to the extended phase stability region for the B4 phase and thus the B4 - B1 coexistence region. Remarkably, it is noticed that a large number of the recovered nanowires still preserve the wire shape (Fig. 8.1 b), in strong contrast to many other metal oxide or nitride nanowires whose morphologies were subject to substantial pressure modifications.[10,11] Such preserved wire morphology together with the larger bulk modulus (discussed later) implies the extreme toughness of the ZnO nanowires.

Table 8.1 Summary of high-pressure studies of ZnO with different morphologies.

			B4-to-B1transition pressure (GPa)				
		pressure transmitting medium	compression[a]		decompression	bulk modulus (GPa)	
morphology	dimension		***P_i***	***P_c***	***P***	B4 phase	B1 phase
Bulk	---	---[b]	---	8.7	2	183	228
	---	Helium [c]	8.8	12.8	3.2	135	178
	---	Silicon oil[d]	8.9	11.5	---	154	229
Nanocrystal	50 nm[d]	Silicon oil	10.5	13	---	151	221
	12 nm[e]	16:3:1 MeOH-EtOH-H_2O	13.2	17.5	1.7	---	---
Nanotube[f]	*d*:10 – 70nm	4:1 MeOH-EtOH	8.0 – 10.5	13.7 – 18.4	---	152	242
Nanowire[g]	w:50 – 100 nm *l*:3-4 μm[h]	Neon	13.7	24.1	0.6	208	334

[a] P_i and P_c indicate the starting and completion pressures of the phase transition, respectively. [b] Ref. 24. [c] Ref. 18. [d] Ref. 14. [e] Ref. 21. [f] Ref. 16. [g] this work. [h] *w*: width. *l*: length.

The backward phase transformation was also investigated. Upon decompression, the B1 phase was found to persist to 0.6 GPa characterized by the reflections exclusively associated with this phase (Fig. 8.2). Then, the recovery of the B4 phase was only observed below 0.6 GPa or at near ambient pressure, as shown by some reflections associated with the B4 phase in the diffraction pattern of the recovered material (Fig. 8.2). Compared with the forward transition pressure of 14.7 GPa, the much lower back transformation pressure indicates a large hysteresis for the pressure-induced transformations of ZnO nanowires. Such large hysteresis suggests that the high-pressure B1 phase is a metastable phase because prominent hysteresis was typically associated with different kinetic barriers that impede the sharp transition often involving a metastable phase.[10,11] Moreover, as indicated in Table 8.1, the backward transition pressure of 0.6 GPa was significantly lower than that observed in bulk materials and nanocrystals (i.e., 2.0[23,36] and 1.7 GPa,[21] respectively). In addition, the B4-to-B1 phase transition is completely reversible for bulk ZnO.[23,36] However, in both nanocrystals[21] and nanowires, the metastable B1 phase can still be detected in the recovered sample as a mixture with the B4 phase. Especially for the ZnO nanowire, the Rietveld refinement (Fig. 8.3b) shows that the B1 phase still has an abundance of ~10%. All of these observations strongly demonstrate the possibility of producing specific structures or phases by combined pressure-morphology tuning.

The compression curves of the ZnO nanowire for the B4 and B1 phases were plotted in Fig. 8.4 in comparison with those for the ZnO nanocrystals and their bulk counterparts previously studied.[14,16,18,24] By fitting the third-order Birch-Murnaghan equation of state, the bulk moduli (B_0) of the B4 and B1 phases for the ZnO nanowire were determined to be 208 and 334 GPa, respectively, with the first derivative ($B_0^{'}$) being fixed at 4. As can be seen, the bulk moduli of both the B4 and B1 phases are significantly larger than those for nanocrystals (i.e., 151 and 221GPa)[14] and their bulk counterparts (i.e., 135 and 178 GPa).[18] In particular, for the high-pressure B1 phase, the ZnO nanowire exhibited a 47% enhancement in the bulk modulus compared with that for bulk ZnO. Such a size- and morphology-induced enhancement of ZnO nanowire stiffness can be understood in parallel with other nanomaterials. For example, CeO_2 and γ-Fe_2O_3 nanoparticles exhibited the same enhancement of the bulk modulus compared with the bulk materials,[35,37] whereas no obvious difference in compressibility was observed for ZnS nanocrystals.[32] In contrast, the compressibility of PbS and γ-Al_2O_3 was found to increase with decreasing nanoparticle size. Furthermore, a strongly contrasting compressibility was observed for TiO_2 nanoparticles; that is, the bulk modulus of the rice-shape particles was reduced, whereas that of the rod-shaped particles was enhanced by > 50% relative to that of the bulk materials.[38] Therefore, multiple factors contribute to the mechanical properties of nanomaterials. In this case, the individual ZnO nanowires can be considered to be single crystals with a strictly 1D morphology that carries very few or no defects.[28] The high crystallinity and defect-free nature of the nanowires may contribute to the enhanced mechanical properties. A similar scenario was also observed in SnO_2 nanowires.[11]

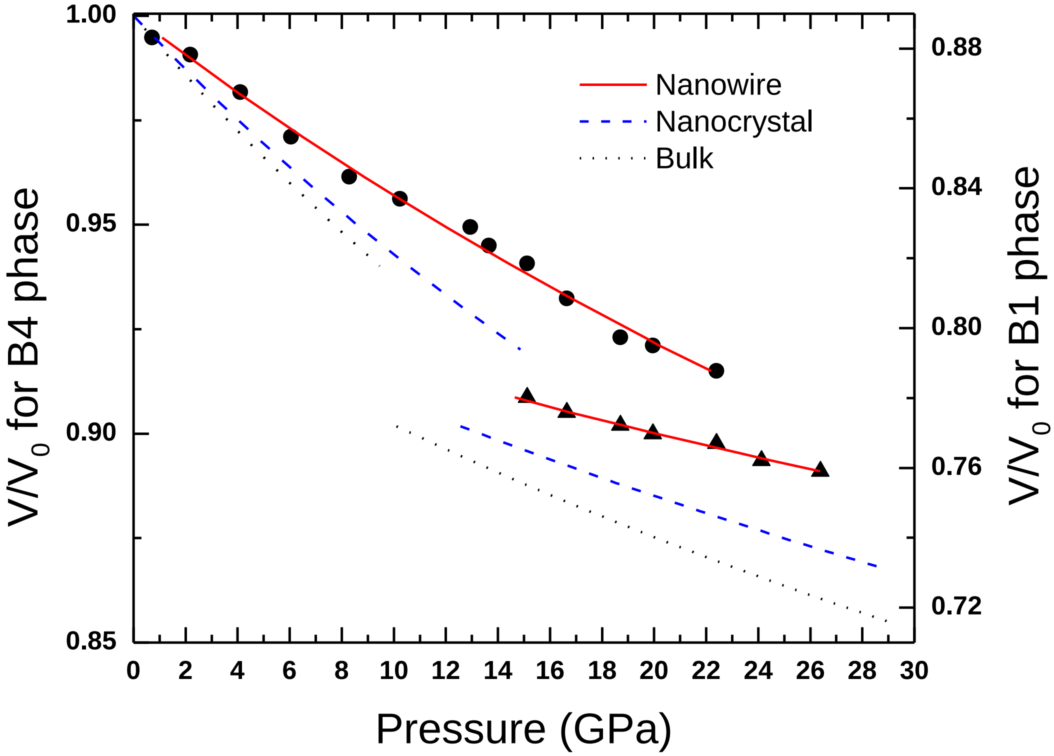

Figure 8.4 Pressure dependence of the unit cell volume for ZnO nanowire at room temperature in comparison with those for bulk, and nanocrystals. Solid circles (B4 phase) and triangles (B1 phase) are the experimental data points obtained from this work. The solid lines represent fits to the Birch-Murnaghan equation of state. Dashed lines and dotted lines are the EOS for nanocrystals and bulk materials from Ref. 14 and Ref. 18, respectively.

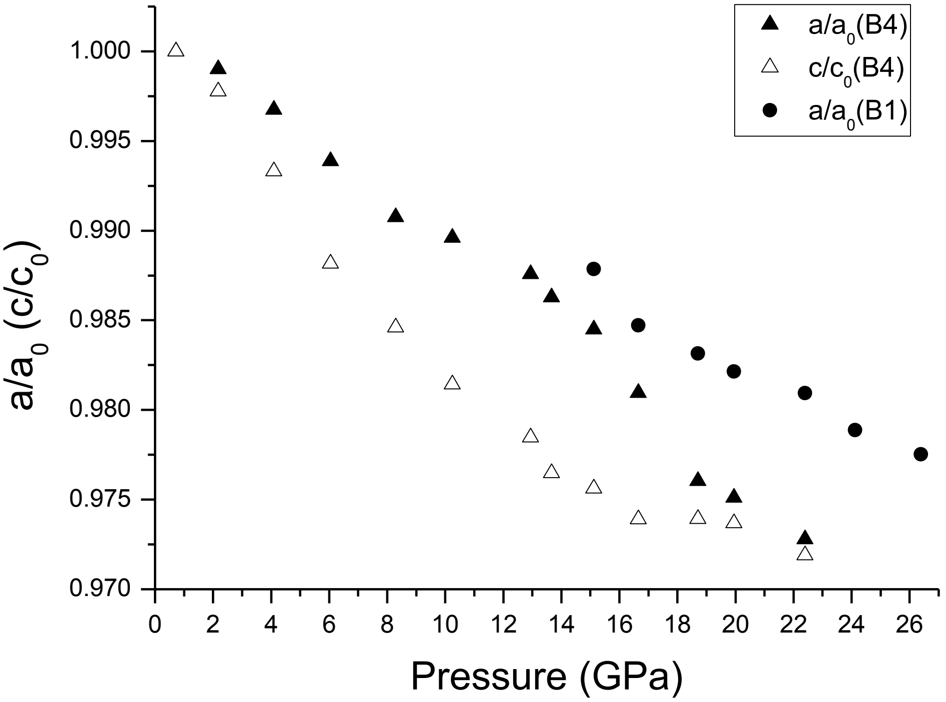

Figure 8.5 Cell parameter ratio as function of pressure for ZnO nanowire. Solid and opened triangle symbols represent the a/a_0 and c/c_0 for the B4 phase, respectively. The solid circles are the a/a_0 ratio for the B1 phase.

To understand the phase transition mechanism, we first plotted the a/a_0 and c/c_0 ratios for the B4 phase as a function of pressure in Fig. 8.5, where a_0 and c_0 represent the ambient pressure unit cell parameters. It can be seen that the c axis exhibits a higher degree of pressure dependence (0.0070 Å/GPa) than the a axis (0.0041 Å/GPa) before the onset pressure for the B4-to-B1 transition, indicating that the pressure-induced lattice deformation was more prominent along the c axis. Moreover, from the pressure dependence of the c/a axial ratio for the B4 phase depicted in Fig. 8.6, a turning point was observed at 14 GPa, coincidental with the onset of the B4-to-B1 phase transition. Below this point, the c/a ratio follows an obvious decreasing trend and then abruptly increases with compression until the transformation is complete. In Fig. 8.6, the internal structural parameter *u* obtained from the Rietveld refinements was plotted as a function of pressure. This parameter *u* is an atomic coordinate along the c axis for oxygen atoms residing on the Wyckoff position (1/3, 2/3, *u*) in space group $P6_3mc$, which defines the relative position of the two sub-lattices in the hexagonal wurtzite structure. Therefore, the pressure dependence of the *u* value could serve as the path indicator of the structural change. As indicated in Fig. 8.6, the *u* value remains almost constant with a very minor decrease below 4 GPa and then increases slightly to 0.411 at 14 GPa. Thereafter, the u values increase quickly up to ~ 0.508 at 22 GPa, beyond which the B4 phase converts to the B1 phase completely.

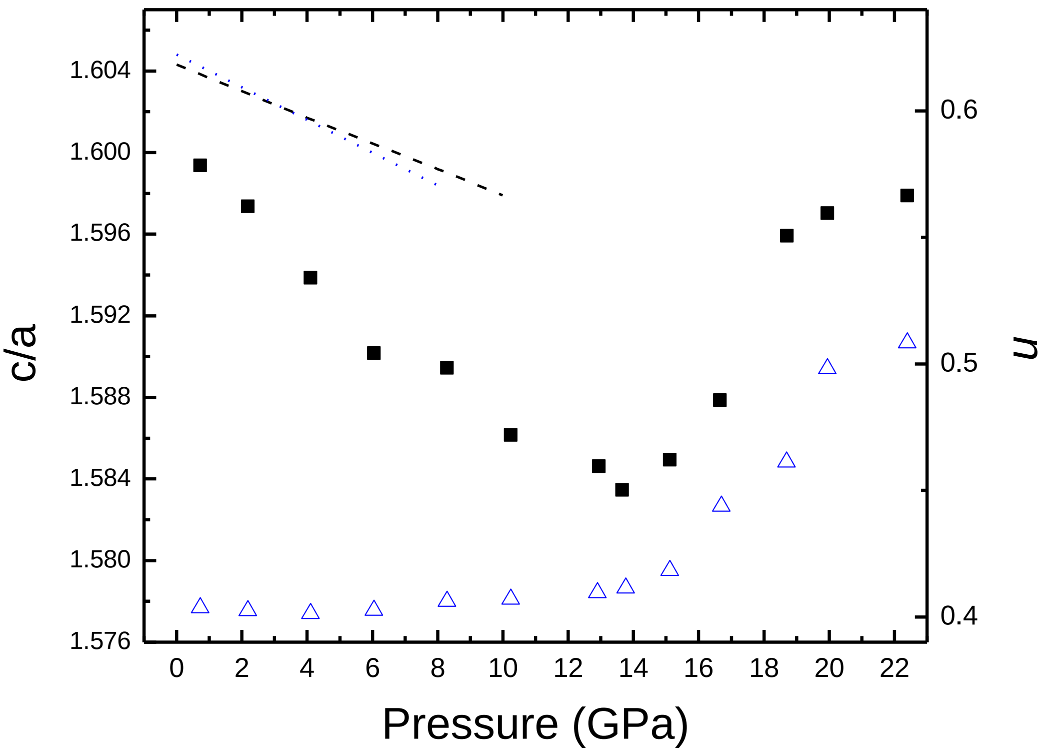

Figure 8.6 Pressure dependence of c/a ratio (solid squares, left vertical axis) and the internal structural parameter *u* of wurtzite structure ZnO (open triangles, right vertical axis) as function of pressure obtained from Rietveld refinement. The lines show the results from Refs. 20 (dashed line) and 16 (dot line), respectively.

These results help to evaluate the previously proposed phase transformation models. As suggested by Saitta and Decremps,[39] the B4 phase can be converted to the B1 phase via a tetragonal path via an intermediate tetragonal phase characterized with each Zn (or O) atom located at the body center of the square pyramid formed by five O (or Zn) atoms. The c/a and *u* remain close to that of the B4 structure first; then, the c/a ratio decreases to bring the Zn atom from the body center to the base center of the pyramid until *u* = 0.5, resulting in the B1 structure. However, Limpijumnong and Jungthawa[40] proposed an alternative model that the B4-to-B1 phase transition could follow a hexagonal path. In this model, the c/a ratio first decreases continuously, whereas the *u* increases to 0.5. Then the γ angle (60°) opens up to 90°, and the B1 phase forms eventually. In this work, the c/a ratio was observed to decrease monotonically with compression before the transition started. Although the *u* values exhibited no obvious increase below 4 GPa, the overall trend still demonstrated an increase in the *u* value with pressure, suggesting that the B4-to-B1 phase transformation in the ZnO nanowire is more likely via the hexagonal rather than the tetragonal path. This hexagonal model was also proposed for other ZnO materials, such as nanocrystals,[14] nanotubes,[16] and their corresponding bulk counterparts,[18] as indicated by either the changes of the c/a ratio or the *u* values. Therefore, our results indicate that the transformation path for the B4-to-B1 of ZnO is independent of the morphologies or one dimensionality.

8.4 Conclusions

In summary, we have investigated the high-pressure structures and properties of the 1D nanostructured ZnO using synchrotron X-ray diffraction. The B4-to-B1 phase transformation was found to start at 13.7 GPa and to complete at 24.1 GPa, the highest completion pressure for the B4-to-B1 phase transformation observed in ZnO so far. Upon decompression, the pure high pressure B1 phase was found to persist down to 0.6 GPa. Bulk moduli for the B4 and B1 phases were determined to be 208 and 334 GPa, respectively, both of which were drastically enhanced as compared with ZnO in other morphologies. Aided by the SEM images, the combined pressure-morphology effects on ZnO wires can be understood based on other nanostructured materials previously studied. Finally, the pressure dependence of both the unit cell parameter c/a ratio and the structure parameter *u* strongly suggests the B4-to-B1 phase transition for ZnO nanowire via the hexagonal path.

8.5 References

(1) Minne, S. C.; Manalis, S. R.; Quate, C. F. *Appl. Phys. Lett.* **1995**, *67*, 3918.

(2) Gorla, C. R.; Emanetoglu, N. W.; Liang, S.; Mayo, W. E.; Lu, Y.; Wraback, M.; Shen, H. *J. Appl. Phys.* **1999**, *85*, 2595.

(3) Huang, Y. H.; Zhang, Y.; Gu, Y. S.; Bai, X. D.; Qi, J. J.; Liao, Q. L.; Liu, J. *J. Phys. Chem. C* **2007**, *111*, 9039.

(4) Huang, M. H.; Mao, S.; Feick, H.; Yan, H. Q.; Wu, Y. Y.; Kind, H.; Weber, E.; Russo, R.; Yang, P. D. *Science* **2001**, *292*, 1897.

(5) Hullavarad, S.; Hullavarad, N.; Look, D.; Claflin, B. *Nanoscale Res. Lett.* **2009**, *4*, 1421.

(6) Wang, X. D.; Song, J. H.; Liu, J.; Wang, Z. L. *Science* **2007**, *316*, 102.

(7) Cheng, H. M.; Hsu, H. C.; Tseng, Y. K.; Lin, L. J.; Hsieh, W. F. *J. Phys. Chem. B* **2005**, *109*, 8749.

(8) Lu, C. Y.; Chang, S. P.; Chang, S. J.; Hsueh, T. J.; Hsu, C. L.; Chiou, Y. Z.; Chen, C. *IEEE Sens. J.* **2009**, *9*, 485.

(9) San-Miguel, A. *Chem. Soc. Rev.* **2006**, *35*, 876.

(10) Dong, Z. H.; Song, Y. *Appl. Phys. Lett.* **2009**, *96*, 151903.

(11) Dong, Z. H.; Song, Y. *Chem. Phys. Lett.* **2009**, *480*, 90.

(12) Dong, Z. H.; Song, Y. *J. Phys. Chem. C* **2010**, *114*, 1782.

(13) Shchennikov, V. V.; Ovsyannikov, S. V. *High Pressure Res.* **2009**, *29*, 514.

(14) Kumar, R. S.; Cornelius, A. L.; Nicol, M. F. *Curr. Appl. Phys.* **2007**, *7*, 135.

(15) Decremps, F.; Datchi, F.; Saitta, A. M.; Itie, J. P.; Polian, A.; Baudelet, F.; Pascarelli, S. *High Pressure Res.* **2002**, *22*, 365.

(16) Hou, D. B.; Ma, Y. Z.; Gao, C. X.; Chaudhuri, J.; Lee, R. G.; Yang, H. B. *J. Appl. Phys.* **2009**, *105*, 104317.

(17) Jiang, J. Z. *J. Mater. Sci.* **2004**, *39*, 5103.

(18) Liu, H. Z.; Ding, Y.; Somayazulu, M.; Qian, J.; Shu, J.; Hausermann, D.; Mao, H. K. *Phys. Rev. B* **2005**, *71*, 212103.

(19) Bates, C. H.; Roy, R.; White, W. B. *Science* **1962**, *137*, 993.

(20) Zhuravlev, K. K.; Oo, W. M. H.; McCluskey, M. D.; Huso, J.; Morrison, J. L.; Bergman, L. *J. Appl. Phys.* **2009**, *106*, 013511.

(21) Jiang, J. Z.; Olsen, J. S.; Gerward, L.; Frost, D.; Rubie, D.; Peyronneau, J. *Europhys. Lett.* **2000**, *50*, 48.

(22) Wu, Z. Y.; Bao, Z. X.; Zou, X. P.; Tang, D. S.; Liu, C. X.; Dai, J. H.; Xie, S. S.; Li, Q. S.; Shen, Z. X.; Zou, B. S. *Mater. Sci. Technol.* **2003**, *19*, 981.

(23) Desgreniers, S. *Phys. Rev. B* **1998**, *58*, 14102.

(24) Karzel, H.; Potzel, W.; Kofferlein, M.; Schiessl, W.; Steiner, M.; Hiller, U.; Kalvius, G. M.; Mitchell, D. W.; Das, T. P.; Blaha, P.; Schwarz, K.; Pasternak, M. P. *Phys. Rev. B* **1996**, *53*, 11425.

(25) Recio, J. M.; Blanco, M. A.; Luana, V.; Pandey, R.; Gerward, L.; Olsen, J. S. *Phys. Rev. B* **1998**, *58*, 8949.

(26) Yan, X. Q.; Gu, Y. S.; Zhang, X. M.; Huang, Y. H.; Qi, J. J.; Zhang, Y.; Fujita, T.; Chen, M. W. *J. Phys. Chem. C* **2009**, *113*, 1164.

(27) Jin, S.; Bierman, M. J.; Morin, S. A. *J. Phys. Chem. Lett.* **2010**, *1*, 1472.

(28) Morin, S. A.; Bierman, M. J.; Tong, J.; Jin, S. *Science* **2010**, *328*, 476.

(29) Maouche, D.; Saoud, F. S.; Louail, L. *Mater. Chem. Phys.* **2007**, *106*, 11.

(30) Liu, H. Z.; Tse, J. S.; Mao, H. K. *J. Appl. Phys.* **2006**, *100*, 093509.

(31) Tolbert, S. H.; Alivisatos, A. P. *Science* **1994**, *265*, 373.

(32) Jiang, J. Z.; Gerward, L.; Frost, D.; Secco, R.; Peyronneau, J.; Olsen, J. S. *J. Appl. Phys.* **1999**, *86*, 6608.

(33) Jiang, J. Z.; Gerward, L.; Secco, R.; Frost, D.; Olsen, J. S.; Truckenbrodt, J. *J. Appl. Phys.* **2000**, *87*, 2658.

(34) Rekhi, S.; Saxena, S. K.; Lazor, P. *J. Appl. Phys.* **2001**, *89*, 2968.

(35) Jiang, J. Z.; Olsen, J. S.; Gerward, L.; Morup, S. *Europhys. Lett.* **1998**, *44*, 620.

(36) Decremps, F.; Datchi, F.; Saitta, A. M.; Polian, A.; Pascarelli, S.; Di Cicco, A.; Itie, J. P.; Baudelet, F. *Phys. Rev. B* **2003**, *68*, 104101.

(37) Wang, Z. W.; Zhao, Y. S.; Schiferl, D.; Zha, C. S.; Downs, R. T. *Appl. Phys. Lett.* **2004**, *85*, 124.

(38) Park, S. W.; Jang, J. T.; Cheon, J.; Lee, H. H.; Lee, D. R.; Lee, Y. *J. Phys. Chem. C* **2008**, *112*, 9627.

(39) Saitta, A. M.; Decremps, F. *Phys. Rev. B* **2004**, *70*, 035214.

(40) Limpijumnong, S.; Jungthawan, S. *Phys. Rev. B* **2004**, *70*, 054104.

Chapter 9 Investigation of Size Effect on High-Pressure Behaviors of ZnO Nanowires

9.1 Introduction

Nanostructured ZnO, particularly ZnO nanowires, has improved performance in applications of nanoelectronics,[1] piezoelectric devices,[2] UV lasers,[3] chemical sensors[4] and atomic force microscopy (AFM) tips[5] in contrast to bulk ZnO. Thus, nanostructured ZnO has been studied extensively focusing on their structures, properties, fabrication routes and applications, etc. High pressure, as a powerful tool, provides an alternative effective driving force to tune the structures and thus properties of nanomaterials. Therefore, high-pressure behaviors of nanostructured ZnO have been widely investigated. It is well established that ZnO undergoes a phase transition from the wurtzite structure (B4) to the rocksalt (B1) structure under high pressures regardless of its morphology and grain size. However, the onset phase transition pressures appeared to be quite different.[6-14] For instance, bulk ZnO exhibited a transition pressure of ~ 9 GPa,[6,15-17] while the transition pressure varies in ZnO nanoparticles from 10 GPa to 15 GPa depending on their particle size. Our previous study showed that the B4 to B1 phase transition occurred at 13.7 GPa in ZnO nanowires.[18] Such a large variation was attributed to the various properties of nanomaterials governed by many factors, such as their grain size, morphology and structure, etc.[19] For instance, our studies on other one dimensional nanomaterials (e.g., SnO_2 nanobelts and nanowires,[20] BN nanotubes,[21] GaN nanowires,[22] ZnO nanowires,[18] etc.) have successfully demonstrated that morphology plays an important role in affecting their high-pressure behaviors. So far, there are several systematic studies of nanocrystals mainly focusing on the size effect on the structural stability, transition pressure and compressibility in different materials.[19,23-27] However, no simple discipline is developed regarding how those factors affected the high-pressure behaviors of nanomaterials. For instance, both elevation (e.g., CdSe,[19] ZnS[23] and PbS[24,25]) and reduction (e.g., CeO_2[26] and γ-Fe_2O_3[27]) of the transition pressure were observed in nanocrystals as the particle size decreased. As mentioned above, ZnO nanocrystals exhibited a large variation of onset phase transition pressures for the B4 to B1 phase transition. The highest transition pressure was 15.1 GPa observed in ZnO nanocrystals with a particle size of 12 nm,[28] while the lowest transition pressure of 10.5 GPa was found in nanoparticles with grain size of 50 nm.[17] However, untill now, there is no systematic high-pressure study on ZnO nanomaterials addressing the size effect.

In this chapter, we present the first systematical study on ZnO nanowires under high pressure. Three ZnO nanowires samples with different widths were investigated under high pressure using synchrotron X-ray diffraction. In addition to our previous study, the size effects on the transition pressure, structural stability as well as the compressibility are addressed. This systematic study will provide a pioneer view of size dependent effect on high-pressure behaviors of ZnO nanowires.

9.2 Experimental section

ZnO nanowires/nanofibers were synthesized using the same method as described in Chapter 8 via changing the concentration of the precursor solutions. Morphology of synthesized samples was examined by SEM/EDX (Leo/Zesis 1540XB FIB/SEM). Three synthesized samples were named as ZnONW1, ZnONW2 and ZnONW3 in the order of decreasing in their widths, and were studied under high pressure.

High-pressure experiments were performed using a symmetric DAC equipped with a pair of type I diamonds with a culet size of 400 μm. *In-situ* synchrotron X-ray diffraction measurements were carried out at room temperature using the 16ID-B beamline of HPCAT at the APS. The wavelength of the monochromatic X-ray used was 0.3980 Å. Detailed information regarding to the beamline setup can be found in Chapter 2. The obtained data were analyzed using Fit2D program. Detailed Rietveld analysis was performed using the GSAS package. Information about the data analysis was included in Appendix I and IV.

9.3 Results and discussion

9.3.1 Results

Fig. 9.1a and c showed the dimensions and morphologies of the ZnONW1 and ZnONW3. ZnONW1 had a width of 150 nm – 200 nm and length of 3 μm – 4 μm. ZnONW3 had a high-aspect-ratio nanostructure with size of 20 nm – 35 nm in width and several hundreds of microns in length. Diameter of ZnONW2 was slightly smaller than the ZnO nanowires (named as ZnONW) that was studied in Chapter 8. The SEM images of ZnONW2 were included as Fig. A22 in Appendix IV.

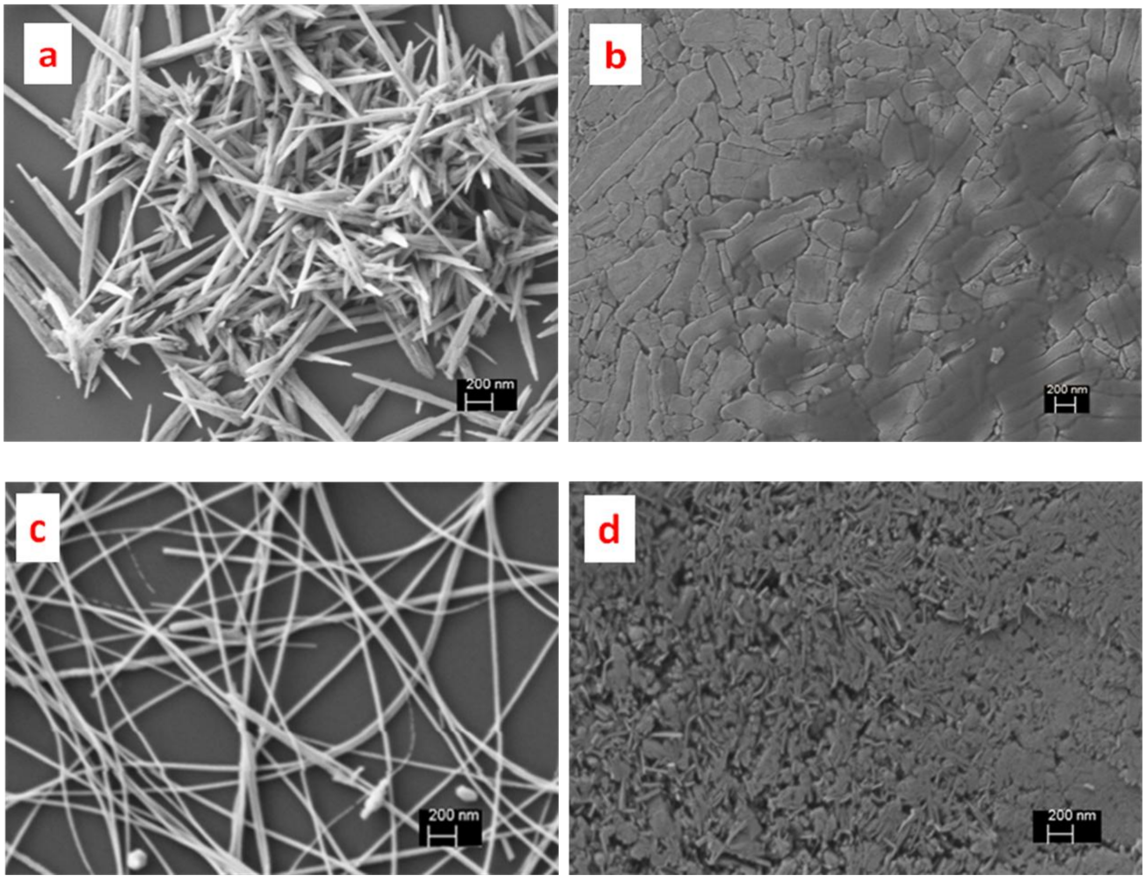

Figure 9.1 SEM images of ZnO nanowires taken before and after compressions. a, c are the images for ZnONW1 and ZnONW3 before compression, respectively. b and d are images of the recovered samples for ZnONW1 and ZnONW3, respectively.

In-situ X-ray diffraction measurements were performed on ZnONW1, ZnONW2 and ZnONW3 under high pressure with selected XRD patterns depicted in Fig. 9.2, 9.3 and 9.4, respectively. All three samples started with a B4 phase indicated by the successful indexing of X-ray patterns at the very bottom of Fig. 9.2, 9.3 and 9.4 using wurtzite structure. Similar cell parameters of a=b=3.2419 Å and c=5.1832 Å with small variation were obtained for all samples, which was in good agreement of previous results.[29]

In ZnONW1, as indicated in Fig. 9.2, the wurtzite phase persisted to 6.5 GPa suggested by the consistent indexing of its associated reflections. When the pressure was increased to 8.7 GPa, a new reflection at 2θ of 10.8178° was observed, which was indexed to the (2 0 0) reflection of rocksalt phase (B1), indicating the onset of B4 to B1 phase transformation. The same phase transition was also observed in ZnONW2 and ZnONW3 supported by the appearance of the (2 0 0) reflection of B1 phase as shown in Fig. 9.3 and 9.4 labeled with black arrows, however, at different pressures (i.e., 9.2 GPa for ZnONW2 and 12.3 GPa for ZnONW3). The B4 to B1 phase transformation competed at 17.3 GPa in ZnONW1 indicated by the depletion of all the reflections of wurtzite phase. The completion of this phase transformation was observed at 19.2 GPa and 18.1 GPa for ZnONW2 and ZnONW3, respectively. Beyond the completion pressure, all samples were found in the B1 phase which sustained to the highest pressure achieved for each sample. Because the B1 phase was reported to persist up to 200 GPa before undergoing another phase transition,[30,31] no further compression was carried out.

In order to check the reversibility and back transformation sequence of ZnO, which may be governed by kinetic of these samples, X-ray diffraction measurements were also carried out upon decompression for each sample. Selected XRD patterns were shown in Fig. 9.2, 9.3 and 9.4 labeled by the dashed arrows. Upon decompression, B4 phase was retrieved below 2.6 GPa in ZnONW1, supported by the reappearance of its representative reflections (1 0 0), (0 0 2) and (1 0 1). Rietveld refinement analysis of the recovered sample showed an abundance of 9% of the rocksalt phase maintained (Fig. A20 in Appendix IV). The same backward phase transition was observed in ZnONW2 below 2.1 GPa. In contrast to these two samples, no B4 phase was obtained in ZnONW3 after the sample was decompressed to near ambient pressure (Fig. A33 in Appendix IV). These strongly contrasting pressure-induced phase transformations of ZnO nanowires were summarized in Fig. 9.5 compared with nanocrystals and bulk materials for following discussion.

In addition, morphology of each sample after the compression was examined in order to study the pressure-induced morphology modification (Fig. 8.1b and d). SEM images for the recovered sample of ZnONW2 were failed to obtain due to the regret of experiments. The morphologies of all the nanowires were modified to fragments with different sizes by pressure. For instance, small wire fragments were maintained in ZnONW1, and widths and length of these fragments are estimated to be > 300 nm and < 1 μm, respectively. From those fragments, the original shape of ZnONW1 can still be speculated. In contrast, in ZnONW3 most nanowires were completely compressed to fine particles with no wire shape preserved.

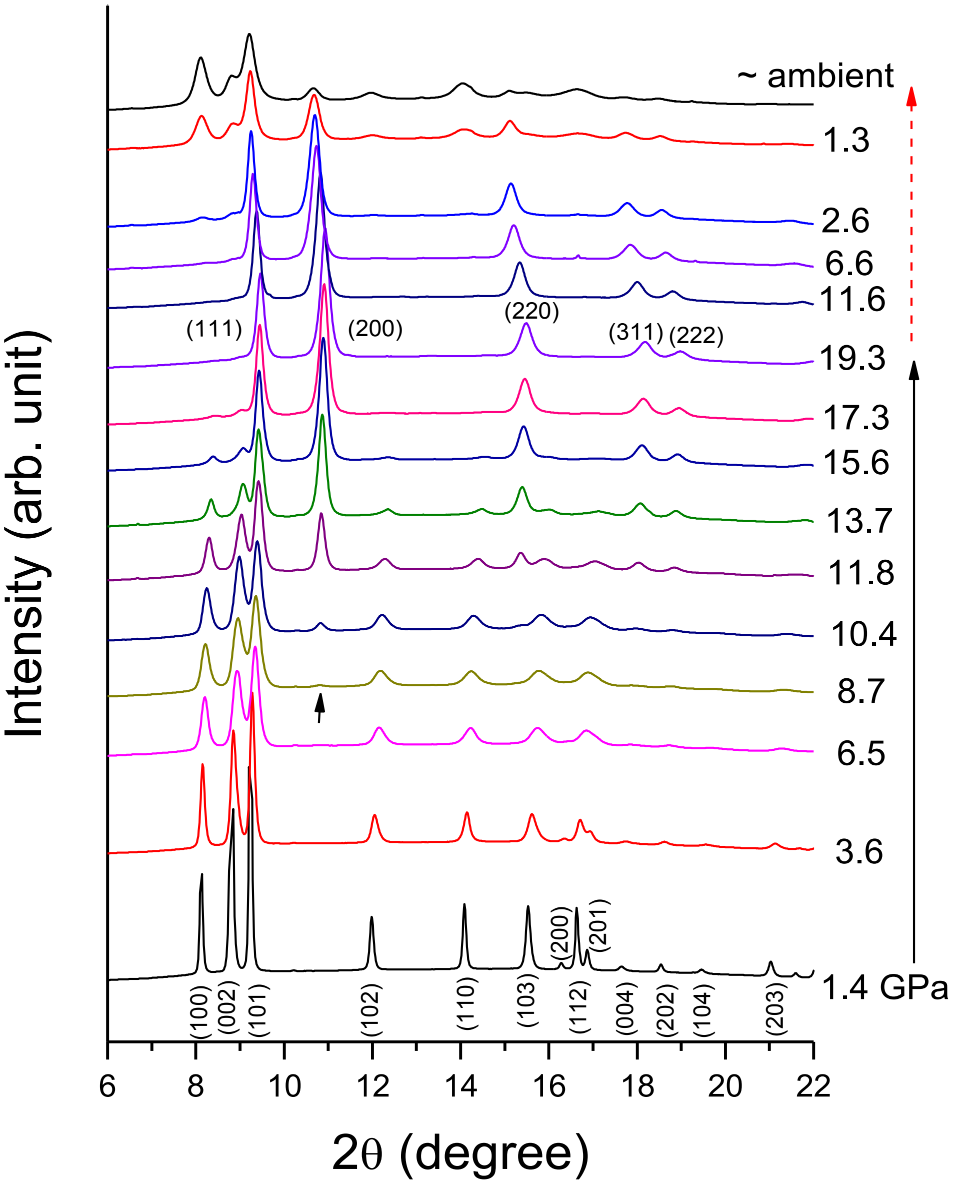

Figure 9.2 **Selected X-ray diffraction patterns of ZnONW1 upon compression and decompression with pressure in GPa labeled. The solid and dashed arrows indicate the compression and decompression sequence, respectively. The small arrow suggests the appearance of reflection (2 0 0).**

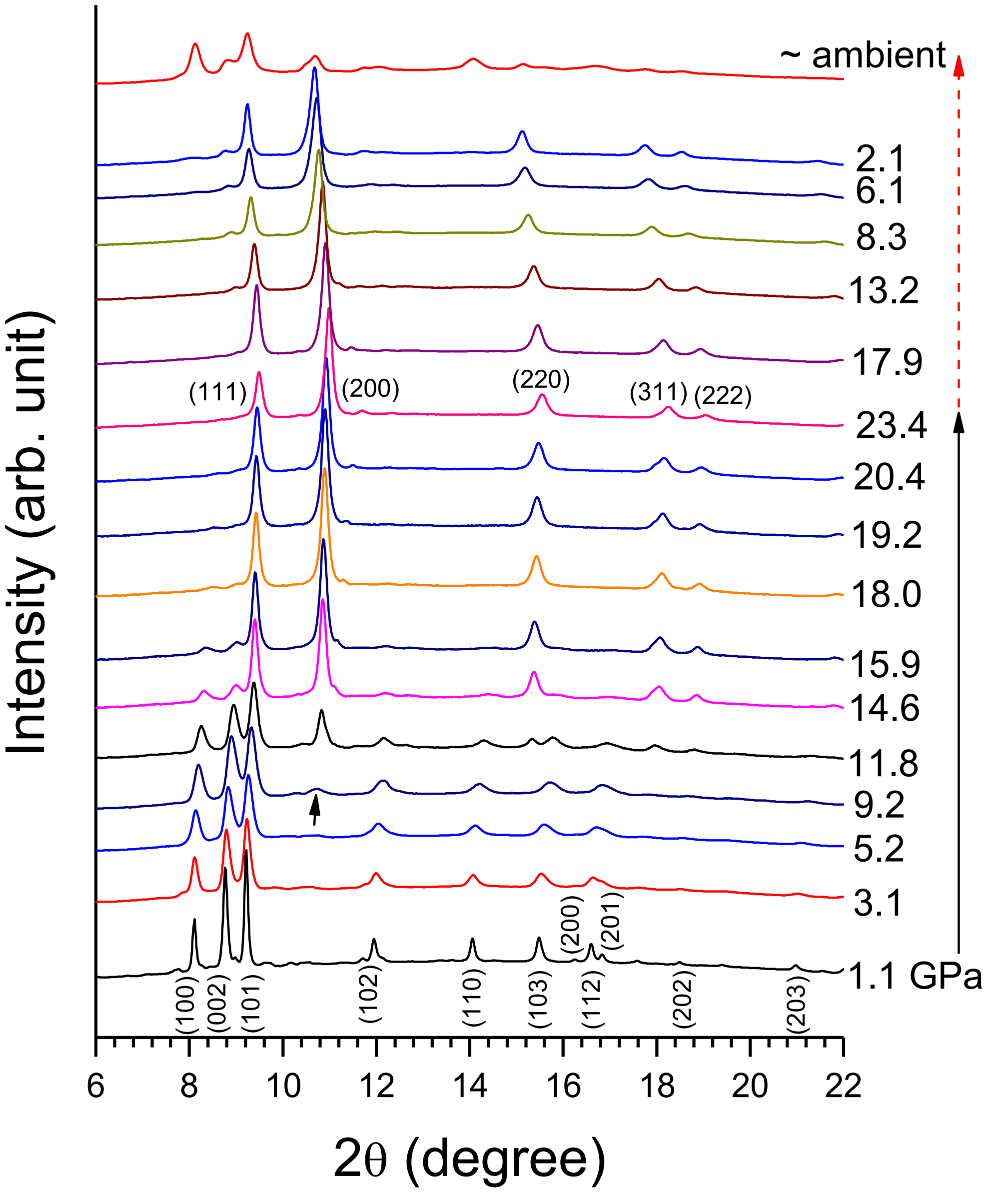

Figure 9.3 Selected X-ray diffraction patterns of ZnONW2 upon compression and decompression with pressure in GPa labeled. The solid and dashed arrows indicate the compression and decompression sequence, respectively. The small arrow suggests the appearance of reflection (2 0 0).

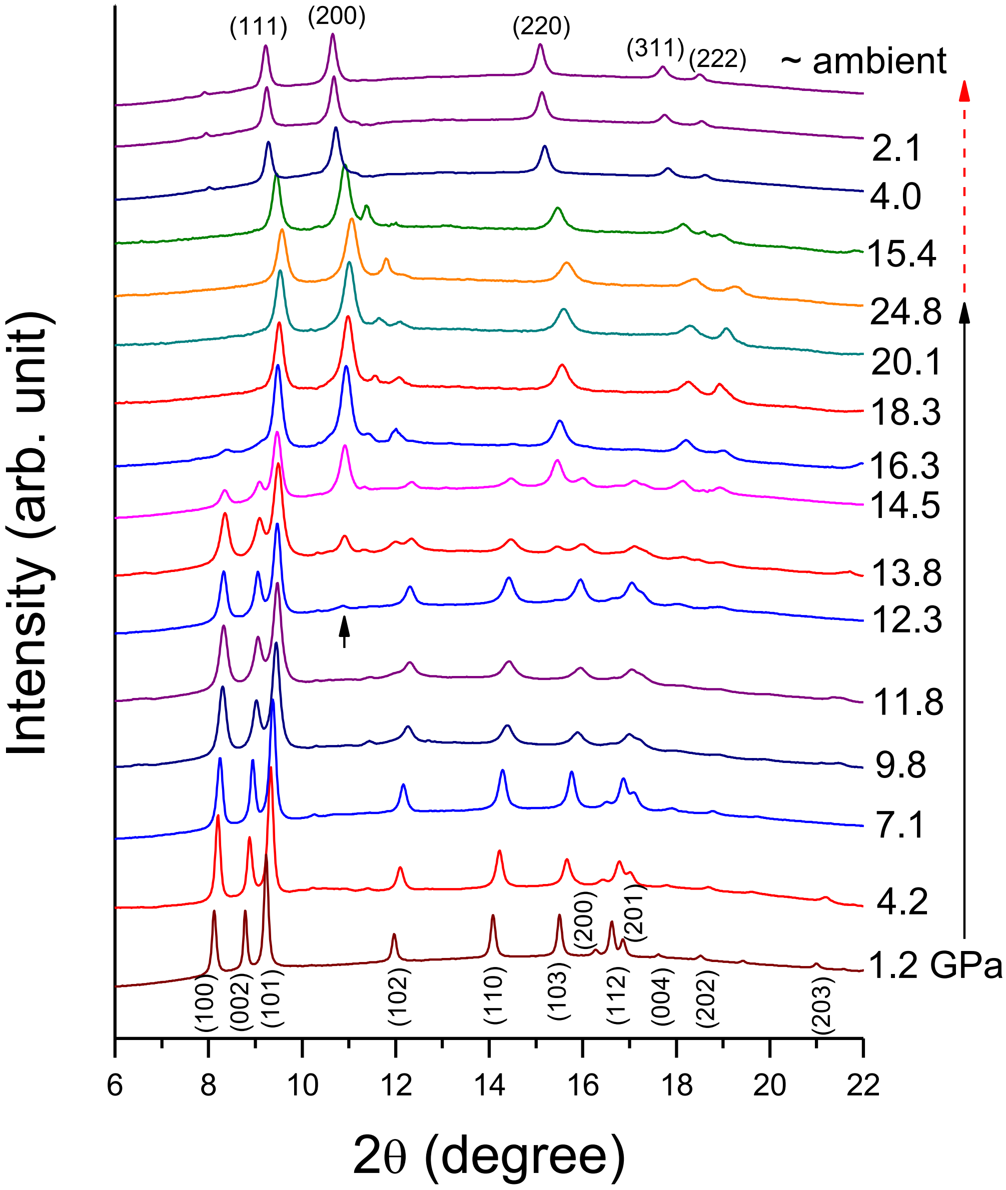

Figure 9.4 Selected X-ray diffraction patterns of ZnONW3 upon compression and decompression with pressure in GPa labeled. The solid and dashed arrows indicate the compression and decompression sequence, respectively. The small black arrow suggests the appearance of reflection (2 0 0).

9.3.2 Discussion

In order to investigate the size effect on ZnO nanowires, results of ZnONW from Chapter 8 were included.[18] It had a width of 50 nm – 100 nm, which was similar to ZnONW2 but with better crystallinity and uniformity. The B4 to B1 phase transformation was observed in all the nanowires studied in this work, however, the onset phase transition pressure as well as the duration regions were drastically different as indicated in Fig. 9.5. Enhanced transition pressures were observed in ZnO nanowires with widths less than 100 nm (i.e., ZnONW, ZnONW2 and ZnONW3). In contrast, no obvious enhancement was found in ZnONW1 whose width was comparable to bulk materials. Such a large size of ZnONW1 leaded to weakening of nano-effect, therefore, it behaved almost equivalently to bulk ZnO under high pressures in terms of phase transition pressure. According to previous study of nanomaterials, enhanced transition pressure were mainly attributed to the increased surface energy of nanomaterilas in contrast to their bulk counterparts.[20,22] Thus, our samples (ZnONW, ZnONW2 and ZnONW3) had higher surface energy comparing to bulk ZnO.

In addition, as seen in Fig. 9.5, completion pressures (P_c) of the B4 to B1 phase transition in nanowires were also significantly higher than those in the corresponding bulk materials, even nanocrystals. For instance, the P_c in ZnONW was almost twice than that in bulk ZnO (i.e., 24.1 GPa in ZnONW vs 12.7 GPa of that in bulk ZnO). Such a high P_c can be attributed to the widening of size distribution due to the broken down of nanowires during compression, which was explained in detail in our previous paper.[22,18]

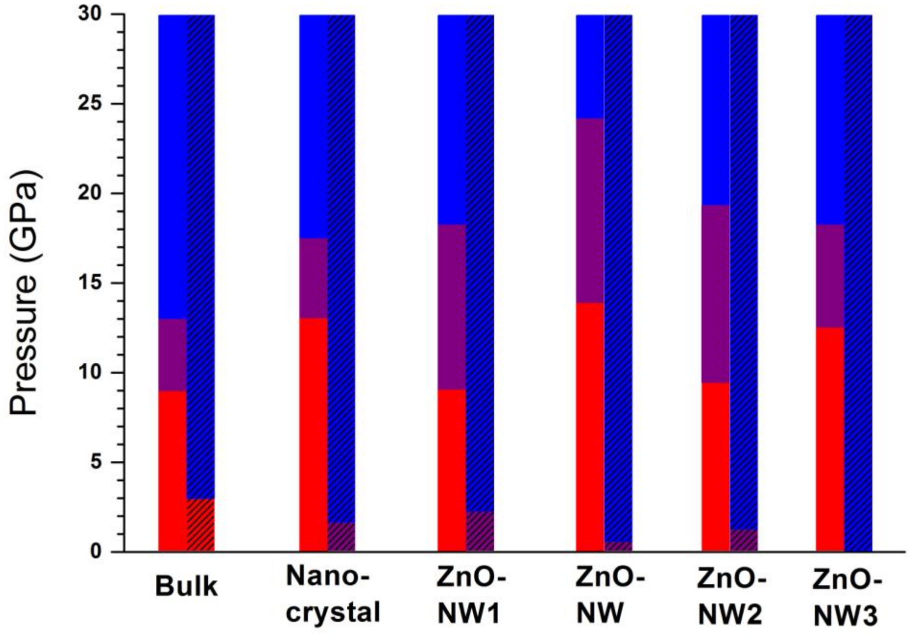

Figure 9.5 Summary of pressure-induced phase transformations for ZnO nanowires upon compression (plain bars) and decompression (hatched bars) compared with those for bulk ZnO and nanocrystals. The red, blue and purple colors stand for wurtzite phase, rocksalt phase and the mixture of both phases, respectively.

Table 9.1 Summary of high-pressure studies of ZnO with different morphologies.

morphology	**dimension**	**pressure transmitting medium**	**bulk modulus (GPa)[g]**	
			B4 phase	**B1 phase**
Bulk[a]	---	Helium	135	178
Nanocrystal[b]	50 nm[d]	Silicon oil	151	221
Nanotube[c]	*d*:10 – 70nm[e]	4:1 MeOH-EtOH	152	242
Nanobelt[d]	*w*: 200 nm[f]	Silicon oil	164	194
nanowires (this work)				
ZnONW1	*w*: 150 – 200 nm	Neon	126	184
ZnONW	*w*: 50 – 100 nm	Neon	208	334
ZnONW2	*w*: 50 – 70 nm	Neon	161	247
ZnONW3	*w*: 20 – 35 nm	Neon	121	154

[a]Ref. 15. [b]Ref. 29. [c]Ref. 14. [d]Ref. 10. [e]*d*: diameter. [f]*w*: width. [g]equation of state for each ZnO nanowires was included in Appendix IV (Fig. A21, Fig. A28, and Fig. A34)

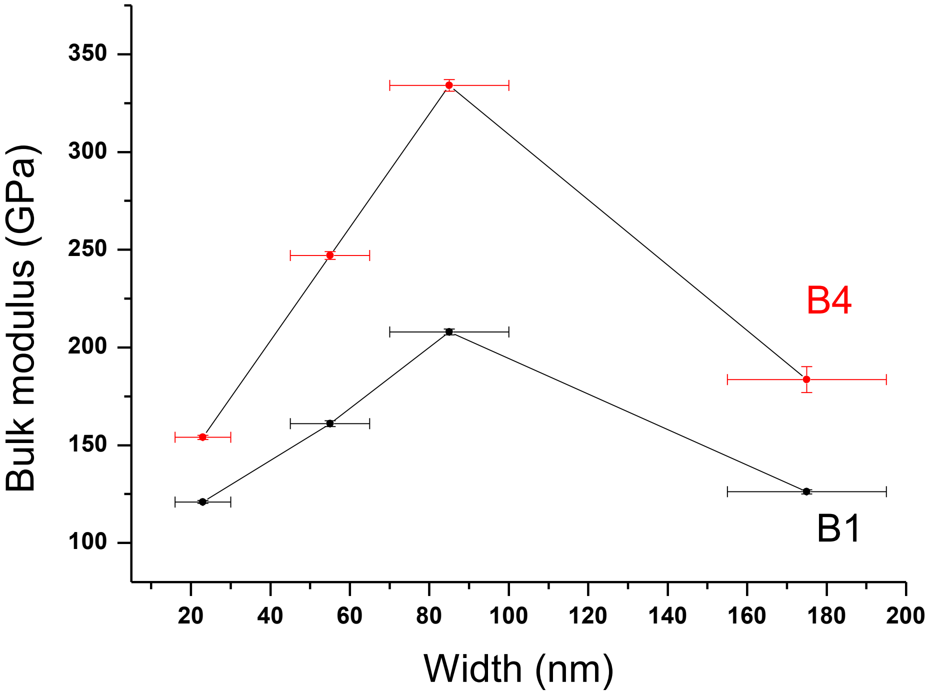

Figure 9.6 Size dependence of the bulk modulus of B4 (square) and B1 (circle) phases for ZnONW, ZnONW1, ZnONW2 and ZnONW3. The lines are only for eye guidance.

The compressibility of B4 and B1 phases were examined and their bulk moduli (B_0) were listed in Table 9.1 in comparison with reference values.[6,7,15,16,18] All the B_0 values were obtained by fitting the pressure-volume curves using the second-order Birch-Murnaghan equation of state with $B_0^{'}$ fixed at 4. B_0 values for B4 and B1 phases of ZnONW1 were 126 GPa and 184 GPa, respectively, which were similar to those for bulk ZnO (i.e. 135 GPa and 178 GPa).[15] This result further supported our previous conclusion that nanomaterials trended to behave more similarly to their bulk counterparts as their sizes became comparable. The relationship between bulk modulus of ZnO nanowires and their widths (as shown in Fig. 9.6) demonstrated a trend that the compressibility was enhanced as the size decreased existing in ZnO nanowires with width less than 100 nm. So far there was no simple explanation for the size effect on the compressibility. The same size induced enhancement of compressibility was reported previously in other nanomaterials such as PbS[24] and γ-Al_2O_3[32]. Both papers proposed an explanation that the enhancements of compressibility might be due to the increasing stress of the nanomaterials upon compression. As particle size decreased, the efficiency of transmitting the compressive stress from environment (e.g. pressure transmitting medium) to the sample may be improved, resulting in the enhancement of compressive stress.[24,32] In this study, the SEM images of the nanowires taken before and after compression clearly showed that their morphology were altered significantly upon compression, especially ZnONW3, in which no wire shape was preserved. The nanowires broke during the compression leading to reduction of grain size, which might further enhance the compressive stress in the sample, resulting in a further increase in the compressibility. Among all the nanowires studied in this paper, ZnONW presented the highest B_0 values of 208 GPa and 334 GPa for B4 and B1 phase, respectively. In contrast, ZnONW2, which had a slightly smaller width, exhibited significantly lower bulk moduli of 161 GPa and 247 GPa for B4 and B1 phases. There are many factors that determine the mechanical properties of nanomaterilas. In this study, the difference in the quality of crystallinity and uniformity may contribute to various compressibilities observed. By examining their morphologies (Fig. 8.1 in Chapter 8 and Fig. A22 of Appendix IV), we found ZnONW had better uniformity and smooth surface, while ZnONW2 had coarse surface. Moreover, impurity was observed in ZnONW2 as well. The coarse surface and impurity may cause more defects in ZnONW2, which may reduce its mechanical strength.[20] Therefore, ZnONW2 showed a significant higher compressibility than ZnONW.

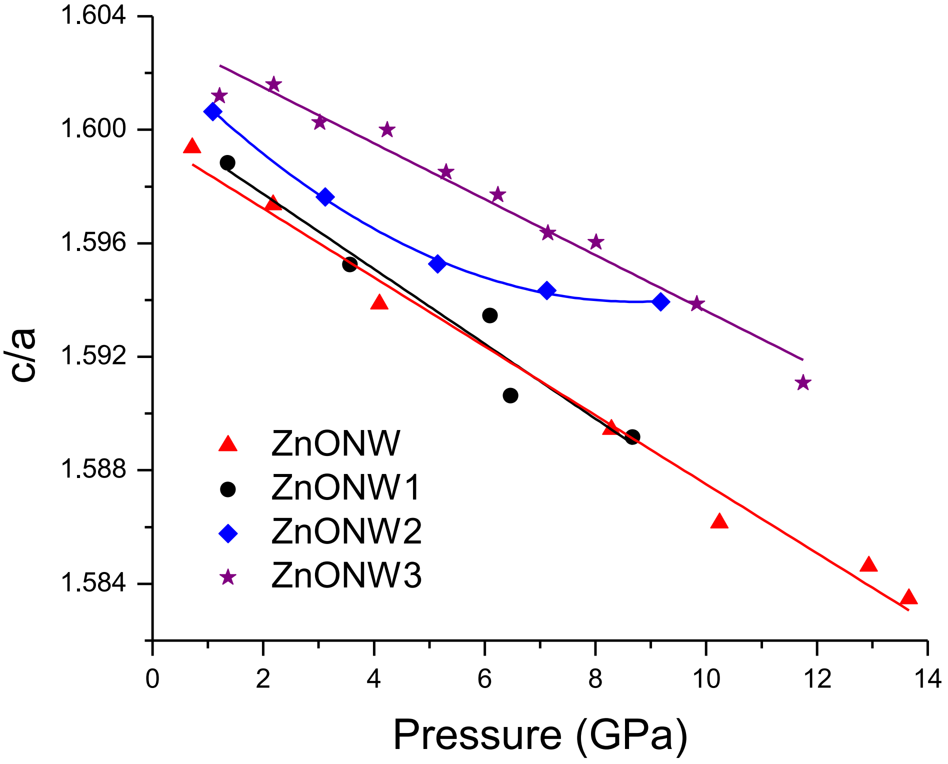

Figure 9.7 **Pressure dependence of c/a for ZnONW, ZnONW1, ZnONW2 and ZnONW3.**

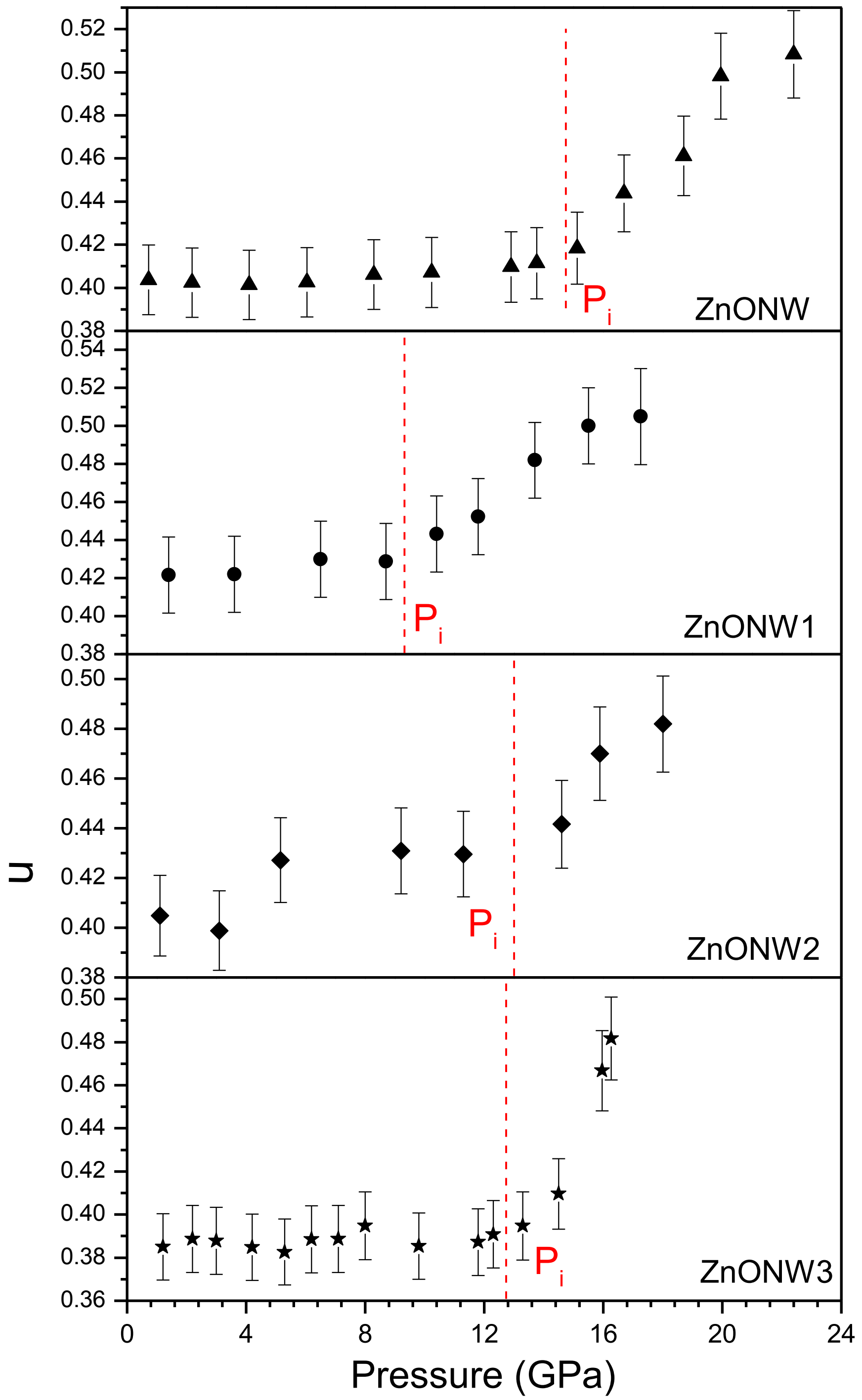

Figure 9.8 Pressure dependence of *u* for ZnONW, ZnONW1, ZnONW2 and ZnONW3. The dotted lines are the boundaries of the B4-to-B1 phase transition labeled with P_i.

In order to understand the phase transition mechanism, the c/a ratio for the B4 phase as a function of pressure was plotted in Fig. 9.7. The slopes of all the samples were negative, which not only confirmed that the pressure induced lattice deformation was more prominent along the c-axis below the onset transition pressure, but also suggested the phase transition in ZnO followed the hexagonal path, which was proposed by Limpijumnong *et al.*[6,9,18] Because following hexagonal path, the c/a ratio first decreased continuously, whereas the *u* increased to 0.5. Then the γ angle (60°) opened up to 90°, and B1 phase formed eventually. In addition, the internal structural parameter *u* for each sample was analyzed as well. The obtained *u* values from the Rietveld refinements for each sample were plotted as a function of pressure in Fig. 9.8. For each sample, the *u* value increased slowly with small variations below the phase transition pressures (P_i). Thereafter, the *u* values increased quickly up to ~ 0.50 at pressure where phase transition completed. These results further suggested that the B4 to B1 phase transformation in ZnO nanowire was more likely via the hexagonal route than the tetragonal path. Same theory was also proposed for other ZnO materials, such as nanocrystals[6], nanotubes[7] and corresponding bulk counterparts[15] indicated by either the changes of c/a ratio or the values of *u*. Therefore, our results indicated that the transformation path for B4 to B1 of ZnO was independent of grain size or one-dimensionality.

9.4 Conclusions

In conclusion, high-pressure behaviors of three different ZnO nanowires samples were investigated and compared with results of previous study as well as corresponding nanocrsytals and bulk counterparts. Our results showed that ZnO nanowires exhibited significantly broadened phase transition regions compared with bulk materials regardless of their width, in which the pressure induced morphology modification was believed to play a major role. Our results also suggested that nanomaterials will behave similarly as bulk materials when their sizes are comparable. Most importantly, a trend, that decreases in the width resulted in the enhancement of compressibility, was observed that in ZnO nanowires with width less than 100 nm. Analysis of the c/a ratio as well as the *u* value further supported that the B4 to B1 phase transition followed the hexagonal path instead of the tetragonal route.

9.5 References

(1) Wang, X. D.; Song, J. H.; Liu, J.; Wang, Z. L. *Science* **2007**, *316*, 102.

(2) Liu, Y.; Yang, Q.; Zhang, Y.; Yang, Z. Y.; Wang, Z. L. *Adv. Mater.* **2012**, *24*, 1410.

(3) Cheng, H. M.; Hsu, H. C.; Tseng, Y. K.; Lin, L. J.; Hsieh, W. F. *J. Phys. Chem. B* **2005**, *109*, 8749.

(4) Lu, C. Y.; Chang, S. P.; Chang, S. J.; Hsueh, T. J.; Hsu, C. L.; Chiou, Y. Z.; Chen, C. *IEEE Sens. J.* **2009**, *9*, 485.

(5) Minne, S. C.; Manalis, S. R.; Quate, C. F. *Appl. Phys. Lett.* **1995**, *67*, 3918.

(6) Kumar, R. S.; Cornelius, A. L.; Nicol, M. F. *Curr. Appl. Phys.* **2007**, *7*, 135.

(7) Hou, D. B.; Ma, Y. Z.; Gao, C. X.; Chaudhuri, J.; Lee, R. G.; Yang, H. B. *J. Appl. Phys.* **2009**, *105*, 104317.

(8) Gao, Z. J.; Gu, Y. S.; Zhang, Y. *J. Nanomater.* **2010**, *5*, 462032.

(9) Zhuravlev, K. K.; Oo, W. M. H.; McCluskey, M. D.; Huso, J.; Morrison, J. L.; Bergman, L. *J. Appl. Phys.* **2009**, *106*, 013511.

(10) Cui, S. X.; Feng, W. X.; Hu, H. Q.; Feng, Z. B.; Wang, Y. X. *J. Alloy. Compd.* **2009**, *476*, 306.

(11) Decremps, F.; eacute; ric; Pellicer-Porres, J.; Saitta, A. M.; Chervin, J.-C.; Polian, A. *Phys. Rev. B* **2002**, *65*, 092101.

(12) Decremps, F.; Datchi, F.; Saitta, A. M.; Itie, J. P.; Polian, A.; Baudelet, F.; Pascarelli, S. *High Pressure Res.* **2002**, *22*, 365.

(13) Wu, H. Y.; Cheng, X. L.; Hu, C. H.; Zhou, P. *Physica B* **2010**, *405*, 606.

(14) Wang, L. H.; Liu, H. Z.; Qian, J.; Yang, W. G.; Zhao, Y. S. *J. Phys. Chem. C* **2012**, *116*, 2074.

(15) Liu, H. Z.; Ding, Y.; Somayazulu, M.; Qian, J.; Shu, J.; Hausermann, D.; Mao, H. K. *Phys. Rev. B* **2005**, *71*, 212103.

(16) Karzel, H.; Potzel, W.; Kofferlein, M.; Schiessl, W.; Steiner, M.; Hiller, U.; Kalvius, G. M.; Mitchell, D. W.; Das, T. P.; Blaha, P.; Schwarz, K.; Pasternak, M. P. *Phys. Rev. B* **1996**, *53*, 11425.

(17) Jiang, J. Z. *J. Mater. Sci.* **2004**, *39*, 5103.

(18) Dong, Z.; Zhuravlev, K. K.; Morin, S. A.; Li, L.; Jin, S.; Song, Y. *J. Phys. Chem. C* **2012**, *116*, 2102.

(19) Tolbert, S. H.; Alivisatos, A. P. *Science* **1994**, *265*, 373.

(20) Dong, Z. H.; Song, Y. *Chem. Phys. Lett.* **2009**, *480*, 90.

(21) Dong, Z. H.; Song, Y. *J. Phys. Chem. C* **2010**, *114*, 1782.

(22) Dong, Z. H.; Song, Y. *Appl. Phys. Lett.* **2009**, *96*, 151903.

(23) Jiang, J. Z.; Gerward, L.; Frost, D.; Secco, R.; Peyronneau, J.; Olsen, J. S. *J. Appl. Phys.* **1999**, *86*, 6608.

(24) Qadri, S. B.; Yang, J.; Ratna, B. R.; Skelton, E. F.; Hu, J. Z. *Appl. Phys. Lett.* **1996**, *69*, 2205.

(25) Jiang, J. Z.; Gerward, L.; Secco, R.; Frost, D.; Olsen, J. S.; Truckenbrodt, J. *J. Appl. Phys.* **2000**, *87*, 2658.

(26) Rekhi, S.; Saxena, S. K.; Lazor, P. *J. Appl. Phys.* **2001**, *89*, 2968.

(27) Jiang, J. Z.; Olsen, J. S.; Gerward, L.; Morup, S. *Europhys. Lett.* **1998**, *44*, 620.

(28) Jiang, J. Z.; Olsen, J. S.; Gerward, L.; Frost, D.; Rubie, D.; Peyronneau, J. *Europhys. Lett.* **2000**, *50*, 48.

(29) Yan, X. Q.; Gu, Y. S.; Zhang, X. M.; Huang, Y. H.; Qi, J. J.; Zhang, Y.; Fujita, T.; Chen, M. W. *J. Phys. Chem. C* **2009**, *113*, 1164.

(30) Maouche, D.; Saoud, F. S.; Louail, L. *Mater. Chem. Phys.* **2007**, *106*, 11.

(31) Liu, H. Z.; Tse, J. S.; Mao, H. K. *J. Appl. Phys.* **2006**, *100*, 093509.

(32) Chen, B.; Penwell, D.; Benedetti, L. R.; Jeanloz, R.; Kruger, M. B. *Phys. Rev. B* **2002**, *66*, 144101.

Chapter 10 Summary and Future work

10.1 Summary

In this thesis, a series of materials were studied under high pressure, which were assembled into two parts. In part I, molecules with ring structures, chlorocyclohexane (CCH), azobenzene (AB) and its derivative compound hydrazobenzene (HAB), were examined under high pressure aiming at investigating pressure-induced phase transformations, molecular conformation change, stability of ring structures, as well as their reactivity. In part II, one dimensional (1D) nanostructured inorganic materials, such as BN nanotubes, GaN nanowires, TiO_2 nanowires, and ZnO nanowires, were studied under high pressure focusing on the pressure-induced structural transitions, compressibility, as well as the size- and morphology- effect on their high-pressure behaviors. From our studies, we could draw some conclusions of pressure effect on molecular structures.

10.1.1 Pressure effect on molecules with ring structures

The results of part I demonstrated that molecules that have high degree of freedom in rearranging molecular conformation would likely undergo physical phase transitions which were characterized of conformational change (e.g., CCH) and distortion of molecular skeleton (e.g., HAB), and so on before chemical transitions occur. For AB molecules, the conjugated electronic configuration increased their reactivity, thus would undergo chemical transitions such as pressure-induced polymerization and amorphization, etc. Moreover, no destruction of ring structure was observed in any of these compounds, indicating their ring structures were surprisingly stable under high pressure.

10.1.2 Pressure effect on 1D structured nanomaterials

Our results in part II showed that 1D nanomaterials behaved differently under high pressure in comparison with their corresponding nanoparticles and bulk counterparts. Broadened phase transition regions were observed in all the 1D nanomaterials studied even in nanowires that have similar size as the bulk materials (e.g., ZnONW1 in Chapter 9), indicating that morphology might be main factor that caused the sluggish phase transition range in 1D nanomaterials comparing with bulk materials. Moreover, our results also indicated that 1D nanomaterials will behave similarly as their corresponding bulk counterparts as their widths become comparable (e.g., NW2 of TiO_2 nanowires in Chapter 7 and ZnONW1 in Chapter 9). In ZnO nanowires, a trend that the compressibility increases as their width decreasing was observed. In addition, by examining the morphology and structures of all the recovered samples in this thesis, we found it is possible to obtain materials with desired structures as well as morphology via combined pressure-morphology tuning.

10.2 Future work

By finishing this thesis, we have accumulated some basic knowledge of pressure effect on molecular structures. However, there are many problems remained for further investigation.

For instance, in part I, the crystal structures of high-pressure phases of CCH are still unclear, which required additional investigations using different probes such as X-ray diffraction to solve the structures. For AB and HAB, higher pressure (e.g., > 30 GPa) is needed to study pressure-induced polymerization involving the phenyl ring. Moreover, it is very interesting to study photon induced chemical reaction in these molecules, especially for AB that has conjugated electronic configuration.

In part II, in order to gain more information to further understanding size- and morphology- effect on the high-pressure behaviors of TiO_2 nanowires and ZnO nanowires, more samples with less impurity and within good uniformity are needed, and investigated under high pressure.

Appendix I Data Analysis Methods

A1.1 FIT2D[*]

FIT2D is both a general purpose and specialist analysis program supporting one and two dimensional data processing. The FIT2D also recognizes data from many types of detectors such as MAR detector which is used widely in synchrotron facilities. Therefore, it is used generally at most of the European Synchrotron Research Facility beam lines and by many other crystallography groups throughout the world. For the XRD experiments, raw data are collected as 2D images of Debye-Scherrer rings which are difficult for further analysis. FIT2D allows the 2D images to be integrated to 1D profile with user specified 2θ or radial direction. Therefore, it provides a variety of different output possibilities, such as a number of different 2θ scans, for different azimuth ranges; a 1D profile of intensity of a ring as a function of azimuth; or a polar transform of the data. In addition, it also allows interactive definition of masked areas i.e. pixel which will be ignored during further operations. Moreover, the output formats are also variable such as GSAS formats, Cerius formats, as well as ASCII format, which can be used for multiple purposes for further analysis. For instance, the GSAS format can be used in the Rietveld refinement analysis. Following are the typical interfaces of the FIT2D program.

---

[*] Website: http://www.esrf.eu/computing/scientific/FIT2D/

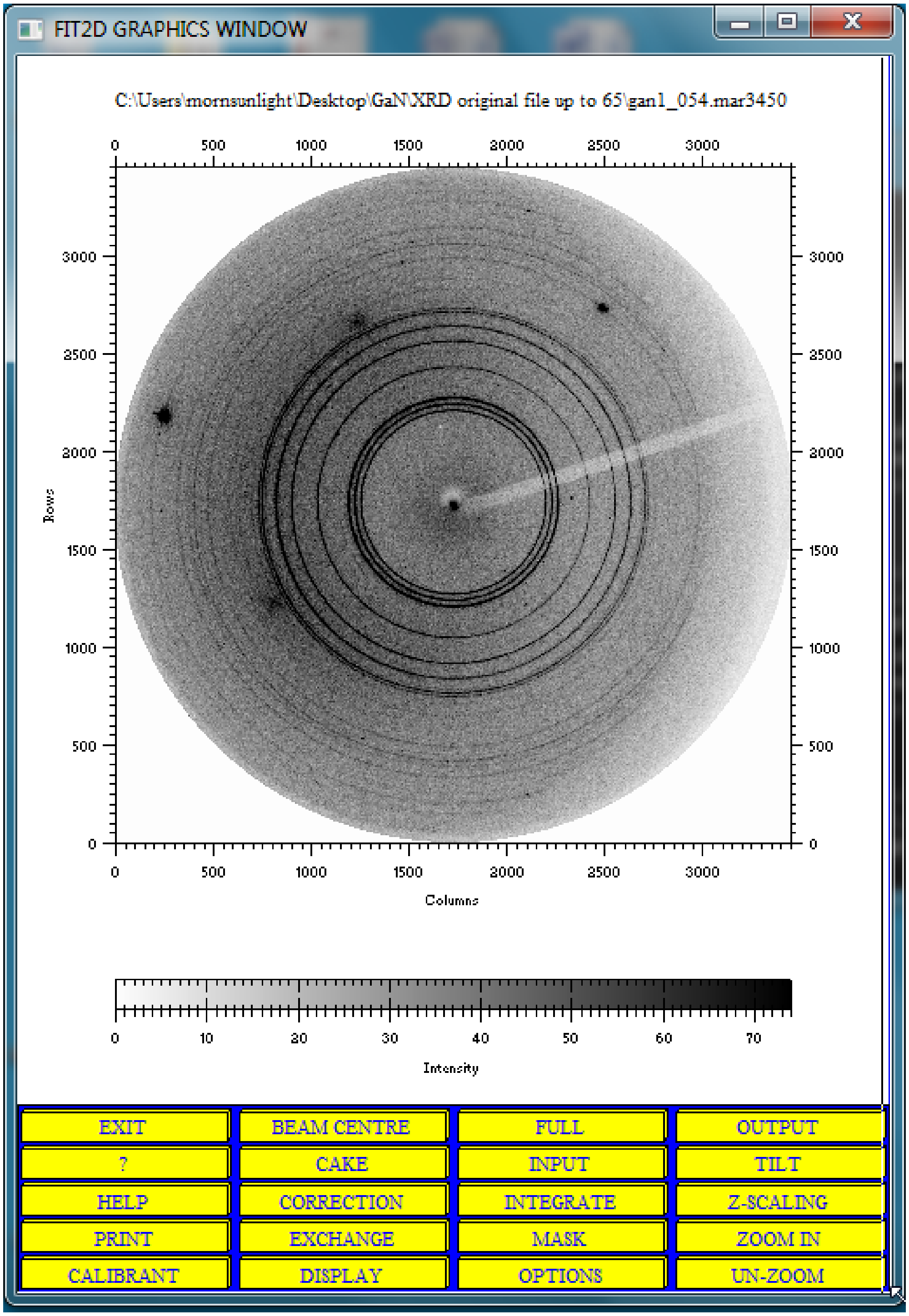

C:\Users\mornsunlight\Desktop\GaN\XRD original file up to 65\gan1_054.mar3450

Figure A1 Raw 2D XRD image of GaN nanowires taken at ambient pressure.

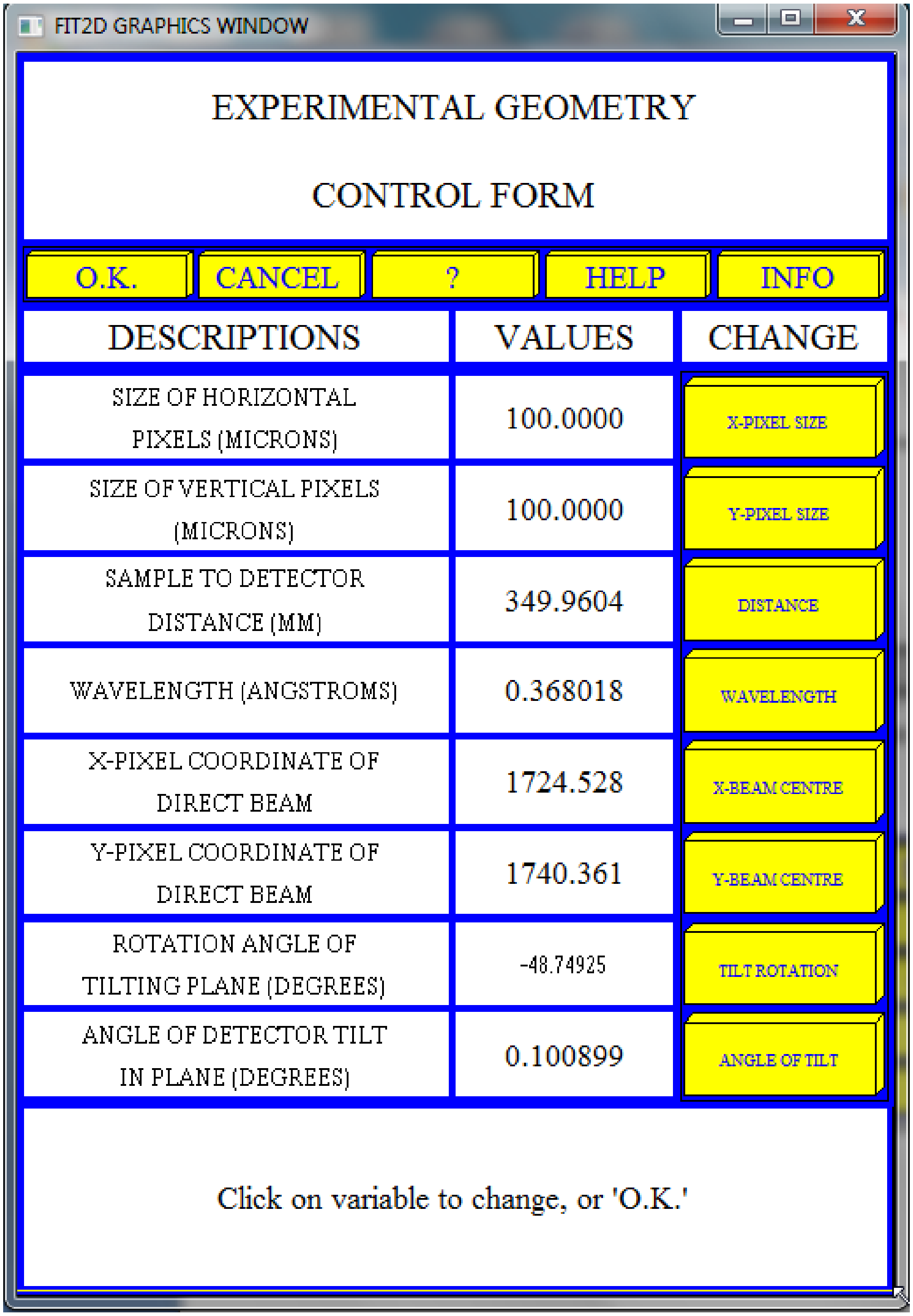

EXPERIMENTAL GEOMETRY

CONTROL FORM

DESCRIPTIONS	VALUES	CHANGE
SIZE OF HORIZONTAL PIXELS (MICRONS)	100.0000	X-PIXEL SIZE
SIZE OF VERTICAL PIXELS (MICRONS)	100.0000	Y-PIXEL SIZE
SAMPLE TO DETECTOR DISTANCE (MM)	349.9604	DISTANCE
WAVELENGTH (ANGSTROMS)	0.368018	WAVELENGTH
X-PIXEL COORDINATE OF DIRECT BEAM	1724.528	X-BEAM CENTRE
Y-PIXEL COORDINATE OF DIRECT BEAM	1740.361	Y-BEAM CENTRE
ROTATION ANGLE OF TILTING PLANE (DEGREES)	-48.74925	TILT ROTATION
ANGLE OF DETECTOR TILT IN PLANE (DEGREES)	0.100899	ANGLE OF TILT

Click on variable to change, or 'O.K.'

Figure A2 Experimental parameters used for data analysis for GaN nanowires.

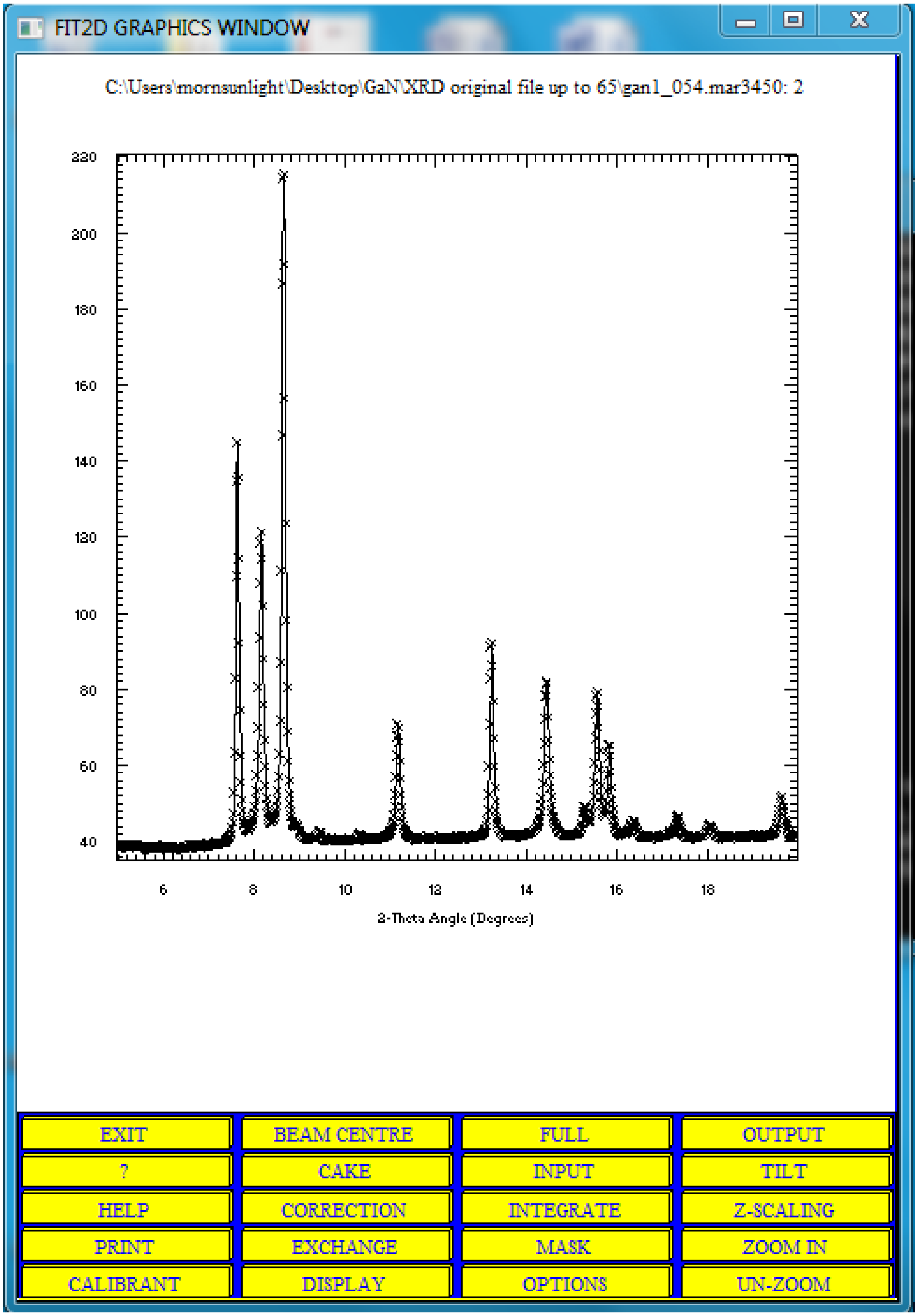

Figure A3 1D X-ray diffraction pattern converted from the original 2D image of GaN nanowires in Fig. A1.

A1.2 Rietveld refinement method[*]

Rietveld refinement is a technique developed by Hugo Rietveld for use in the characterization of crystalline materials. The neutron and XRD of powder samples result in patterns characterized by peaks in intensity at certain positions. The height, width and position of these peaks can be used to determine many aspects of the materials structure. The Rietveld method uses a least squares approach to refine a theoretical line profile until it fits the measured profiles.

The principle of the Rieveld method is to minimize a function M which represents the difference between a calculated profile y(calc) and the observed profile y(obs). The function M is defined as following.

$$M = \sum_i W_i \left\{ y_i^{obs} - \frac{1}{c} y_i^{calc} \right\}^2 \qquad \text{(A1)}$$

where W_i is the statistical weight and c is an overall scale factor such that $y^{calc} = c\, y^{obs}$. The most used software for Rietveld refinement is the General Structure Analysis System (GSAS), see Appendix III.

Many programs are written to process Rietveld refinement, such as GSAS + EXPGUI, Fullprof and PowderCel, which can be used freely and are available on the internet. There are other commercial programs such as MDI Jade and Bruker ToPAS. In this project, the program GSAS + EXPGUI is used for all the refinements.

---

[*] Website: http://www.ccp14.ac.uk/ccp/web-mirrors/lutterotti/~luttero/laboratoriomateriali/Rietveld.pdf

A1.3 GSAS[*]

GSAS is a comprehensive system for the refinement of structural models to both X-ray and neutron diffraction data, which is created by Allen C. Larson and Robert B. Von Dreele of Los Alamos National Laboratory. The GSAS package can be used with both single and powder crystal diffraction data, even both simultaneously. In GSAS, up to 99 different sets of data can be modeled using mixtures of up to 9 different phases. However, GSAS is copyright and cannot be used freely. The advance software is EXPGUI.

EXPGUI, written by Brian H. Toby of the NIST Center for Neutron research, is a graphical interface package that allows many of the most commonly used features within GSAS to be accessed, but far from all these features. EXPGUI does two things: it can be used to directly modify the data profile in a GSAS format with a graphical user interface (GUI), and it can also be used to invoke the programs inside the GSAS package such as EXPEDT, GENLES and FOURIER etc.

---

[*] http://www.ccp14.ac.uk/ccp/ccp14/ftp-mirror/gsas/public/gsas/manual/GSASManual.pdf

Appendix II Supporting Materials for Chapter 6

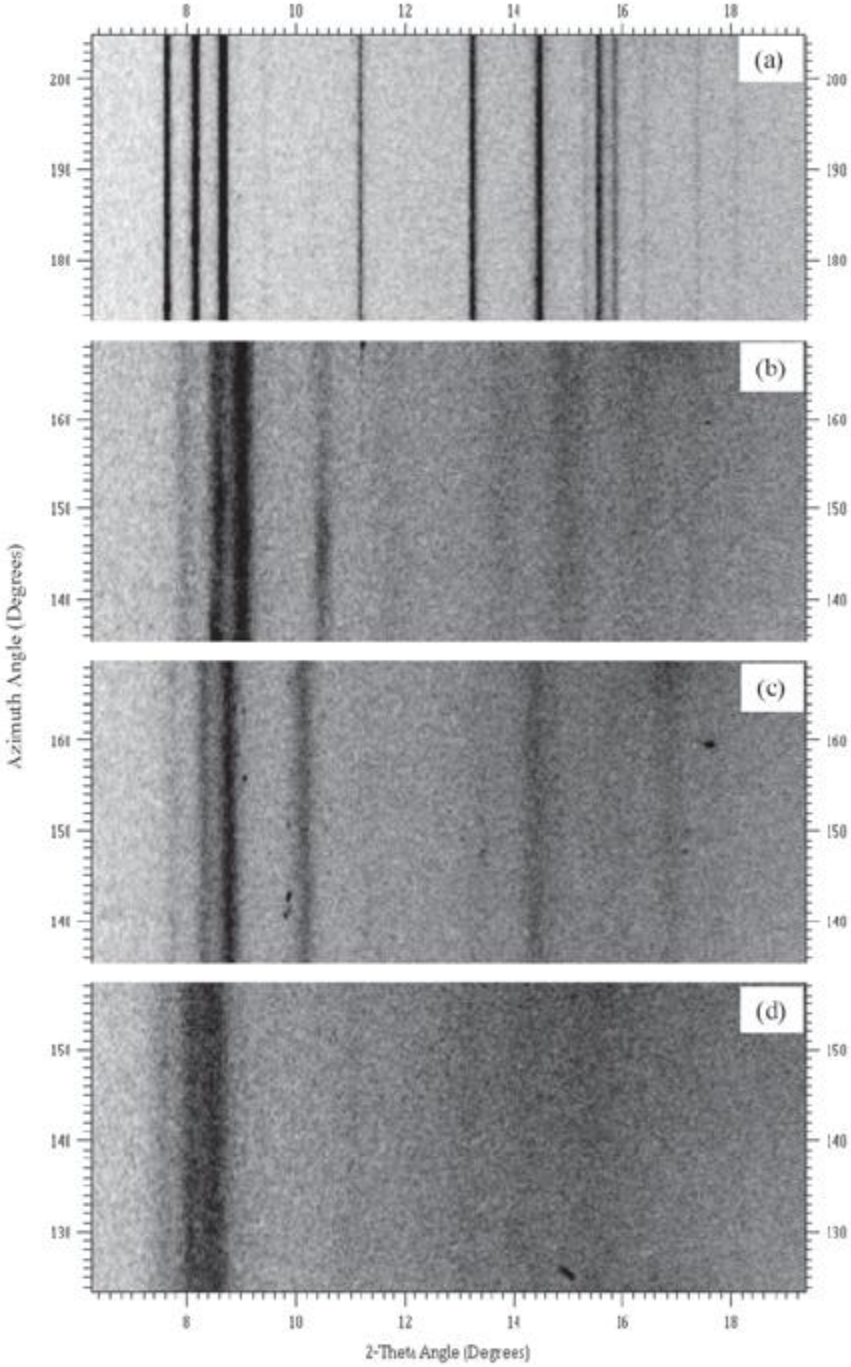

Figure A4 Debye-Scherrer 2D X-ray diffraction patterns of GaN nanowires at ambient pressure (a), 65 GPa (b), 20.9 GPa upon decompression (c) and ambient pressure upon complete decompression (d).

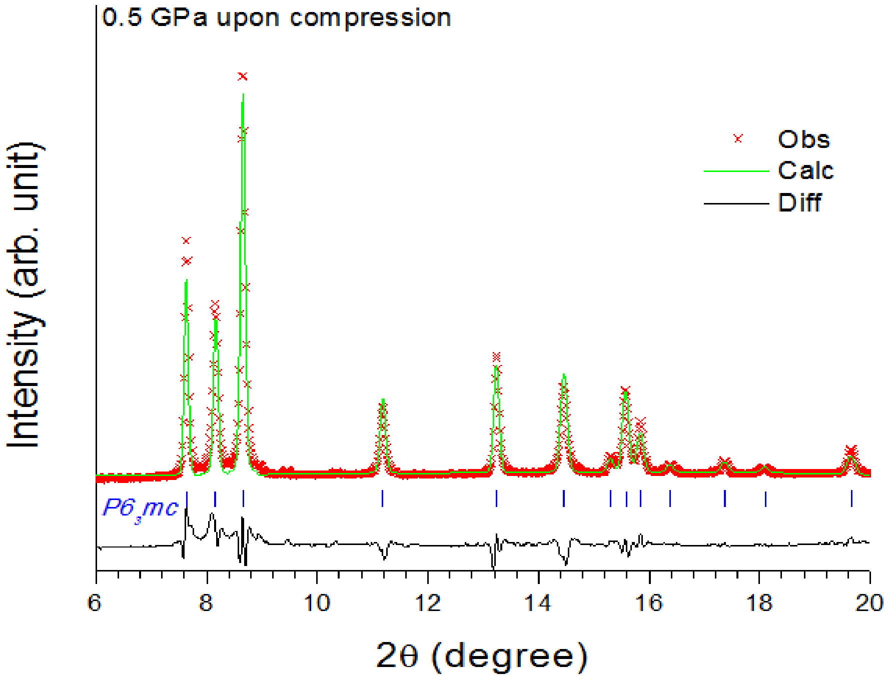

Figure A5 Rietveld refinement of XRD pattern for GaN nanowires at 0.5 GPa on compression. The observed data are depicted in crosses (obs), while green and black solid lines are the calculated (calc) profile and the difference (diff: $I_{obs} - I_{calc}$) curve, respectively. The vertical bars indicate the reflection positions for crystal structures: blue: B4 phase with $P6_3mc$ space group; and magenta: B1 phase with $Fm\bar{3}m$ space group.

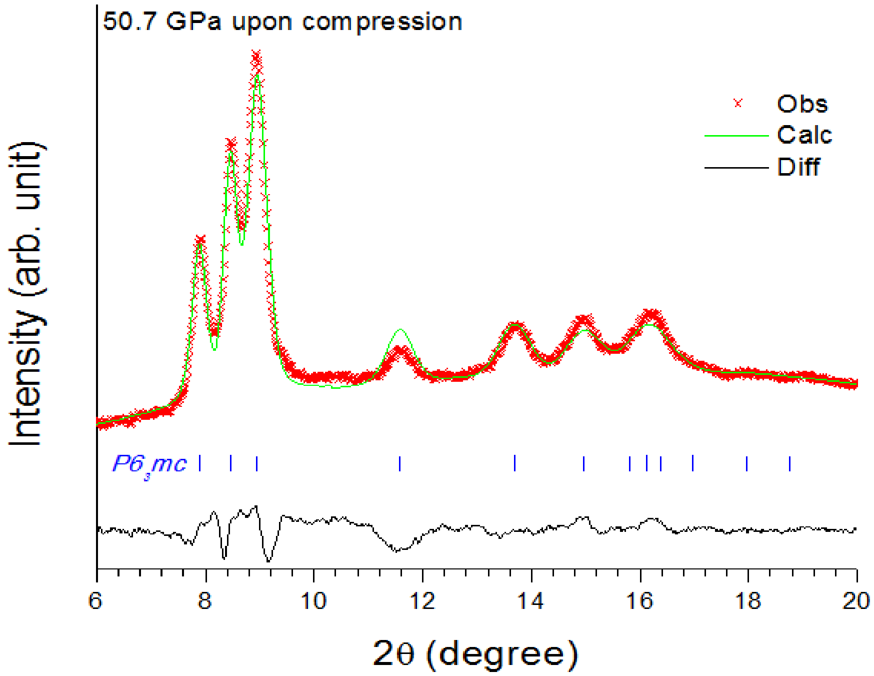

Figure A6 Rietveld refinement of XRD pattern for GaN nanowires at 50.7 GPa on compression. See Fig. A5 for figure caption.

Appendix III Supporting Materials for Chapter 8

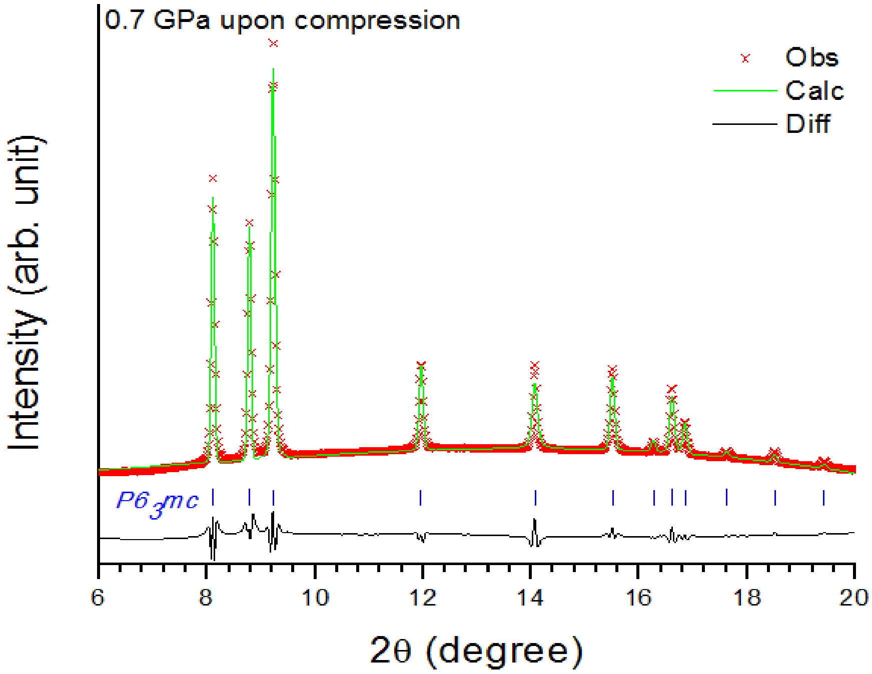

Figure A7 Rietveld refinement of XRD pattern for ZnONW at 0.7 GPa on compression. The observed data are depicted in crosses (obs), while green and black solid lines are the calculated (calc) profile and the difference (diff: $I_{obs} - I_{calc}$) curve, respectively. The vertical bars indicate the reflection positions for crystal structures: blue: B4 phase with *P*6₃mc space group; and magenta: B1 phase with *F*m$\bar{3}$m space group.

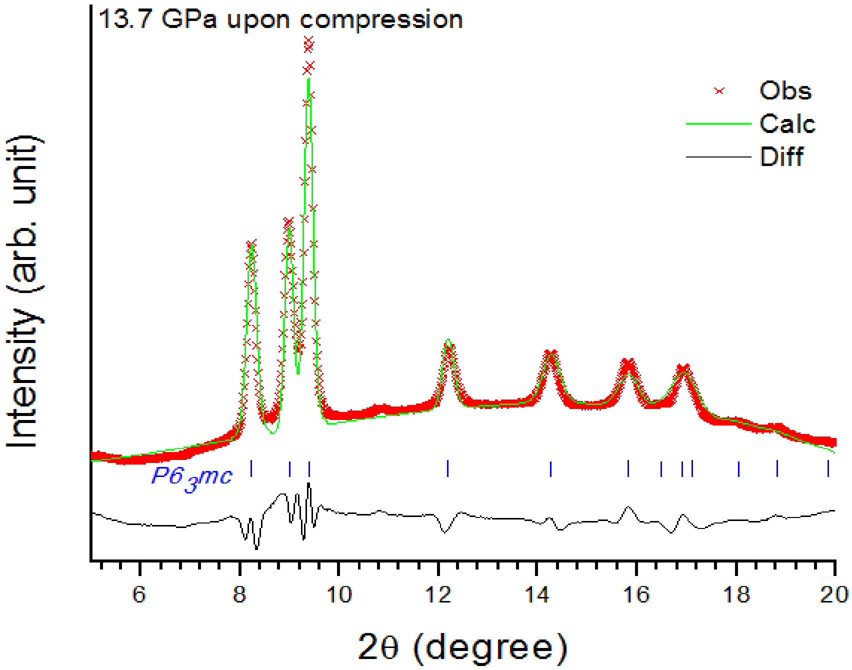

Figure A8 Rietveld refinement of XRD pattern for ZnONW at 13.7 GPa on compression. See Fig. A7 for figure caption.

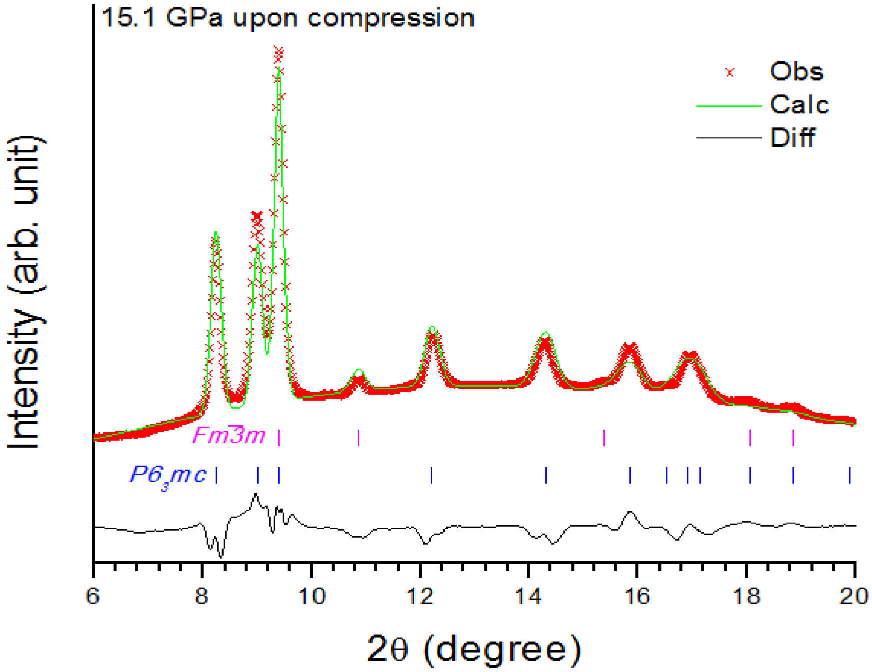

Figure A9 Rietveld refinement of XRD pattern for ZnONW at 15.1 GPa on compression. See Fig. A7 for figure caption.

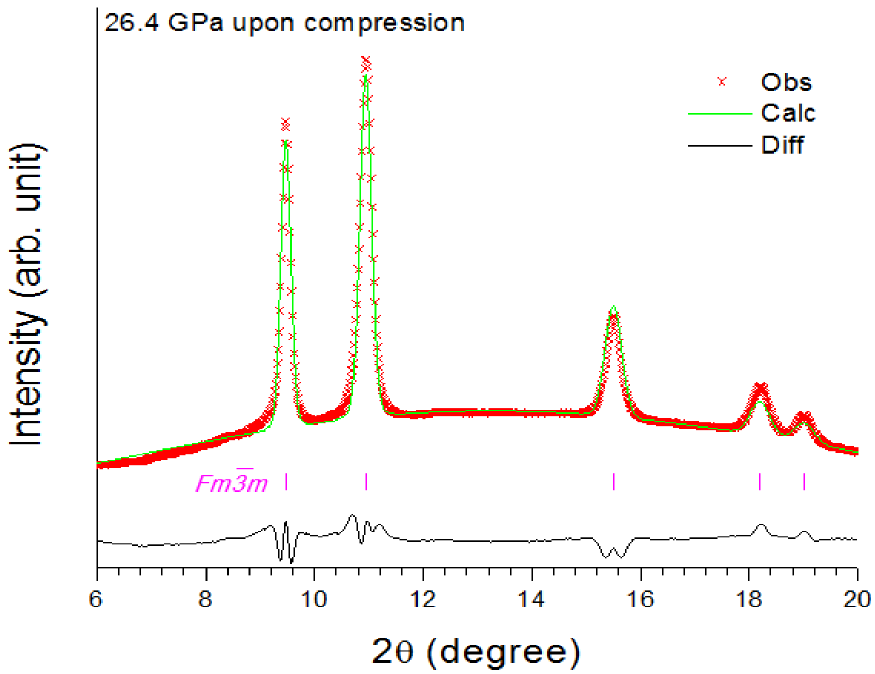

Figure A10 Rietveld refinement of XRD pattern for ZnONW at 26.4 GPa on compression. See Fig. A7 for figure caption.

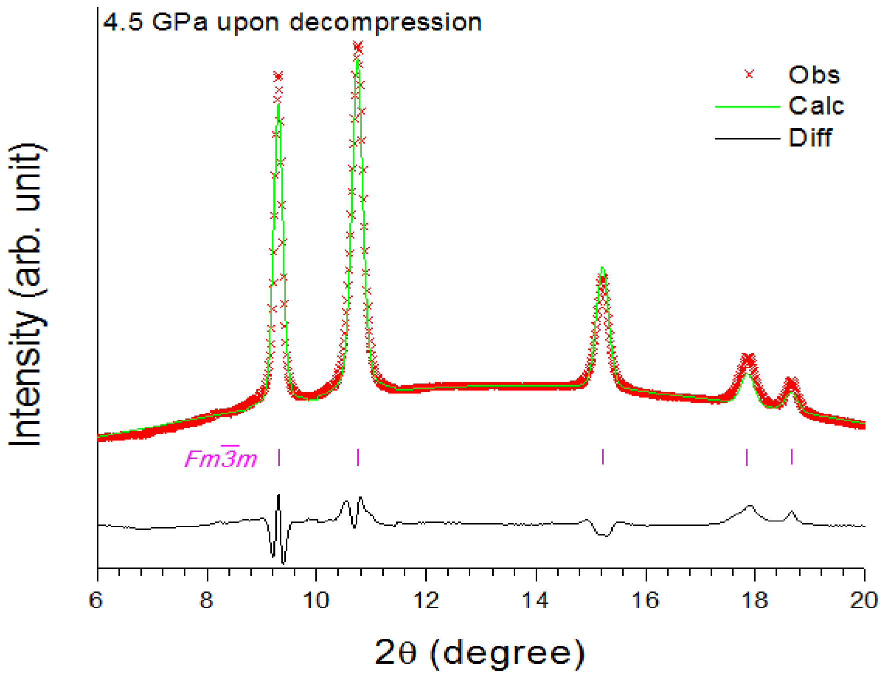

Figure A11 Rietveld refinement of XRD pattern for ZnONW at 4.5 GPa on decompression. See Fig. A7 for figure caption.

Appendix IV Supporting Materials for Chapter 9

A 4.1 Rietveld refinement analysis of ZnONW1

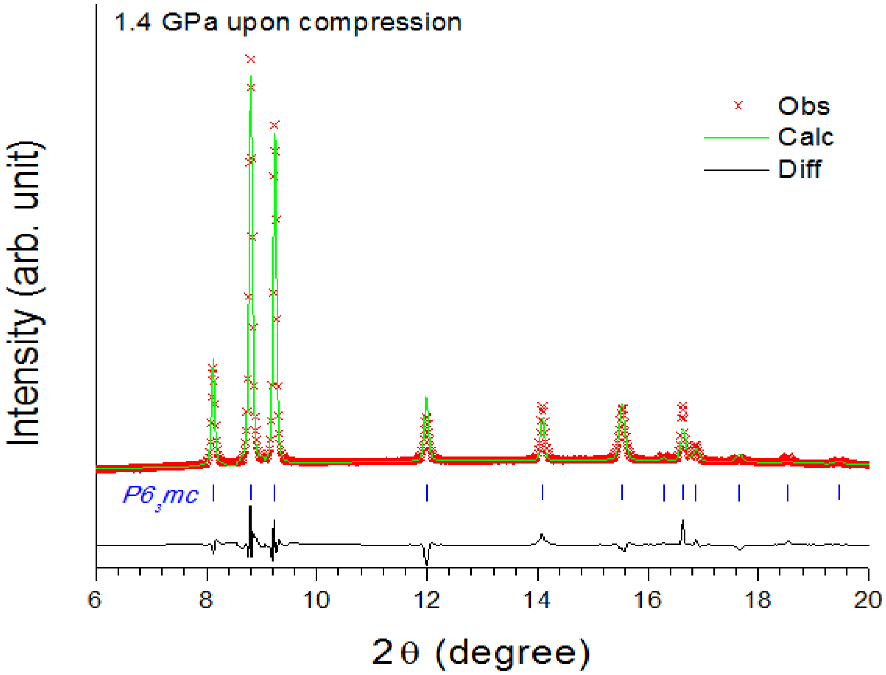

Figure A12 Rietveld refinement of XRD pattern for ZnONW1 at 1.4 GPa on compression. See Fig. A7 for figure caption.

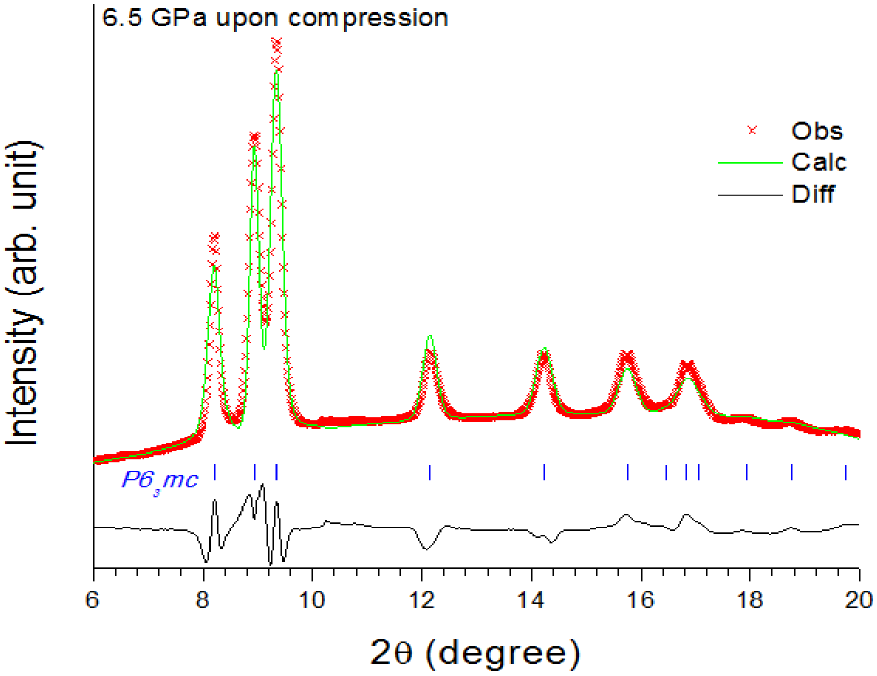

Figure A13 Rietveld refinement of XRD pattern for ZnONW1 at 6.5 GPa on compression. See Fig. A7 for figure caption.

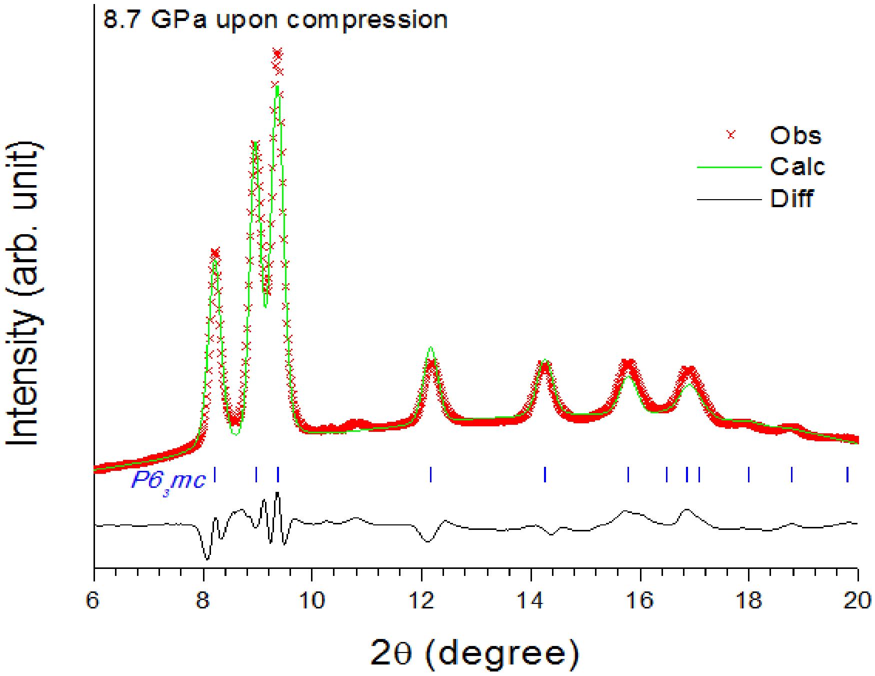

Figure A14 Rietveld refinement of XRD pattern for ZnONW1 at 8.7 GPa on compression. See Fig. A7 for figure caption.

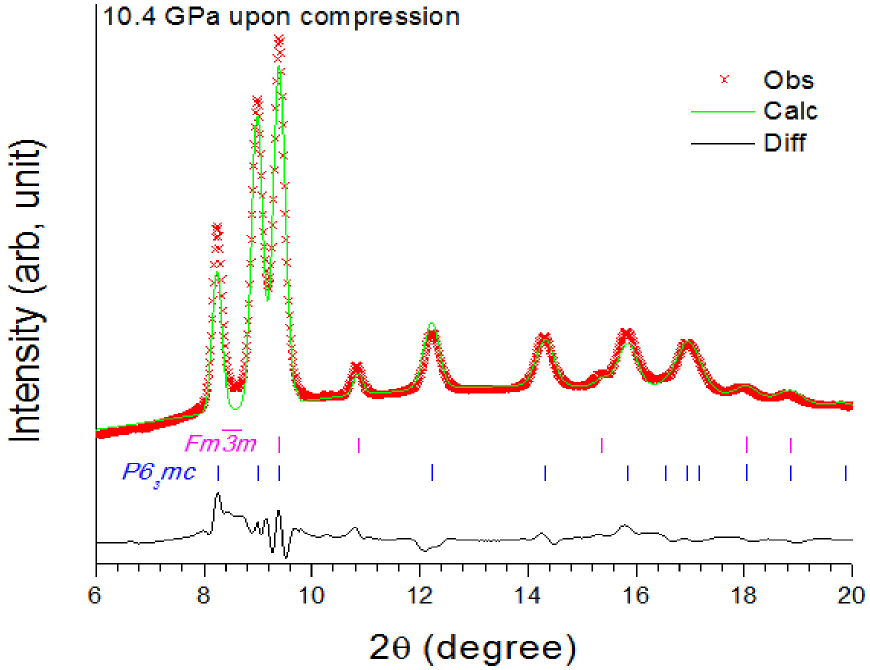

Figure A15 Rietveld refinement of XRD pattern for ZnONW1 at 10.4 GPa on compression. See Fig. A7 for figure caption.

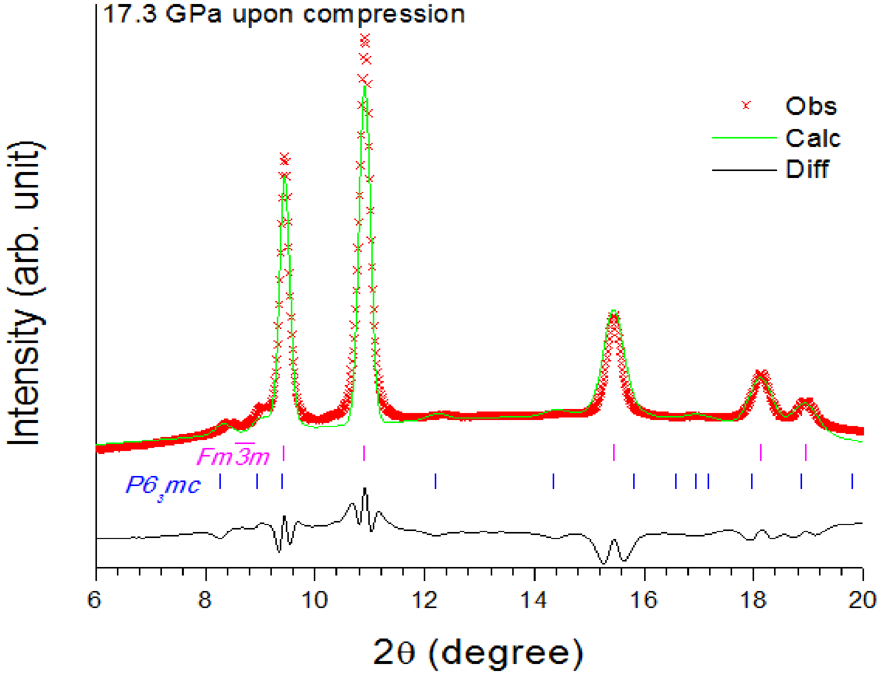

Figure A16 Rietveld refinement of XRD pattern for ZnONW1 at 17.3 GPa on compression. See Fig. A7 for figure caption.

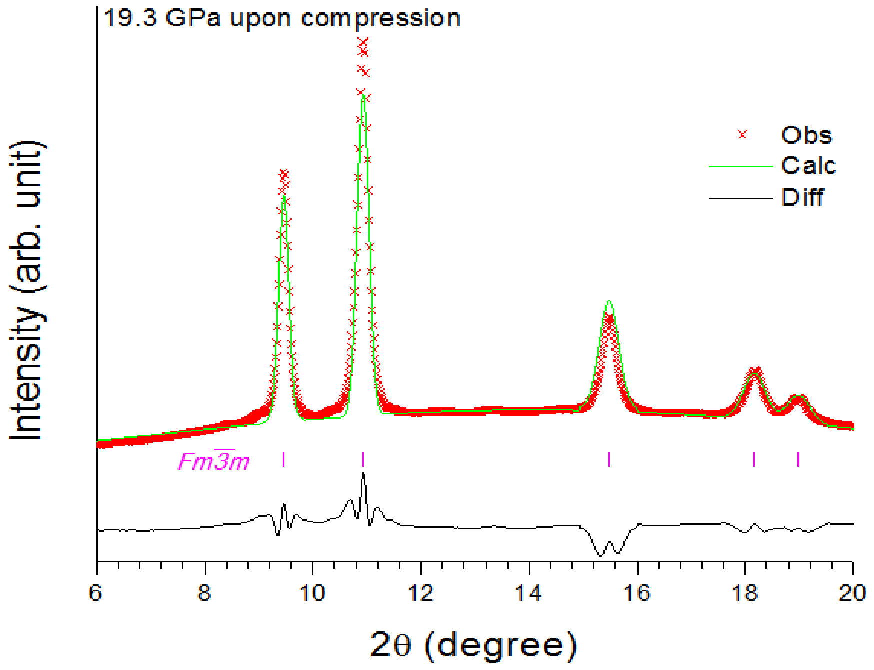

Figure A17 Rietveld refinement of XRD pattern for ZnONW1 at 19.3 GPa on compression. See Fig. A7 for figure caption.

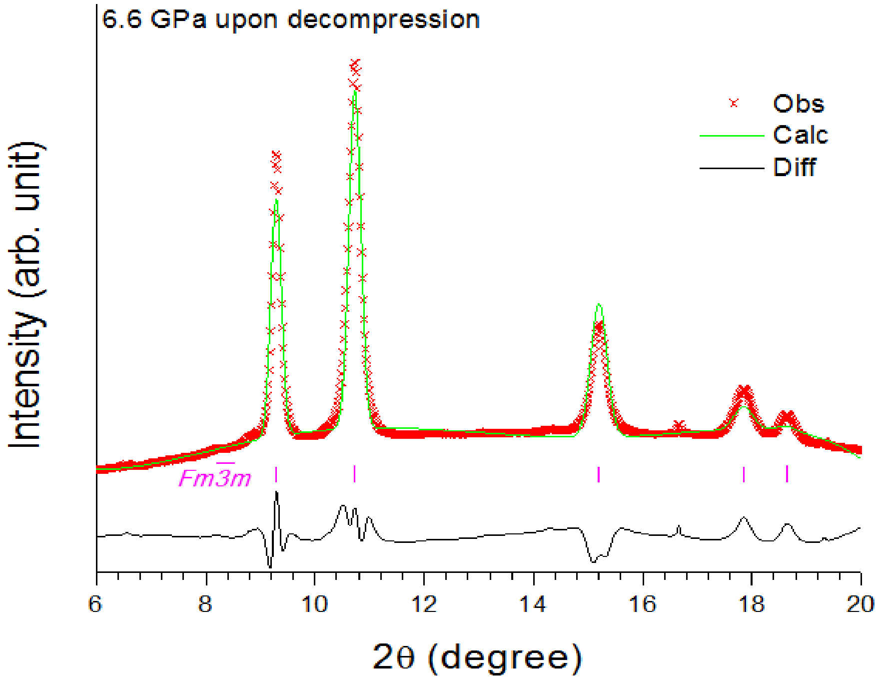

Figure A18 Rietveld refinement of XRD pattern for ZnONW1 at 6.6 GPa on decompression. See Fig. A7 for figure caption.

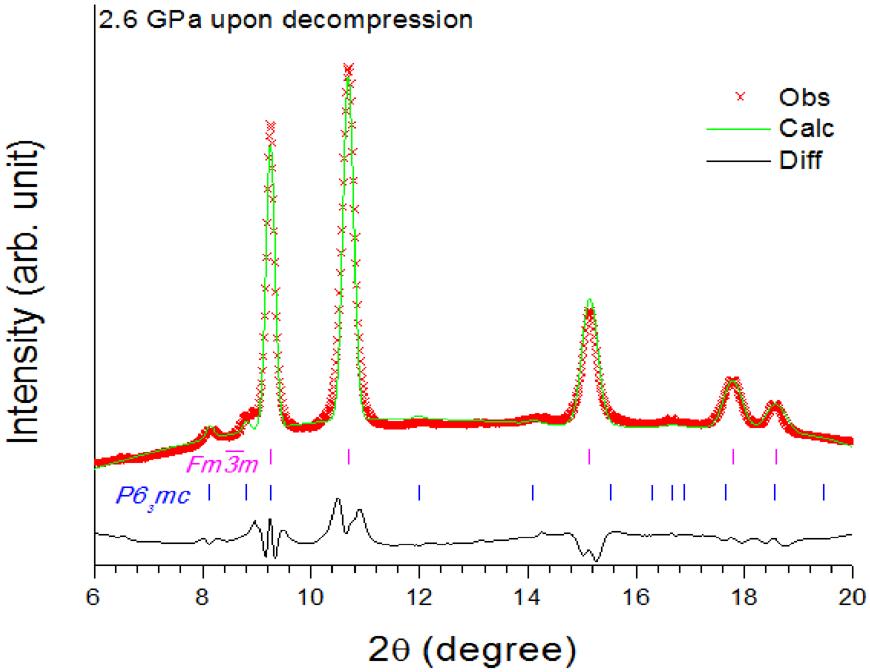

Figure A19 Rietveld refinement of XRD pattern for ZnONW1 at 2.6 GPa on decompression. See Fig. A7 for figure caption.

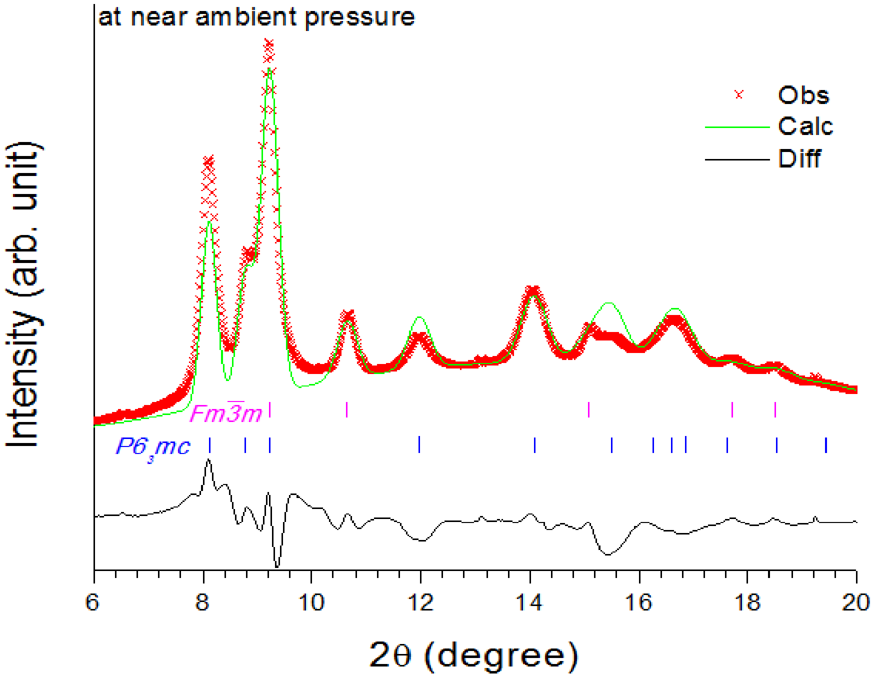

Figure A20 Rietveld refinement of XRD pattern for ZnONW1 at near ambient pressure on decompression. See Fig. A7 for figure caption.

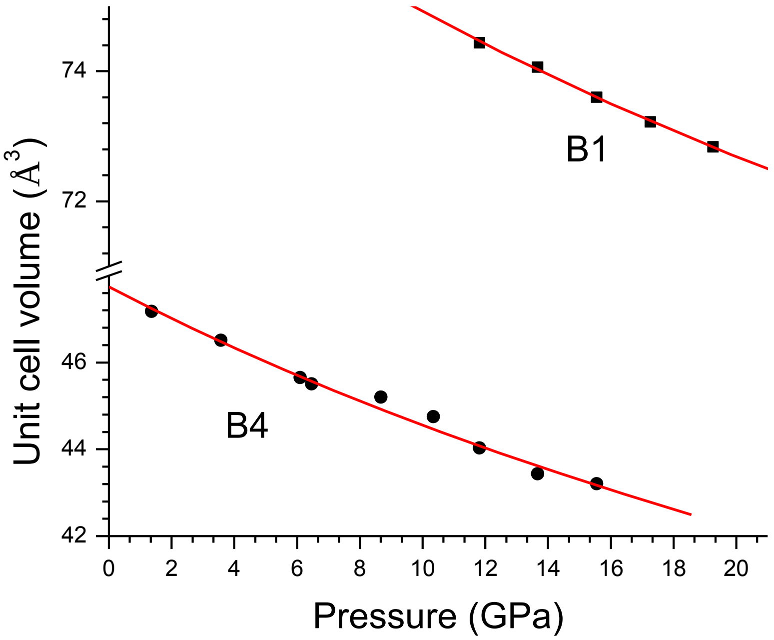

Figure A21 Pressure dependence of the unit cell volume for ZnONW1 at room temperature. Solid circles and solid squares are the experimental data points obtained from this work. Solid lines represent fits to the Birch-Murnaghan equation of state[*].

---

[*] Birch-Murnaghan equation of state: $P = \frac{3B_0}{2}\left[\left(\frac{V_0}{V}\right)^{7/3} - \left(\frac{V_0}{V}\right)^{5/3}\right]\left\{1 + \frac{3}{4}\left(B_0^{'} - 4\right)\left[\left(\frac{V_0}{V}\right)^{2/3} - 1\right]\right\}$

A 4.2 Rietveld refinement analysis of ZnONW2

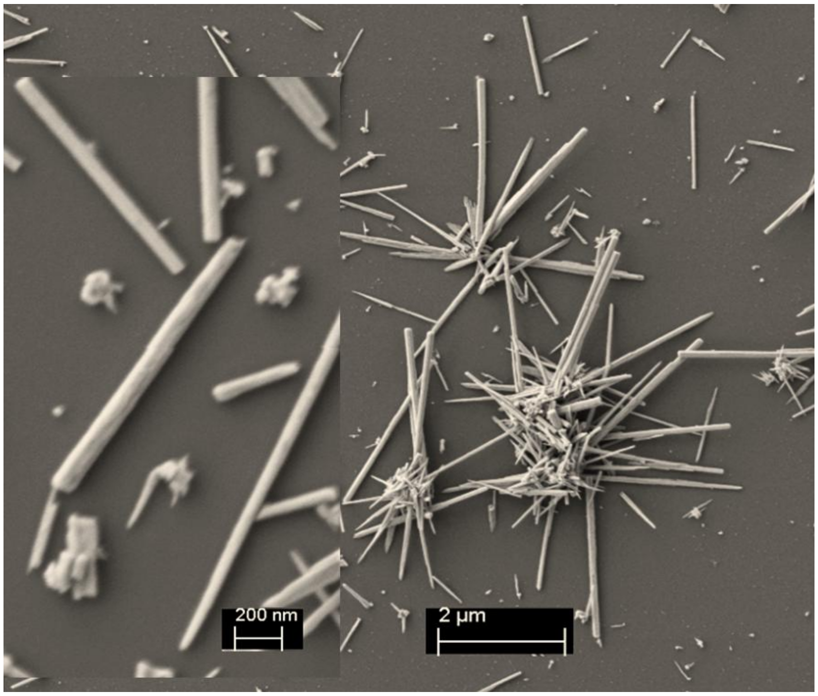

Figure A22 SEM image of ZnONW2 taken before compression. The inset was taken with a larger magnification.

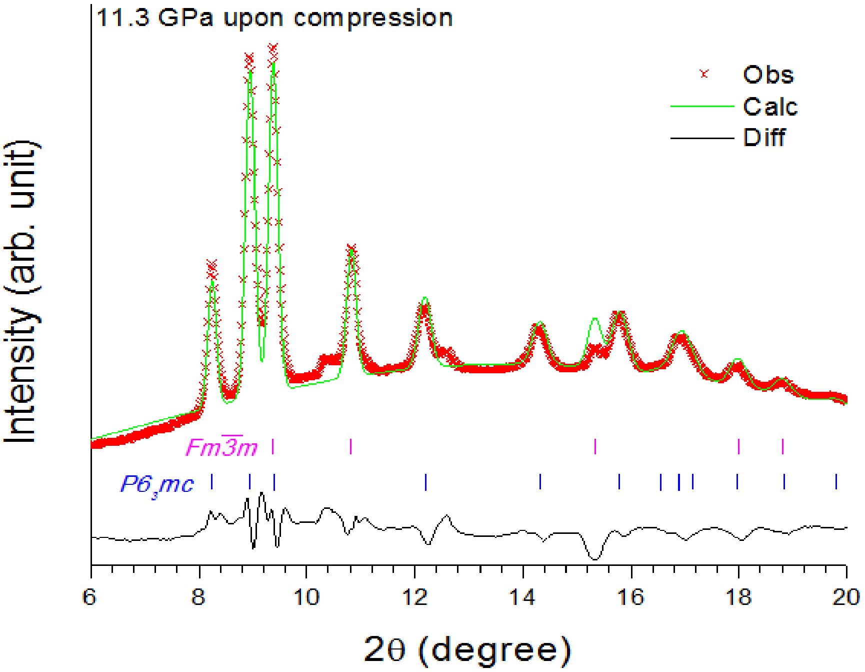

Figure A23 Rietveld refinement of XRD pattern for ZnONW2 at 11.3 GPa on compression. See Fig. A7 for figure caption.

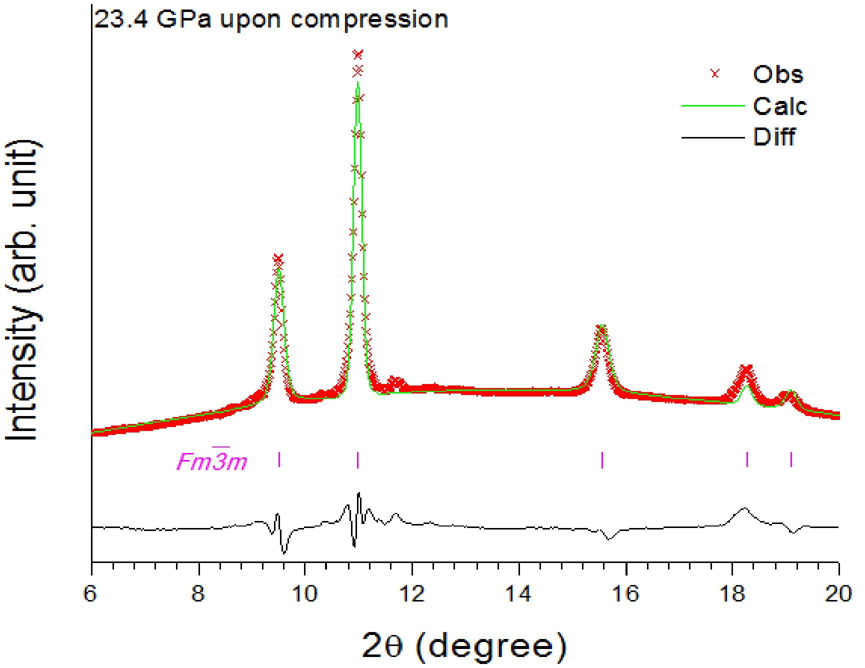

Figure A24 Rietveld refinement of XRD pattern for ZnONW2 at 23.4 GPa on compression. See Fig. A7 for figure caption.

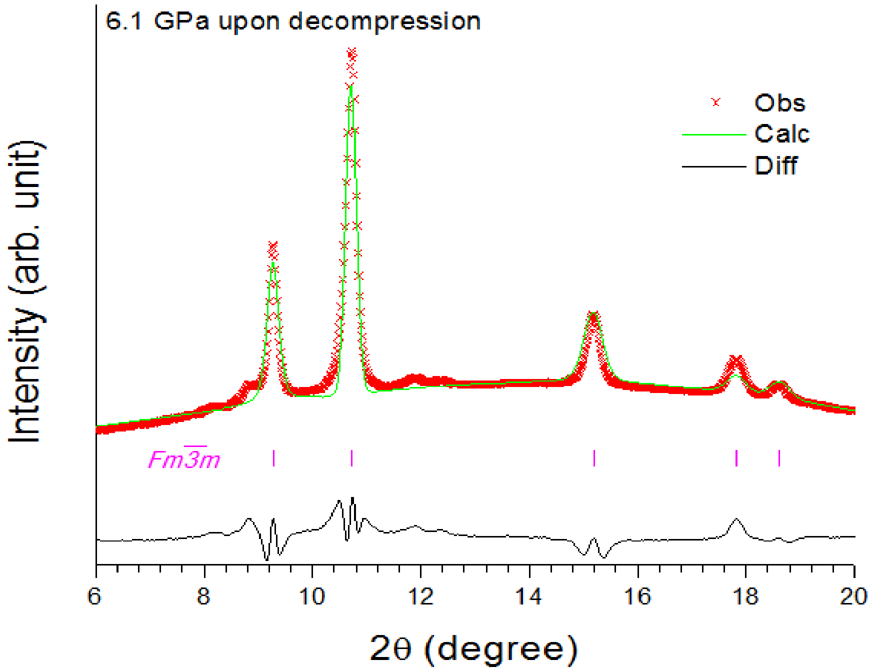

Figure A25 Rietveld refinement of XRD pattern for ZnONW2 at 6.1 GPa on decompression. See Fig. A7 for figure caption.

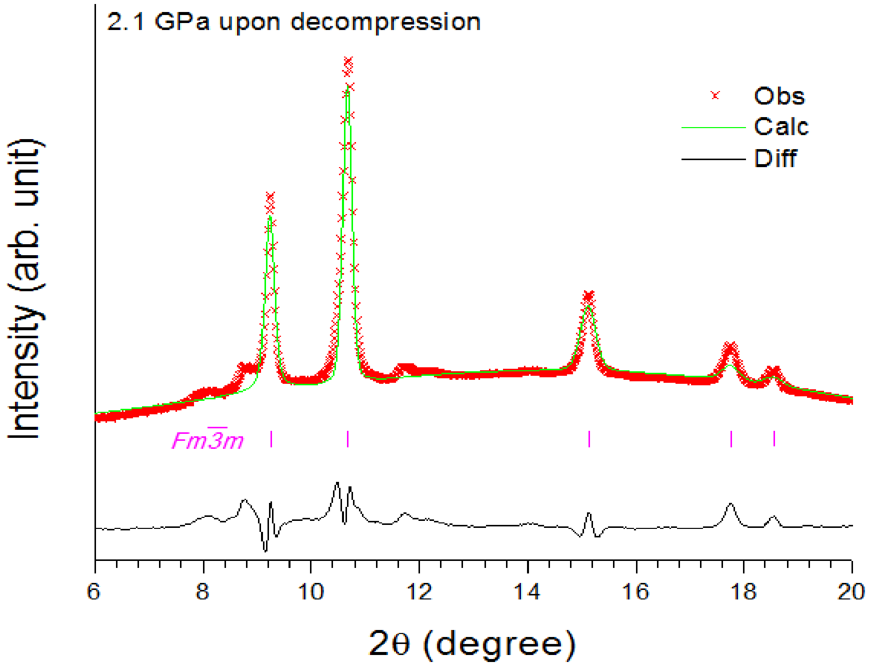

Figure A26 Rietveld refinement of XRD pattern for ZnONW2 at 2.1 GPa on decompression. See Fig. A7 for figure caption.

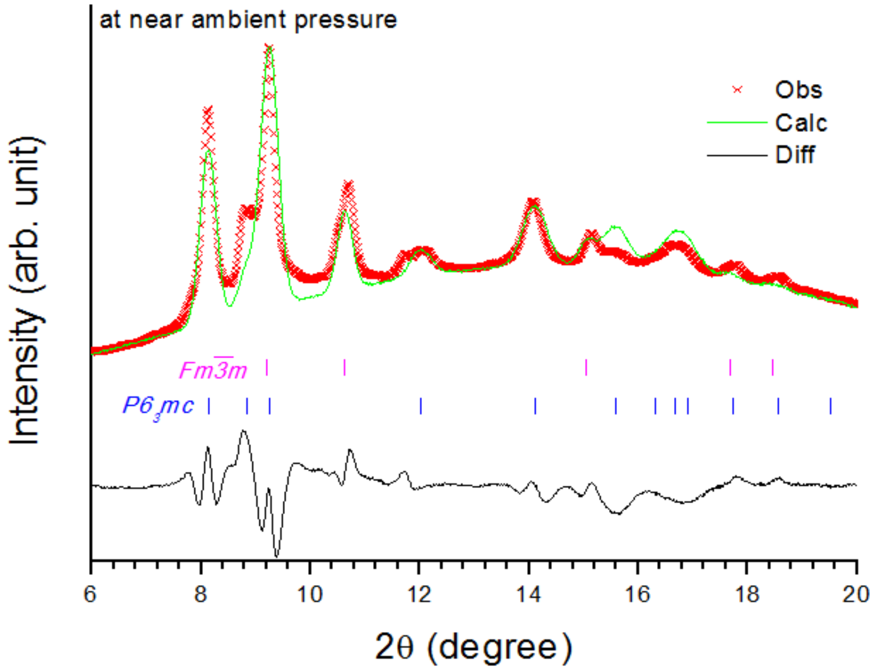

Figure A27 Rietveld refinement of XRD pattern for ZnONW2 at neat ambient pressure on decompression. See Fig. A7 for figure caption.

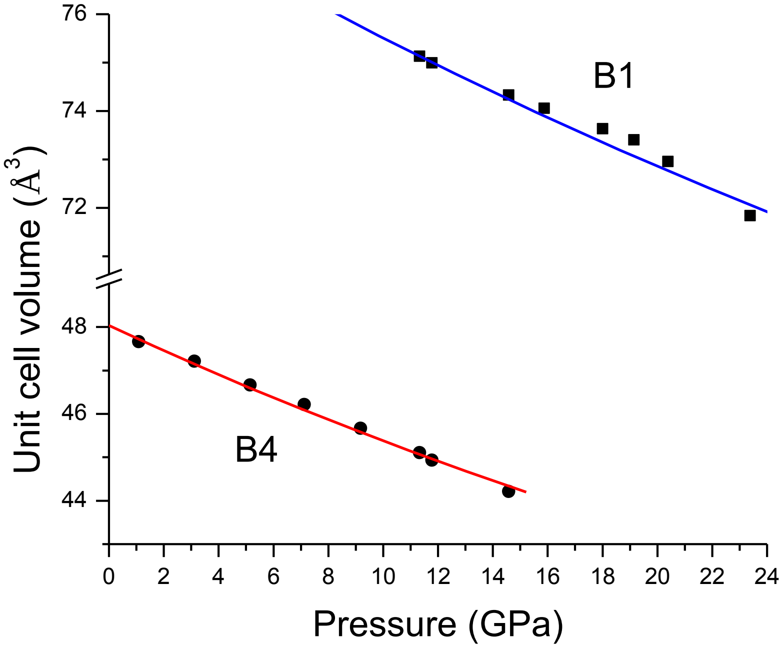

Figure A28 Pressure dependence of the unit cell volume for ZnONW2 at room temperature. Solid circles and solid squares are the experimental data points obtained from this work. Solid lines represent fits to the Birch-Murnaghan equation of state.

A 4.3 Rietveld refinement analysis of ZnONW3

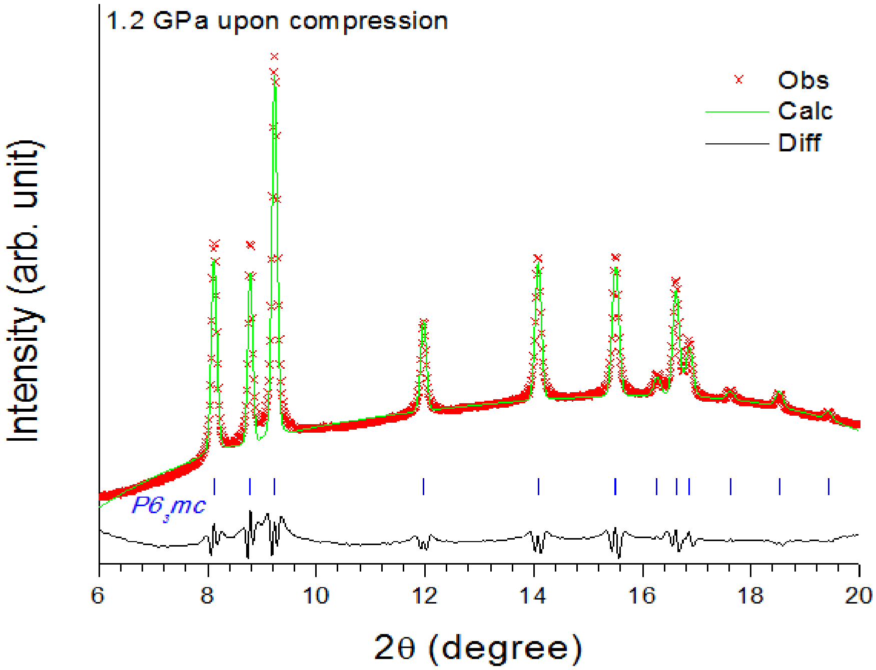

Figure A29 Rietveld refinement of XRD pattern for ZnONW3 at 1.2 GPa on compression. See Fig. A7 for figure caption.

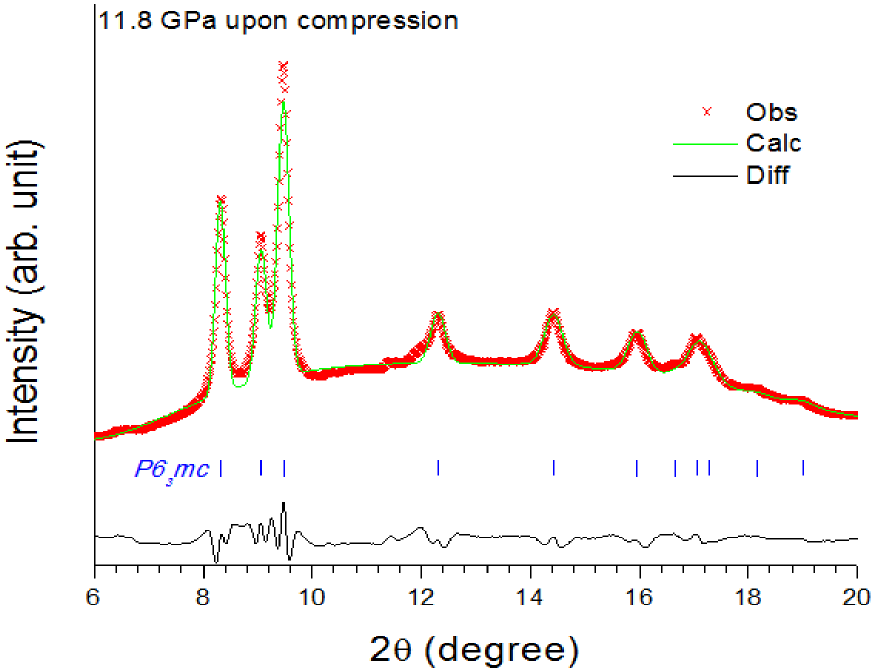

Figure A30 Rietveld refinement of XRD pattern for ZnONW3 at 11.8 GPa on compression. See Fig. A7 for figure caption.

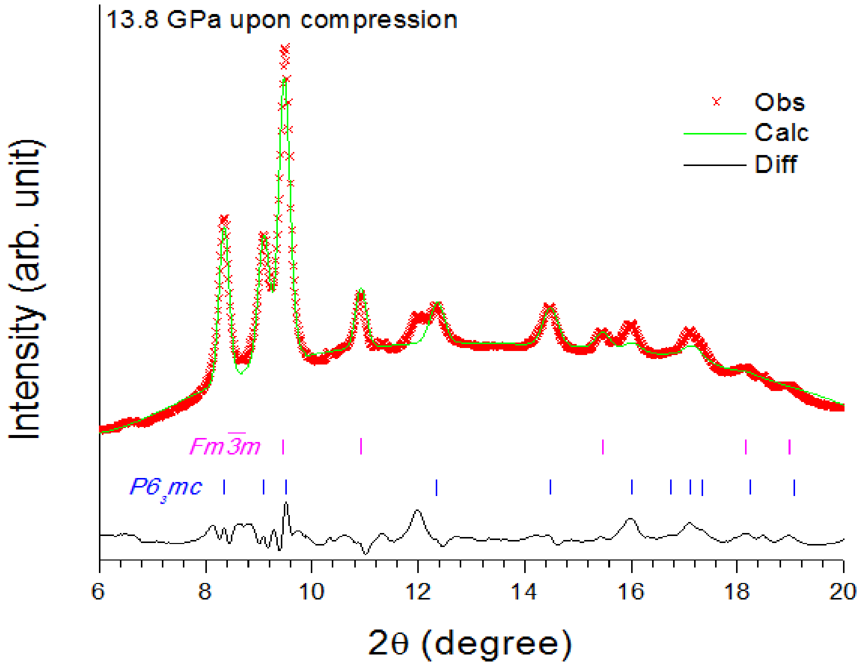

Figure A31 Rietveld refinement of XRD pattern for ZnONW3 at 13.8 GPa on compression. See Fig. A7 for figure caption.

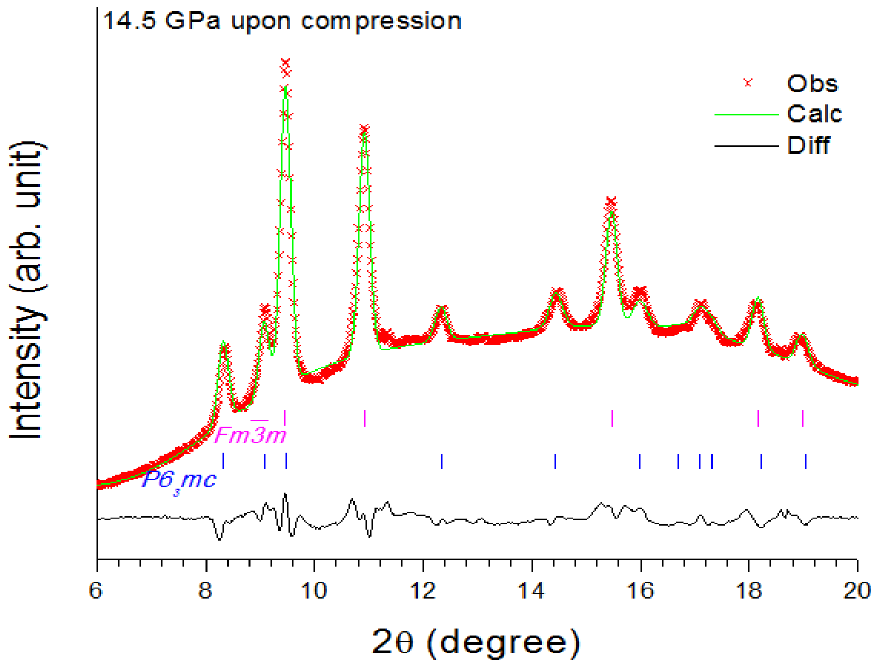

Figure A32 Rietveld refinement of XRD pattern for ZnONW3 at 14.5 GPa on compression. See Fig. A7 for figure caption.

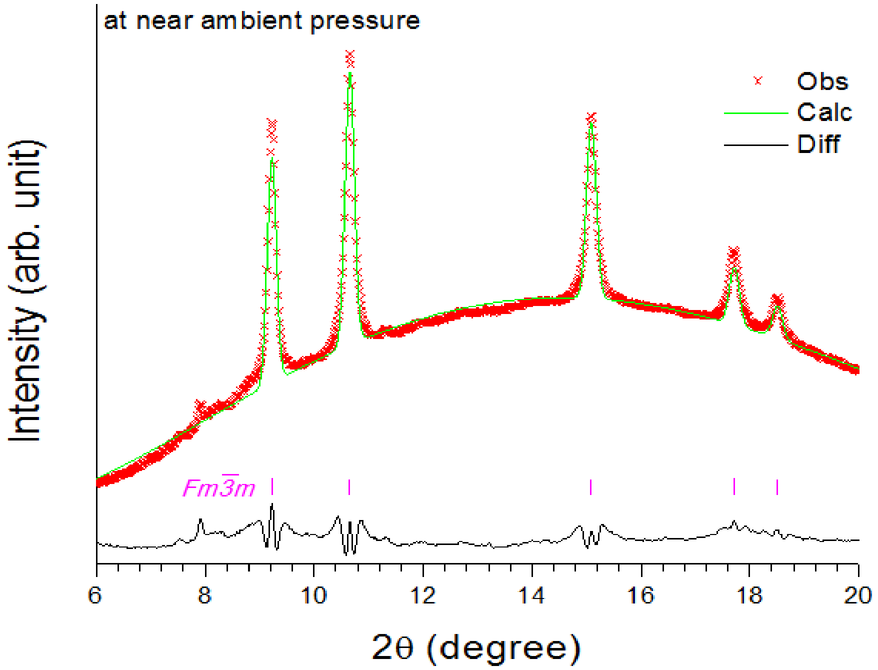

Figure A33 Rietveld refinement of XRD pattern for ZnONW3 at near ambient pressure on decompression. See Fig. A10 for figure caption.

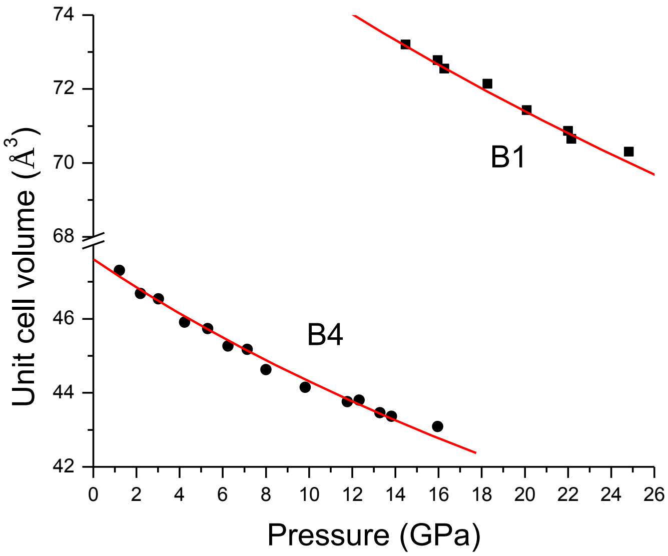

Figure A34 Pressure dependence of the unit cell volume for ZnONW3 at room temperature. Solid circles and solid squares are the experimental data points obtained from this work. Solid lines represent fits to the Birch-Murnaghan equation of state.

Appendix V Copyright Permissions

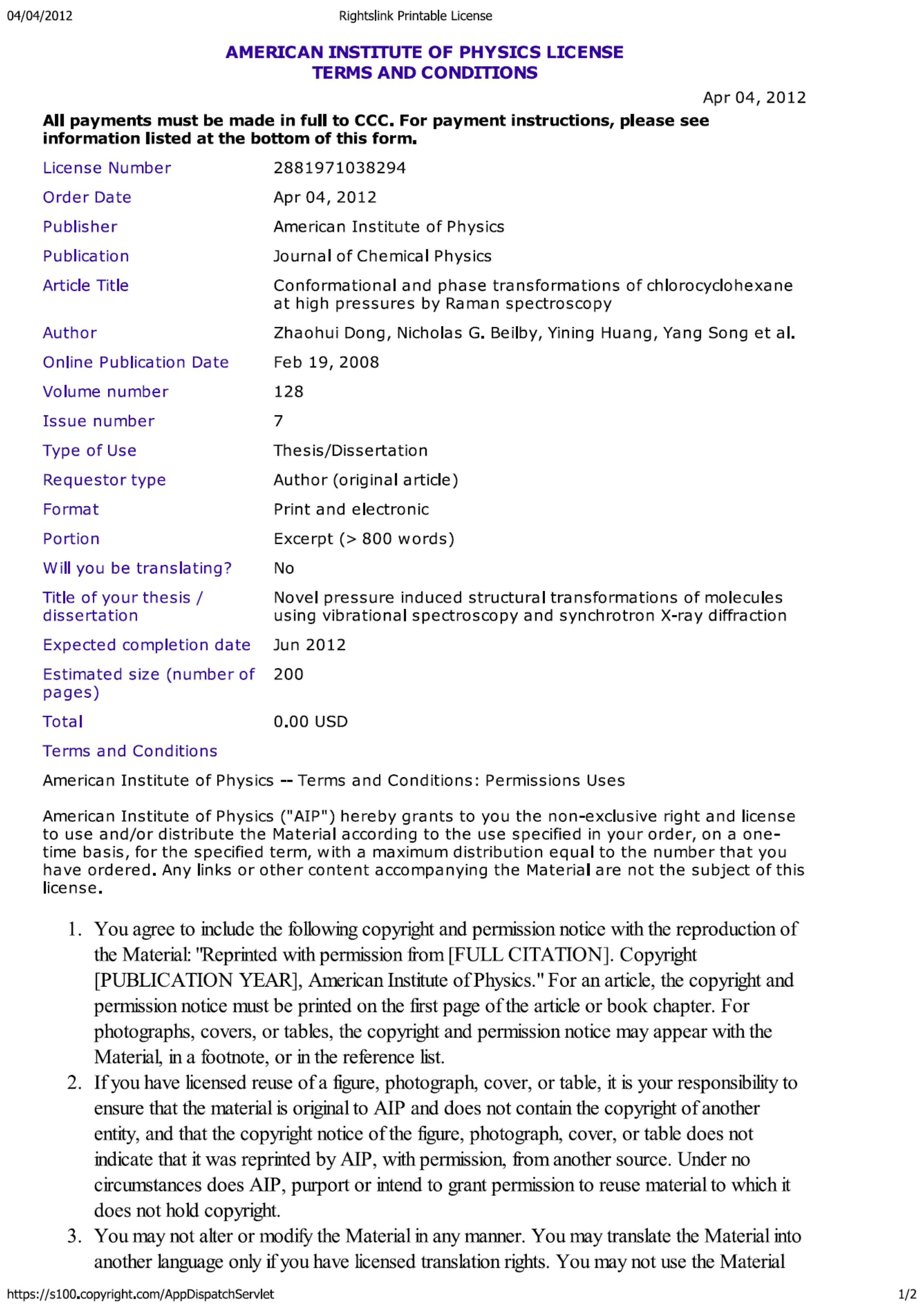

04/04/2012 Rightslink Printable License

AMERICAN INSTITUTE OF PHYSICS LICENSE
TERMS AND CONDITIONS

Apr 04, 2012

All payments must be made in full to CCC. For payment instructions, please see information listed at the bottom of this form.

License Number	2881971038294
Order Date	Apr 04, 2012
Publisher	American Institute of Physics
Publication	Journal of Chemical Physics
Article Title	Conformational and phase transformations of chlorocyclohexane at high pressures by Raman spectroscopy
Author	Zhaohui Dong, Nicholas G. Beilby, Yining Huang, Yang Song et al.
Online Publication Date	Feb 19, 2008
Volume number	128
Issue number	7
Type of Use	Thesis/Dissertation
Requestor type	Author (original article)
Format	Print and electronic
Portion	Excerpt (> 800 words)
Will you be translating?	No
Title of your thesis / dissertation	Novel pressure induced structural transformations of molecules using vibrational spectroscopy and synchrotron X-ray diffraction
Expected completion date	Jun 2012
Estimated size (number of pages)	200
Total	0.00 USD

Terms and Conditions

American Institute of Physics -- Terms and Conditions: Permissions Uses

American Institute of Physics ("AIP") hereby grants to you the non-exclusive right and license to use and/or distribute the Material according to the use specified in your order, on a one-time basis, for the specified term, with a maximum distribution equal to the number that you have ordered. Any links or other content accompanying the Material are not the subject of this license.

1. You agree to include the following copyright and permission notice with the reproduction of the Material: "Reprinted with permission from [FULL CITATION]. Copyright [PUBLICATION YEAR], American Institute of Physics." For an article, the copyright and permission notice must be printed on the first page of the article or book chapter. For photographs, covers, or tables, the copyright and permission notice may appear with the Material, in a footnote, or in the reference list.
2. If you have licensed reuse of a figure, photograph, cover, or table, it is your responsibility to ensure that the material is original to AIP and does not contain the copyright of another entity, and that the copyright notice of the figure, photograph, cover, or table does not indicate that it was reprinted by AIP, with permission, from another source. Under no circumstances does AIP, purport or intend to grant permission to reuse material to which it does not hold copyright.
3. You may not alter or modify the Material in any manner. You may translate the Material into another language only if you have licensed translation rights. You may not use the Material

https://s100.copyright.com/AppDispatchServlet 1/2

for promotional purposes. AIP reserves all rights not specifically granted herein.

4. The foregoing license shall not take effect unless and until AIP or its agent, Copyright Clearance Center, receives the Payment in accordance with Copyright Clearance Center Billing and Payment Terms and Conditions, which are incorporated herein by reference.
5. AIP or the Copyright Clearance Center may, within two business days of granting this license, revoke the license for any reason whatsoever, with a full refund payable to you. Should you violate the terms of this license at any time, AIP, American Institute of Physics, or Copyright Clearance Center may revoke the license with no refund to you. Notice of such revocation will be made using the contact information provided by you. Failure to receive such notice will not nullify the revocation.
6. AIP makes no representations or warranties with respect to the Material. You agree to indemnify and hold harmless AIP, American Institute of Physics, and their officers, directors, employees or agents from and against any and all claims arising out of your use of the Material other than as specifically authorized herein.
7. The permission granted herein is personal to you and is not transferable or assignable without the prior written permission of AIP. This license may not be amended except in a writing signed by the party to be charged.
8. If purchase orders, acknowledgments or check endorsements are issued on any forms containing terms and conditions which are inconsistent with these provisions, such inconsistent terms and conditions shall be of no force and effect. This document, including the CCC Billing and Payment Terms and Conditions, shall be the entire agreement between the parties relating to the subject matter hereof.

This Agreement shall be governed by and construed in accordance with the laws of the State of New York. Both parties hereby submit to the jurisdiction of the courts of New York County for purposes of resolving any disputes that may arise hereunder.

If you would like to pay for this license now, please remit this license along with your payment made payable to "COPYRIGHT CLEARANCE CENTER" otherwise you will be invoiced within 48 hours of the license date. Payment should be in the form of a check or money order referencing your account number and this invoice number RLNK500754295. Once you receive your invoice for this order, you may pay your invoice by credit card. Please follow instructions provided at that time.

Make Payment To:
Copyright Clearance Center
Dept 001
P.O. Box 843006
Boston, MA 02284-3006

For suggestions or comments regarding this order, contact RightsLink Customer Support: customercare@copyright.com or +1-877-622-5543 (toll free in the US) or +1-978-646-2777.

Gratis licenses (referencing $0 in the Total field) are free. Please retain this printable license for your reference. No payment is required.

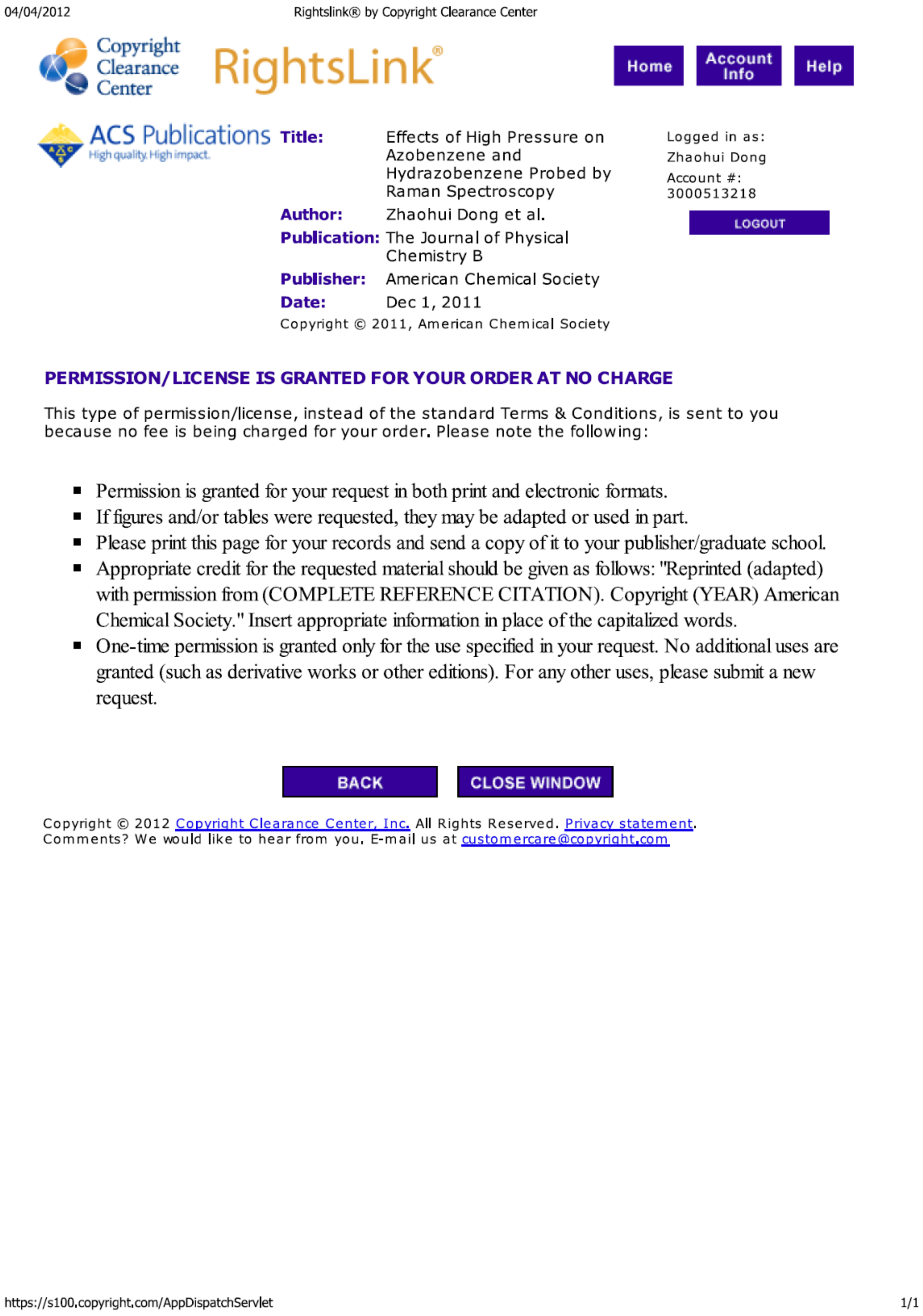

04/04/2012 Rightslink® by Copyright Clearance Center

Title:	Effects of High Pressure on Azobenzene and Hydrazobenzene Probed by Raman Spectroscopy
Author:	Zhaohui Dong et al.
Publication:	The Journal of Physical Chemistry B
Publisher:	American Chemical Society
Date:	Dec 1, 2011

Logged in as:
Zhaohui Dong
Account #:
3000513218

PERMISSION/LICENSE IS GRANTED FOR YOUR ORDER AT NO CHARGE

This type of permission/license, instead of the standard Terms & Conditions, is sent to you because no fee is being charged for your order. Please note the following:

- Permission is granted for your request in both print and electronic formats.
- If figures and/or tables were requested, they may be adapted or used in part.
- Please print this page for your records and send a copy of it to your publisher/graduate school.
- Appropriate credit for the requested material should be given as follows: "Reprinted (adapted) with permission from (COMPLETE REFERENCE CITATION). Copyright (YEAR) American Chemical Society." Insert appropriate information in place of the capitalized words.
- One-time permission is granted only for the use specified in your request. No additional uses are granted (such as derivative works or other editions). For any other uses, please submit a new request.

https://s100.copyright.com/AppDispatchServlet 1/1

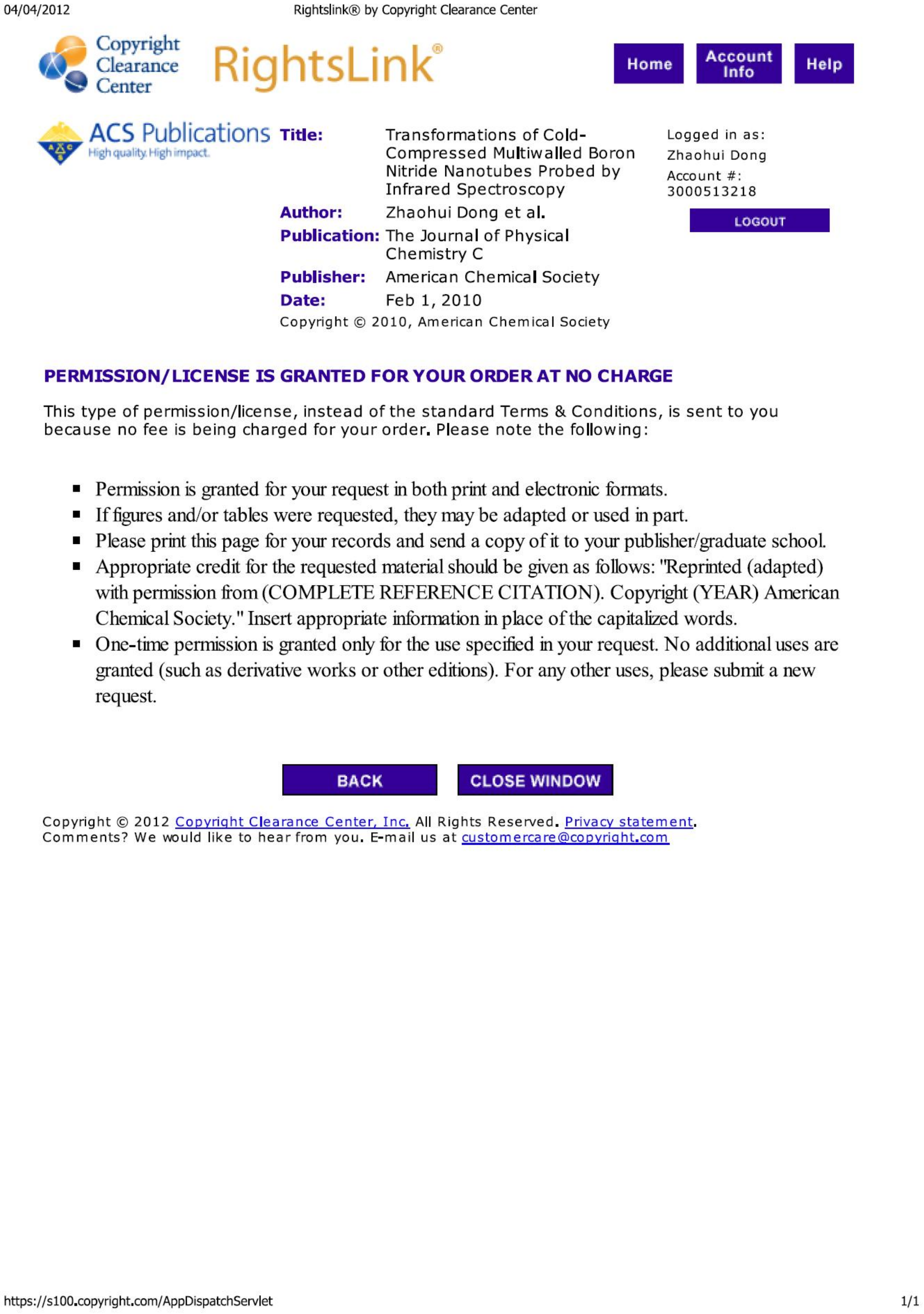

04/04/2012 Rightslink® by Copyright Clearance Center

Title:	Transformations of Cold-Compressed Multiwalled Boron Nitride Nanotubes Probed by Infrared Spectroscopy
Author:	Zhaohui Dong et al.
Publication:	The Journal of Physical Chemistry C
Publisher:	American Chemical Society
Date:	Feb 1, 2010

Copyright © 2010, American Chemical Society

Logged in as:
Zhaohui Dong
Account #:
3000513218

PERMISSION/LICENSE IS GRANTED FOR YOUR ORDER AT NO CHARGE

This type of permission/license, instead of the standard Terms & Conditions, is sent to you because no fee is being charged for your order. Please note the following:

- Permission is granted for your request in both print and electronic formats.
- If figures and/or tables were requested, they may be adapted or used in part.
- Please print this page for your records and send a copy of it to your publisher/graduate school.
- Appropriate credit for the requested material should be given as follows: "Reprinted (adapted) with permission from (COMPLETE REFERENCE CITATION). Copyright (YEAR) American Chemical Society." Insert appropriate information in place of the capitalized words.
- One-time permission is granted only for the use specified in your request. No additional uses are granted (such as derivative works or other editions). For any other uses, please submit a new request.

Copyright © 2012 Copyright Clearance Center, Inc. All Rights Reserved. Privacy statement.
Comments? We would like to hear from you. E-mail us at customercare@copyright.com

https://s100.copyright.com/AppDispatchServlet 1/1

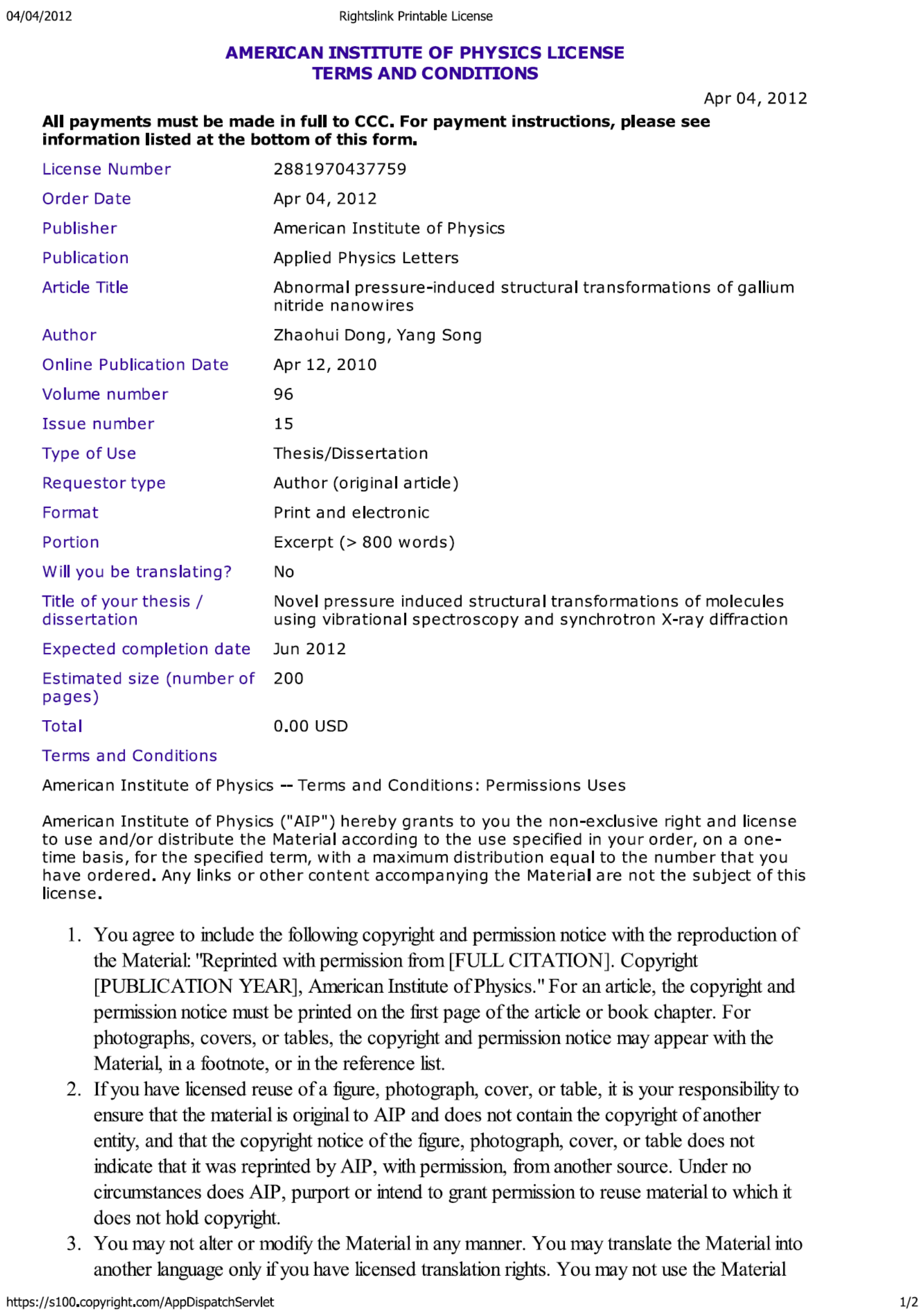

AMERICAN INSTITUTE OF PHYSICS LICENSE
TERMS AND CONDITIONS

Apr 04, 2012

All payments must be made in full to CCC. For payment instructions, please see information listed at the bottom of this form.

License Number	2881970437759
Order Date	Apr 04, 2012
Publisher	American Institute of Physics
Publication	Applied Physics Letters
Article Title	Abnormal pressure-induced structural transformations of gallium nitride nanowires
Author	Zhaohui Dong, Yang Song
Online Publication Date	Apr 12, 2010
Volume number	96
Issue number	15
Type of Use	Thesis/Dissertation
Requestor type	Author (original article)
Format	Print and electronic
Portion	Excerpt (> 800 words)
Will you be translating?	No
Title of your thesis / dissertation	Novel pressure induced structural transformations of molecules using vibrational spectroscopy and synchrotron X-ray diffraction
Expected completion date	Jun 2012
Estimated size (number of pages)	200
Total	0.00 USD

Terms and Conditions

American Institute of Physics -- Terms and Conditions: Permissions Uses

American Institute of Physics ("AIP") hereby grants to you the non-exclusive right and license to use and/or distribute the Material according to the use specified in your order, on a one-time basis, for the specified term, with a maximum distribution equal to the number that you have ordered. Any links or other content accompanying the Material are not the subject of this license.

1. You agree to include the following copyright and permission notice with the reproduction of the Material: "Reprinted with permission from [FULL CITATION]. Copyright [PUBLICATION YEAR], American Institute of Physics." For an article, the copyright and permission notice must be printed on the first page of the article or book chapter. For photographs, covers, or tables, the copyright and permission notice may appear with the Material, in a footnote, or in the reference list.
2. If you have licensed reuse of a figure, photograph, cover, or table, it is your responsibility to ensure that the material is original to AIP and does not contain the copyright of another entity, and that the copyright notice of the figure, photograph, cover, or table does not indicate that it was reprinted by AIP, with permission, from another source. Under no circumstances does AIP, purport or intend to grant permission to reuse material to which it does not hold copyright.
3. You may not alter or modify the Material in any manner. You may translate the Material into another language only if you have licensed translation rights. You may not use the Material

for promotional purposes. AIP reserves all rights not specifically granted herein.

4. The foregoing license shall not take effect unless and until AIP or its agent, Copyright Clearance Center, receives the Payment in accordance with Copyright Clearance Center Billing and Payment Terms and Conditions, which are incorporated herein by reference.
5. AIP or the Copyright Clearance Center may, within two business days of granting this license, revoke the license for any reason whatsoever, with a full refund payable to you. Should you violate the terms of this license at any time, AIP, American Institute of Physics, or Copyright Clearance Center may revoke the license with no refund to you. Notice of such revocation will be made using the contact information provided by you. Failure to receive such notice will not nullify the revocation.
6. AIP makes no representations or warranties with respect to the Material. You agree to indemnify and hold harmless AIP, American Institute of Physics, and their officers, directors, employees or agents from and against any and all claims arising out of your use of the Material other than as specifically authorized herein.
7. The permission granted herein is personal to you and is not transferable or assignable without the prior written permission of AIP. This license may not be amended except in a writing signed by the party to be charged.
8. If purchase orders, acknowledgments or check endorsements are issued on any forms containing terms and conditions which are inconsistent with these provisions, such inconsistent terms and conditions shall be of no force and effect. This document, including the CCC Billing and Payment Terms and Conditions, shall be the entire agreement between the parties relating to the subject matter hereof.

This Agreement shall be governed by and construed in accordance with the laws of the State of New York. Both parties hereby submit to the jurisdiction of the courts of New York County for purposes of resolving any disputes that may arise hereunder.

If you would like to pay for this license now, please remit this license along with your payment made payable to "COPYRIGHT CLEARANCE CENTER" otherwise you will be invoiced within 48 hours of the license date. Payment should be in the form of a check or money order referencing your account number and this invoice number RLNK500754288. Once you receive your invoice for this order, you may pay your invoice by credit card. Please follow instructions provided at that time.

Make Payment To:
Copyright Clearance Center
Dept 001
P.O. Box 843006
Boston, MA 02284-3006

For suggestions or comments regarding this order, contact RightsLink Customer Support: customercare@copyright.com or +1-877-622-5543 (toll free in the US) or +1-978-646-2777.

Gratis licenses (referencing $0 in the Total field) are free. Please retain this printable license for your reference. No payment is required.

Copyright Clearance Center RightsLink®

Home | Account Info | Help

ACS Publications
High quality. High impact.

Title: Pressure-Induced Structural Transformations of ZnO Nanowires Probed by X-ray Diffraction

Author: Zhaohui Dong et al.

Publication: The Journal of Physical Chemistry C

Publisher: American Chemical Society

Date: Jan 1, 2012

Copyright © 2012, American Chemical Society

Logged in as:
Zhaohui Dong
Account #:
3000513218

LOGOUT

PERMISSION/LICENSE IS GRANTED FOR YOUR ORDER AT NO CHARGE

This type of permission/license, instead of the standard Terms & Conditions, is sent to you because no fee is being charged for your order. Please note the following:

- Permission is granted for your request in both print and electronic formats.
- If figures and/or tables were requested, they may be adapted or used in part.
- Please print this page for your records and send a copy of it to your publisher/graduate school.
- Appropriate credit for the requested material should be given as follows: "Reprinted (adapted) with permission from (COMPLETE REFERENCE CITATION). Copyright (YEAR) American Chemical Society." Insert appropriate information in place of the capitalized words.
- One-time permission is granted only for the use specified in your request. No additional uses are granted (such as derivative works or other editions). For any other uses, please submit a new request.

BACK | CLOSE WINDOW

Curriculum Vitae

Name: Zhaohui Dong

Post-secondary Education and Degrees:

University of Western Ontario
London, Ontario, Canada
2008 – 2012 Ph.D.

University of Western Ontario
London, Ontario, Canada
2006 – 2008 M.Sc.

University of Science and Technology of China
Hefei, Anhui, P.R.China
2002 – 2006 B.Sc.

Honors and Awards:

Western Graduate Research Scholarship
University of Western Ontario
2006 – 2008, 2009 – 2010, 2011 – 2012

CSC 2004 Travel Award for the year 2011
University of Western Ontario
2010 – 2011

Young Scientist Travel Awards
By Pacifichem2010 symposium # 239 (IUCr)
2009 – 2010

Chinese Government Award for Outstanding Self-financed Student Abroad
Chinese Scholarship Council
2009 – 2010

Robert and Ruth Lumsden Graduate Awards in Science
University of Western Ontario
2009 – 2010

Graduate Thesis Research Award
University of Western Ontario
2009 – 2010

Excellent Student Scholarship of Grade 3
University of Science and Technology of China
2004 – 2005

Excellent Student Scholarship of Grade 2

University of Science and Technology of China
2003 – 2004

Related Work Experience:
Teaching Assistant/Research Assistant
University of Western Ontario
2006 – 2012

Publications:

Book Chapter

1. Yang Song and **Zhaohui Dong**, Novel pressure-induced structural transformations of inorganic nanowires in book “Nanowires”, ed. A. Hashim, *Intech*, **2011**, ISBN 978-953-307-327-9, P527-552.

Journal Articles

2. **Dong Z.**, Zhuravlev K. K., Morin S., Li L., Jin S., and Song Y., Pressure-induced structural transformations of ZnO nanowires probed by X-ray diffraction, *J. Phys. Chem. C*, **2012**, *116*, 2102.
3. **Dong Z.**, Seemann M. N., Lu N., and Song Y., Effects of high pressure on azobenzene and hydrazobenzene probed by Raman spectroscopy, *J. Phys. Chem. B*, **2011**, *115*, 14912.
4. **Dong Z.**, and Song Y., Abnormal pressure-induced structural transformations of gallium nitride nanowires, *Appl. Phys. Lett.*, **2010**, *96*, 151903.
5. **Dong Z.**, and Song Y., Transformations of cold-compressed multi-walled boron nitride nanotube probed by infrared spectroscopy, *J. Phys. Chem.*, **2010**, *114*, 1782.
6. Zhuravlev K. K., Traikov K., **Dong Z.**, Xie S., Song Y., and Liu Z., Raman and infrared spectroscopy of pyridine under high pressure, *Phys. Rev. B.*, **2010**, *82*, 064116.
7. **Dong Z.**, and Song Y., Pressure-induced morphology-dependent phase transformations of nanostructured tin dioxide, *Chem. Phys. Lett.*, **2009**, *480*, 90.
8. **Dong Z.**, Beiby N. G., Huang Y., and Song Y., Conformational and phase transformations of chlorocyclohexane at high pressure by Raman spectroscopy, *J. Chem. Phys. C.*, **2008**, *128*, 125108
9. Safa M., **Dong Z.**, Song Y., and Huang Y., Examining the structural changes in $Fe_2(CO)_9$ under high external pressures by Raman spectroscopy, *Can. J. Chem.*, **2007**, *85*, 866.

Presentations:

Oral Presentations

1. **Dong Z.** and Song Y., Pressure-induced structural transformations of ZnO nanowires probed by X-ray diffraction, the 94th CSC, Montreal, Québec, Canada. (06/2011).
2. **Dong Z.** , Zhuravlev K. K., Jin S., and Song Y., Pressure-induced structural transformation of ZnO nanowires probed by X-ray diffraction, Pacifichem 2010, Honolulu, Hawaii, US. (12/2010)
3. **Dong Z.** and Song Y., Novel pressure-induced transformations observed

in boron nitride nanotubes, the 92nd CSC, Hamilton, Ontario, Canada. (05/2009).

4. **Dong Z.** and Song Y., High pressure study of nanostructured SnO_2 by Raman spectroscopy and X-ray diffraction with synchrotron radiation, the 91st CSC, Edmonton, Albert, Canada. (05/2008).

Poster Presentations

5. **Dong Z.** and Song Y., *In-situ* high-pressure study of GaN nanowire by X-ray diffraction, CAMBR distinguished lecture and research day, London, Ontario, Canada. (06/2011)
6. **Dong Z.** and Song Y., Abnormal pressure-induced structural transformations of gallium nitride nanowires, the 93rd CSC, Toronto, Ontario, Canada. (05/2010)
7. Zhuravlev K. K., **Dong Z.**, and Song Y., *In-situ* high pressure study of PbS nanowire by X-ray diffraction, the 93rd CSC, Toronto, Ontario, Canada. (05/2010)
8. **Dong Z.** and Song Y., *In-situ* high-pressure study of GaN nanowire by X-ray diffraction, Workshop “Advances in X-ray diffraction and scattering, Guelph, Ontario, Canada. (10/2009)
9. **Dong Z.** and Song Y., *In-situ* high-pressure study of GaN nanowire by X-ray diffraction, the international union of crystallography (ICUr), Harbin, P. R. China. (07/2009)

Graduate-level Courses:	Synchrotron radiation (2006) Topics in surface science (2007) Seminar (2007) Crystallograhy I (2008) Structural chemistry of solid materials (2008) Nanomaterials and nanotechnology (2010) Condensed matter physics (2011)